1982

Effect of particle shape on prediction of velocity-voidage relationship in fluidized solid-liquid systems

Anthonisamy Herman Dharmarajah
Iowa State University

Dharmarajah, Anthonisamy Herman

EFFECT OF PARTICLE SHAPE ON PREDICTION OF VELOCITY-VOIDAGE RELATIONSHIP IN FLUIDIZED SOLID-LIQUID SYSTEMS

Iowa State University PH.D. 1982

PLEASE NOTE:

In all cases this material has been filmed in the best possible way from the available copy. Problems encountered with this document have been identified here with a check mark ✓.

1. Glossy photographs or pages _____
2. Colored illustrations, paper or print _____
3. Photographs with dark background _____
4. Illustrations are poor copy _____
5. Pages with black marks, not original copy _____
6. Print shows through as there is text on both sides of page _____
7. Indistinct, broken or small print on several pages ✓
8. Print exceeds margin requirements _____
9. Tightly bound copy with print lost in spine _____
10. Computer printout pages with indistinct print _____
11. Page(s) _____ lacking when material received, and not available from school or author.
12. Page(s) _____ seem to be missing in numbering only as text follows.
13. Two pages numbered _____. Text follows.
14. Curling and wrinkled pages _____
15. Other _____

Effect of particle shape on prediction of velocity-voidage relationship in fluidized solid-liquid systems

by

Anthonisamy Herman Dharmarajah

A Dissertation Submitted to the

Graduate Faculty in Partial Fulfillment of the

Requirements for the Degree of

DOCTOR OF PHILOSOPHY

Department: Civil Engineering
Major: Sanitary Engineering

Approved:

Signature was redacted for privacy.

In Charge of Major Work

Signature was redacted for privacy.

For the Major Department

Signature was redacted for privacy.

For the Graduate College

Iowa State University
Ames, Iowa
1982

TABLE OF CONTENTS

LIST OF FIGURES

Page

LIST OF TABLES

LIST OF SYMBOLS

A asymptotic value of u_R at low Reynolds number Re_t

$A1$ function $\dfrac{\varepsilon^3}{(1-\varepsilon)^2}\ \dfrac{\rho(\rho_s-\rho)g}{S^3\mu^2}$

A_p projected area of a particle perpendicular to the direction of motion

a longest triaxial dimension of a irregular particle

B asymptotic value of u_R at high Reynolds number Re_t

B_o function $\dfrac{u_N^3\rho^2}{g\mu(\rho_s-\rho)}$

b intermediate triaxial dimension of a irregular particle

C_D drag coefficient

$C_{D\phi}$ function $\dfrac{4d(\rho_s-\rho)g}{3\mu\, u_{t\infty}^2}\ \left[\dfrac{\varepsilon^3}{1+(1-\varepsilon)^{1/3}}\right]$

c shortest triaxial dimension of a irregular particle

D_M maximum diameter of a bubble in a fluidized bed

D_T diameter of column or bed

d diameter of a spherical particle

d_a diameter of a circle having the same area as the projected area of the particle when resting in the most stable position

d_e effective diameter

d_m arithmetic mean of two adjacent sieve openings

d_s diameter of a sphere having the same surface area as the particle

d_{cs} diameter of the smallest circle which circumscribes the projected outline of the particle

d_{eq} equivalent diameter of a sphere of same volume as the non-spherical particle

d_{gm} geometric mean of the two adjacent sieve openings

f friction factor

f_1 Heywood's surface area coefficient

F_D drag force

F_k drag force of fluid acting on a constituent sphere in a multi-particle system

g acceleration due to gravity

G mass flow rate based on superficial velocity

Ga Galileo number = $\dfrac{d^3(\rho_s - \rho)\rho g}{\mu^2}$

G_{mf} mass flow rate at minimum fluidization

k Stokes law correction factor = $\dfrac{\text{actual settling velocity}}{\text{settling velocity given by Stokes law}}$

k'' Kozeny's coefficient

L depth of bed

N number of particles

n slope of log u versus log ε plot

Re Reynolds number based on superficial velocity = $\dfrac{\rho u d}{\mu}$

Re_i Reynolds number based on intercept velocity u_i

Re_t Reynolds number based on terminal settling velocity in a column

$Re_{t\infty}$ Reynolds number based on terminal settling velocity in an infinite fluid

Re_N Reynolds number based on velocity u_N

Re_1 Blake's modified Reynolds number = $\dfrac{\rho u}{S\mu(1 - \varepsilon)}$

Re_{mf} Reynolds number at minimum fluidization

Re_ϕ Barnea and Mizrahi's modified Reynolds number = $\dfrac{\rho\, ud}{\mu\varepsilon^{\exp\left(\frac{5(1-\varepsilon)}{3\varepsilon}\right)}}$

S specific surface = particle surface area per unit volume

S' surface area of the particle

s surface area of equivalent volume sphere

SF triaxial dimension shape factor = $\dfrac{c}{\sqrt{ab}}$

u superficial velocity

u_i velocity intercept at porosity ratio of one of log u vs. log ε plot

u_R velocity ratio $\dfrac{u/\varepsilon}{u_t}$

u_t terminal settling velocity in a column

$u_{t\infty}$ terminal settling velocity in an infinite fluid

u_{mf} minimum fluidization velocity expressed as superficial velocity

u_N terminal settling velocity of a sphere of diameter d_{eq}

W_i weight of i^{th} layer

x subscript denotes the 'x' component

y subscript denotes the 'y' component

Z Heywood's volume coefficient = $\dfrac{\pi d_{eq}^3/6}{d_a^3}$

Greek Symbols

γ_s specific weight of particle

ε porosity ratio

ε_e effective porosity

ε_{mf} porosity at minimum fluidization

μ fluid viscosity

ρ fluid density

ρ_b bulk density

ρ_s particle density

ψ sphericity = ratio of surface area of equivalent volume sphere to actual surface area of the particle

ψ_{opt} operation sphericity

ψ_{max} maximum projected area sphericity

Ω hydraulically equivalent diameter shape factor = d_h/d_{eq}

ABBREVIATIONS

Centimeter	cm
Centi poise	cp
Cubic centimeter	cm^3
Cubic feet per minute	ft^3/min
Degree(s) of celsius	c
Feet	ft
Gallon(s) per minute	gpm
Gram(s)	g
Hour(s)	hr
Inche(s)	in
Logarithm to the base 10	log
Milliliter(s)	ml
Millimeter(s)	mm
Pound(s)	lb
Pounds per square inch	psi
Second(s)	sec
Standard cubic feet per minute	SCFM

INTRODUCTION AND SPECIFIC AIMS

Until recent times in Sanitary Engineering, the fluidization process found its application only in backwashing of granular filters. Backwashing of granular filters is the usual way to clean the filters to remove the solids accumulated in the pores of the filter during the filtration process. Fluidized beds are now being used in denitrification and some other wastewater treatment processes. The advantages in using fluidized bed reactors for those processes in wastewater treatment is that,

1. greater surface area for growth per unit reactor volume
2. smaller head loss
3. no danger of clogging.

This study does not deal with the treatment aspect of fluidized beds, but the void ratio at which the fluidized bed should be operated for maximum efficiency is crucial. The mass, momentum and heat transfer rates in a fluidized bed reach a maximum value at a optimum porosity ratio which is usually near 0.7. Even for backwashing of granular filters the maximum shear force on the grains occur at a optimum porosity around 0.7. There are several mathematical models available to predict the velocity-voidage relationship of spherical particles. However, most of the media used in fluidized beds are not spherical. Very few models are available to predict the velocity-voidage relation during fluidization of non-spherical materials. Some of these models are specific for the materials used by the investigator.

Some of the empirical models, because of the limited data used in deriving a particular model, have given rise to less than satisfactory or sometimes unsatisfactory correlations. One of the objectives of this study was to gather data reported by several investigators and attempt to formulate a prediction model encompassing most of those data. The use of a large data set is expected to eliminate to some extent, the possibility of reaching any erroneous conclusions.

From the principles of similitude, it can be shown that a model valid for a system of spherical particles is rigorously valid for a system of non-spherical particles only if the latter system is dynamically and geometrically similar to that of the spheres. Thus, the characteristic length parameter or equivalent diameter of a non-spherical particle must be related to the diameter of a similarly moving spherical particle by a suitable scale factor, usually termed a shape factor. Four different shape parameters are tried in this work. They are sphericity (ψ), Dynamic Shape Factor (DSF), hydraulically equivalent diameter shape factor (Ω), and Heywood's volume coefficient (Z).

In general, the specific aims of this study are to:

1. Develop a model to predict velocity-voidage relationships during liquid fluidization using the relationship between a voidage function and modified Reynolds number. The voidage function is similar to packed bed friction factor. The advantage of using such a prediction equation is that the terminal settling velocity of the particle is not required.

2. Evaluate how different shape factors perform for predicting velocity-voidage relationship during liquid fluidization of non-spherical particles.

3. Measure sphericity of angular material by air permeability measurements and compare the results with values obtained from fixed bed water permeability data.

4. Check the adequacy of the Cleasby and Fan model (32) for the data gathered from different sources and the experiments conducted herein, and possibly improve it by using a larger data set.

5. Check whether the Garside and Al-Dibouni logistic model (54) for predicting the velocity-voidage relationship for spherical particles could be extended to non-spherical particles.

6. Check whether Beranek and Klumpar method (19) of correlating fluidization data of non-spherical particles is satisfactory.

REVIEW OF LITERATURE

General

Fluidization, which had its beginning in the oil industry, is now being successfully employed in many and quite unrelated fields due to its many inherent advantages. The discipline of Chemical Engineering, within the last three decades, has built a large reservoir of literature on many aspects of fluidization. A newcomer to this area is greatly benefited by these early works.

Fluidization spans the region between the flow through packed bed and discrete particle settling. Any attempt to study fluidized beds is either based on the flow through a packed bed (inner problem) or on discrete particle settling (outer problem). Therefore, it is reasonable to expect the fluidized systems behavior to be influenced by the properties of flow through packed beds and by the behavior of discrete particle settling.

The Motion of a Single Particle in Fluids

The literature dealing with the motion of particles in fluids or of fluids past particles contain a number of intriguingly detailed analyses of boundary-layer theory in laminar and turbulent flow; wakes; vortices; skin friction; profile drag; mean free path; and terminal and pick-up velocities. Each has its region of major significance, and interrelations with commonly observed process phenomenon are continuously being sought to strengthen the fundamental approach to design problems.

The analysis of single particle dynamics lends itself quite well to theoretical as well as experimental treatment and thus offers a firm reference point for the study of more complex multi-particle systems.

Drag force

The cause of the drag force on a particle moving in fluid can be explained using the principles of both laminar and turbulent flow.

Laminar flow Laminar flow is a result of the fluid property, viscosity, which may be defined as that property of a liquid or gas which gives rise to an internal stress opposing deformation of the fluid during flow. Viscosity may also be defined as the ratio of the gradient of momentum flux to the rate of diffusion of momentum per unit area in the direction of the gradient. Any relative motion between a particle and the fluid causes internal viscous stress in the fluid medium and produces a deformation of fluid adjacent to the particle. Drag on the particle is a result of transfer of momentum by molecular diffusion from the moving particle to the fluid.

Turbulent flow The distinction between laminar and turbulent flow can be made by considering the difference between the molecular diffusion of momentum as compared to turbulent diffusion of momentum. The diffusion by molecular action is sufficiently slow that its effect may be felt over a widespread region. Turbulent diffusion, however, is a result of the gradient of momentum flux being so great that the flow becomes unorderly and turbulent mixing results. With turbulent diffusion, finite masses of fluid are moving in somewhat random fashion

through the fluid and the mixing process is much more rapid and intense. These phenomena are involved to varying extents in the different types of drag experienced by falling particles.

One of the important variables associated with drag is the Reynolds number which is the ratio of inertia forces to the viscous forces involved in the flow, and may be used as a criterion for determining the type of drag which exist on a falling particle.

Cause of drag The drag forces on a particle are a result either one or both of: (1) The shear along the boundary of the particle in the direction of motion. This is called surface drag. (2) The pressure difference between the upstream and downstream side of the particle. This is called the pressure drag.

The drag resulting from shear along the boundary in the direction of motion is of secondary importance except for small particles with low particle Reynolds numbers.

Discussion of C_D vs. $Re_{t\infty}$ relationship

The drag on the particle can be classified as one or a combination of two different types of drag.

1. Deformation drag which is a combination of surface drag and pressure drag.
2. Form drag which is entirely due to pressure drag.

Deformation drag is principally the result of viscous forces and is characterized by a flow pattern where the deformation of the fluid laminae is widespread. Form drag results from inertial forces and is

characterized by a flow pattern in which there is a separation. The relative importance of these two types of drag depends on the particle Reynolds number.

Low particle Reynolds numbers At low particle Reynolds numbers (for spheres, $Re_{t\infty} < 0.2$, the Reynolds number based on the settling velocity of the particle in an infinite fluid) the effects of the inertial forces caused by the motion of the particle may be ignored and the drag on the body is exclusively one of deformation, caused by viscous stress. Deformation drag may be divided further as a combination of surface drag due to boundary shear and pressure drag due to the shape of the projected area. The motion in this range of particle Reynolds numbers is characterized by a widespread distortion of the basic flow pattern and is defined mathematically by Stoke's Law for spheres. Theoretically, it can be shown one-third of the drag on a sphere is due to pressure difference and two-thirds is due to boundary shear. Furthermore, it can be shown that in the direction of motion the sum of the shear and pressure difference is the same at all points of the body. For a thin cylindrical disc falling flat face down, however, the viscous drag is entirely due to the pressure difference, since it has no boundary in the direction of motion to produce shear stress.

Intermediate Reynolds numbers As the Reynolds number is increased to the range of $0.2 < Re_{t\infty} < 1000$, the viscous flow pattern is disrupted and the inertial forces gradually assume greater importance. The region of viscous flow, though still present, is confined

to a relatively thin layer at the surface of the particle known as the boundary layer. Outside the boundary layer the flow is laminar but the inertial forces predominate. The shape of the particle determines to a large extent the path taken by the fluids as it flows about the particle, hence determines the radial and tangential accelerations necessary for the fluid to travel this path.

As a result of the instability of the laminar flow and increased importance of the inertial forces, a zone of separation is formed downstream side of the particle as shown in Figure 1. This separation has a poorly defined appearance at $Re_{t\infty} = 3$ but gradually takes on a more clearly defined appearance as the Reynolds number is increased, until at $Re_{t\infty} = 20$ the separation zone has a well-defined vortex pattern downstream from the particle.

Separation occurs at the point where the flow is expanding (streamlines are spreading) and the local velocity in the boundary layer becomes zero. Any further expansion of the boundary layer causes flow near the boundary layer in the reverse direction to the main stream flow. The point of separation may occur at any position along the boundary of the particle (as in the case of a sphere) or the point of separation may be fixed always by a sudden change in curvature of the boundary of the particle (as in the case of a disk).

Thus in the intermediate range of Reynolds number, the type of drag gradually changes from about half surface drag and half pressure drag ($Re_{t\infty} = 0.5$) to almost exclusively pressure drag ($Re_{t\infty} = 1000$).

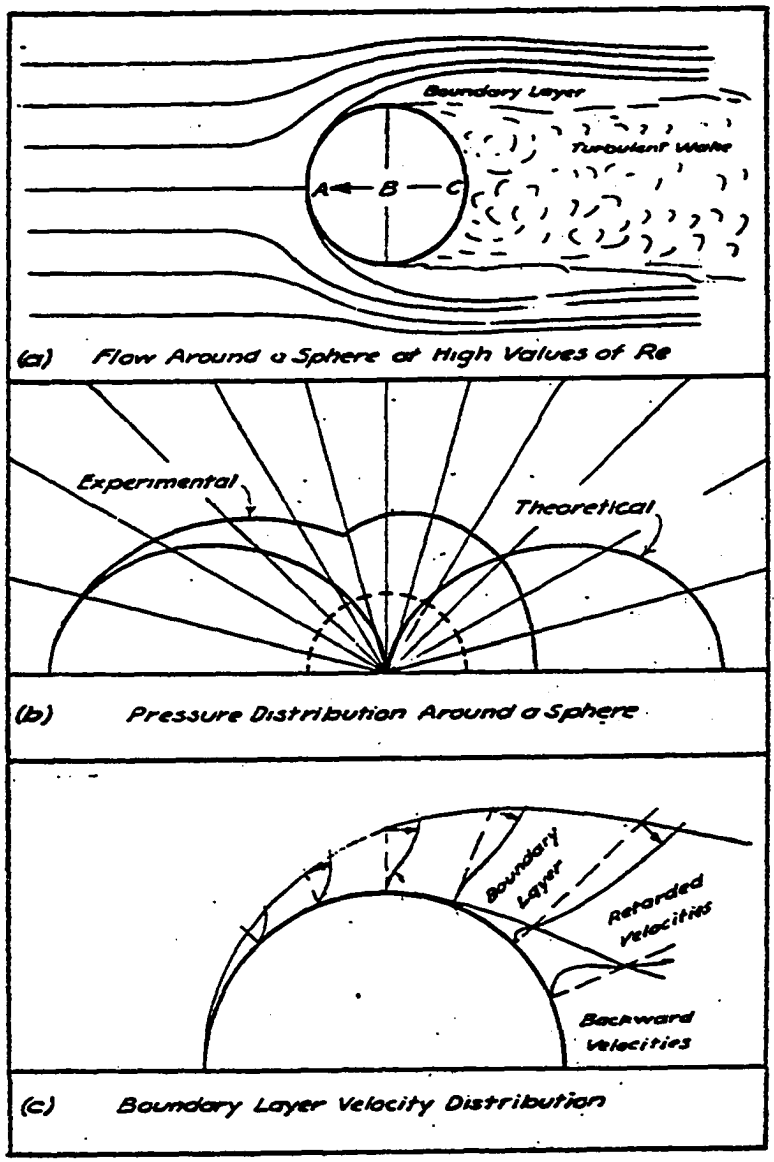

Figure 1. Flow of fluid past a sphere with separation (95)

High Reynolds numbers As the Reynolds number is increased further ($Re_{t\infty} > 1000$), the influence of viscosity becomes of less and less importance until around $Re_{t\infty} = 2 \times 10^5$ for spheres and $Re_{t\infty} = 5000$ for disks, the flow pattern in general and the drag in particular becomes independent of Reynolds number. Throughout this range the separation is well-defined, but the point of its beginning upstream, and hence its size varies with the nature and extent of the viscous sublayer surrounding the particle upstream from the point of separation. This viscous sublayer becomes a turbulent sublayer at about $Re_{t\infty} = 200,000$ for smooth spheres and for disks at about $Re_{t\infty} = 5000$. The turbulent boundary layer is more stable than the laminar boundary layer and therefore, the separation point is delayed. This in turn produces smaller wake region and therefore the drag coefficient suddenly decreases.

Figure 2 shows the curve of drag coefficient versus Reynolds number ($Re_{t\infty} = \rho u_{t\infty} d/\mu$) based on experimental measurements of the terminal velocities of spheres falling under gravity in an expanse of stagnant fluid. This curve is called the standard drag curve for spheres. If a sphere is falling in a cloud of other spheres or in a container, the drag coefficient is higher; the correction may be significant even when cloud has a voidage of as high as 99 percent or when a sphere has a diameter as little as 1 percent of the container diameter. In addition, this curve will not be adequate for conditions in which particle velocity approaches the mean free path of the medium molecules or in which the

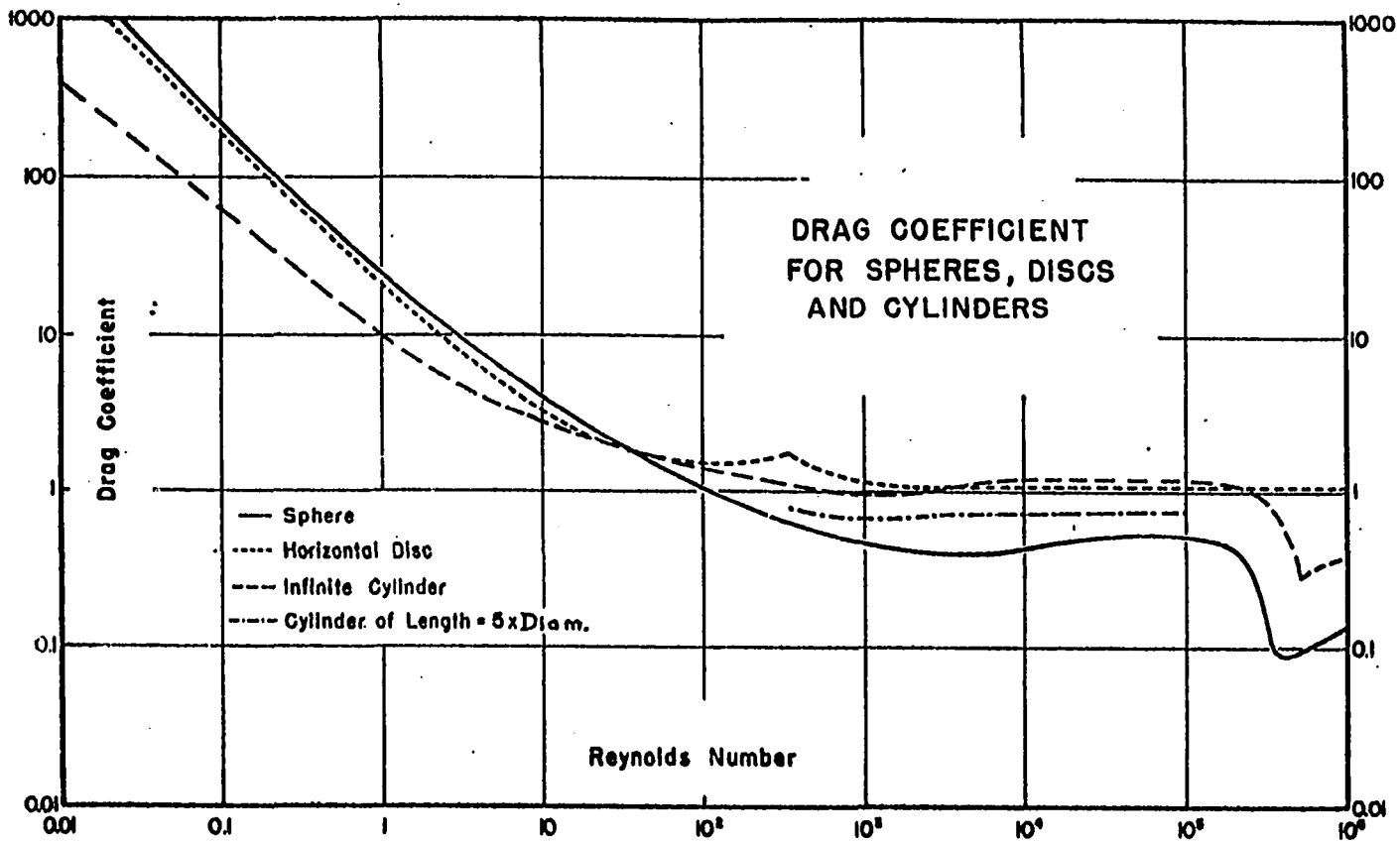

Figure 2. C_D vs. $Re_{t\infty}$ relationship for a isolated sphere, disc and cylinder where the characteristic dimension in $Re_{t\infty}$ is the diameter of the sphere, disc or cylinder (112)

diameter approaches molecular size.

Bailey (8) discussed the drag coefficient for spheres obtained by many investigators. He noted several instances where sphere oscillations occurred for $Re_{t\infty} > 300$, the drag coefficient observed was higher than that of the standard drag curve. He noted that the measurement of drag coefficient can differ due to particle sphericity, oscillations, free stream turbulence and surface roughness.

The drag force on an isolated sphere moving in an infinite expanse of stagnant fluid is given by

$$F_D = \frac{1}{2} C_D \rho A_p u^2 \tag{1}$$

where

F_D = drag force

A_p = the projected area, perpendicular to the direction of motion

ρ = density of the fluid

u = the velocity of the body with respect to the fluid

C_D = drag coefficient.

For a sphere settling at its terminal velocity in an infinite fluid, $u_{t\infty}$, the drag force is equal to the buoyant weight of the sphere, therefore,

$$F_D = \frac{1}{2} C_D \rho A_D u_{t\infty}^2 = \frac{\pi d^3}{6} (\rho_s - \rho) g$$

$$C_D = \frac{4}{3} \frac{(\rho_s - \rho) g d}{\rho u_{t\infty}^2} \tag{1a}$$

The Reynolds number based on terminal settling velocity in an infinite expanse of stagnant fluid is $Re_{t\infty}$, and is defined by the equation

$$Re_{t\infty} = \frac{\rho u_{t\infty} d}{\mu} \quad . \tag{2}$$

If $Re_{t\infty} < 0.2$ then,

$$C_D = \frac{24}{Re_{t\infty}}$$

which is consistent with the Stoke's expression for settling velocity of a sphere.

$$u_{t\infty} = \frac{d^2(\rho_s - \rho)g}{18\mu} \quad . \tag{3}$$

If $1000 < Re_{t\infty} < 10^5$ the drag coefficient C_D can be considered to be of constant value 0.44 (which is the mean value of C_D in this region). The terminal settling velocity of sphere in Newton region is given by

$$u_{t\infty} = 1.75 \sqrt{\frac{gd(\rho_s - \rho)}{\rho}} \quad . \tag{4}$$

The use of drag curve such as given in Figure 2, to predict free fall velocity of a given sphere in a given fluid or to calculate the diameter of a sphere corresponding to a given free fall velocity involves a trial-error calculation. In order to alleviate this problem, a more useful plot can be derived by plotting $(Re_{t\infty}/C_D)$ versus $(C_D\ Re_{t\infty}^2)$ so as to eliminate velocity term from abscissa and diameter term from ordinate. These modified plots are found in Zenz and Othmer (112) and Kunii and Levenspiel (70), and the equations are developed as follows:

$$\left(\frac{Re_t}{C_D}\right)^{1/3} = \left[\frac{u_{t\infty}\rho d}{\mu} \Big/ \frac{4gd(\rho_s - \rho)}{3\rho u_{t\infty}^2}\right]^{1/3} \tag{5}$$

$$= \frac{u_{t\infty}}{\left[\frac{4g\mu(\rho_s - \rho)}{3\rho^2}\right]^{1/3}} = \frac{u_{t\infty}}{\sigma} \tag{6}$$

where

$$\sigma = \left[\frac{4g\mu(\rho_s - \rho)}{3\rho^2}\right]^{1/3}$$

$$(C_D\ Re_{t\infty}^2)^{1/3} = \left\{\frac{4gd(\rho_s - \rho)}{3\rho u_{t\infty}^2} \times \left[\frac{\rho d u_{t\infty}}{\mu}\right]^2\right\}^{1/3}$$

$$= d\left\{\frac{4g(\rho_s - \rho)\rho}{3\mu^2}\right\}^{1/3} = P.d \tag{7}$$

where

$$P = \left[\frac{4g(\rho_s - \rho)\rho}{3\mu^2}\right]^{1/3}.$$

Fouia and Capes (49) fitted a fifth degree polynomial of the form

$$Y = \sum_{n=0}^{5} a_n x^n$$

to the $(C_D\ Re_{t\infty}^2)^{1/3}$ and $(Re_{t\infty}/C_D)^{1/3}$ values reported by Heywood (63). To calculate terminal settling velocity of a sphere of known diameter, the following equation is used:

$$\log\left(\frac{u_{t\infty}}{\sigma}\right) = -1.37323 + 2.06962 \log (Pd) - 0.453219 (\log Pd)^2$$

$$- 0.334612 \times 10^{-1} (\log Pd)^3 - 0.745901 \times 10^{-2} (\log Pd)^4 + 0.249580 \times 10^{-2} (\log Pd)^5. \quad (8)$$

Standard deviation for estimation of $\log \left(\frac{u_{t\infty}}{\sigma}\right)$ = 0.0079528.

Coefficient of determination, $r^2 = 0.9996$.

To calculate the diameter of a sphere of known terminal settling velocity, the following equation is used:

$$\log (Pd) = 0.785724 + 0.684342 \log \left(\frac{u_{t\infty}}{\sigma}\right) + 0.168457 \left(\log \frac{u_{t\infty}}{\sigma}\right)^2 + 0.103834 \left(\log \frac{u_{t\infty}}{\sigma}\right)^3 + 0.020901 \left(\log \frac{u_{t\infty}}{\sigma}\right)^4 + 0.0057664 \left(\log \frac{u_{t\infty}}{\sigma}\right)^5 . \quad (9)$$

Standard deviation for estimation of log Pd = 0.0215341. Coefficient of determination $r^2 = 0.9975$.

There are some other approximate analytical expressions relating drag coefficient with Reynolds number. Not all of them are as accurate as using the standard drag curve for computations.

Schiller and Naumann (as cited by Heywood (62)) deduced the following equation

$$C_D = \frac{24}{Re_{t\infty}} (1 + 0.15 \, Re_{t\infty}^{0.687}). \quad (10)$$

Davis (39) analyzed statistically the experimental results obtained by a number of researchers and proposed the following expressions:

(i) For $Re_{t\infty} < 4$

$$Re_t = \frac{C_D Re_{t\infty}^2}{4} - 0.00023363\ (C_D Re_{t\infty}^2)^2 + 2.0154 \times 10^{-6}\ (C_D Re_{t\infty}^2)^3 - 6.9105 \times 10^{-9}\ (C_D Re_{t\infty}^2)^4 \quad (11)$$

(ii) For $4 < Re_{t\infty} < 10^4$

$$\log Re_{t\infty} = -1.29536 + 0.986 \log (C_D Re_{t\infty}^2) - 0.046677\ (\log C_D Re_{t\infty}^2)^2 + 0.0011235\ (\log C_D Re_{t\infty}^2)^3 . \quad (12)$$

The author of this thesis used the values C_D and Re_t that are used to plot the standard drag curve and obtained the following equation for the Reynolds number range between 4 and 104.

$$\log Re_t = 1.34313 + 1.003356\ (\log C_D Re_t^2) - 0.05771\ (\log C_D Re_t^2)^2 + 0.00187\ (\log C_D Re_t^2)^3 \quad (13)$$

and the 95% confidence intervals of the coefficients are as follows:

-1.34313 ± 0.053

1.003356 ± 0.037

-0.05771 ± 0.008

0.00187 ± 0.0005.

Effect of shape on drag coefficient

The general form of drag coefficient for non-spherical particle is

$$C_D = \frac{F_D/A_p}{\frac{1}{2}\rho u_{t\infty}^2} \tag{14}$$

Some investigators use the projected area of a sphere of equivalent volume for A_p (77, 82, 101, 104) whereas there are some who advocate the use of a diameter based on projected area as the characteristic dimension in C_D and Reynolds number (63, 65).

Albertson (3) showed that by using the diameter of a sphere of equivalent volume as the characteristic dimension in Reynolds number and drag coefficient the scatter in the C_D vs. Reynolds number plot for different types of gravel could be reduced.

Malaika (77) offered the following reasoning for using the projected area of sphere of equivalent volume for A_p:

"If A_p is the actual projected area then by comparing equations (1) and (14) it will be seen that for a given size (same equivalent volume diameter) and dynamic properties C_D in equation (1) will vary inversely with $u_{t\infty}^2$ as the shape is deformed; hence, C_D will directly reflect the velocity change due to shape distortion. On the other hand, C_D in equation (14) varies inversely with $A_p u_{t\infty}^2$. Since in general $u_{t\infty}$ and A_p vary in opposite direction, a plot where actual projected area is used the drag would not clearly reflect the effect of shape distortion in settling."

Non-spherical particles generally tend to orient in a preferred direction during fall. Becker (12) studied the fall of cylinders, rectangular prisms and right triangular prisms whose sphericities ranged from 0.146 to 0.86. His observations with regard to orientation of the falling particles are summarized in Table 1.

Malaika (77) investigated free fall velocities of particles with two axes of symmetry and conducted experiments with cylinders, square prisms, double cones and spheroids with axis ratios 4:1:1, 1:1:1 and 1:1:4. The particle shape varied from long and slender to flat and thin. His findings are summarized as follows:

1. Zone of deformation drag ($Re_{t\infty} < 0.1$). The particles were stable in any settling position provided the particles were symmetrical about three mutually perpendicular planes. Particles which lacked this symmetry tended to orient themselves at particular settling position depending on the position of their center of gravity relative to the center of force, since these two centers must fall on the same line of direction of motion.

2. Zone of surface drag ($0.1 < Re_{t\infty} < 500$). The particles tended to orient themselves with largest cross-section in the three mutually perpendicular planes of symmetry in a position normal to the direction of motion. Evidently this was not necessarily the maximum cross-sectional area of the particle. The only exception was cubes, which did not show any stable settling position.

Table 1. Orientation of freely falling non-spherical particles (12)

Re_s	Free Orientation
< 0.1	All orientation are stable when there are three or more perpendicular axes of symmetry.
0.5 - 200	Stable in the position of maximum drag.
200 - 500	Unpredictable. Disks and plates tend to wobble, while fuller bluff (non-streamlined) bodies tend to rotate.
> 500	Rotation about axis of least inertia, frequently coupled with spiral translation.

where $Re_s = \frac{Re_{t\infty}}{\sqrt{\psi}}$

ψ = sphericity = $\frac{\text{surface area of equivalent volume sphere}}{\text{surface area of the particle}}$

3. Zone of form drag ($Re_{t\infty}$ > = 500). In this region the formation of eddies affected the stability of the position of the settling particles. The particles oscillated in the path of motion and their projected area was changing continuously with time.

The surface texture of falling particles has a definite effect on their settling velocities. Kumar (69) studied this problem and the main conclusion of his work was:

1. Cylindrical or disk shaped particles falling freely in quiescent medium have five different fall patterns:

(a) Stable fall

(b) Regular oscillation

(c) Gliding

(d) Gliding-tumbling

(e) Tumbling.

2. Considering the five fall patterns, the terminal settling velocity is greater for particles with rough surface texture. This is mainly due to:

(a) Roughness of the particle stabilizes the separation of flow around them.

(b) The flow pattern relative to the particles is seldom stabilized.

3. For rough particles, the average drag coefficient was reduced 2.5 to 14 percent in comparison with the drag coefficient of similar smooth particles. This drag reduction ranged from 17 to 33 percent when the pattern of fall was regular oscillation.

Some published correlation for C_D vs. $Re_{t\infty}$ relationship for non-spherical particles

Several attempts have been made to produce a general correlation of drag coefficient versus Reynolds number with a shape factor as a parameter. Wadell (104) in 1934 used sphericity to correlate the drag coefficient versus Reynolds number data for various shapes. Wadell's correlation of C_D vs. Reynolds number is shown in Figure 3. He defined true sphericity of a particle by the formula:

$$C_D = \frac{4}{3}\frac{d_{eq}(\rho_s - \rho)g}{\rho u_t^2}$$

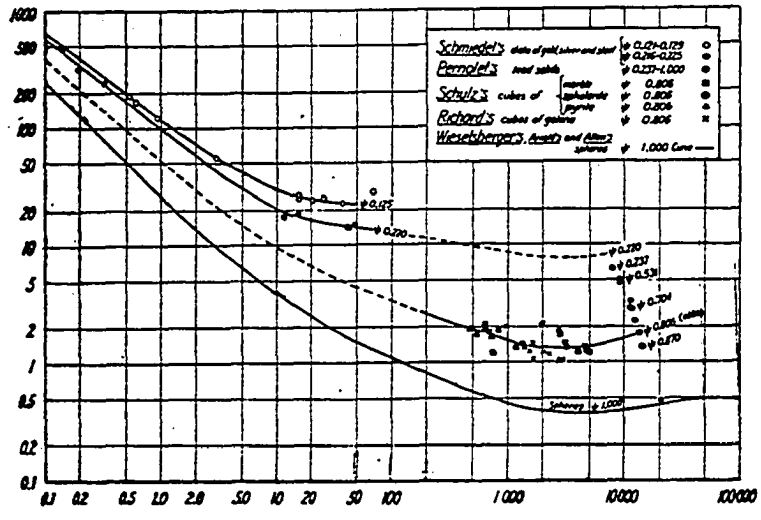

$$Re_t = \rho u\, d_{eq}/\mu$$

Figure 3. C_D vs. $Re_{t\infty}$ relationship obtained by Wadell with sphericity as shape parameter and diameter of equivalent volume sphere (d_{eq}) was used in C_D and $Re_{t\infty}$ (104)

$$\psi = \frac{s}{S} \tag{15}$$

where

s = the surface area of a sphere of equal volume as the particle

S = the actual surface area of the particle

Other shape factors that are used to characterize a non-spherical particle will be considered in detail later under shape measurements.

Heywood (63) introduced a new measure of particle dimension, the projected diameter equal to the diameter of a circle having an area equal to the projected area of the particle when placed in the most stable position (presumably the position during fall). He defined the volume of the particle is given by the equation

$$V = Z\, d_a^{\,3}$$

where

d_a = the diameter of the circle having area equal to projected area.

Z = volume constant.

Heywoods definition would modify the drag coefficient and Reynolds number equation as

$$C_D = \frac{8Z(\rho_s - \rho)d_a}{\pi\, \rho\, u_{t\infty}^{\,2}} \tag{16}$$

$$Re_{t\infty} = \frac{\rho u_{t\infty} d_a}{\mu} \tag{17}$$

Pettyjohn and Christiansen (82) used both Wadell's approach and Heywood's approach to study drag coefficient versus Reynolds number

relationships of spheres, cube octahedrons, octahedrons, cubes and tetrahedrons in the Reynolds number range from 0.01 to 20,000. Their correlation for the drag coefficient is shown in Figure 4 with appropriate sphericity values. These investigators found that Heywood's volume shape factor Z did not appear to be a useful criterion for correlating the effect of particle shape with resistance to motion since there was no apparent relationship between C_D and Z. This was particularly evident in the highly turbulent region. However, they observed that when $Re_t < 30$ the drag curve for spheres, octahedrons and tetrahedrons practically coincide. This suggests the possibility of bringing the data for widely disimilar particles together at low Reynolds numbers by the selection of the diameter based on projected area.

Zenz and Othmer (112) showed that the correlation of Pettyjohn and Christiansen (82) can be improved by using for the diameter term the diameter of a sphere having the same surface area as the particle and in addition, multiplying the drag coefficient by the particle shape factor "j" defined as the ratio of particle volume to volume of a sphere having the same surface area as the particle. The improved correlation is shown in Figure 5.

$$C_{Ds} = \frac{4gj\ d_s\ (\rho_s - \rho)}{3\rho u_{t\infty}^{\ 2}} \tag{18}$$

$$Re_s = \frac{\rho u_{t\infty}\ d_s}{\mu} \tag{19}$$

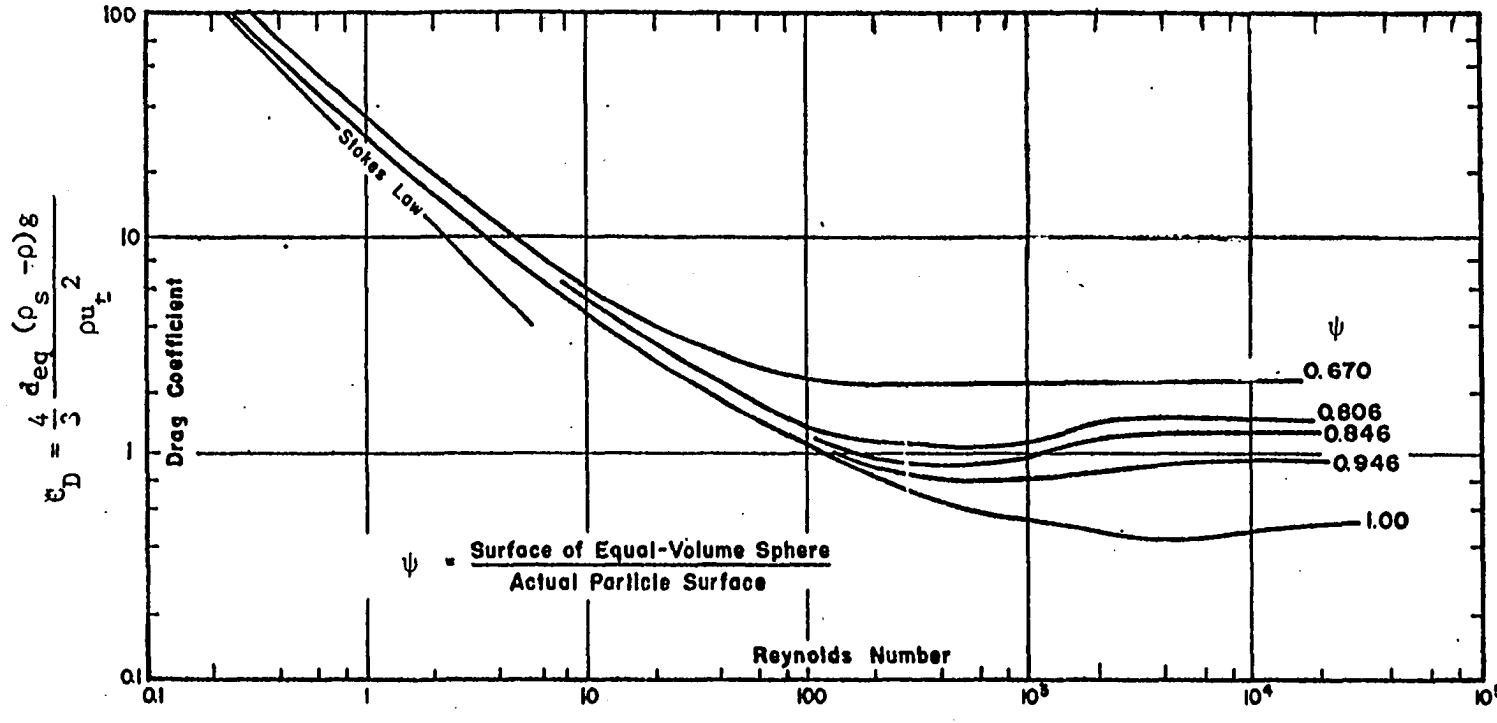

Figure 4. C_D vs. Re_t relationship for isometric particles studied by Pettyjohn and Christiansen (82), d_{eq} was used in $Re_{t\infty}$ and C_D for the diameter term (82)

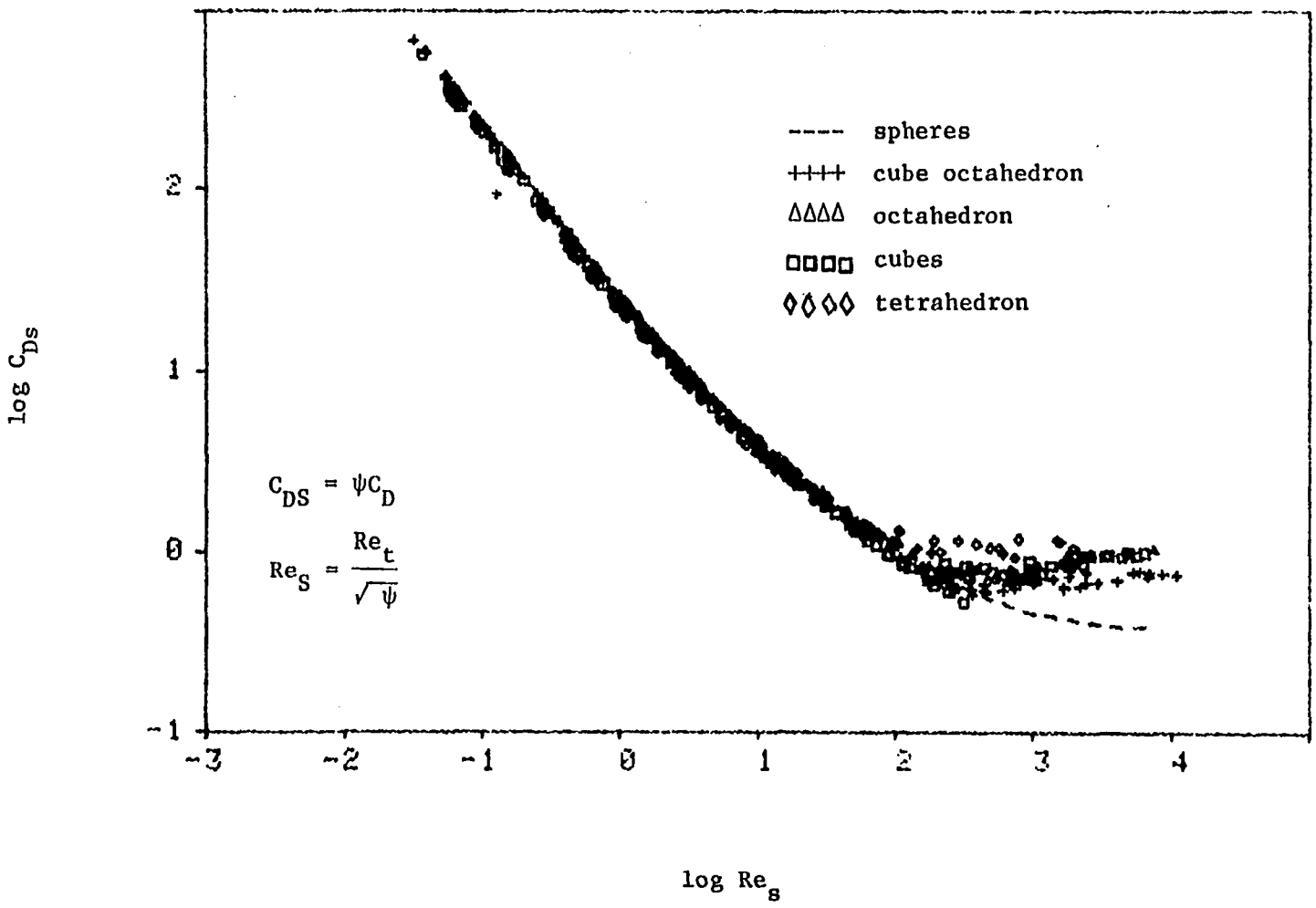

Figure 5. log C_{Ds} versus log Re_s relationship for Pettyjohn and Christiansen's data

where

d_s = the diameter of a sphere having same surface area as the particle

j = volume particle/$(\frac{\pi}{6} d_s^3)$

If deq is the diameter of the equivalent sphere and ψ is the sphericity of the particle, then

$$\pi d_s^2 = \frac{\pi d_{eq}^2}{\psi}$$

$$d_s = \frac{d_{eq}}{\sqrt{\psi}} \tag{20}$$

$$j = \frac{\frac{\pi}{6} d_{eq}^3}{\frac{\pi}{6} d_s^3} = \frac{d_{eq}^3}{d_s^3} = \psi^{3/2} \tag{21}$$

On substituting for d_s and 'j' in equation (18) and (19) one arrives at

$$C_{Ds} = 4g \psi^{3/2} \frac{d_{eq}}{\sqrt{\psi}} \frac{(\rho_s - \rho)}{3\rho u_{t\infty}^2}$$

$$= \frac{4g \psi d_{eq}}{3\rho u_{t\infty}^2} \frac{(\rho_s - \rho)}{} = \psi C_D \tag{22}$$

$$Re_s = \frac{\rho u_{t\infty} \frac{d_{eq}}{\sqrt{\psi}}}{\mu} = \frac{Re_{t\infty}}{\sqrt{\psi}} \tag{23}$$

Wadell's plot and Pettyjohn and Christiansen's plot for correlation of drag coefficient versus Reynolds number with sphericity as parameter gives a illusory feeling that C_D vs. Re_t relationship for non-spherical particles can be completely characterized by the use of sphericity, but in reality this is not true. If one carefully studies the plots of C_D vs. Re_t in Malaika's work, a double cone with length to diameter ratio 1:1, and sphericity of 0.891 has a higher drag coefficient compared with a cylinder with length to diameter ratio of 1:1 and a sphericity of 0.873 or a cube which has a sphericity of 0.805, at the same Reynolds number. In addition, when length to diameter ratio was 4:1 the drag curve for the double cones, prisms and the cylinders were nearly identical although their sphericity ranged from 0.680 for the prism to 0.771 for the double cones.

Heiss and Coull (59) studied the orientation and shape on settling velocity of non-isometric particle in the laminar region of Re_t. They showed that for the same particle, depending on the orientation of the particle, the Stoke's law correction factor k (the ratio of actual settling velocity to settling velocity predicted by Stoke's law) had two distinct values.

Squires and Squires (99) verified Overbecks (as cited by Lamb (71)) theoretical equation for drag force encountered by a very thin moving disk in the creeping flow region. Overbeck showed it to be

$$F_D = 8\mu\, u_{t\infty} d \qquad (24)$$

when the disk is moving with its flat face in the direction of motion, and

$$F_D = \frac{16}{3} \mu u_{t\infty} d \tag{25}$$

when moving edgewise, where d is the diameter of the disk. They showed that for a horizontal disc the drag coefficient was $C_D = 20.34/Re_{t\infty}$ for $Re_{t\infty} < 0.3$ where the Reynolds number is based on disc diameter. For a disc falling edgewise, if the $Re_{t\infty}$ is based on twice the thickness (equal to four times the hydraulic radius of the projected area perpendicular to the direction of motion), the drag coefficient is $C_D = 21.36/Re_{t\infty}$ for $Re_t < 0.02$. It is remarkable that the drag coefficient equations for the extreme cases of sphere ($C_D = 24/Re_{t\infty}$) and disk can be made so nearly the same by selecting an appropriate characteristic length term for the Reynolds number.

United States Inter Agency Committee on Water Resources (101) published a correlation for drag coefficient with Reynolds number for naturally worn sediment particles with Corey's (33) shape factor, S.F. as the shape parameter. The plot of C_D vs. $Re_{t\infty}$ is shown in Figure 6. The shape parameter S.F. is defined as follows:

$$S.F. = \frac{c}{\sqrt{ab}} \tag{26}$$

a, b, c are triaxial dimensions of the particle, and

a = longest dimension

b = intermediate dimension

c = shortest dimension.

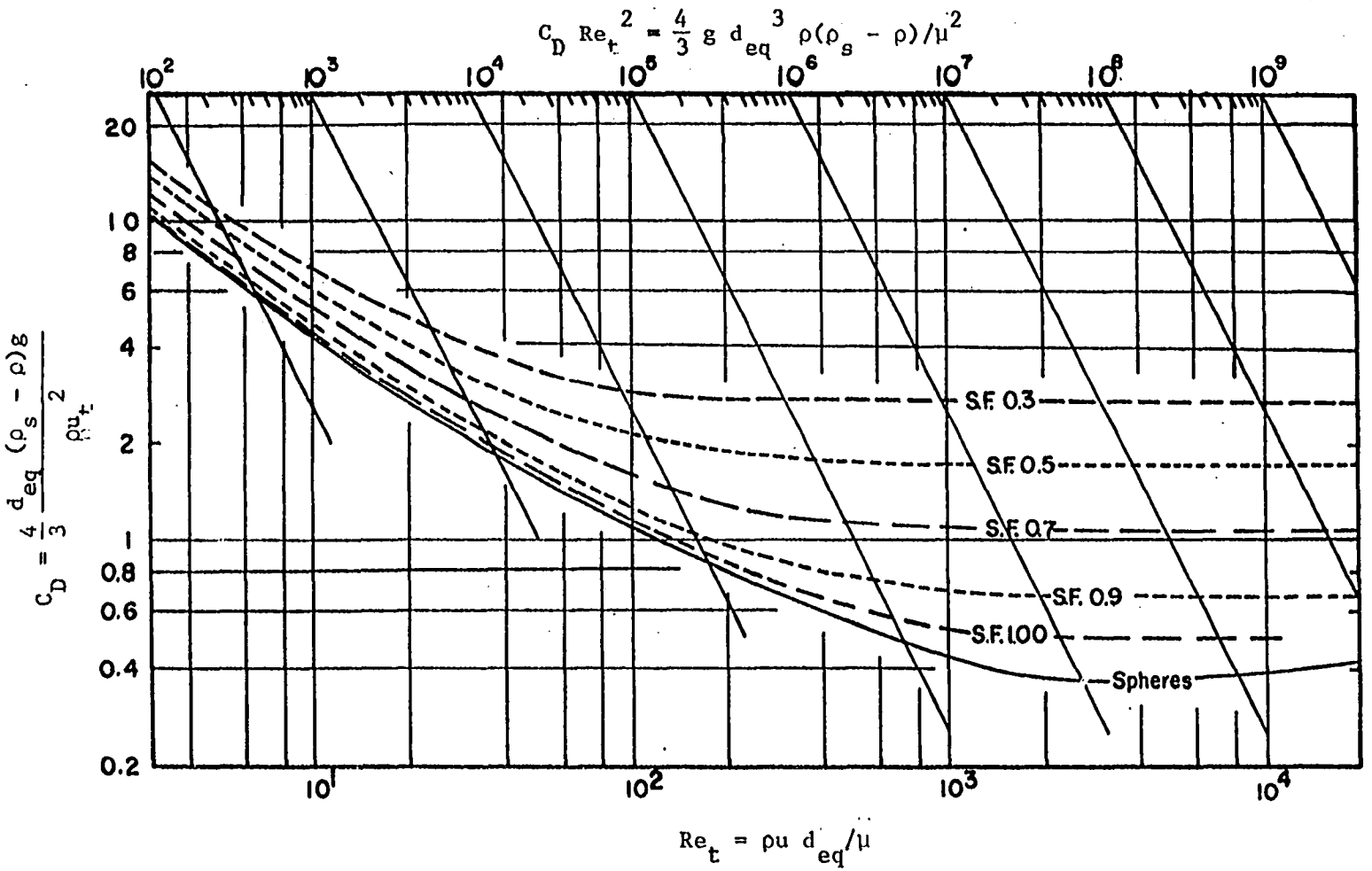

Figure 6. Relationship between drag coefficient C_D, and Reynolds number, Re_t, with S.F. as shape parameter. SF = $c/\sqrt{ab}$ where a, b, and c are the long, intermediate and short dimension of the particle in three mutually perpendicular directions (101)

McNown and Malaika (79) found that S.F. alone is not sufficient to characterize the Stoke's law correction factor k (given previously), and suggested in addition a second shape factor expressed as 'a/b' be used to emphasize relative particle length.

The particle shape effects have been explored to some extent to permit a reasonable estimation of particle-fluid flow characteristic despite the fact no single shape criterion has yet evolved. One has to remember that the cardinal principle in similitude analysis is that to achieve dynamic similarity there should be geometric similarity. It will be futile to expect two particles of widely varying shapes to exhibit dynamic similarity even-though they may have nearly the same sphericity, S.F. or any other shape factor.

Boundary effects on motion of single particle

Stoke's law as given by equation (3) applies to spherical particles falling in an infinite fluid medium. When the boundaries of the medium approach the particle as in the case of a particle falling in a cylinder, the displacement of the particle volume creates additional retarding effect.

Fidleris and Whitmore (46) and McNown et al. (78) showed the retarding effect of wall is greatest in the viscous region and progressively decreases and reaches another constant value in the turbulent region.

Ladenburg's equation (as cited by Fidleris and Whitmore (46)) for wall effect in the viscous region is

$$\frac{u_t}{u_{t\infty}} = \frac{1}{1 + 2.1\ (d/D_T)} \tag{27}$$

where D_t is the diameter of the tube.

This equation is the first approximation of a theoretical equation derived by Faxen (as cited by Fidleris and Whitmore (46)) which for low Reynolds numbers may be expressed as:

$$\frac{u_t}{u_{t\infty}} = 1 - 2.104\ (d/D_T) + 2.09\ (d/D_T)^3 + 0.95\ (d/D_T)^5 . \tag{28}$$

Equation (28) is limited to values of d/D_T below 0.2 while equation 27 is satisfactory when d/D_T ratio is less than 0.1.

Francis (51) gave the following empirical equation for wall effect correction at low Reynolds numbers

$$\frac{u_t}{u_{t\infty}} = \left\{\frac{1 - d/D_T}{1 - 0.475\ (d/D_T)}\right\}^4 . \tag{29}$$

The above equation was found to be satisfactory for d/D_T ratios less than 0.9.

McNown et al. (78) proposed the following equation for d/D_T ratio less than 0.25 in the viscous region :

$$\frac{u_t}{u_{t\infty}} = \frac{1}{1 + \frac{9}{4}\ (d/D_T) + \{\frac{9}{4}\ (d/D_T)\}^2} . \tag{30}$$

Fidleris and Whitmore (46) found that Newton's equation given below for wall effect in the turbulent range, to agree within 2 percent of their

experimental results up to a d/D_T ratio of 0.3 but worsened considerably at higher d/D_T ratios,

$$\frac{u_t}{u_{t\infty}} = (1 - d/D_T)^2 \left(1 - \frac{1}{2} (d/D_T)^2\right)^{1/2} . \tag{31a}$$

Fidleris and Whitmore also reported that in the particle Reynolds number range between 1000 and 3000, Munroe's equation for wall effect (equation 31b) showed best agreement with their experimental results

$$\frac{u_t}{u_{t\infty}} = 1 - \left(\frac{d}{D_T}\right)^{3/2} . \tag{31b}$$

Malaika (77) presented Figure 7 for drag coefficient correction factor "m" with Reynolds number and d/D_T ratio as a parameter. This figure was based on the work of McNown et al. (78). This figure is the only comprehensive work available for drag coefficient correction for wall effects in the intermediate range of Reynolds number for small $\frac{d}{D_T}$ ratios.

Garside and Al-Dibouni (54) proposed the following equation for correcting for wall effects for d/D_T ratios less than 0.1 in Reynolds number range between 3 and 1000:

$$\frac{u_t}{u_{t\infty}} = \frac{1}{1 + 2.35 (d/D_T)} . \tag{32}$$

Richardson and Zaki's (92) equation for correcting for wall

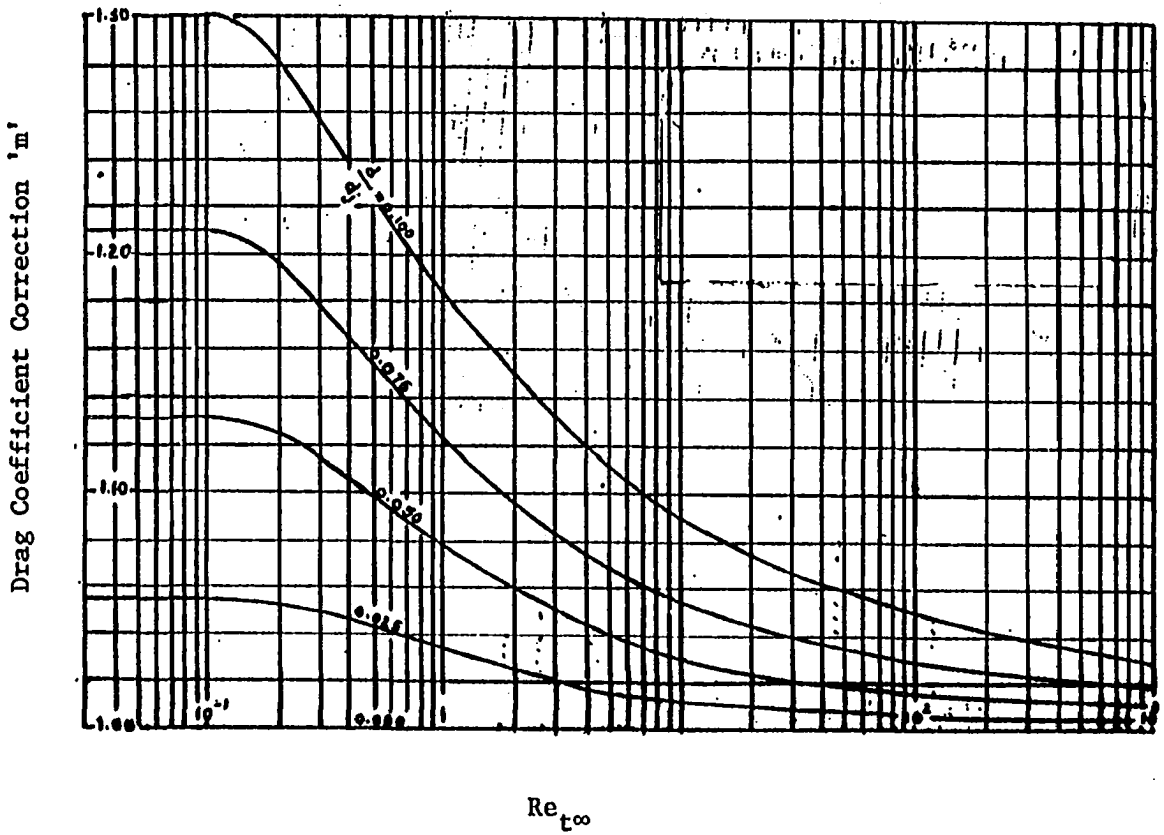

Figure 7. Relationship of wall effect correction for drag coefficient, C_D, with Reynolds number, $Re_{t\infty}$, (77)
Note: $\frac{d}{d_j} = d/D_T$

$$\frac{u_t}{u_{t\infty}} = 10^{-d/D_T}, \tag{33}$$

which they claimed to be valid over a Reynolds number range from 0.2 to 1000.

Equations 32 and 33 are inconsistent with the findings of Fidleris and Whitmore (46) and McNown et al. (78) for these two equations, 32 and 33, imply that wall effect is independent of Reynolds number, whereas Fidleris and Whitmore and McNown et al. showed that the wall effect varies with the particle Reynolds number.

However, these two equations, 32 and 33, at the same d/D_T ratios predict correction factors which are more in agreement with those predicted by equations 27 through 30 rather than with Munroe's equation 31b. The equations 27 through 30 are applicable only in the viscous range whereas Munroe's equation is valid in the lower end of the turbulent range ($10^3 < Re_t < 3 \times 10^3$). This is illustrated by Figure 8.

No investigation is documented in the literature as to the influence of a finite fluid container on the drag of non-spherical particles. Malaika (77) suggested using the diameter of a circle having the same area as the projected area of the particle for the diameter term in d/D_T ratio. This is based on the assumption that the projected area influences the return flow which in turn affects the velocity gradient and hence the shearing force.

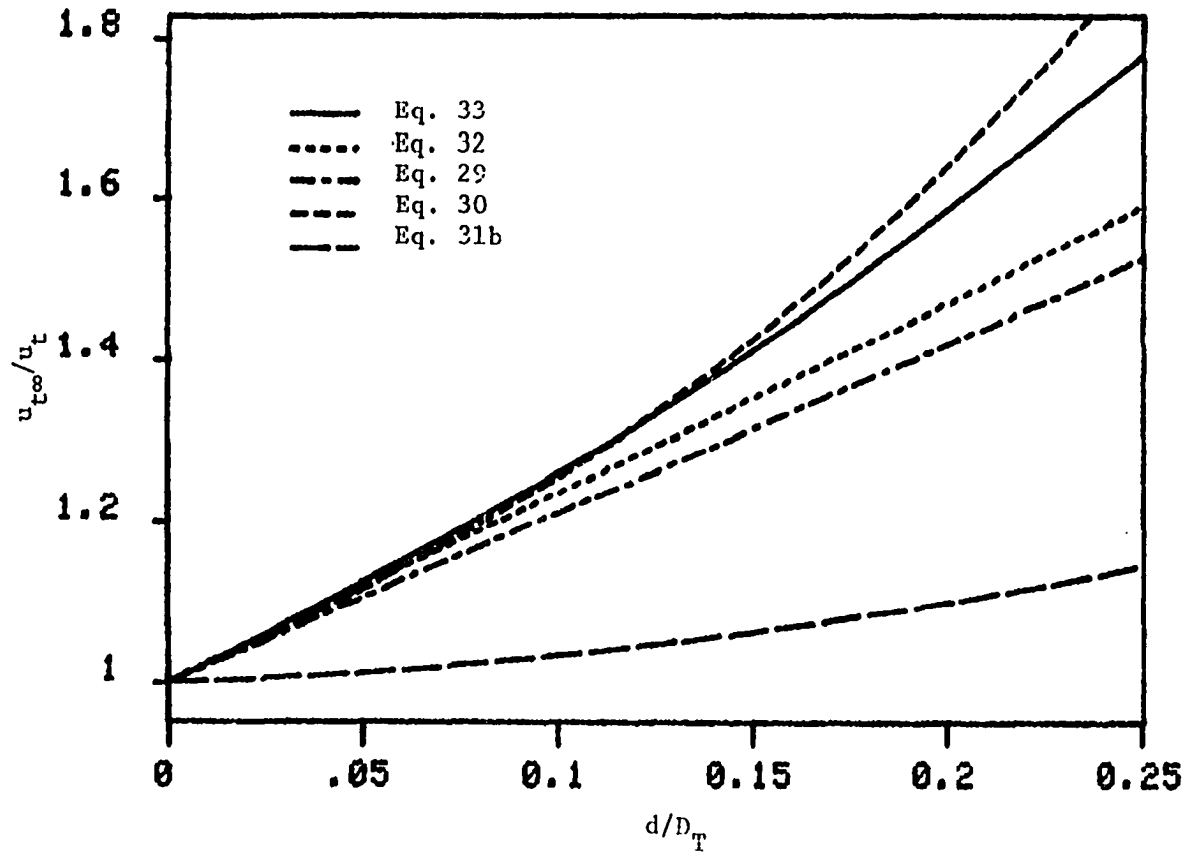

Figure 8. Comparison of different wall effect correction equations for $u_{t\infty}/u_t$ ratio with d/D_T ratio

Flow Through Packed Bed of Granular Materials

Darcy, in 1830 (as cited by Coulson and Richardson (35)) carried out the first experimental work on flow through packed beds when he examined the rate of flow from the local fountains through beds of sands of various thickness. He showed that average velocity of flow measured over the whole area of bed was directly proportional to the driving force and inversely proportional to thickness of the bed. This relation is termed as Darcy's law and is written as follows:

$$u = B' \frac{(\Delta P/L)}{\mu} \tag{34}$$

where

ΔP = the pressure drop across the bed

L = thickness of the bed

u = the average velocity of the fluid or superficial velocity

B' = coefficient of permeability

μ = coefficient of viscosity.

The value of permeability coefficient varies over a wide range of values depending on the shape, size and packing of the granular material. Equation 34 is valid only under laminar flow regime.

Kozeny (67) developed the following well-known equation in the laminar flow regime

$$\frac{\Delta P}{L} = k'' \frac{(1 - \varepsilon)^2}{\varepsilon^3} \mu S^2 u \tag{35}$$

where

S = specific surface

$= \frac{6}{d}$ for spherical and $\frac{6}{\psi \cdot d_{eq}}$ for non-spherical particles

ψ = sphericity

d_{eq} = diameter of a equivalent volume sphere

d = diameter of spherical particle

ε = porosity of the bed.

The pressure drop ΔP in a stream of fluid flowing through length L of a particle bed of uniform spheres can be expressed by the equation

$$\frac{\Delta P}{L} = \frac{2 f \rho u^2}{g d} \tag{36}$$

where

f = friction factor

u = superficial velocity

d = diameter of spheres

ρ = density of the fluid.

One can observe the similarity between equation 36 and the Darcy-Weisbach equation used to calculate the friction loss in pipe flow. Many investigators (23, 24, 43) have sought to derive empirical correlation for the friction factor f. However, the variables like particle shape, roughness, distribution, manner of packing and similar less definable parameters have made the task quite involved. There are at present several well-recognized correlations which permit

reasonable prediction of the pressure drop through bed of spherical and non-spherical material.

From dimensional analysis it follows that the pressure drop per unit bed height for geometrically similar beds may be written as

$$\frac{\Delta P}{L} = \lambda \mu^{2-\chi} \underset{\sim}{u}^{\chi} \underset{\sim}{d}^{\chi-3} \rho^{\chi-1} \tag{37}$$

where

$\underset{\sim}{u}$ = representative velocity

$\underset{\sim}{d}$ = representative dimension of the grains

μ = coefficient of viscosity of the fluid

ρ = density of fluid

λ = constant of proportionality

χ = exponent depends on the flow regime

$\frac{\Delta P}{L}$ = pressure drop per unit bed height.

Blake (20) suggested that average interstitial velocity be used for $\underset{\sim}{u}$, and $\underset{\sim}{d}$ to be chosen as a length analogous to the hydraulic radius of a conduit. Accordingly,

$$\underset{\sim}{u} = \frac{u}{\varepsilon} \tag{38}$$

$$\underset{\sim}{d} = \frac{\text{mean cross-sectional area of flow channels through the bed}}{\text{mean wetted perimeter of flow channels}}$$

If the numerator and denominator of the above ratio are multiplied by the bed depth L, one obtains

$$\underset{\sim}{d} = \frac{(\text{total bed volume}) \times \varepsilon}{\text{total bed surface}} = \frac{\varepsilon}{S_1} = \frac{\varepsilon}{S(1-\varepsilon)} \tag{39}$$

where

u = superficial velocity

ε = porosity

S_1 = surface area per unit bed volume

S = specific surface of the particles.

For a bed of uniform spheres

$$\underset{\sim}{d} = \frac{\varepsilon d}{6(1 - \varepsilon)} \quad . \tag{40}$$

Substituting equations 38 and 40 in 37, the following equation is obtained

$$\frac{\Delta P}{L} = \lambda \, \mu^{2-\chi} \, d^{\chi-3} \, \rho^{\chi-1} \, u^{\chi} \, \frac{(1 - \varepsilon)^{3-\chi}}{\varepsilon^3} \quad . \tag{41}$$

The friction factor f, defined by equation 36, is given by,

$$f = \frac{\lambda \mu^{2-\chi} \, u^{\chi-2} \, \rho^{\chi-2} \, d^{\chi-2} \, (1 - \varepsilon)^{3-\chi}}{\varepsilon^3}$$

$$f = \lambda^1 \, \frac{(1 - \varepsilon)^{3-\chi} / \varepsilon^3}{Re^{2-\chi}} \tag{42}$$

where

$$Re = \frac{\rho u d}{\mu} \quad .$$

At low Reynolds number where the pressure drop does not depend on fluid density, equation 41 implies that $\chi = 1$, and therefore the friction factor

$$f \alpha \frac{(1 - \varepsilon)^2}{\varepsilon^3 \quad Re} ; \tag{43}$$

and at high Reynolds numbers, the viscosity is unimportant which means $\chi = 2$, then friction factor

$$f \alpha \frac{(1 - \varepsilon)}{\varepsilon^3} : \tag{44}$$

This hypothesis is exemplified in Ergun 's (41) empirical correlation for the pressure drop in packed bed which is as follows:

$$\frac{\Delta p}{L} = 4.17 \frac{(1 - \varepsilon)^2}{\varepsilon^3} \mu S^2 u + 0.29 \frac{(1 - \varepsilon)}{\varepsilon^3} S \rho u^2 \tag{45a}$$

where

S = specific surface

u = superficial velocity

L = depth of the bed

Δp = pressure drop.

To obtain the specific surface from permeability data as will be shown later in the illustrative calculations, it is desirable to rearrange equation 45a to the following form:

$$\frac{\Delta p}{Lu} = 4.17 \frac{(1 - \varepsilon)^2}{\varepsilon^3} \mu S^2 + 0.29 \frac{(1 - \varepsilon)}{\varepsilon^3} S \rho u \quad . \tag{45b}$$

If a modified Reynolds number is defined in terms of $\underset{\sim}{u}$, $\underset{\sim}{d}$

$$Re_1 = \frac{\underset{\sim}{u}\,\underset{\sim}{d}}{\mu} = \frac{\rho \frac{u}{\varepsilon} \frac{\varepsilon}{S(1-\varepsilon)}}{\mu}$$

$$Re_1 = \frac{\rho u}{S(1 - \varepsilon)} . \tag{46}$$

Equation 45a can be written as:

$$\frac{\Delta p}{sL}\ \frac{\varepsilon^3}{\rho u^2(1-\varepsilon)} = 4.17\ \ Re_1^{-1} + 0.29 \tag{47}$$

Ergun (41) found equation 47 to correlate experimental data well for values of Re_1 from 1 to over 2000.

Carman (27) took a different approach and found the following correlation.

$$\frac{\Delta P}{SL\rho u^2}\ \frac{\varepsilon^3}{(1-\varepsilon)} = 5\ Re_1^{-1} + 0.4\ Re_1^{-0.1} \tag{48}$$

for Re_1 from 0.5 to over 1000

For small Re_1 values (less than about 2), the second term on the right hand side of equation 47 and 48 is small and negligible. In this Re_1 range, both equations 47 and 48 are of the same form except for the constants 4.17 and 5.0.

Coulson (34) found this constant k" (constant in the 1st term of equation 45) to vary with porosity of packed bed and the shape of the particles, with extreme values occurring with thin plates. But, for normal granular material Kihn (as cited by Coulson and Richardson (35)) and Pirie (84) found that k" is reasonably constant.

At high Reynolds number (Re_1), Blake's (20) theory predicts that $\frac{\Delta p}{SL\rho u^2}\ \frac{\varepsilon^3}{(1-\varepsilon)}$ should be a constant. Although Ergun (41) found this to be true in his work, other workers had only limited success. Carman (27) analyzed large amounts of data for beds of spheres, rings and saddles and found deviations of the order of $\pm$ 50 percent.

There is some doubt about the form of equation 45 in which the viscosity is completely absent from the inertial term (2nd term). In pipe flow, the viscosity enters to the 0.1 to 0.3 power in its effect on pressure drop. It might be expected that a similar effect would be present in flow through a porous medium. Fahien and Shriver (as cited by Tiller (100)) proposed an equation of the form

$$\frac{\Delta p}{L} = C_3 \left[\frac{\mu(1-\varepsilon)^2}{\varepsilon^3} \frac{u}{d_{eq}^2}\right] + \frac{1}{C_2}\left[\frac{\rho(1-\varepsilon)}{\varepsilon^3} \frac{u^2}{d_{eq}}\right] \tag{49}$$

where the constants C_2 and C_3 were function of modified Reynolds number $\frac{\rho u\, d_{eq}}{\mu(1-\varepsilon)}$.

Blake's (20) suggestions regarding $\underset{\sim}{u}$, $\underset{\sim}{d}$, have been criticized by Chilton and Colburn (29), Bakhmeteff and Feodoroff (9) and Furnas (as cited by Carman (27)) who stress the fact that the pressure drop through the bed results not only from frictional resistance at the particle surface but also from loss of head owing to expansion and contraction of flow. Furnas considered that the fractional effective free (cross-sectional) area for flow is only about 0.10 to 0.20 ε rather than ε as assumed by Blake. For example, in a bed of spheres packed in the most loose arrangement (cubic packing) the voidage ε is 0.476, but the fractional free area in a plane of centers is only 0.215; in a plane parallel to this plane one-half diameter away, the fractional free area is unity. A fluid flowing through such a bed would undergo a large contraction and expansion as it traverses each layer of spheres. Graton and Fraser (56) have pointed out, however, that such a packing

should offer different flow characteristics according to the direction of flow, whereas natural granular beds with random packing have the same flow characteristics in all directions. In a random packing, the fractional free area at any cross-section is constant and equal to voidage ε. Carman (27) argues therefore, that interstitial velocity does not alternatively increase and decrease but is a constant. Carman (27) offers the following description of flow through the bed:

> "Within the bed there cannot be any isolated pore channel given the whole system of voids is inter-connected so that where the section of one void is decreasing in the direction of flow, the velocity does not increase but the excess of fluid escapes to a neighboring void, the section which is enlarging in the direction of flow. While this emphasizes the constancy of the rate of flow at each point of the bed it also makes the sinous character of the flow clear. It is obvious every flow line of the fluid in the continual division and rejunction with other flow lines, must follow a very tortuous path."

The success of Blake's suggestion in the viscous range indicates that Carman's discription is probably correct at low Reynolds numbers. The inconsistency of the constant in the second term of equation 45 as reported previously by Carman would indicate that equation 44 places too great a dependence of the friction loss f on porosity ε at high Reynolds numbers and suggests that the loss of head owing to expansion and contraction becomes a significant fraction of overall pressure drop at high Reynolds numbers. Chilton and Colburn (29) gave an expression for the part of the pressure through a bed which is due to expansion and contraction losses. According to this expression at high Reynolds numbers that part of friction factor f arising from these losses varies approximately as $\frac{1}{\varepsilon^2}$ rather than as $(1 - \varepsilon)/\varepsilon^3$ according to

Blake's theory.

Although one cannot deduce the relative contributions that friction losses and expansion and contraction losses make toward the overall pressure drop at high Reynolds numbers, it is reasonable to assume that both effects are important.

Characterization of Non-Spherical Particles

Unlike spherical particles, there is no single diameter to describe a non-spherical particle. The following table reproduced from Allen (5) gives the definition of different diameters used to describe a non-spherical particle.

Heywood (61) has presented an interesting discussion on the meaning of sieve size in defining the diameter of a sample of sieved, irregular particles. Although a definite answer could not be given, he concluded that the sieve size i.e., the size of the smallest passing sieve, was an indication only of the intermediate dimension of three mutually perpendicular axes of a particle. Figure 9 shows the relationship between sieve diameter and intermediate axis length and sieve diameter and equivalent spherical diameter (d_{eq}) for naturally worn river gravel.

The shape factors that are used to characterize non-spherical particles can be expressed in terms of two more diameters defined in Table 2. A wide range of techniques has been suggested in the last fifty years or so. Fleming (48) described many of the concepts for analysis of particles by shape. He commented that the theory and

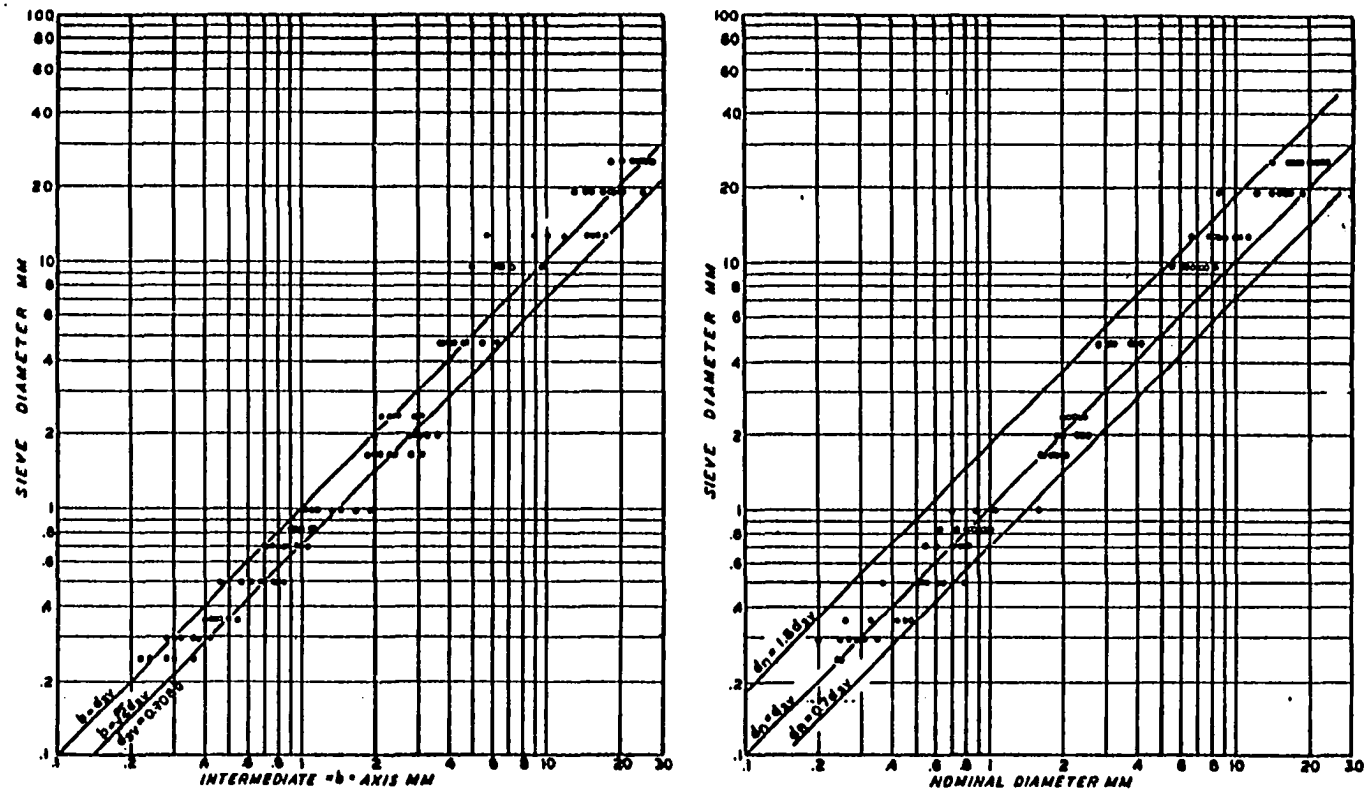

Figure 9. Comparison of smallest passing sieve size with intermediate axis length and equivalent spherical diameter, d_{eq}, for naturally worn gravel (95). d_{sv} = smallest passing sieve size, d_n = equivalent spherical diameter d_{eq}

Table 2. Different diameters used to characterize non-spherical particles (5)

1.	Sieve diameter 1	d_{A1}	Smallest sieve aperature through which particle will pass
2.	Sieve diameter 2	d_{A2}	Mean aperture of smallest passing and largest retaining sieves
3.	Volume diameter (equivalent spherical diameter)	d_{eq}	Diameter of a sphere having the same volume as the particle
4.	Surface diameter	d_s	Diameter of a sphere having the same surface area as the particle
5.	Surface-volume diameter	d_{sv}	Diameter of a sphere having the same external surface to volume ratio as particles
6.	Drag diameter	d_d	Diameter of a sphere having the same resistance to motion (i.e., drag force) as the particle in a fluid of same density and viscosity and at the same relative velocity
7.	Free-falling diameter	d_h	Diameter of a sphere having the same density and the same free falling speed as the particle in a fluid of same density and viscosity
8.	Stoke's diameter	d_{st}	The free falling diameter of a particle in laminar flow region (i.e., $Re_{t\infty} < 0.2$)
9.	Projected area diameter 1	d_a	Diameter of a circle having the same area as the projected area of the particle resting in a stable position
10.	Projected area diameter 2	d_p	Diameter of a circle having the same area as the projected area of the particle in random orientation
11.	Perimeter diameter	d_c	Diameter of a circle having the same perimeter as the projected outline of the particle

12. Feret's diameter	d_f	The mean value of the distance between parallel tangents on opposite sides of the particle measured in a fixed direction for a number of particles.
13. Martin's diameter	d_M	The chord length of the projected outline of the particle. i.e., the length of the line which bisects the image of the particle. The line may be drawn in any direction which must be maintained constant for all the image measurements
14. Circumscribing diameter	d_{cs}	The diameter of the smallest circle which circumscribes the projected outline of the particle
15. Inscribing diameter	d_2	The diameter of the largest circle which will fit inside the projected outline of the particle

practice of many such measurements are based on work of Wadell (102, 103, 104).

Wadell defined the term sphericity by saying, "it is evident that the most exact shape expression approximately reflecting the behavior of a particle in suspension is the ratio of the surface area of the sphere of the same volume as the particle to the actual surface area of the particle."

The techniques for measuring shape can be divided into two groups, namely direct and indirect methods.

Direct methods

While many direct measures have been reported in the literature of sedimentary petrology, powder technology and geology, only a very few will be considered here to illustrate the nature of measurements. One is referred to Davies (38) for a critical review of particle shape measurements.

Wadell's sphericity ψ is defined as follows:

$$\psi = \frac{\text{surface area of a sphere of same volume}}{\text{surface area of the particle}}$$

Since the true surface area of a particle is difficult to measure, unless the particle conforms to a known geometric shape, Wadell proposed a operational formula for sphericity

$$\psi_{opt} = \frac{d_a}{d_{cs}} \tag{50}$$

where

d_a = diameter of a circle having the same area as the projected area of the particle when resting in a stable position.

d_{cs} = the diameter of the smallest circle which circumscribes the projected outline of the particle.

Wadell pointed out that for quartz particles the value of operational sphericity generally approached the true sphericity. But this modified definition gives a sphericity of one for circular discs, which is diametrically opposite to sphere with regard to shape. Therefore, the validity of this modified definition for flat platy particles is questionable.

Krumbein (68) presented a similar expression for operational sphericity using calculated volumes instead of areas.

$$\psi_{opt} = \frac{\text{volume of the particle}}{\text{volume of the circumscribing sphere}} \qquad (51)$$

He approximated the volume of the particle to a triaxial ellipsoid:

$$\text{Volume of the ellipsoid} = \frac{\pi}{6} abc$$

where

a = the longest dimension of the irregular particle

b = the intermediate dimension

c = the shortest dimension.

If the volume of circumscribing sphere is taken as $\frac{\pi a^3}{6}$, then,

$$\psi_{opt} = \left\{ \frac{\frac{\pi}{6}(abc)}{\frac{\pi}{6} a^3} \right\}^{1/3} = 3\sqrt{\frac{bc}{a^2}} \qquad (52a)$$

Sneed and Folk (98) argued that Wadell's sphericity, although a geometrically valid parameter, is not a behavioristic parameter if one is considered with dynamics of particles under natural hydraulic conditions. They proposed a maximum projection sphericity which is defined as follows:

$$\psi_{max} = \frac{\text{maximum projection area of a sphere of equal volume}}{\text{maximum projection area of a particle}}$$

in terms of triaxial dimensions

$$\psi_{max} = \frac{\frac{\pi}{4}\{(abc)^{1/3}\}^2}{\frac{\pi}{4}.ab} = 3\sqrt{\frac{c^2}{ab}} \qquad (52b)$$

Sneed and Folk (98) showed that the Krumbein (68) data, when re-analyzed, gave better correlation for settling velocity against maximum projection sphericity for different shaped particles of nearly the same equivalent spherical diameter and density.

Corey (33) analyzed sedimentation data and concluded that the ratio $\frac{c}{\sqrt{ab}}$ gave the most significant expression for particle shape.

Heywood (61) moved away from the concepts of sphericity to define what he termed as shape coefficient. He began by defining three dimensions of a particle.

1. Breadth B - The minimum distance between two parallel lines tangent to the profile of the particle when viewed

perpendicularly to the plane of maximum stability.

2. Length L - The maximum distance between two parallel lines tangent to the profile of the particle as defined above and perpendicular to the lines defining the breadth.
3. Thickness T - The distance between the two planes parallel to the plane of maximum stability and tangent to the surface of the particle.

Heywood also defined the following coefficients:

1. Volume of the particle = V = $Z\ d_a^3$
2. Surface area of the particle = S = $f_1\ d_a^2$.

where

d_a = the diameter of a circle having the same area as the projected area of the particle in its most stable position

Z = volume coefficient

f_1 = surface area coefficient.

Heywood gave empirical equations to obtain d_a, Z and f_1 from B, L, T and their ratios for seven different shapes. One is referred to Allen (5) for a detailed description of this method for calculating settling velocity of known size particle.

Pettyjohn and Christiansen (82) showed that for isometric particles they investigated, the Heywood's volume coefficient (Z) was not satisfactory for correlating the drag coefficient data with particle Reynolds number. However, Johnstone et al. (65) have found that Heywood's approach with small modification can be used to correlate C_D vs Re_t data for discs, sand, carborundum and aloxite. They used a

diameter based on mean projected area of the particle (the average of the projected area in several random stable orientations).

Indirect methods

Indirect methods do not require the individual measurement of particle dimension. These methods, instead, rely on some non-dimensional property of a particle which varies with particle shape or is based on some statistical analysis of a set of particles.

Use of liquid or air permeability and BET adsorption isotherm methods for determining the specific surface of a collection of particles are examples of two frequently used indirect methods.

Austin et al. (7) measured the specific surface of anthracite and bituminous coal of various size ranges, ground in a standard hard-grove grinding mill. They measured the specific surface of the material by a liquid permeability technique and apparent density by mercury porosimeter. The sphericity (which they called the shape factor) was calculated by the equation

$$\psi = \frac{6}{Sd_m} \tag{53}$$

where

S = specific surface

d_m = arithmetic average of passing and retaining sieve.

After analyzing several sources of coal, they concluded that the sphericity was constant with size for a given coal source over a size range from 16 to 325 U.S. mesh.

Presler (85) determined the specific surface of different size

fractions of crushed magnesite and galena ore by measuring the pressure drop across a bed of known height and porosity at varying flow rates of water through the bed. He used Ergun's equation to calculate the specific surface but used Kozeny's coefficient of 4.97 instead of 4.17 which Ergun recommended in his equation for the first term. The author of this thesis calculated the sphericities for different size fractions of the ores using the specific surface values obtained after adjusting the coefficient to 4.17 and the sphericities are tabulated in Table 3.

Table 3 shows that the sphericity values generally increase as the size fractions become finer even though there are occasional irregularities in that pattern. In light of the above observations, the conclusion of Austin et al., that sphericity essentially remains constant with size for a given coal source seems questionable.

Briggs, McCulloch and Moser (22) defined a term called, "Dynamic Shape Factor", which was based on hydraulic properties of the irregular particle. They used measured settling velocity of the particle and the calculated settling velocity of smooth sphere of equal volume and density with diameter d_{eq}. The dynamic shape factor was expressed as follows:

$$DSF = a_1 \left(\frac{u_t}{u_N}\right) + b_1 \left(\frac{u_t}{u_N}\right)^2 \qquad (54)$$

where

u_t = terminal free settling velocity of particle

Table 3. Sphericities for different size fractions of galena and magnesite ores (original data from Presler (85))

Sieve Size[a]	Sphericity ψ	
	Galena	Magnesite
9–10	-	0.554
10–12	-	0.475
12–14	-	0.491
14–16	0.635	0.440
16–20	0.601	0.498
20–24	0.581	0.489
24–28	0.657	0.522
28–32	0.668	0.612
32–35	0.742	0.586
35–42	0.839	0.573
42–48	0.954	0.666
48–60	1.000	0.693
60–65	1.148	0.744
65–80	1.109	0.809

[a]Tyler sieve passing and retaining the material.

u_N = the free settling velocity of the equivalent volume sphere in the same fluid at the same temperature.

$$a_1 + b_1 = 1$$

$$\frac{b_1}{a_1} = Re_N$$

$$Re_N = \rho u_N d_{eq}/\mu .$$

Although Briggs et al., gave equation 54 as the definition DSF, they used the ratio $(u_t/u_N)^2$ for determining the values of DSF. The two formulae differ significantly only at low particle Reynolds numbers.

Gunasingham et al. (57) in order to correlate the fluidization expansion data, used the ratio Ω. This shape factor is defined as follows:

$$\Omega = \frac{\text{diameter of a sphere with settling velocity equal to irregular particle in the same fluid at the same temperature}}{\text{equivalent spherical diameter}}$$

$$= \frac{d_h}{d_{eq}} \qquad (55)$$

Discussion on the Variation of DSF and Ω with Particle Reynolds Number

In some sanitary engineering, literature the shape factor Ω has erroneously been equated to sphericity. The author of this thesis, from the data presented by Pettyjohn and Christiansen (82) for different geometric shapes, calculated the DSF and Ω values at different

Reynolds number regions. Table 4 shows the asymptotic values of DSF and Ω at very low Reynolds numbers and very high Reynolds numbers.

Table 4. The values of DSF and Ω for the isometric particles studied by Pettyjohn and Christiansen (82) at low and high particle Reynolds numbers

Shape	Sphericity	Upper Limiting Value at Low Reynolds No.		Lower Limiting Values at High Reynolds No.	
	ψ	DSF	Ω	DSF	Ω
Cube octahedron	0.906	0.972	0.986	0.495	0.495
Octahedron	0.846	0.939	0.969	0.372	0.372
Cube	0.806	0.929	0.964	0.319	0.319
Tetrahedron	0.670	0.846	0.920	0.216	0.216

Figure 10 shows the variation DSF with particle Reynolds number (Re_t) for tetrahedrons and Figure 11 shows variation of Ω with particle Reynolds number (Re_t) for tetrahedrons.

This clearly illustrates that the two shape factors, DSF and Ω, are not constant for a particular geometric shape but vary with Re_t. This fact can be demonstrated clearly with help of Figure 12.

Let C_D and Re_t be the drag coefficient and Reynolds number of non-spherical particle and it's true position on log C_D vs log Re_t plot is located by P.

$$C_D = \frac{4}{3} \frac{g\, d_{eq}\, (\rho_s - \rho)}{\rho u_t^2} \tag{56}$$

$$Re_t = \frac{\rho u_t\, d_{eq}}{\mu} \tag{57}$$

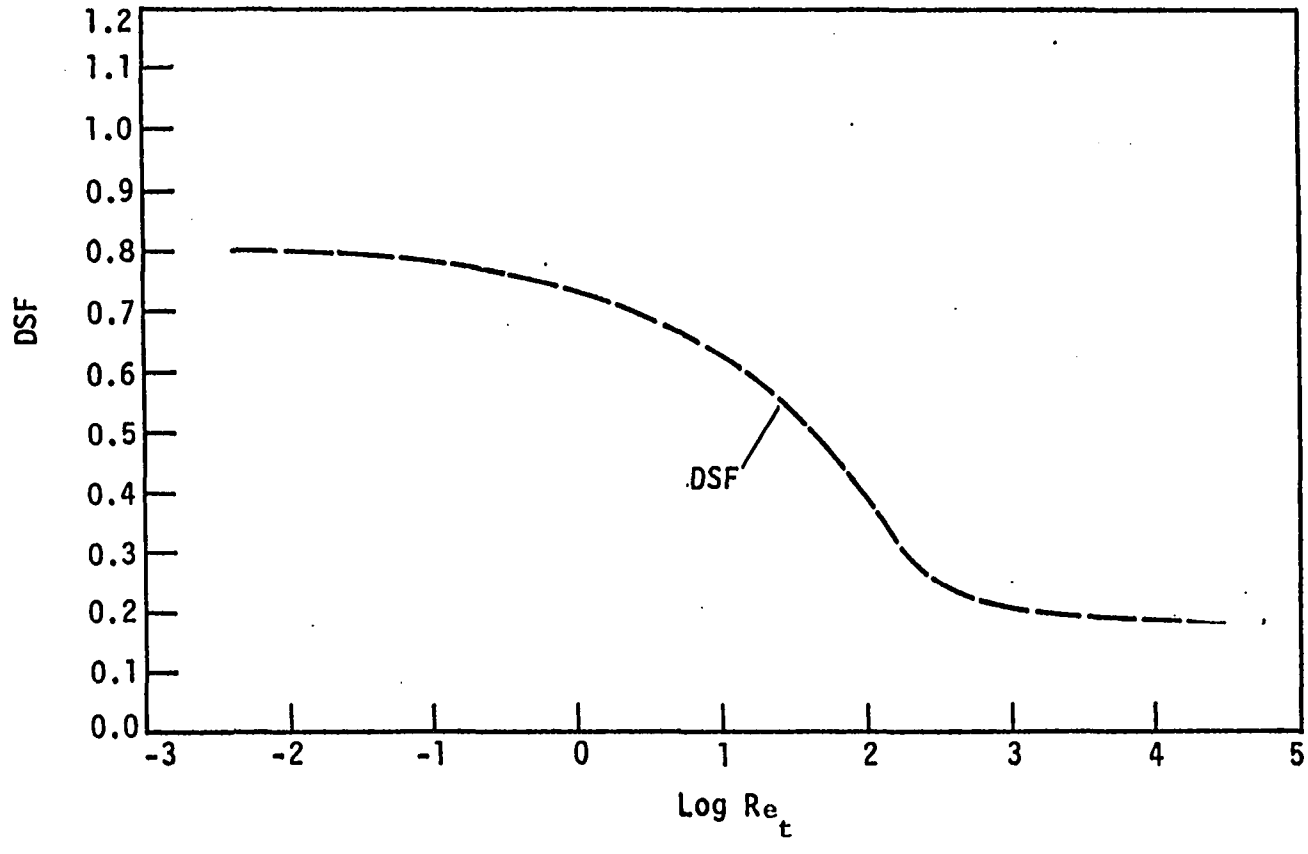

Figure 10. Dynamic shape factor, DSF, versus Re_t relationship for tetrahedron (Tetratedron ψ = 0.670)

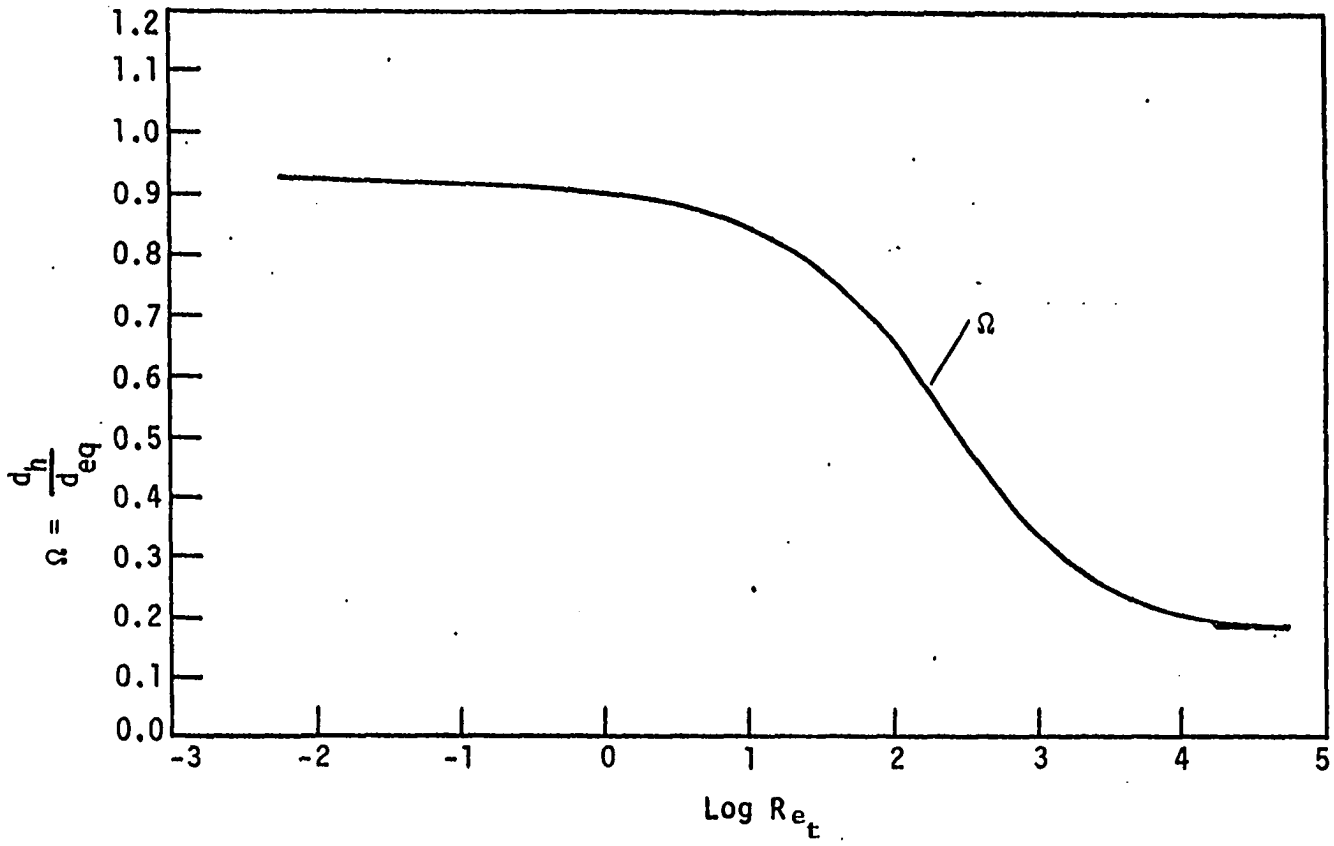

Figure 11. Hydraulically equivalent diameter shape factor, Ω, versus Re_t relationship for tetrahedrons (Tetrahedron ψ = 0.670)

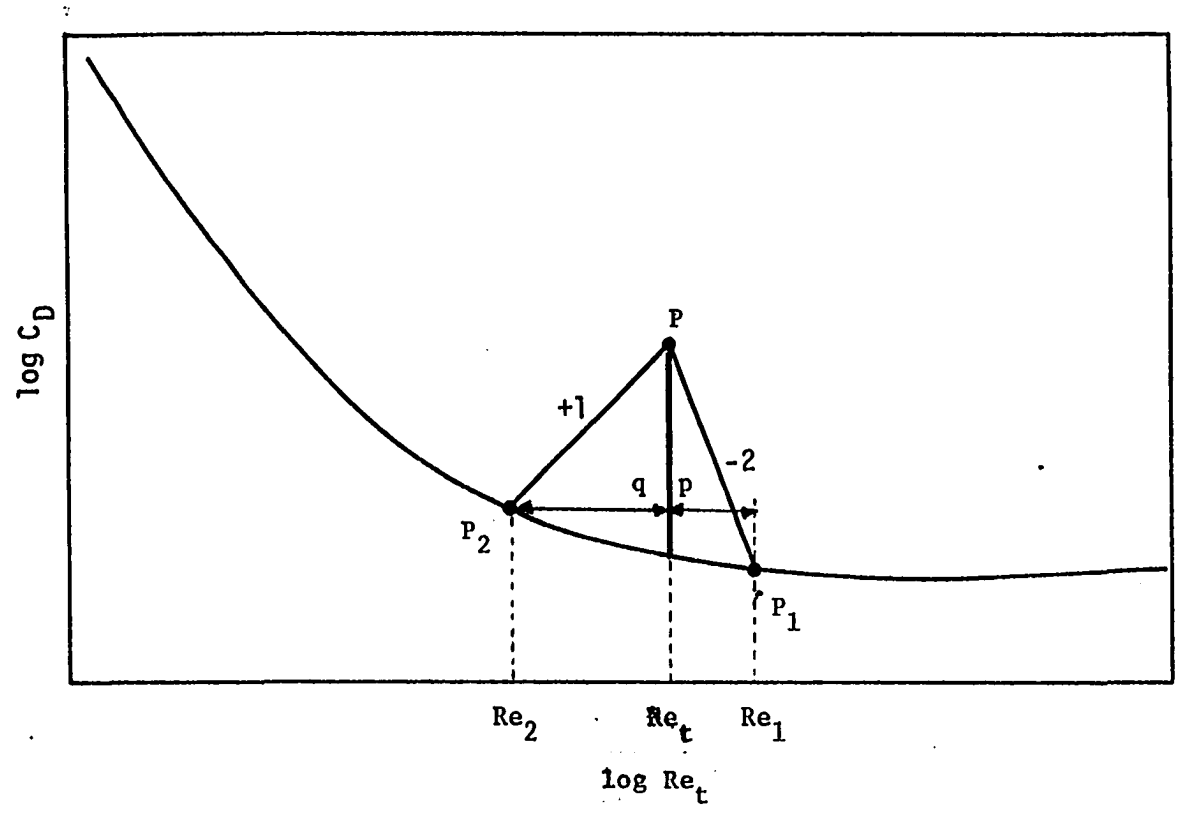

Figure 12. C_D versus Re_t relationship for spheres and for particular non-sphere at point P

$$C_D \, Re_t^2 = \frac{4}{3} \frac{g \, d_{eq}^3 \rho(\rho_s - \rho)}{\mu^2}$$

$$C_D = \frac{4}{3} \frac{g \, d_{eq}^3 \rho(\rho_s - \rho)}{\mu^2} \frac{1}{Re_t^2} \tag{58}$$

If a straight line is drawn with a slope-2 through the point P, from equation 58, it is seen that the points characterizing particles with same equivalent spherical diameter but different settling velocities will fall on this line. If this line intersects the drag curve for the spheres at P_1, P_1 will characterize the spherical particle with diameter equal to d_{eq} and settling velocity u_N with particle Reynolds number Re_N.

$$DSF = \left(\frac{u_t}{u_N}\right)^2 = \left(\frac{Re_t}{Re_N}\right)^2 \tag{59}$$

From Figure 12,

$$\log Re_N - \log Re_t = p$$

therefore,

$$\frac{Re_t}{Re_N} = 10^{-p}$$

$$DSF = \left(\frac{Re_t}{Re_N}\right)^2 = 10^{-2p} \tag{60}$$

By substituting for d_{eq} in equation 56, from 57 the following equation is obtained

$$C_D = \frac{4}{3} \frac{g\,(\rho_s - \rho)}{\rho^2\, u_t^3}\, Re_t \,. \tag{61}$$

From equation 61, it is evident that a straight line drawn with slope + 1 in log C_D vs log Re_t through the point P, characterizes all the particles with settling velocities u_t but with different equivalent spherical diameters. If this line intersects the drag curve for spheres at P_2, P_2 characterizes the spherical particle with settling velocity u_t and diameter d_h.

$$\Omega = \frac{d_h}{d_{eq}} = \frac{Re_2}{Re_t} \tag{62}$$

In the same manner, since Figure 12 is in logarithmic coordinators, it follows that

$$\frac{Re_2}{Re_t} = 10^{-q}$$

$$\Omega = 10^{-q} \tag{63}$$

If Re_1 and Re_2 lie on the constant drag coefficient segment of the drag curve (high Re), from the principles of geometry it is seen that $q = 2p$ and therefore, Ω = DSF at high Reynolds numbers. For small Reynolds numbers, the drag curve for non-spherical particles are closer to the drag curve for a sphere as shown earlier in Figure 4. If the point P in Figure 12 is closer to the drag curve for spheres, the magnitudes of p and q are small and therefore DSF and Ω will have higher values. In the turbulent region, the point P is farther away

from the drag curve for spheres. In this region, the DSF and Ω are lowest in magnitude. Furthermore, in the low or intermediate regions of Re, $q \neq 2p$ and therefore, DSF $\neq \Omega$.

In view of the above facts, the relationships between triaxial shape factors and DSF as reported by Briggs et al. (22) are not correct. For that matter, it is not possible to obtain a relationship between geometric shape factors and DSF or Ω unless one could restrict the measurements to the turbulent region of particle Reynolds number.

Fluidized Beds

Introduction

Fluidization can be observed by passing a fluid (gas or liquid) upwards through a bed of solids wherein it encounters a resistance to flow and a resultant pressure drop. As the flow rate is increased the pressure drop increases approximately linearly with flow rate. As the flow rate is increased further, a point is reached where the pressure drop is sufficient to bear the bouyant weight of particles. Any further increase in flow rate causes the bed to expand and accommodate the increased flow rate while maintaining the pressure drop effectively the same. In the fluidized state, the bed exhibits liquid like characteristics of mobility, hydrostatic pressure and an observable upper free boundary. In general, the transition from fixed bed to fluidized bed resembles the conduct of many solids in melting; the bed initially passes from solid into plastic state and finally becomes

completely liquid. Each particle then possesses an individual freedom of motion paralleling that of a molecule in a true liquid. The characteristics of an ideal fluidized bed and the distortion due to real conditions are shown in Figure 13.

General definition of fluidized beds

The point of incipient fluidization In the transition from fixed beds to fluidized beds, there is a change in the regime of flow from one where the frictional energy losses increase with increasing flow rate and are independent of weight of the particles to one where they are nearly constant and essentially dependent on the gravitational forces. While the transition is usually rather gradual and proceeds over a range of flow rates depending on the nature of the bed, it is desirable to define some definite point of incipient fluidization at which the complete change in regimes is assumed to take place. This point is selected as the intersection of the two linear segments of the curve depicting pressure drop versus superficial velocity and is shown in Figure 13.

Particulate or homogeneous fluidization Particulate fluidization refers to a condition in which the solids are individually and uniformly dispersed and is commonly observed in beds fluidized by liquids. Figure 14b shows particulate fluidization. The motion of the particles consists chiefly of a Brownian-like oscillation but under turbulent flow conditions there may also be a rotational motion. In addition, there may be a mixing effect causing a circulation of particles in the bed as a whole. In general, a bed in which there is little or no mixing of

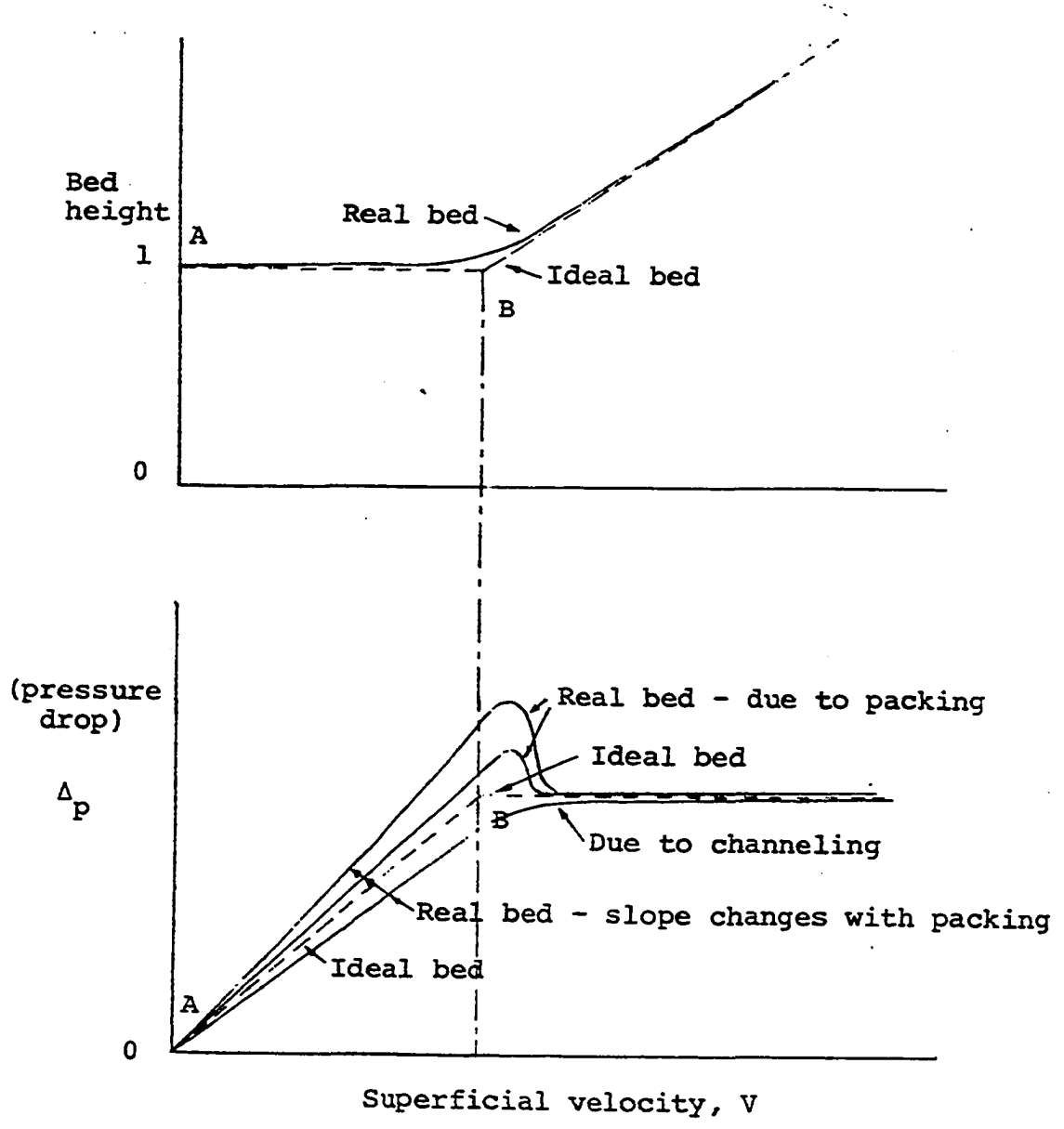

Figure 13. Characteristics of a fluidized bed (36)

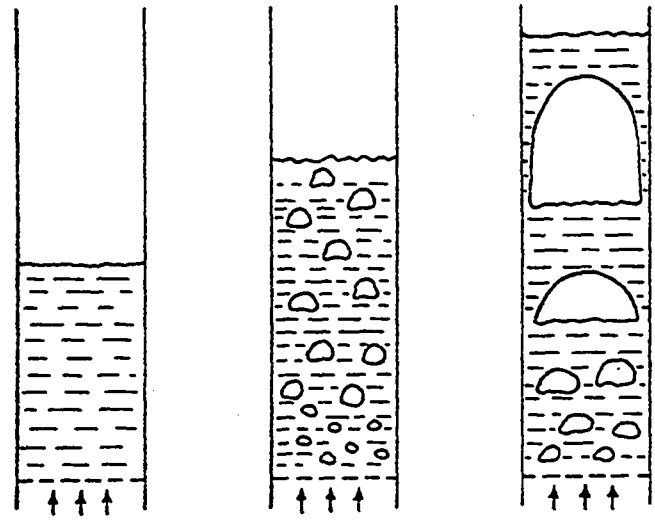

Figure 14a. Flow regimes in an aggregative fluidized system (36)

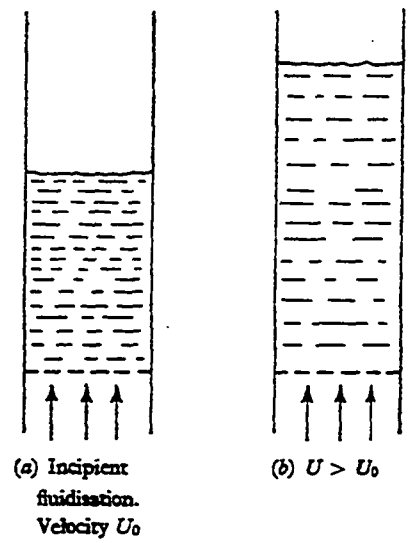

Figure 14b. Flow regimes in a particulate fluidized system (36)

the particles is called a quiescent fluidized bed.

The term "teetering", used in the mineral industry refers to suspensions of the particularly fluidized type and describes a practical application of particulate fluidization. The term hindered settling means an operation which is the reverse of particulate fluidization when a suspension settles in a column of fluid instead of being supported by upward flowing stream of fluid.

Aggregative fluidization In particulate fluidization, when the whole bed has been fluidized, the flow of increasing volumes of fluid is facilitated by a continuous uniform expansion of the bed which provides a flow path between particles. In contrast, in aggregative fluidization, the bulk of the bed tends to maintain itself in a dense state in which conditions are near the point of full fluidization or point of loosest contact and additional volumes of fluid flow through the dense phase in a fashion resembling passage of gases through liquids. The volume of flow in excess of the flow required to maintain the dense phase in suspended state generally carries a dispersed population of particles and is therefore referred to as the dilute phase. Aggregative fluidization is thus characterized by the coexistence of a dense and dilute suspension and is frequently referred to as a two phase fluidization. The two phase theory of aggregative fluidization postulated that all gases in excess of minimum fluidization passed through the bed as bubbles. The bubbles increase

in size as they pass through the bed and burst at the surface of the fluidized bed, with a light scattering of the solid particles at the surface and particles carried by the bubbles themselves. At higher rates of gas flow, the frontal diameter of the bubbles builds up to the diameter of the container and a condition called "slugging" of the bed is developed.

The following relations represent some criteria that are available to distinguish between particulate and aggregative fluidization;

(a) Wilhelm and Kwauk (109).

$$\text{Froude Number } Fr = \frac{u_{mf}}{g d_{eq}} < 1 \quad \text{for particulate fluidization} \tag{64}$$

(b) Zenz and Othmer (112).

$$\frac{\rho_s}{\rho} < 2 - 3 \quad \text{for particulate fluidization} \tag{65}$$

(c) Davidson and Harrison (36).

$$\frac{D_m}{d_{eg}} = \frac{u_t^2}{0.5 g d_{eq}} \left[\frac{\frac{\rho_s}{\rho_s - \rho} - \varepsilon_{mf}}{1 - \varepsilon_{mf}} \right] \tag{66}$$

where

D_m = maximum diameter of the bubble

u_t = terminal settling velocity of the particle

d_{eq} = equivalent spherical diameter of the particle.

$$\frac{D_m}{d_{eq}} \leq 1 \text{ particulate fluidization}$$

$$1 \leq \frac{D_m}{d_{eq}} \leq 10 \text{ transitional region of fluidization}$$

$$\frac{D_m}{d_{eq}} > 10 \text{ aggregative fluidization.}$$

(d). Romero and Johnson (93).

$$[(Fr_{mf})(Re_{mf})\left[\frac{\rho_s - \rho}{\rho}\right]\frac{L_o}{D_t}] < 100 \text{ for particulate fluidization.} \qquad (67)$$

where

$$Fr_{mf} = \frac{u^2_{mf}}{g\, d_{eq}}$$

$$Re_{mf} = \frac{\rho u_{mf}\, d_{eq}}{\mu}$$

L_o = depth of the bed

D_t = diameter of the column.

Channelling Channelling is an abnormality of an idealized fluidized system and is characterized by the establishment of preferential flow paths of pure fluid through the bed. It can occur both in particulate and aggregative fluidized systems. It is often caused in beds of fine particles or of sticky particles which tend to agglomerate. The calming section at the bottom of the bed that is used to distribute fluid has a profound effect on channelling (73). The extreme form of channelling is called a "spouting bed." A rapid upward

flow of particles is observed in the channel while in the bulk of the continuous phase there is a balancing downward movement. Figure 15 shows channelling and spouting conditions.

Prediction of Minimum Fluidization Velocity

Several equations have been proposed to predict the minimum fluidization velocity of unisized spherical materials. Some of these equations have correction factors incorporated into them to account for non-spherical materials.

Sen-Gupta and Rao (96) have published a review paper on the equations that have been presented over the years by several workers. They presented 45 different equations to predict minimum fluidization velocity. Some of the equations these authors chose to present in the form given by the original worker. This has led to a situation where the numerical constant reported in some of the equations is not compatible with units reported in the article.

Three fundamental approaches are followed to develop an equation to predict minimum fluidization velocity, even though the three approaches may not be mutually exclusive. The three methods are:

(1) Use of a fixed bed pressure drop equation and equating the pressure drop to the bouyant weight of the bed.

(2) Extrapolation of velocity-voidage expansion relationship to the fixed bed porosity.

(3) Obtaining a ratio between minimum fluidization velocity and terminal settling velocity in terms of the Galileo number or

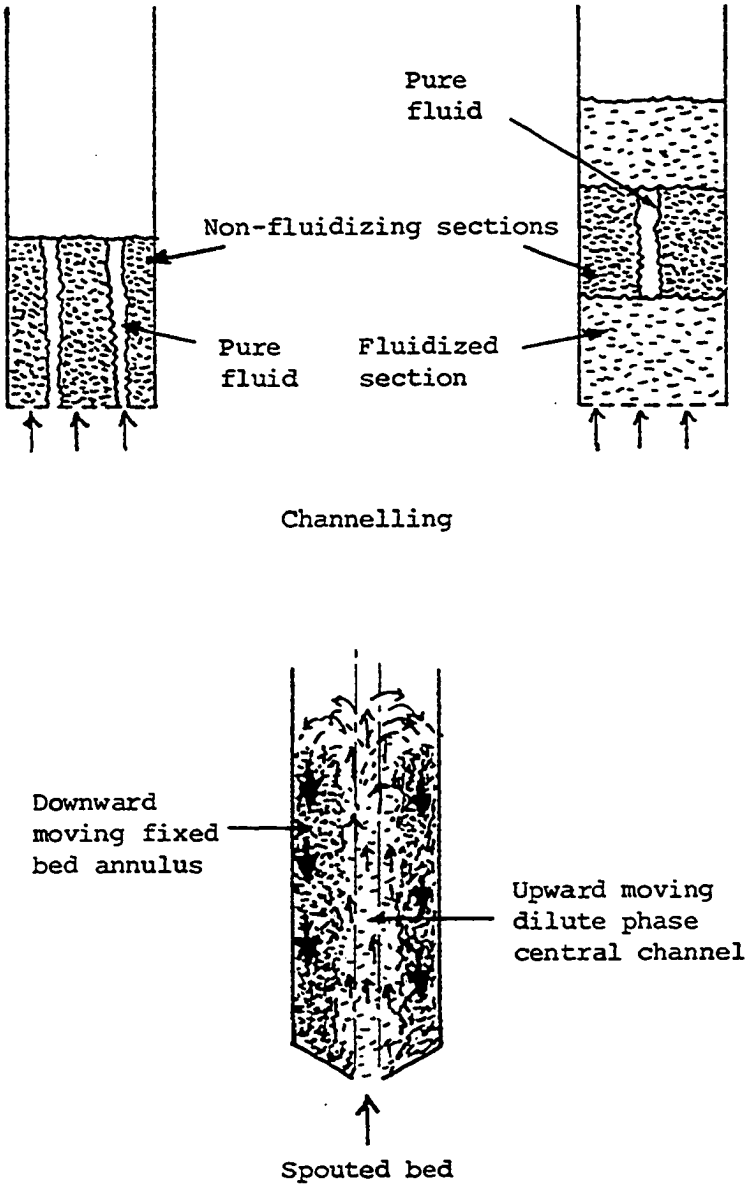

Figure 15. Channelling and spouting conditions (36)

some other parameter of the bed material.

Of the equations found in literature to predict the minimum fluidization, only a few of each method will be considered here for illustration.

Equations based on fixed bed pressure drop equation (method 1)

Leva's equation (73).

$$G_{mf} = \frac{688\ d^{1.82}\ (\gamma(\gamma_s - \gamma))^{0.94}}{\mu^{0.88}} \tag{68}$$

where

G_{mf} = superficial fluid mass velocity at minimum fluidization in $lb_m/hr - ft^2$.

d = diameter of the particle in inches.

γ and γ_s = fluid and particle specific weights respectively, in lb_f/ft^3.

μ = viscosity in centipoise.

This equation can be applied only when flow in the fixed bed is in the laminar flow regime because this equation was based on Kozeny's equation which is limited to laminar flow. The use of equation 68 was limited to $Re_{mf} < 10$, where Re_{mf} is the Reynolds number based on minimum fluidization velocity.

Zabrodsky (111) proposed a multiplying correction factor to expand its use for $Re_{mf} > 10$, the correction factor is

$$K_{mf} = 1.775\ Re_{mf}^{-0.272} \tag{69}$$

for

$$10 < Re_{mf} < 300 .$$

Frantz (52) performed regression analysis on his data and data of some other workers and from the line of best fit he was able to modify the exponents of Leva's equation. From a statistical analysis of his data, Frantz developed the following equation,

$$G_{mf} = \frac{1.69\, d_{eq}^{1.21}\, \rho^{1.02}\, (\rho_s - \rho)^{1.43}}{\mu^{0.73}\, D_t} \tag{70}$$

where

G_{mf} = superficial mass flow rate at minimum fluidization velocity in $lb_m/hr - ft^2$.

d_{eq} = equivalent spherical diameter of the particle in ft.

μ = fluid viscosity $lb_m/hr - ft$.

ρ_s, ρ = density of solid and fluid respectively in lb_m/ft^3.

D_t = diameter of the tube in ft.

Wen and Yu (106) based their equation for minimum fluidization on Ergun equation for fixed bed pressure drop, and equating the bouyant weight of the bed to pressure drop. The general equation is as follows:

$$\frac{1.75}{\psi \varepsilon_{mf}^{3}} Re_{mf}^{2} + 150 \frac{(1 - \varepsilon_{mf})}{\psi^2\, \varepsilon_{mf}^{3}} \quad Re_{mf} - Ga = 0 \tag{71}$$

where

$$Ga = \text{Galileo number} = \frac{d_{eq}^{3} \rho (\rho_s - \rho) g}{\mu^2}$$

ψ = sphericity of the particle.

Further, they incorporated an approximation in order to simplify the above equation by introducing

$$\frac{1 - \varepsilon_{mf}}{\psi^2 \varepsilon_{mf}^{3}} \simeq 11 \tag{72}$$

and

$$\frac{1}{\psi \varepsilon_{mf}^{3}} \simeq 14. \tag{73}$$

The simplified equation yields

$$Re_{mf} = \left[\sqrt{(33.7)^2 + 0.0408\ Ga}\right] - 33.7 \tag{74}$$

Both equations 71 and 74 are valid in the range $0.001 < Re_{mf} < 4000$. However, the relationship between ψ and ε_{mf} are not entirely satisfactory and whenever ψ and ε_{mf} are available the general equation 71 should be used as it is more accurate. ε_{mf} must be the loose bed porosity typical of incipient fluidization.

For mono disperse material of any shape, Bena et al. (17) proposed the following empirical equations to determine the minimum fluidization velocities.

$$Re_{mf} = \frac{0.00138\ Ga}{(Ga + 19)^{0.11}} \qquad \begin{array}{l} Ga \leq 1.06 \times 10^{5} \\ Re_{mf} < 41.0 \end{array}$$

and

$$Re_{mf} = 0.03865\ Ga^{0.602} \qquad 1.06 \times 10^5 < Ga < 2.13 \times 10^8$$
$$41.0 < Re_{mf} < 3.99 \times 10^3 \tag{75}$$

For non-spherical particles, the diameter of a sphere of equivalent volume was used as the characteristic dimension.

Equations based on extrapolation velocity-voidage relationship (method 2)

Garside and Al-Dibouni (54) and Barnea and Mendick (10) assumed that the correlation for predicting bed expansion with superficial velocity is valid at the limiting case of incipient fluidization too. Garside and Al-Dibouni gave the parameter of the logistic curve to predict the minimum fluidization of spherical particles at porosities 0.4 and 0.45. Barnea and Mednick used the generalized correlation of Barnea and Mizrahi (11) to demonstrate how that correlation could be used to predict the minimum fluidization velocities of spheres. These two correlations will be considered in detail under bed expansion correlations.

Equation based on ratio of minimum fluidization velocity and terminal settling velocity (method 3)

This approach has been generalized by number of workers including Pinchbeck and Popper (83), Goddard and Richardson (55) and Bourgeoise and Grenier (21) and can be used to obtain minimum fluidizing velocity for spherical particles in terms of their settling velocities.

The Ergun equation for pressure drop is equated to the bouyant weight of the bed per unit area and the terms rearranged to yield the following equation.

$$Ga = 150 \frac{(1 - \varepsilon_{mf})}{\varepsilon_{mf}^3} Re_{mf} + 1.75 \frac{1}{\varepsilon_{mf}} Re_{mf}^2 \qquad (76)$$

For spherical particles, the terminal settling velocity can be expressed in terms of Ga as follows:

$$\begin{aligned} Ga &= 18\ Re_t && Ga < 3.6 \\ Ga &= 18\ Re_t + 2.7\ Re_t^{1.687} && 3.6 < Ga < 105 \\ Ga &= \frac{1}{3} Re_t^2 && Ga > 10^5 \end{aligned} \qquad (77)$$

using these relationships it is possible to obtain a relationship between $\frac{Re_t}{Re_{mf}}$ and the Galieo number as shown in Figure 16, for different fixed bed porosities.

It should be borne in mind that these relationships, as given in equation 77 are valid only for spherical particles, and the terminal settling velocity of a non-spherical particle cannot be estimated from its Galileo number alone. This imposes a restriction on extending this approach to non-spherical particles.

Beranek (18) gave the following empirical relationship to estimate minimum fluidization for non-spherical particles

$$\begin{aligned} \frac{u_{mf}}{u_t} &= 0.019 \pm 0.003 && B_o < 0.3 \\ \frac{u_{mf}}{u_t} &= 0.022\ B_o^{0.2} && 0.3 < B_o < 10^3 \\ \frac{u_{mf}}{u_t} &= 0.09 \pm 0.005 && B_o > 10^3 \end{aligned} \qquad (78)$$

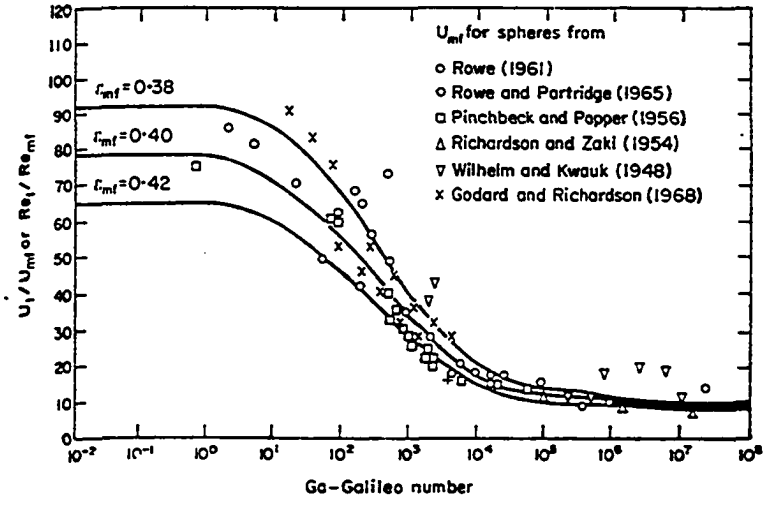

Figure 16. Re_t/Re_{mf} or u_t/u_{mf} versus Galileo number relationship for spheres at different fixed bed porosities (88, p. 51)

where

$$B_o = \frac{u_N^3 \rho^2}{g\mu (\rho_s - \rho)}$$

u_N = terminal settling velocity of a sphere of diameter d_{eq}

d_{eq} = diameter of a sphere of equal volume as that of the irregular particle.

In addition to the foregoing, a number of the equations have also been published for the prediction of minimum fluidization velocity. The equations not only differ in their basic approach, but also in the values of constants, exponents, dimensionless group or groups used to the correlations. For more elaborate review on this topic, one is referred to Sen-Gupta and Rao (96), or Zabrodsky (111).

Bena et al. (13, 14, 15) have published three articles on determining minimum fluidization velocity for beds of multisize particles during gas fluidization using a relationship for unisize particle bed. They suggested that in a liquid fluidized multisize bed of a single particle density, the particles segregate along the height of the bed in accordance with their terminal settling velocities. This fact enables one to calculate the point of incipient fluidization, to fluidize the entire bed, by calculating minimum fluidization velocity by applying any relationship valid for a unisize bed to the largest particle present in the bed.

Particulately Fluidized Bed Expansion Correlations

Since this section covers one of the major objectives of the

present study, a critical review of the expansion correlations available in the literature will be presented here.

Table 5, which is reproduced from Garside and Al-Dibouni (54) (Table 3 of their paper) shows some of the correlations reported in the literature for bed expansion of liquid fluidized spherical particles. Some of these correlations will be discussed herein in detail.

Richardson and Zaki correlation

The most widely used correlation for predicting expansion with flow rate is one due to Richardson and Zaki (92). They observed that when superficial velocity was plotted against the expanded bed porosity for unisized spherical material, a straight line resulted as shown in Figure 17.

Such a straight line can be described by the following equation

$$\log u = \log u_i + n \log \varepsilon$$

or

$$\frac{u}{u_i} = \varepsilon^n \tag{79}$$

where u_i is the intercept velocity at $\varepsilon = 1.0$.

Richardson and Zaki reported that during sedimentation of small particles

$$u_i \approx u_t$$

and during fluidization

$$\frac{u_t}{u_i} = 10^{d/D_T} \tag{80}$$

where

$\frac{d}{D_T}$ = ratio of particle diameter to column diameter.

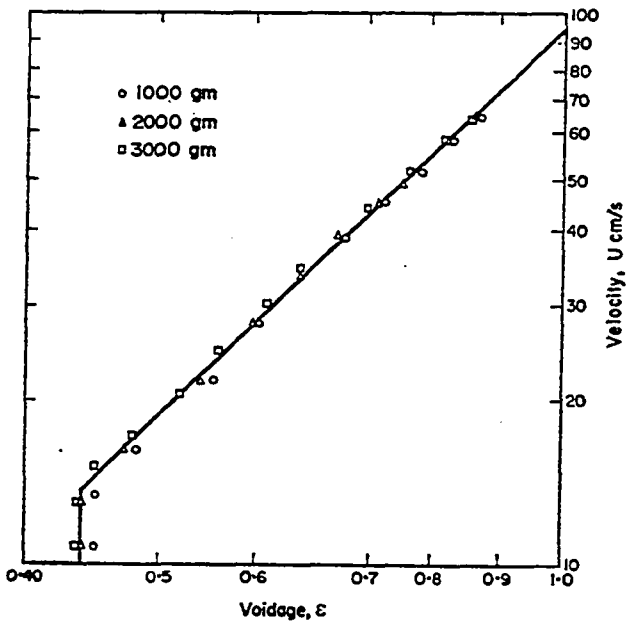

Figure 17. The relationship between log superficial velocity and log porosity as described by Richardson and Zaki (92)

Table 5. Some of the published correlations for bed expansion characteristics of liquid fluidized beds of spherical particles (Garside and Al-Dibouni (54) Table III)

Date	Author	Equation	Range of Applicability
1944	Steinour	$\frac{u}{u_t} = \varepsilon^2 \exp(-4.19(1-\varepsilon))$	$Re_t < 0.2$; $\varepsilon \leq 0.85$
1947	Brinkman	$\frac{u}{u_t} = \{1 + 0.75\ (1 - \varepsilon)[1 - \{\frac{8}{(1-\varepsilon)} - 3\}^{1/2}]\}$	$Re_t < 0.2$
1949	Lewis et al.	$\frac{u}{u_t} = \varepsilon^{4.65}$	$1.1 < Re_t < 2.6$
1951	Hawksley	$\frac{u}{u_t} = \varepsilon^2 \exp\left[\frac{-2.5(1-\varepsilon)}{1 - \frac{39}{64}(1-\varepsilon)}\right]$	$0.001 < Re_t < 58$
1952	Jottrand	$\frac{u}{u_t} = \varepsilon^{5.6}$	$0.001 < Re_t < 0.4$
1952	Lewis and Bowerman	$\frac{u}{u_t} = 0.7\ \varepsilon^{2.32}$	$2 < Re_t < 500$
		$\frac{u}{u_t} = 0.7\varepsilon^{2.32}$	$Re_t > 500$; $\varepsilon \leq 0.9$
1954	Richardson and Zaki	$\frac{u}{u_t} = \varepsilon^n$	

		where	
		$n = 4.65 + 20\ d/D_T$	$Re_{t\infty} < 0.2$
		$n = (4.4 + 18\ d/D_T)\ Re_{t\infty}^{-0.03}$	$0.2 < Re_{t\infty} < 1$
		$n = (4.4 + 18\ d/D_T)\ Re_{t\infty}$	$1 < Re_{t\infty} < 200$
		$n = 4.4\ Re_{t\infty}^{-0.1}$	$200 < Re_{t\infty} < 500$
		$n = 2.4$	$Re_{t\infty} > 500$
1958	Happel	$\frac{u}{u_t} = \left[\frac{3 - \frac{9y}{2} + \frac{9y^5}{2} - 3y^6}{3 + 2y^5}\right]$	$Re_t < 0.2$
		where	
		$y = 1 - \varepsilon$	
1959	Loeffler and Ruth	$\frac{u}{u_t} = \frac{\varepsilon}{(1-\varepsilon)\left[5.7 + \frac{\varepsilon^2}{(1-\varepsilon)}\right]}$	$Re_t < 0.5$
1961	Oliver	$\frac{u}{u_t} = (1 - 2.15(1 - \varepsilon))(1 - 0.75(1 - \varepsilon)^{1/3})$	$Re_t < 0.4$
1966	Wen and Yu	$\varepsilon^{4.7}\ Ga = 18\ Re + 2.7\ Re^{1.687}$	$10^{-3} < Re_t < 10^4$
		$Ga = \frac{\rho(\rho_s - \rho)gd^3}{\mu^2}$	
		$Re = \frac{\rho u d}{\mu}$	

Table 5. continued

Date	Author	Equation	Range of Applicability
1973	Barnea and Mizrahi	$C_{D\phi} = \left[\frac{4d(\rho_s - \rho)g}{3\rho u^2}\right] \left[\frac{\varepsilon^3}{(1 + (1 - \varepsilon)^{1/3})}\right]$ $Re_\phi = \frac{\rho u d}{\mu} \frac{1}{\varepsilon \exp\left[\frac{5(1-\varepsilon)}{3\varepsilon}\right]}$ The relationship between $C_{D\phi}$ vs. Re_ϕ is coincidental with the standard drag curve for spheres (C_D vs. $Re_{t\infty}$) for $10^{-3} < Re\phi < 3 \times 10^4$.	
1974	Letan	$\frac{u}{u_t} = \frac{(1 + 0.15\ Re_t^{0.687})\ \varepsilon^{3.5}}{1 + 0.15\ (Re_t \cdot \frac{u}{u_t})^{0.687} \cdot \varepsilon^{1.72}}$	$1.5 < Re_t < 2200$

Further, they presented the following empirical equations for the expansion coefficient n for spherical particles

$$
\begin{aligned}
n &= 4.65 + 20\left(\frac{d}{D_T}\right) && Re_{t\infty} < 0.2 \\
n &= (4.4^{a} + 18\ (d/D_T))Re_{t\infty}^{-0.03} && 0.2 < Re_{t\infty} < 1.0 \\
n &= (4.4^{a} + 18\ (d/D_T))Re_{t\infty}^{-0.1} && 1 < Re_{t\infty} < 200 \\
n &= 4.4^{a}\ Re_{t\infty}^{-0.1} && 200 < Re_{t\infty} < 500 \\
n &= 2.4 && Re_{t\infty} > 500
\end{aligned}
\tag{81}
$$

Discussion on the shortcomings of Richardson and Zaki correlation

Richardson and Zaki (92) failed to observe that beyond a porosity of approximately 0.9 the log u vs. log ε plots deviates significantly from linearity. Adler and Happel (1) suggested that equation (79) underestimates the mutual influences of particles in very dilute systems where ε approaches unity and therefore gives values of u which are too high this region. Adler and Happel (1) presented Figure 18 and commented that the curvature in the plot is more pronounced with increasing particle Reynolds number. Bena et al. (16) also made similar observation. These observations lead one to believe that the characteristics of a liquid fluidized system change drastically when the expanded bed porosity is approaching unity. The intercept velocity u_i, is obtained by extrapolating the straight line in log u vs. log ε plot to ε = 1. The u_i value thus obtained, bears no relationship to the actual physical process involved

[a] The values were changed by Richardson (88).

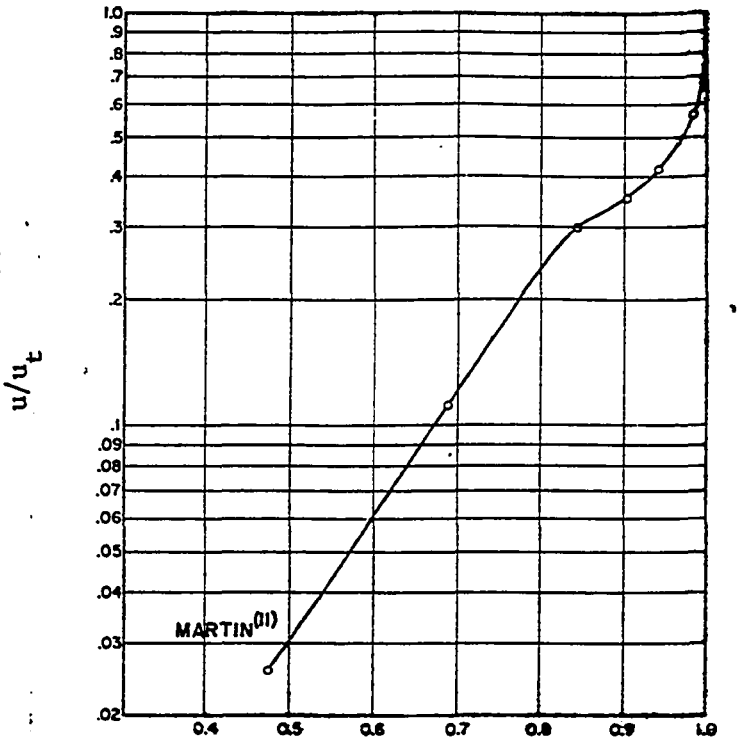

Figure 18. The relationship between u/u_t and porosity as reported by Alder and Happel[1] (1)

at $\varepsilon = 1$. Due to this fact u_i cannot be accurately estimated.

Table 6 shows the relationship between superficial velocity and terminal settling velocity for dilute suspensions in creeping flow regime. Except for one equation the general form of the equation is:

$$\frac{u}{u_t} = \frac{\varepsilon}{1 + \beta\ (1 - \varepsilon)^{1/3}} \tag{82}$$

and this equation is quite different from the exponential equation given by Richardson and Zaki (92).

The author of this thesis plotted $\log \frac{u_t}{u_i}$ vs. d/D_T in Figure 19 for the data obtained by Richardson and Zaki (92), Lewis et al. (75), and Loeffler (76). This figure clearly indicates that equation 80 is not valid and leads one to believe that u_i is a mathematical artifact without any physical significance.

Bena et al. (16) have proposed that the general relationship between Reynolds number based on superficial velocity and porosity on a log-log plot can be approximated by two straight lines and a curve as shown in Figure 20.

Re_{k1} and Re_{k2} are obtained from the following equations for the spherical particles

$$Re_{k1} = 0.0157\ Ga^{0.698} + 0.400$$

$$Re_{k2} = 0.192\ Ga^{0.548} + 1.000 \tag{83}$$

Although Richardson and Zaki (92) observed discontinuity in the expansion line in log u vs. log ε plot, they attributed this to bridging of the particles from wall to wall and considered this effect to be absent at relatively high expansion. The discontinuities observed

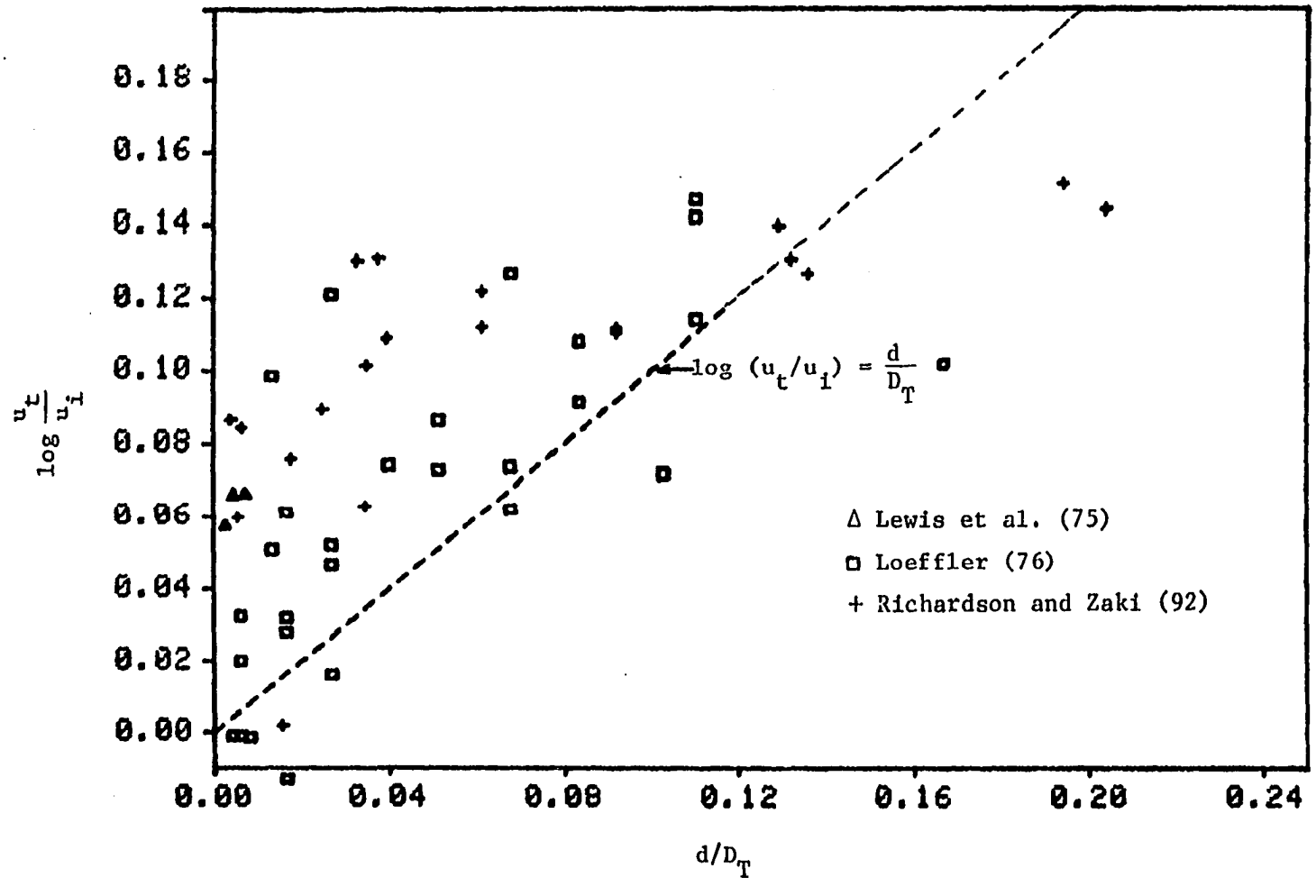

Figure 19. The relationship between log u_t/u_i and d/D_T ratio for spherical particles

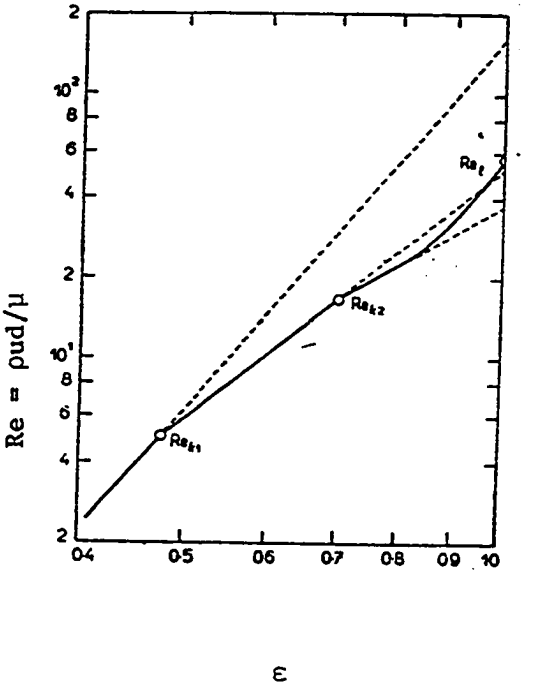

Figure 20. The relationship between Reynolds number based on superficial velocity and porosity for fluidization data as reported by Bena et al. (16)

Table 6. Comparison of the asymptotic analytical solution for very dilute suspension of spheres in the creeping flow region (reproduced from Barnea and Mizrahi (11))

Date	Investigators	Equation
1949	Uchida	$\frac{u}{u_t} = \frac{\varepsilon}{1 + 2.1(1 - \varepsilon)^{1/3}}$
1958	Happel	$\frac{u}{u_t} = \frac{\varepsilon}{1 + 1.5(1 - \varepsilon)^{1/3}}$
1968 1970	Leclair and Hamielec Gal-or	$\frac{u}{u_t} = \frac{\varepsilon}{1 + 1.8(1 - \varepsilon)^{1/3}}$
1959	Hasimoto	$\frac{u}{u_t} = \frac{\varepsilon}{1 + 1.76(1 - \varepsilon)^{1/3}}$
1952	McNown and Lin	$\frac{u}{u_t} = \frac{\varepsilon}{1 + 1.6(1 - \varepsilon)^{1/3}}$
1911 1952 1965	Smoluchowski McNown and Lin Famularo and Happel	$\frac{u}{u_t} = \frac{\varepsilon}{1 + 1.92(1 - \varepsilon)^{1/3}}$
1965	Famularo and Happel	$\frac{u}{u_t} = \frac{\varepsilon}{1 + 1.79(1 - \varepsilon)^{1/3}}$
1942	Burgers	$\frac{u}{u_t} = \frac{1}{1 + 6.88\ (1 - \varepsilon)}$

by Richardson and Zaki were much sharper than those observed by Bena et al. (16). Wilhelm and Kwauk (109) did extensive study on expansion of liquid and air fluidized systems. Their plots of $Re(\rho ud/\mu)$ vs. porosity also show some degree of curvature (Figure 10 in their paper). The curvature is more pronounced when the particle Reynolds number (Re_t) is high. Due to this non-linearity of log u vs. log ε plots the actual value of n determined during fluidization experiments depends to some extent on the range of porosity over which measurements have been made and the distribution of experimental points over this range.

Deviations from equation 79 occur with solid of high density and divergences are particularly marked with deep beds of particles of small size (37). Simpson and Rodger (97), Harrison et al. (58) and Richardson and Smith (91) have observed that lead shot fluidized by water gave rise to non-uniform fluidized beds. Hessett (60) also noted instabilities and non-uniformities in solid-liquid systems particularly in beds of narrow diameters. Cairns and Prausnitz (25) and Reuter (87) have published photographs of bubbles in solid-liquid fluidized systems. Richardson (88) quoted unpublished work of Bailey who studied the fluidization of lead shots with water and reported the occurrence of non-uniformities but not well-defined bubbles. He showed, as seen in Figure 21, that the logarithmic plots of voidage against velocity are no longer linear and that the deviations from the line given by equation 79 increases with:

(a) increase in bed weight per unit area

(b) decrease in particle size.

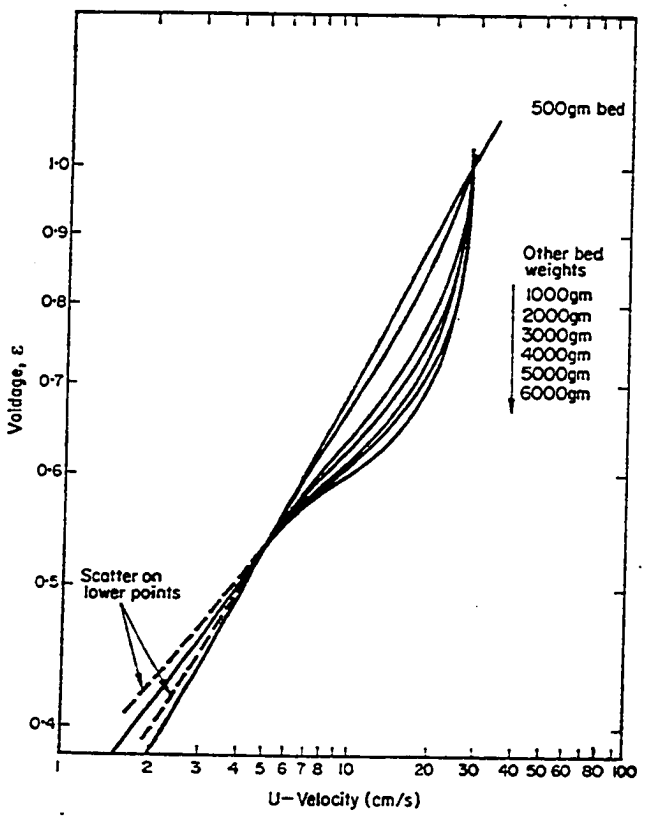

Figure 21. Bed expansion for fluidization of 0.05 - 0.06 cm lead shot in water in 10. cm tube (88,p. 40)

The effect of particle density in determining the nature of fluidized systems has been established, and an increase in density generally results in less uniform fluidized systems (37, 39). The reasons for the deviation from equation 79 for reduction in particle size are not as clear as that for increased bed weight per unit area. One explanation for this observation is that part of the fluid takes a path of low resistance through the bed, remaining there for less than the average residence time and not therefore contributing fully to the expansion of the bed. The effect of partial channelling will certainly be more marked with fine solids than with coarse solids since the ratio of the resistance of the bed to that of the channel will be much greater and a comparatively small channel will accomodate flow of a proportionately larger amount of fluid.

Wen and Yu correlation and Richardson and Jeromino correlation

Wen and Yu (106) and Richardson and Jeromino (89) assumed that at a given superficial velocity, the ratio of the drag force on a single particle in multiparticle system to drag force on a discrete particle to be some function of the porosity of the fluidized bed. Mathematically stated

$$\frac{F_k}{F_D} = f(\varepsilon) \tag{84}$$

where

F_D = is the drag force on a single particle

$$= C_D \times \frac{\pi d^2}{4} \frac{1}{2} \rho u^2$$

F_k = drag force on a single particle in a multiparticle system = bouyant weight of the particle

$$= \frac{\pi d^3}{6} (\rho_s - \rho) g$$

$$f(\varepsilon) = \frac{(\pi d^3/6)(\rho_s - \rho)g}{C_D \cdot \frac{\pi}{4} d^2 \frac{1}{2} \rho u^2} = \frac{4}{3} \frac{G_a}{C_D \cdot Re^2} \tag{85}$$

$$Ga = \frac{\rho(\rho_s - \rho)gd^3}{\mu^2}$$

$$Re = \frac{\rho ud}{\mu}$$

Wen and Yu (106) assumed the Schiller and Naumann equation for C_D to be valid in the Reynolds number range from 0.001 to 1000. Then equation 85 can be written as

$$f(\varepsilon) = \frac{Ga}{18\ Re + 2.7\ Re^{1.687}} \tag{86}$$

These authors used the data reported by Wilhelm and Kwauk (109), Richardson and Zaki (92), Lewis et al. (75) and data from their own experiments, and showed that

$$f(\varepsilon) = \varepsilon^{-4.7} \tag{87}$$

Insertion of the function in Equation 86 leads to the prior equation in Table 5. Richardson and Jeronimo (89) proceed as shown below to obtain a

relationship for function $f(\varepsilon)$:

By differentiating equation 85 with respect to log ε, the following equation is obtained

$$\frac{d \log f(\varepsilon)}{d \log \varepsilon} = -\frac{d \log C_D}{d \log \varepsilon} - 2 \frac{d \log Re}{d \log \varepsilon}$$

$$= -\frac{d \log C_D}{d \log Re} \cdot \frac{d \log Re}{d \log \varepsilon} - 2 \frac{d \log Re}{d \log \varepsilon}$$

Thus,

$$\frac{d \log Re}{d \log \varepsilon} = - \frac{\frac{d \log f(\varepsilon)}{d \log \varepsilon}}{\frac{d \log C_D}{d \log Re} + 2} \tag{88a}$$

For spherical particles with $Re_t < 0.2$.

$$\frac{d \log C_D}{d \log Re} = -1 \text{ (from the slope of the } C_D \text{ vs. } Re_{t\infty} \text{ curve).}$$

then

$$\frac{d \log Re}{d \log \varepsilon} = - \frac{d \log f(\varepsilon)}{d \log \varepsilon} \tag{88b}$$

for $Re_t > 500$

$$\frac{d \log C_D}{d \log Re} \simeq 0$$

then

$$\frac{d \log Re}{d \log \varepsilon} = - \frac{1}{2} \frac{d \log f(\varepsilon)}{d \log \varepsilon} \tag{89}$$

further they assumed

$$\frac{u}{u_t} = \varepsilon^n \text{ or } \frac{Re}{Re_t} = \varepsilon^n \tag{90}$$

by differentiating equation 90 with respect to log ε, one obtains

$$\frac{d \log u}{d \log \varepsilon} = n \text{ or } \frac{d \log Re}{d \log \varepsilon} = n \tag{91}$$

for $Re_t < 0.2$ $\quad n = 4.6$

$$\frac{d \log Re}{d \log \varepsilon} = 4.6 \tag{92}$$

for $Re_t > 500$ $\quad n = 2.3$

$$\frac{d \log Re}{d \log \varepsilon} = 2.3 \tag{93}$$

Solving either equation 88b and 92, or 89 and 93 leads to the same expression

$$\frac{d \log f(\varepsilon)}{d \log \varepsilon} = -4.6$$

$$f(\varepsilon) = \varepsilon^{-4.6} \tag{94}$$

Therefore, it can be concluded that the function $f(\varepsilon)$ is independent of Reynolds number Re.

Equation 94 shows close agreement with equation 87 which Wen and Yu (106) obtained by a different approach.

Richardson and Jeromino (89) then proceeded to obtain a relationship between n, C_D and $Re_{t\infty}$ as indicated below:

From equation 88a, 94

$$\frac{d \log Re}{d \log \varepsilon} = \frac{4.6}{\frac{d \log C_D}{d \log Re} + 2} = n \tag{95}$$

If the Schiller and Naumann equation for C_D vs. Re_t relationship is assumed to be valid in the Reynolds number range 0.2 to 500

$$C_D = 24 Re_{t\infty}^{-1} (1 + 0.15\ Re_{t\infty}^{0.687}) \tag{96}$$

$$\log C_D = \log 24 - \log Re_{t\infty} + \log (1 + 0.15\ Re_{t\infty}^{0.687}) \tag{97}$$

differentiating 97 with respect to $\log Re_{t\infty}$

$$\frac{d \log C_D}{d \log Re_{t\infty}} = -1 + \frac{0.15(0.687) Re_{t\infty}^{0.687}}{1 + 0.15\ Re_{t\infty}^{0.687}}$$

$$= -\frac{1 + 0.0470\ Re_{t\infty}^{0.687}}{1 + 0.15\ Re_{t\infty}^{0.687}} \tag{98}$$

Substituting 98 in 95

$$n = \frac{4.6}{2 - \left[\frac{1 + 0.0470\ Re_{t\infty}^{0.687}}{1 + 0.15\ Re_{t\infty}^{0.687}}\right]} \tag{99}$$

Richardson and Jeronimo (89) compared the n values obtained from equation 99 and experimentally observed n values. For particle Reynolds numbers less than 30, both computed and experimental n values agreed closely but beyond $Re_t > 30$ computed values were higher than

experimental values. The disagreement between computed and experimental values can be attributed to the following reasons.

(1) The assumed relationship $\frac{u}{u_t} = \varepsilon^n$ is not valid even when d/D_T ratio is negligibly small. This effect becomes more pronounced in the turbulent region.

(2) The drag coefficient C_D was assumed equal to that for a isolated spherical particle in a quiescent medium of infinite extent. During fluidization, the scale and intensity of turbulence vary with bed voids ratio. It has been observed that under the effect of free stream turbulence and particle oscillation the drag coefficient changes drastically from standard drag curve.

Zuber and Letan's correlations

Zuber (113) theoretically analyzed dispersed two phase flow in the laminar flow regime and showed that $\frac{u}{u_t} = \varepsilon^{4.65}$. Letan (72) extended the work of Zuber to the intermediate range of particle Reynolds number. By considering equations of continuity for continuous and dispersed phase and equations of motion for a suspension, she obtained the following equation

$$u^2 = \frac{4}{3} \frac{d(\rho_s - \rho)g}{\rho} \frac{\varepsilon}{C_D} \tag{100}$$

where

u = superficial velocity of fluidization

C_D = drag coefficient of a single spherical particle in an infinite fluid.

Then she incorporated two assumptions.

(1) The drag coefficient C_D of a spherical particle in a bed of like particles would be the same as would be observed in a fluid of the same apparent viscosity of the suspension.

(2) The apparent viscosity of a suspension varies with porosity only.

By utilizing Roscoe's (94) equation for apparent viscosity $\mu_A = \mu\varepsilon^{-2.5}$ and Schiller and Naumann equation for drag coefficient she obtained the following relationship

$$\frac{u}{u_t} = \frac{(1 + 0.15\ Re_t^{0.687}) \cdot \varepsilon^{3.5}}{\{1 + 0.15\ (Re_t \cdot \frac{u}{u_t})^{0.687}\ \varepsilon^{1.72}\}} \qquad (101)$$

Letan demonstrated equation 101 and Richardson and Zaki's empirical equation predict very similar values for the ratio $\frac{u}{u_t}$; but, deviation of porosity up to 0.1 for data of Mertes and Rhodes (80) and Wilhelm and Kwauk (109) was also observed.

Barnea and Mizrahi's correlation

Barnea and Mizrahi (11) came up with extended definitions for Reynolds number and drag coefficient which includes the porosity of the bed or the suspension. Using these extended definitions they were able to bring together data from 12 different sources into a single correlation covering a wide range of particle Reynolds number. The correlation between the modified Reynolds number and the modified drag coefficient coincided with the standard drag curve relating the drag coefficient with Reynolds number for spheres.

They considered the hinderence effect in multi-particle systems can be broken down into the following:

(1) The pseudo-hydrostatic effect. The average effective hydrostatic pressure gradient of the suspension is greater than that of the fluid alone, and consequently the effective bouyancy effect is greater,

$$\rho_b = \rho_s (1 - \varepsilon) + \rho\varepsilon \tag{102}$$

(2) The momentum transfer effect. The presence of other particles affects the mechanism of the transfer of momentum between each particle and the fluid medium. This effect is related, although not strictly equivalent to increase in 'apparent' bulk viscosity of the suspension, which becomes evident when the bulk suspension is sheared. This effect calls for a correction factor in terms of ε.

(3) The return flow effect. A settling cloud of particles causes an opposite motion of the fluid which develops drag forces on all particles and limits the flow field around the individual particles. This effect calls for another correction factor in terms of ε.

In the creeping flow range,they obtained a relationship for $U_R = \left(\frac{u/\varepsilon}{u_t}\right)$ as follows:

The drag force is increased by momentum transfer hinderance and the proximity of other particles. The former was postulated to have the same general form as the viscosity increase and is given by the following equation,

$$\mu_\phi = \mu \exp\left[\frac{k_1 (1 - \varepsilon)}{1 + k_2\varepsilon}\right] \tag{103}$$

The return flow effect was assumed to increase the drag force by $\{1 + k_3 (1 - \varepsilon)^{1/3}\}$

where

k_1, k_2 and k_3 are empirical constants.

The drag force F_D is given by,

$$F_D = 3\pi d \frac{u}{\varepsilon}\left[1 + k_3(1 - \varepsilon)^{1/3}\right] \exp\left[\frac{k_1(1 - \varepsilon)}{1 + k_2 \varepsilon}\right] \tag{104}$$

The driving force or bouyant force F_g, if the hydrostatic effect of suspension is taken into account, is given by

$$F_g = \frac{\pi d^3}{6} g (\rho_s - \rho_b)$$

$$= \frac{\pi d^3}{6} g (\rho_s - \rho) (\varepsilon). \tag{105}$$

Equating 104 and 105, one obtains

$$\frac{u}{\varepsilon} = \frac{d^2 g(\rho_s - \rho)}{18\mu} \frac{\varepsilon}{\{1 + k_3(1 - \varepsilon)^{1/3}\}} \exp\left[\frac{k_1(1 - \varepsilon)}{1 - k_2 \varepsilon}\right]. \tag{106}$$

Using published experimental data in the creeping flow regime, they showed

$$k_2 = k_3 = 1.0 \text{ and } k_1 = 5/3$$

The final form of the equation in the creeping flow regime was

$$\frac{u}{u_t} = \left[\frac{\varepsilon^2}{1 + (1 - \varepsilon)^{1/3}}\right] \exp\left[\frac{5(1 - \varepsilon)}{3\varepsilon}\right] \tag{107}$$

They claimed equation 107 predicted the reported experimental data very well.

The successful correlation in the creeping flow regime led them to search for modified definitions for Reynolds number Re_ϕ and drag coefficient $C_{D\phi}$ which would make the relationship of Re_ϕ and $C_{D\phi}$ coincide with the standard drag curve for a single particle. The interstitial velocity, u/ε, was used as the characteristic velocity in the modified definitions of Re_ϕ and $C_{D\phi}$.

The modified Reynolds number was defined as follows assuming k_1, k_2 and k_3 remained unchanged.

$$Re_\phi = \frac{\frac{u}{\varepsilon} \cdot d\rho}{\mu_\phi} = \frac{\frac{u}{\varepsilon} \cdot d.\rho}{\mu \exp\left[\frac{5(1-\varepsilon)}{3\varepsilon}\right]} \tag{108}$$

The drag coefficient is the ratio of drag forces to the dynamic pressure on the particle cross-sectional area. It should take into consideration the return flow effect and hydrostatic effect as follows:

$$C_{D\phi} = \frac{C_D}{1 + (1-\varepsilon)^{1/3}} = \frac{F_D}{\frac{1}{2}\rho A. \left(\frac{u}{\varepsilon}\right)^2 \{1 + (1-\varepsilon)^{1/3}\}} \tag{109}$$

where

$C_{D\phi}$ = the modified drag coefficient

C_D = the drag coefficient on a single particle.

F_D = drag force $= \frac{\pi d^3}{6}(\rho_s - \rho_b)g$

$$= \frac{\pi d^3}{6}(\rho_s - \rho)g\varepsilon$$

A = cross sectional area of the particle = $\frac{\pi d^2}{4}$.

Thus,

$$C_{D\phi} = \frac{\pi d^3}{6} \frac{(\rho_s - \rho)g\varepsilon}{\frac{1}{2}\rho \frac{\pi d^2}{4} \cdot \frac{u^2}{\varepsilon^2} \{1 + (1 - \varepsilon)^{1/3}\}}$$

$$C_{D\phi} = \frac{4d(\rho_s - \rho)g}{3\rho u^2} \frac{\varepsilon^3}{\{1 + (1 - \varepsilon)^{1/3}\}} \quad (110)$$

$$= C_D \frac{u_t^2}{u^2} \frac{\varepsilon^3}{\{1 + (1 - \varepsilon)^{1/3}\}} \quad (111)$$

where

C_D = drag coefficient of an isolated particle.

u_t = terminal settling velocity = $\left[\frac{4d(\rho_s - \rho)g}{3\rho C_D}\right]^{1/2}$.

From equations 108 and 111, it is seen that as $\varepsilon \to 1$, $Re_\phi \to Re_t$ and $C_{D\phi} \to C_D$. Using these modified definitions of Re_ϕ and $C_{D\phi}$, Barnea and Mizrahi were able to bring together data from twelve different sources into a single correlation as shown in Figure 22.

Garside and Al-Dibouni's correlation

Garside and Al-Dibouni (54) showed that at a particular expanded bed voidage the relationship between $u_R = \frac{u/\varepsilon}{u_t}$ and Re_t can be correlated by a logistic curve of the form

$$\frac{u_R - A}{B - u_R} = C\, Re_t^{\,m} \quad (112)$$

where A and B are asymptotic values of u_R at low and high particle Reynolds number Re_t. Figure 23 shows relationship between u_R and Re_t at expanded bed voidages of 0.5, 0.7 and 0.9.

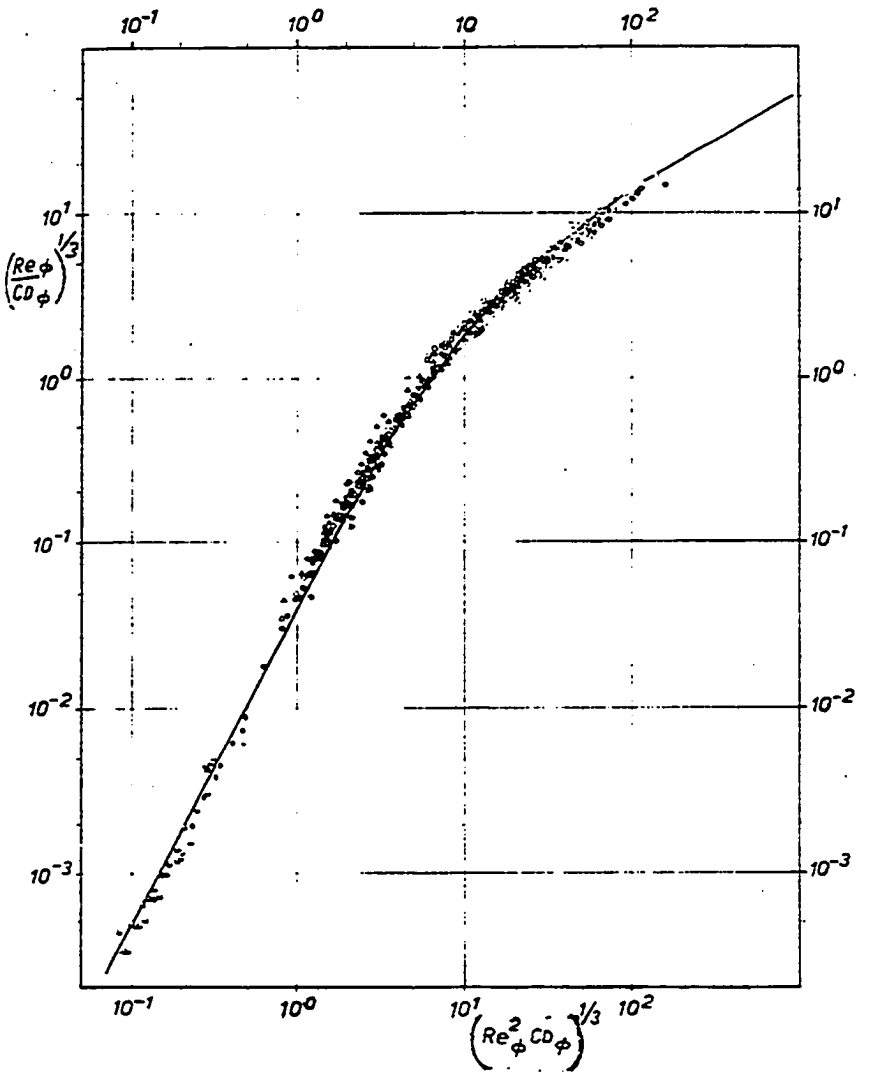

Figure 22. Correlation of Barnea and Mizrahi for fluidization and sedimentation of solid-liquid systems using modified definitions $C_{D\phi}$ and Re_ϕ (11)

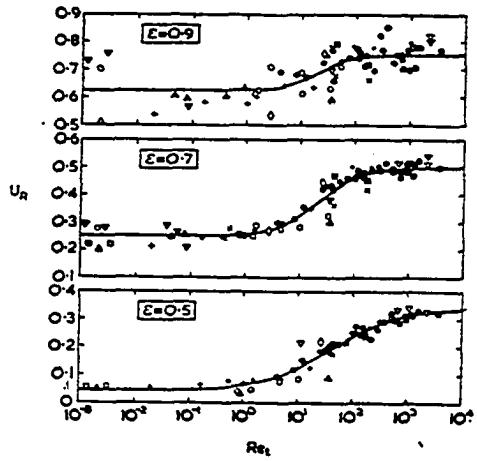

Figure 23. The relationship between $u_R = u/\varepsilon u_t$ and Re_t at constant expanded bed porosity for spherical particles (54 p. 209)

Using several experimenters' data for spherical particles and based on the values for A, B, C and m at porosities 0.4, 0.45, 0.5, 0.6, 0.7, 0.8, 0.9 and 0.95, they proposed following empirical relationships.

$$\begin{aligned} A &= \varepsilon^{4.14} \\ B &= 0.8\varepsilon^{1.28} \qquad \varepsilon \leq 0.85 \\ B &= \varepsilon^{2.65} \qquad \varepsilon > 0.85 \\ C &= 0.06 \\ m &= \varepsilon + 0.2 \text{ or } 1.0 \end{aligned} \tag{113}$$

The proposition of a simple exponential correlation of the form $A = \varepsilon^{4.14}$ is somewhat self-defeating in that it reduces equation 112 at very low particle Reynolds numbers to one similar to that of Richardson and Zaki (where right hand term of equation 112 approaches zero). As discussed previously, an equation of the form $\frac{u}{u_t} = \varepsilon^n$ cannot adequately describe the expansion data at high porosities or sedimentation of very dilute suspensions ($\varepsilon > 0.9$). This was borne out by the fact $\varepsilon^{4.14}$ predicted a value of A which was 16 percent higher than the 0.699 which gave the best fit to the logistic curve for porosity at 0.95 (54).

Comparison between Barnea and Mizrahi's correlation and Garside and Al-Dibouni's correlation

The value of u/u_t in Barnea and Mizrahi's approach in the creeping flow region should be equal to the value of $A\varepsilon$ in Garside and Al-Dibouni's approach (because as Re_t approaches zero in equation 112, then $u_R = A$).

$$A = \frac{\varepsilon}{(1 + (1 - \varepsilon)^{1/3})} \exp\left[\frac{5(1 - \varepsilon)}{3\varepsilon}\right] \tag{114}$$

On rearranging equation 111, one obtains

$$\frac{u/\varepsilon}{u_t} = \left(\frac{C_D}{C_{D\phi}}\right)^{1/2} \left[\frac{\varepsilon}{1 + (1 - \varepsilon)^{1/3}}\right]^{1/2} \tag{115}$$

At high particle Reynolds number both C_D and $C_{D\phi}$ are independent of Reynolds number and reach the same constant value as stated earlier. According to Garside and Al-Dibouni, u_R in the high particle Reynolds number region is equal to B (because the denominator of the left hand side of equation 112 must approach zero at very high Re_t values, thus $u_R = B$). Therefore, from 115,

$$B = \left[\frac{\varepsilon}{1 + (1 - \varepsilon)^{1/3}}\right]^{1/2} \tag{116}$$

Table 7 shows the values of A and B determined from Barnea and Mizrahi's equation and the logistic values found empirically by Garside and Al-Dibouni (Table II in their paper).

From Table 7 it can be seen that Barnea and Mizrahi's approach predicts lower u_R values at low particle Reynolds numbers and higher u_R values at very high Reynolds numbers compared with values obtained by Garside and Al-Dibouni. From equations 114 and 116, it follows that

$$\frac{B^2}{A} = \exp\left[\frac{5(1 - \varepsilon)}{3\varepsilon}\right] \tag{117}$$

However, Garside and Al-Dibouni's values for A and B do not support this form of relationship. On the contrary, as shown in Figure 24, A

Table 7. Comparison of A and B values empirically obtained by Garside and Al-Dibouni with those calculated using Barnea and Mizrahi's method

	A (Low Reynolds Number)		B (High Reynolds Number)	
Porosity	Barnea & Mizrahi (Eq. 114)	Garside Al-Dibouni (Table II, 54)	Barnea & Mizrahi (Eq. 116)	Garside & Al-Dibouni (Table II, 54)
0.45	0.032	0.041	0.497	0.293
0.50	0.053	0.044	0.528	0.345
0.60	0.114	0.120	0.588	0.423
0.70	0.205	0.251	0.647	0.503
0.80	0.333	0.410	0.710	0.605
0.90	0.511	0.624	0.784	0.755
0.95	0.636	0.699	0.833	0.866

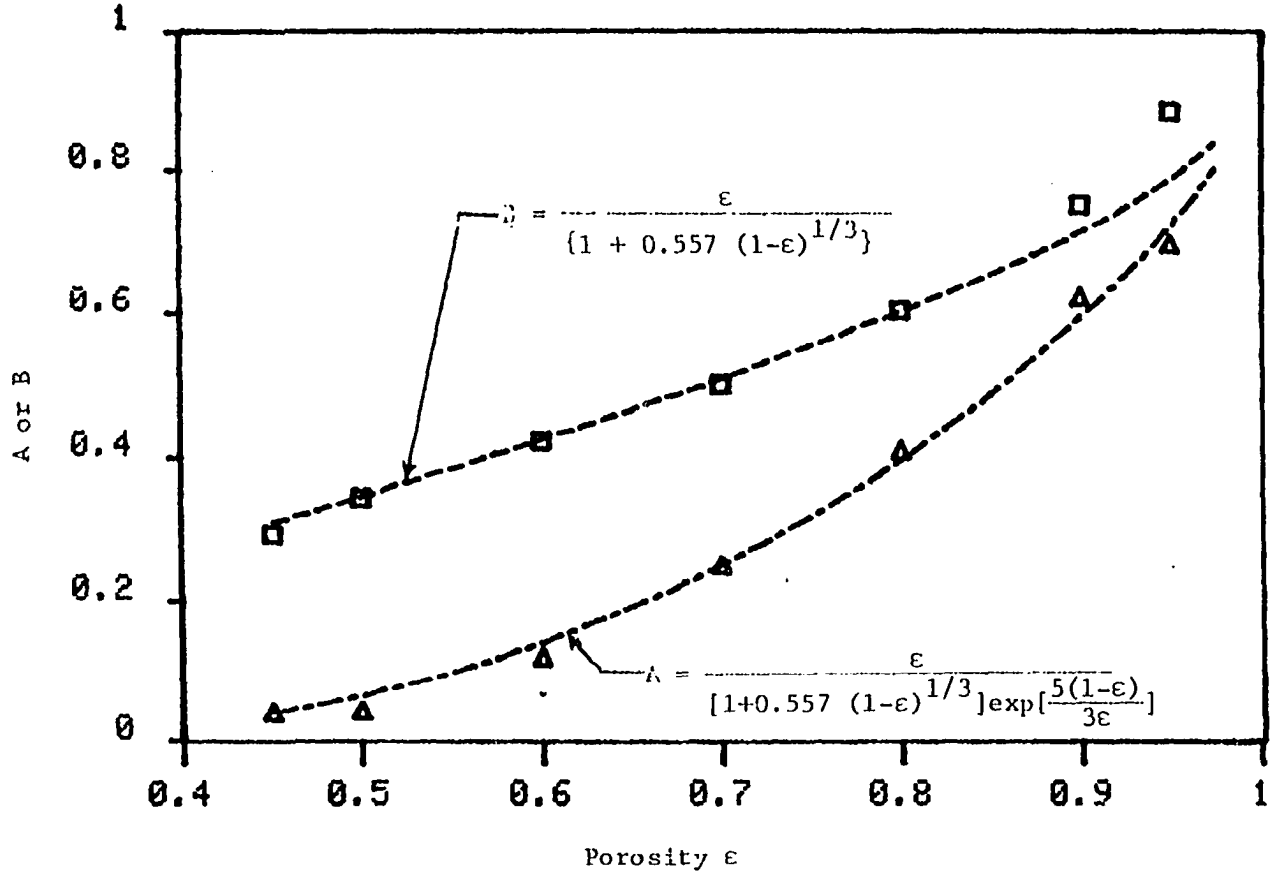

Figure 24. A new curve fit for A and B, the asymptotic values of $u_R = u/\varepsilon u_t$ at low and high particle Reynolds numbers, respectively

and B values can be made to fit the following equations

$$B = \frac{\varepsilon}{[1 + 0.557\ (1 - \varepsilon)^{1/3}\ ]} \tag{118}$$

$$A = \frac{\varepsilon}{[(1 + 0.557(1 - \varepsilon)^{1/3}]\exp[\frac{5(1 - \varepsilon)}{3\varepsilon}]} \tag{119}$$

from which it follows that

$$\frac{B}{A} = \exp\ [\frac{5(1 - \varepsilon)}{3\varepsilon}\ ] \tag{120}$$

Note that in this case B/A is obtained rather than the B^2/A in equation 117. At present, it is not possible to give any reason for this apparent conflict or any means of resolving it.

Garside and Al-Dibouni's alternative correlation

Garside and Al-Dibouni (54) also presented an empirical correlation of the form

$$\frac{u}{u_t} = \varepsilon^n$$

where n is obtained from the equation

$$\frac{5.09 - n}{n - 2.73} = 0.194\ Re_t^{0.877} \tag{121}$$

In obtaining the above correlation, the straight line on the plot of log u vs. log ε was forced through minimum fluidization point (ε_{mf}, u_{mf}). This probably accounts for the higher values of n in laminar and turbulent range compared to Richardson and Zakis values of 4.65 and 2.4 respectively.

Richardson and Meikle's correlation

Richardson and Meikle (90) using an approach based on fixed bed pressure drop equation, defined a modified Reynolds number Re_1 and friction factor F as follows

$$Re_1 = \frac{\rho u}{S\mu(1 - \varepsilon)} \tag{122}$$

$$F = \frac{\varepsilon^3 (\rho_s - \rho)g}{\rho u^2 S} \tag{123}$$

where

S = specific surface

$= \frac{6}{d}$ for spherical particles.

For $Re_1 < 1$ and for expanded bed porosity $\varepsilon < 0.78$, they showed that

$$F = 3.36\ Re_1^{-1} \tag{124a}$$

Thus, substituting 122 and 123 into 124a yields

$$\frac{\varepsilon^3(\rho_s - \rho)g}{S\rho u^2} = 3.36\ \frac{S\mu(1 - \varepsilon)}{\rho u} \tag{124b}$$

rearranging

$$\frac{u}{\frac{(\rho_s - \rho)gd^2}{18\mu}} = \frac{\varepsilon^3}{6.72(1 - \varepsilon)}$$

If particle Reynolds number $Re_t < 0.2$, substituting equation 3 for the denominator of the left hand term leads to

$$\frac{u}{u_t} = \frac{\varepsilon^3}{6.72\ (1 - \varepsilon)} \tag{125}$$

In this section, several different equations to predict the velocity-voidage relationship of spherical particles were presented. Some equations are applicable only in a limited range of particle Reynolds numbers while some are applicable from very low particle Reynolds number to very high particle Reynolds number. The Richardson and Zaki equation is perhaps the most widely used equation due to its simplicity. Garside and Al-Dibouni (54) compared different equations available in literature for predicting the velocity-voidage relationship of liquid fluidized systems. They concluded that their logistic approach gives the most accurate representation of bed expansion characteristics for solid-liquid system under conditions of fluidization and sedimentation. The author of this thesis feels that even though Garside and Al-Dibouni's logistic approach may seem to be more accurate, the empirical equation 113 proposed to estimate the logistic curve parameters A, B, C and m needs to be improved.

Expansion Correlation for Non-Spherical Particles

Richardson and Zaki (92), in addition to their extensive work on spherical particles, fluidized four non-spherical particles of regular shape (cylinders, hexagonal prisms, cubes and plates). However, their work was restricted to the turbulent regime. They claimed the volumetric shape factor Z was better than sphericity for correlating the 'n' values obtained. The 'n' values were found to fit the equation

$$n = 2.7\ Z^{0.16} \tag{126}$$

where

Z = Heywood volumetric shape factor.

The validity of equation 126 is questionable since the n values ranged from 2.4 to 2.6 except for the plates, and the sphericities and Z values ranged from 0.806 to 0.874 and 0.517 to 0.694, respectively. It is possible that the difference in 'n' values are statistically insignificant. The plates had an 'n' value of 2.1 which is much less than that for spheres. This author was not able to find any evidence in the literature to support this observation.

Lewis and Bowerman (74) fluidized series of catalyst granules in liquid hydrocarbons in the laminar range. They also analyzed the data of other workers in the transitional and turbulent regimes. It was observed that the expansion of non-spherical particles was higher than the expansion of spheres at a given upflow rate. They said this was because the drag force was proportional to the area of contact, and that non-spherical particles for same equivalent spherical diameter offer more area of contact than spheres. Therefore, they suggested that the product of sphericity and porosity $\psi\varepsilon$, could be used instead of the porosity, ε, in the expansion correlations. They verified this for a material with sphericity of 0.92 in the transitional flow regime. However, this method of prediction for non-spherical particle is not well substantiated and was found to be unsatisfactory by Fan (45).

Whitmore (107) conducted sedimentation experiments with very small non-spherical particles of ground methyl-methacrylate in a solution of lead nitrate and glycerol. The particle size range was from 0.194 to

0.065 mm and the experiments were all in the laminar regime. He found that the 'n' values were higher than the 'n' values reported by Richardson and Zaki for spherical particles in the laminar regime. He hypothesized that a fraction of the fluid roughly proportional to the surface area of the solid material is carried with the particles. It makes the hydrodynamic volume of the particle greater than its dry volume so that the constituent particles behave as spheres of reduced density.

Fouda and Capes (49) made use of the concept of immobile liquid trapped with solids to analyze expansion data of irregular shaped particles such as crushed silica and crushed steel and flat particles like mica and aluminum squares. They considered that the trapped immobile liquid effectively reduces the porosity. The effective porosity is

$$\varepsilon_e = 1 - k_1(1 - \varepsilon) \tag{127}$$

where k_1 is the volume of solids plus immobilized fluid per unit solid volume. Further, it can be shown that the effective diameter and the density of the solid-fluid particle are given by the following equations which they presented:

$$d_e = (k_1)^{1/3}\, d \tag{128}$$

$$\rho'_e = \frac{\rho_s + \rho(k_1 - 1)}{k_1} \tag{129}$$

where

d = average sieve diameter for equidimensional particles and d_{eq} for flat particles.

k_1, which they termed as hydrodynamic volume fraction was obtained by an iterative procedure. For an assumed value of k_1, the effective diameter d_e, and density ρ'_e were calculated from equations 128 and 129, respectively. The terminal settling velocity of a spherical particle with diameter d_e and density ρ'_e was calculated then. Using Richardson and Zaki's empirical relationship for n values in various flow regimes, the 'n' value was calculated from the calculated terminal settling value. This 'n' value was compared with the 'n' value obtained by plotting log u vs. log ε_e. If the 'n' values did not match, k_1 value was changed and the calculations were repeated until the 'n' values agreed reasonably well. The k_1 values ranged from 1.17 to 1.32 for crushed silica while for flat particles like mica it was greater than 2 and was sometimes greater than 3. The hydrodynamic volume fraction, k_1, exhibited no consistent trend with particle diameter, but overall particle shape or form and surface roughness did have some influence.

The author of this thesis has some doubt about this method. Since ε_e is linear function of ε as given by equation 127, both plots log u vs. log ε_e and log u vs. log ε will not produce straight lines for the same set of data. The plot of log u vs. log ε_e may show some degree of scatter from a straight line and therefore, the 'n' values again will depend on the porosity range over which the measurements were taken.

Jottrand (66) fluidized uniform sands with water in the laminar regime. His plot of log u versus log ε resulted in series of parallel

straight lines with a 'n' slope of 5.60.

Chong et al. (30) also studied the effect of particle shape on hindred settling in creeping flow regime. They used spheres, cubic crystals of salt and plastic pellets, brick like sugar crystals and angular mineral crystals. They found that the Richardson Zaki 'n' slope varied from 4.8 for smooth spheres to 5.4 for cubes to 5.8 for angular particles. No consistent trend of 'n' with d/D_T ratio was observed, and the empirical correction proposed by Richardson and Zaki, equation 80, over corrects for the wall effect. The intercept velocity u_i obtained by extrapolating log u versus log ε graph for hindered settling (ε data in range $0.65 < \varepsilon < 0.9$) to $\varepsilon = 1$, was consistently lower than the terminal settling velocity, $u_{t\infty}$, for spheres and cubes. u_i for spheres approached u_t, obtained by correcting $u_{t\infty}$ for wall effect by Ladenburg equation 27.

Carvalho (28) plotted log u versus log ε and determined the u_i and 'n' for crushed anthracite coal of uniform sizes. He found that the terminal settling velocity u_t determined experimentally in the same column was approximately 25 percent lower than the u_i. However, it should be noted that in his experiments the expanded bed porosities were less than 0.7, therefore the resulting 'n' and u_i values will be strongly influenced by initial segment of the expansion line.

Wood (110) studied the expansion of garnet sand of 3 different sizes during fluidization with water at 16° C and 25° C. The sizes ranged from 0.274 mm to 1.351 mm. He showed that Richardson and Zaki 'n' values can be correlated with Re_i, Reynolds number based on intercept

velocity u_i at $\varepsilon = 1$. Further, he found a correlation between Re_i and the Galileo number for the garnet sand he studied.

Gunasingham et al. (57) used the same approach of Wood to study the expansion uniform sized sand, anthracite, polystyrene, and ballotini. They proposed Richardson-Zaki 'n' values can be represented by the equation

$$n = pRe_i^q \tag{130}$$

where p and q were dependent on some property of the material. In addition, they considered that for all the materials investigated, Re_i can be approximated by the equation

$$Re_i = 0.599\ Ga^{0.536} \tag{131}$$

The following empirical equations were proposed for p and q

$$p = \frac{3.693}{\Omega^{1.45}} \tag{132}$$

$$q = \frac{0.246}{(\frac{\rho_s}{\Omega})^{0.73}} \tag{133}$$

where

$\Omega = \frac{d_h}{d_{eq}}$

ρ_s = density of the material.

They observed that the general model of equation 131 did not predict as accurately as the specific model for each material, for it gave a maximum error of + 21 percent at 100 percent expansion. Although Gunasingham et al. (57) used equation 131 as the general

empirical equation for relating Re_i to Galileo number, the specific equations for each material were also presented as follows :

$$\begin{aligned} &\text{Sand} && Re_i = 0.368\ Ga^{0.66} \\ &\text{Ballotini} && Re_i = 0.617\ Ga^{0.529} \\ &\text{Anthracite} && Re_i = 0.618\ Ga^{0.538} \\ &\text{Polystyrene} && Re_i = 0.377\ Ga^{0.582} \end{aligned} \qquad (134)$$

Wood obtained the following equation for the garnet sand for which Ω ranged from 0.65 to 0.71.

$$Re_i = 0.0702\ Ga^{0.823}$$

One cannot fail to realize the variation of the exponent on Ga and multiplying coefficient in these equations. They do not follow a systematic variation with shape factor Ω of the particle. These empirical equations yield a high correlations coefficient due to the fact that Galileo number Ga, is highly correlated with the terminal settling velocity of the particle u_t. But u_i does not show any systematic variation with u_t.

Further, an equation of the form given in 134 is not satisfactory to cover a wide range of Galileo numbers, since even for spherical particles the relationship between Re_t and Ga depends on the Ga value as illustrated by the three equations required for different ranges of Ga for spheres as given in equation 77.

Cleasby and Fan (32) showed that 'n' values for non-spherical particles like sand, anthracite and flintag could be estimated by multiplying the 'n' values for a spherical particle of the same

equivalent diameter by a correction factor which is a function of DSF or sphericity and the particle Reynolds number. Their equations were as follows:

$$n = n_{spherical} \quad (DSF)^{\alpha}$$

$$\alpha = -2.2715 \ (DSF)^{0.420} \ (Re_t)^{-0.441} \tag{135}$$

and

$$n = n_{spherical} \cdot \quad (\psi)^{\beta}$$

$$\beta = -2.9237 \ . \ (\psi)^{0.884} \ (Re_t)^{-0.363} \tag{136}$$

where n spherical is obtained from Richardson-Zaki's empirical equation 81.

Further, they proposed u_i can be obtained from the equations

$$\frac{u_i}{u_t} = 0.90 \ (DSF)^{-0.261} \tag{137}$$

and

$$\frac{u_i}{u_t} = 0.91 \ (\psi)^{-0.400} \tag{138}$$

These two equations indicate that $u_i = u_t$ when DSF = 0.668 or $\psi = 0.790$ or for spherical particles $u_i \approx 0.9 \ u_t$. As discussed previously, the value of u_i depends to some extent upon the porosity range over which the expansion was carried out. Cleasby and Fan reported u_i values greater than u_t for the non-spherical material except for the coarsest sand. Chong et al. (30) found that u_i was less than the free terminal settling velocity for cubes in the

creeping flow region. Gunasingham et al. (57) also reported u_i greater than the free terminal settling velocity u_t for the anthracite, polystyrene and sand they investigated. But all sizes of ballotini gave u_i values less than free terminal settling velocities. It is not clear yet whether the particle Reynolds number or Galileo number has any effect on u_i or if the wide variability of u_i values reported in the literature is due to the inherent nature of log u vs. log ε plot, which is not strictly linear.

Beranek and Klumpar (19) suggested that the fluidization data of different shaped particles can be correlated by plotting

$$\frac{1 - \varepsilon}{1 - \varepsilon_{mf}} \text{ vs. } \frac{u - u_{mf}}{u_t}$$

on logarithmic coordinates. Chong et al. (30) had limited success by plotting

$$\frac{1 - \varepsilon}{1 - \varepsilon_{mf}} \text{ vs. } \frac{u - u_{mf}}{u_i}$$

for correlating hindered settling data they obtained in the creeping flow regime for non-spherical particles.

Effect of Particle Size Distribution on Expansion Correlations

The expansions correlations, obtained either empirically or theoretically, generally are for unisized materials. In most of the practical applications where fluidization is employed, the medium is far from unisized but contains range of particle sizes. Many

investigators have studied the effect of particle size distribution on expansion correlations.

In sanitary engineering practice, the total expansion of a filter bed during backwashing is determined by summing the expansion of different sizes, which are characterized by adjacent sieve sizes (26, 31, 44). Although no experimental evidence has been found in sanitary engineering literature to substantiate the validity of this procedure, evidence can be found in the work of Epstein et al. (40), Al-Dibouni and Garside (4), Akkoyunlu (2) and Hoffman et al. (64).

Epstein et al. (40) termed the summing approach a serial model. The overall porosity of the bed is given by

$$1 - \varepsilon = \frac{1}{\sum_{i=1}^{n} \frac{x_i}{1-\varepsilon_i}} \quad (139)$$

where

ε_i = the porosity of the species i, when fluidized alone at a given superficial velocity

x_i = volume fraction of species i in the total solid (excluding fluid)

Experimentally, they obtained the expansion line for both species of a binary mixture separately and for the binary mixture. In all, 20 binary mixtures of same density and different diameters and different density and diameters were studied. The Reynolds number based on intercept velocity (u_i) ranged from 0.034 to 3279. The predicted expansion curve based on equation 139 compared very well with that obtained experimentally for all binary mixtures. They found that the

serial model worked very well even when there was considerable intermixing.

Hoffman et al. (64) also made similar studies with six binary mixtures and one ternary mixture of spheres of same density but different diameters. They also showed that serial model predicted overall expansion very well even if there was intermixing.

An alternative approach assumes that a bed of mixed sized particles behaves as equivalent to single species which, in the case of constant density solids can be characterized by some mean particle diameter. Epstein et al. (40) termed this approach as a "averaging model". Wen and Yu (106) suggested that for a bed where intermixing is pronounced (particle diameter ratios < 1.3:1) use of an average diameter given by

$$d_{avg} = \frac{1}{\sum_{1}^{n} x_i/d_i} \tag{140}$$

can be used to predict the expansion approximately.

Epstein et al. (40) clearly demonstrated the inadequacy of the averaging model by showing that over the porosity range over which each single species plotted as a straight line in log u vs. log ε plot, the binary mixture showed a sharp curvature at higher porosities towards the line representing the single species with higher terminal settling velocity. Further, they quoted the work of Wakeman and Stopp, who found that only when the two species had the same terminal settling velocities u_t or more precisely, intercept velocity u_i, the binary mixture exhibited a straight line.

Al-Dibouni and Garside (4) used two models to predict the variation of size distribution with bed height during expansion of solid spheres of constant density. One was based on complete stratification and the other was based on diffusion mixing of solids. They found that although the mixing model was more successful than the stratification (serial) model in predicting the size variation particularly in beds containing narrow size ranges and regions where porosity of the expanded bed was about 0.7, it required experimental values of eddy diffusion coefficients and was found to be mathematically complicated to solve. On the other hand, they found that the loss of accuracy involved in assuming perfect stratification is unlikely to warrant the extra effort required to solve the mixing model.

Stratification and Intermixing

Although no work was done in this thesis regarding stratification and intermixing effects, a review of the literature would not be complete without delving a little bit into this topic. Particles stratify or intermix in a medium consisting of different size particles during fluidization depending on the range of particle sizes involved and the density of the particles.

Leva (73) quoted the studies of Verschoor and Andrieu which showed that even narrow size ranges of particles (0.015 cm to 0.0125 cm) of constant density are stratified at all porosities during fluidization. Wen and Yu (106) pointed out that a medium will be stratified if the range of particle sizes is larger than 1:1.3. Pruden (86) reported that the stratification of different size particles of same density

is driven by the differences of bulk densities between sizes. He defined bulk density (ρ_b) of a material of uniform density as:

$$\rho_b = (1 - \varepsilon)\rho_s + \rho\varepsilon = (1 - \varepsilon)(\rho_s - \rho) + \rho \tag{141}$$

The bulk density difference between two sizes of particles is given

$$\rho_{bx} - \rho_{by} = (1 - \varepsilon_x)(\rho_{sx} - \rho) - (1 - \varepsilon_y)(\rho_{sy} - \rho) \tag{142}$$

where

x = large particle

y = smaller particle

ρ_{bx}, ρ_{by} = bulk density of x, y particles respectively

ρ_{sx}, ρ_{sy} = density of x, y particles, respectively.

Pruden (86) showed that reduced bulk density β could be used as criterion to determine whether intermixing will occur or not

$$\beta = \frac{\rho_{bx} - \rho_{by}}{\rho_{sx} - \rho} \tag{143}$$

He noted the following with regard to mixing as a function of the value of β

$0 \leq \beta \leq 0.01$ mixing was observed.

$0.01 \leq \beta \leq 0.04$ partial segregation occurred.

$\beta > 0.04$ segregation with interface occurred.

Wood (110) and Fan (45) found the difference in bulk density gave

the correct tendencies towards intermixing during fluidization of dual media of different densities, but found it to be not as sensitive as desired for use as a predictive tool.

The work of Furukawa and Ohmae (53) is of interest to anybody who is studying stratification or intermixing during fluidization. They performed miscibility experiments with binary mixtures of sand-sand and coal-sand using water as the fluidizing medium. The studies of particle diameter ratios in the range 2.31:1 to 1.38:1 indicated that segregation was only partial. For each sand-sand system studied, there was an extrapolated minimum velocity below which no segregation occurred of the initially mixed systems. This minimum velocity increased with decreasing particle diameter ratios.

Al-Dibouni and Garside (4) found that for spherical particles of constant density up to particle size ratio of 2.0, mixing occurred to a varying degree throughout the bed and was particularly intense when the voidage was about 0.7. For size ratios greater than 2.2, stratification dominated.

Effect of Container Walls on the Expansion of Fluidized Beds

The effect of container walls is negligible in most industrial operations but a delicate point in laboratory scale equipment. A number of workers (76, 81, 108) have drawn their attention to the problem of wall effect on fluidization. Some authors attempted to define a limit for the value of d/D_T ratio, below which the wall

effect is negligible. For $(d/D_T) > (d/D_T)_{crit}$ the porosity of the fluidized bed is higher (other conditions being the same) or in other words the desired porosity is attained at a lower velocity. Wicke and Hedden (108) considered $(d/D_T)_{crit} = 0.01$ to be sufficiently small for wall effects to be negligible while Loeffler (76) found that at $\frac{d}{D_T} = 1/4.7$ wall effects are still negligible. From the work of Fidleris and Whitmore (46) or McNown et al. (78), one finds that the wall effect on the settling of a isolated spherical particle depends not only on d/D_T ratio but also on the particle Reynolds number. Likewise, the wall effect on the expansion of a fluidized bed will also be expected to depend on d/D_T ratio and Re_t. Table 8, prepared from the data of Loeffler, illustrates this phenomenon. The superficial velocity required to attain a certain porosity for the same material when fluidized in two different columns of diameter 2.477 cm and 5.508 cm was obtained by interpolation of experimental data. The ratio of velocities to attain same expanded bed porosities in two different columns is close to unity when $Re_{t\infty}$ is very high. However, when the particle Reynolds number is low the same expanded bed porosity is reached in smaller column at a lower superficial velocity.

Richardson and Zaki (92) attempted to correct for wall effect by incorporating a correction term as function of d/D_T in their empirical equation for obtaining 'n'. Although there is some disagreement over the magnitude of the wall effect correction proposed by Richardson and Zaki, they recognized the importance of particle Reynolds number in addition to d/D_T ratio for correcting for wall effects. At higher Re_t, the d/D_T effect was absent (Equation 81).

Table 8. The velocities required to attain the same expanded bed porosity in two different columns (prepared from the data of Loeffler (76))

Porosity	$Re_{t\infty}$ = 2769			$Re_{t\infty}$ = 1529			$Re_{t\infty}$ = 114.1		
	$\frac{d}{D_T}$ = 0.1291	$\frac{d}{D_T}$ = 0.061		$\frac{d}{D_T}$ = 0.1942	$\frac{d}{D_T}$ = 0.0918		$\frac{d}{D_T}$ = 0.0394	$\frac{d}{D_T}$ = 0.0177	
	u_1 cm/sec	u_2 cm/sec	$R=u_1/u_2$	u_1 cm/sec	u_2 cm/sec	$Re=u_1/u_2$	u_1 cm/sec	u_2 cm/sec	$R=u_1/u_2$
0.5	-	-	-	5.790	5.567	1.04	-	-	-
0.6	11.468	10.726	1.069	8.424	8.540	0.986	4.290	4.933	0.870
0.7	15.185	15.578	0.974	11.872	12.193	0.919	7.188	7.631	0.942
0.8	20,277	21.214	0.956	16.515	16.785	0.984	10.336	11.235	0.920
0.9	27.783	29.099	0.955	23.377	23.369	1.00	-	-	-
	$Re_{t\infty}$ = 47.10			$Re_{t\infty}$ = 2.71			$Re_{t\infty}$ = 1.79		
	$\frac{d}{D_T}$ = 0.1354	$\frac{d}{D_T}$ = 0.0615		$\frac{d}{D_T}$ = 0.0394	$\frac{d}{D_T}$ = 0.0177		$\frac{d}{D_T}$ = 0.0344	$\frac{d}{D_T}$ = 0.0155	
	u_1 cm/sec	u_2 cm/sec	$R=u_1/u_2$	u_1 cm/sec	u_2 cm/sec	$Re=u_1/u_2$	u_1 cm/sec	u_2 cm/sec	$R=u_1/u_2$
0.5	-	-	-	-	-	-	-	-	-
0.6	2.758	3.108	0.887	-	-	-	0.272	0.341	0.797
0.7	4.633	4.880	0.950	-	-	-	0.558	0.650	0.858
0.8	7.261	7.576	0.958	1.247	1.461	0.85	0.981	1.136	0.863
0.9	-	-	-	1.945	2.242	0.867	1.568	1.830	0.857

Neuzil and Hrdina (81) conducted an extensive study on the effect of wall on the expansion of spherical particles. Unfortunately, their study was not presented in a manner that could be easily understood. In a region defined by $(\frac{u}{u_t})_{k_2} < (\frac{u}{u_t}) < (\frac{u}{u_t})_{k_3}$ they proposed the following equation to obtain the porosity of the expanded bed

$$\varepsilon = \frac{1.16\ (u/u_t)^{0.37}}{(1-2.7(d/D_T)^{1.15})}\ Re_t^{-0.011} \tag{144}$$

where Re_t ranged from 75.5 to 1795 and (d/D_T) ratio ranged from 0.0454 to 0.299.

$(\frac{u}{u_t})_{k_2}$ and $(\frac{u}{u_t})_3$ are defined by the equations

$$(\frac{u}{u_t})_{k_2} = (0.192\ Ga^{0.548} - 1.00)\ Re_t^{-1.0} \tag{145}$$

$$(\frac{u}{u_t})_{k_3} = 0.390\ (d/D_T)^{-0.174} \tag{146}$$

Further they established that the porosity of a loosely packed bed of spherical particles at minimum fluidization is given by the equation

$$\varepsilon_{mf} = 0.429\ \frac{d}{D_T} + 0.404 \tag{147}$$

It is fervently hoped that this chapter on literature review, although quite voluminous, sheds light on various aspects of fluidization. This prior knowledge will be of much use in studying the principal objectives of this dissertation.

EXPERIMENTAL INVESTIGATIONS

Fluidization Apparatus

General layout of the experimental system

A schematic layout of the fluidized apparatus is shown in Figure 25. Tank A was filled with water obtained from Iowa State University tap water supply. The water was pumped through one of the flow meters F1, F2 and F3 depending on the flow rate to the fluidization column D. A small portion of the pumped water passed through the cooler C which was used to maintain the temperature at the desired level. The water flow through D and C was recirculated back to the tank A. The water was recirculated in the system until it was too dirty to be used. Water temperature was also controlled by a heater, but during the latter stages of the experiment the thermostat was not functioning and the heater was only used to bring the water temperature to close to 25° C at the commencement of the experiments. The flow rate through each flow meter was controlled by a needle valve connected to each flow meter. Water was pumped through only one flow meter at a time. Two pressure taps inserted in the fluidization column were connected to an inverted water manometer G to measure the head loss across the bed.

Tank

A 45 cm diameter and 70 cm deep cylindrical plastic tank was used in this experiment as a recirculation reservoir.

Pump

Two centrifugal pumps with 0.5 and 2 horse power were used in the

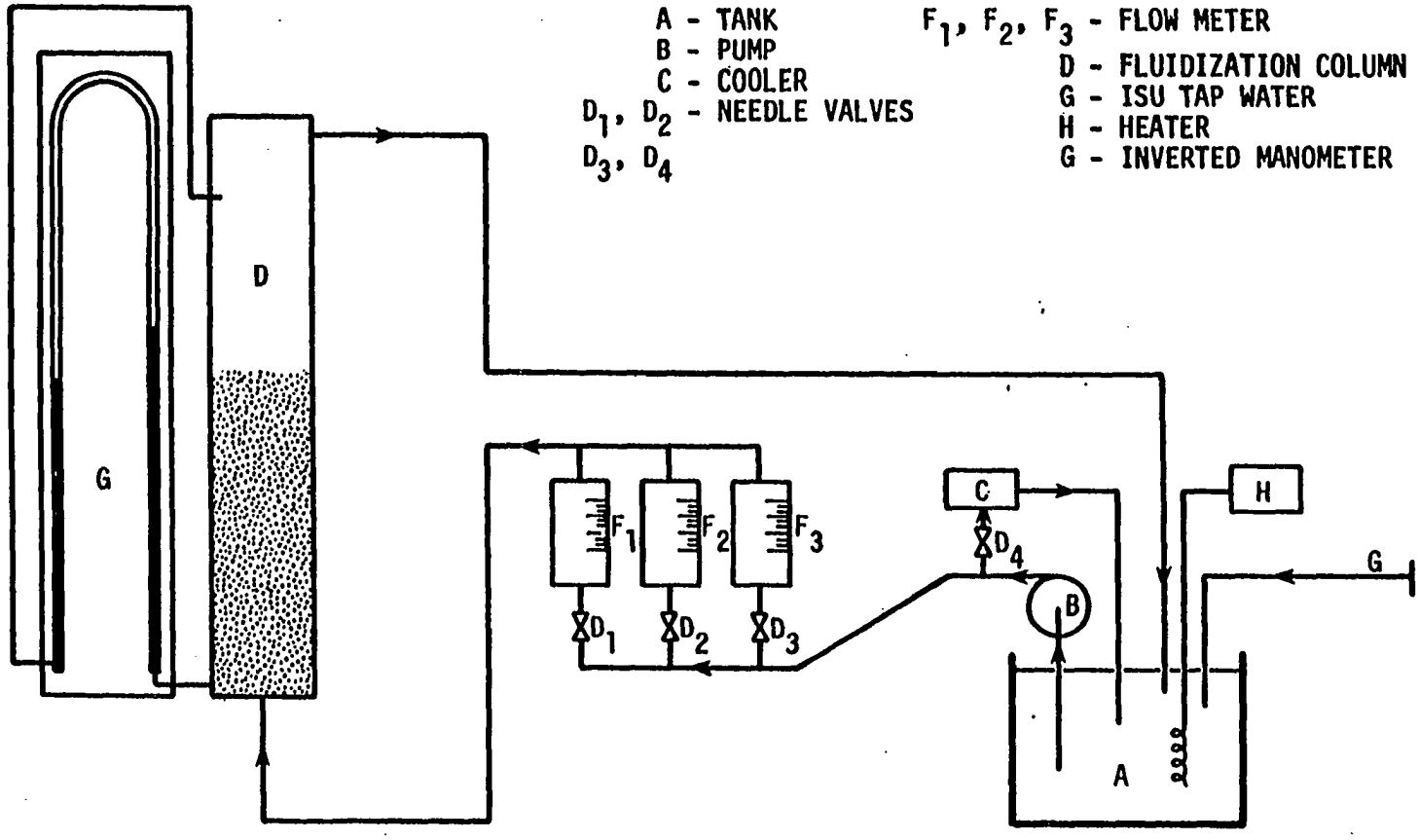

Figure 25. General layout of experimental system

system. For coarser and heavier material that required higher flow rates, the 2 HP pump was connected instead of the 0.5 HP pump.

Cooler and heater

The cooler was manufactured by Cordley Co., Michigan, Model CR2-5. The water to be cooled flowed through the heat exchanger coil in the cooler. The water temperature was adjustable between 24 and 26° C.

The heater was made by Polyscience Corp., Niles, Illinois, Model 73. The heater consisted of a thermometer, thermostat, a heating coil and a propeller. The heating coil and the propeller were immersed in the water; the coil functioned as a heat source while the propeller was used for circulating the water in the tank to make the temperature more uniform. After the thermostat stopped functioning, the heater was used only at the beginning of the experiment to raise the temperature of the water. Once the temperature was close to 25° C, by regulating the flow through the cooler, the temperature was kept near 25° C.

Flow meters

Three rotameter type flow meters F_1, F_2 and F_3 were used. The range of flows, scale of the flow meter and the tube number of the meter are as follows. All were manufactured by the Fisher and Porter Company.

Flow Meter	Range	Scale	Tube Number
F_1	0-2 gpm	in gpm	B5-15-10/70
F_2	0-9.5 gpm	in percent of maximum flow	B6-35-10/77

F_3	0-30 gpm	in percent of maximum flow	FP-2-27-9-10/83 Float T6-SVT-96

Flow meters F2 and F3 were calibrated at 20° C and the flow meter F1 was calibrated at 24° C. The flow meters were calibrated by a weighing technique. The time to collect a given weight of water in a container was determined by the use of a stop watch. The weight of water collected varied depending upon the flow meter being calibrated. The inertia effects were eliminated by duplicating these effects at the start and finish of the timed weighings. A least square fit was used in determining the calibration equation for the flow meters. The equations are as follows:

Meter	Temperature	Flow in gpm	
F_1	24° C	0.0689 + 0.885 (Reading)	r^2 = 99.9%
F_2	20° C	0.102 + 0.0956 (Reading in %)	r^2 =100%
F_3	20° C	0.0354 + 0.291 (Reading in %)	r^2 = 100%

Flow meters F_2 and F_3 are designed to function at high Reynolds number so they are reported by the manufacturer to be viscosity immune.

Fluidization column

The fluidization column is shown in Figure 26. The column consisted of several 10.16 cm inside diameter, 0.50 cm thick plexiglass cylinders of various height. The initial section of the column was 120 cm high. A 5.10 cm high calming section shown in Figure 27 was located at the bottom and the top of the column was open to the atmosphere. Various

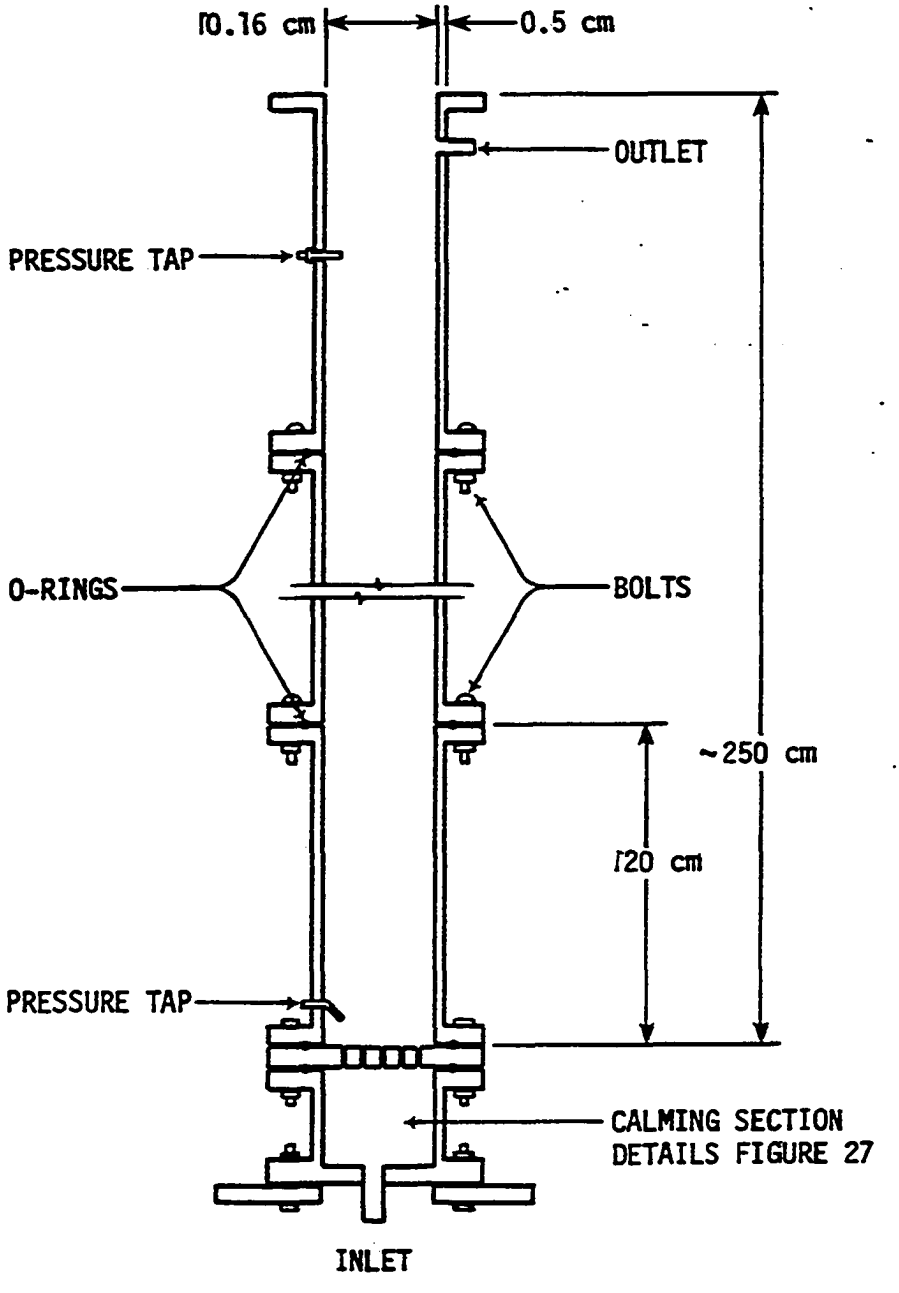

Figure 26. Sketch of fluidization column

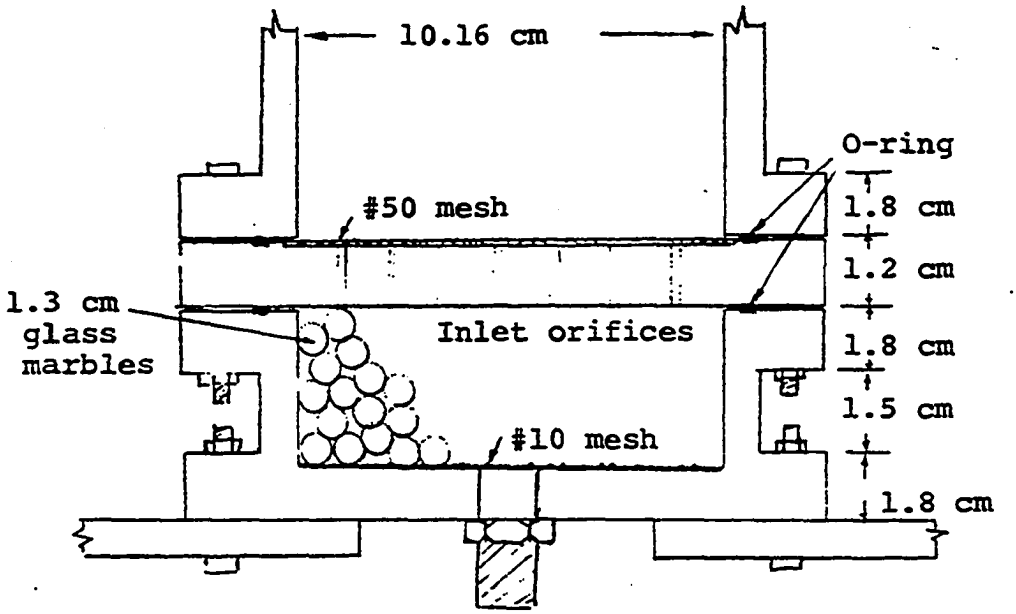

Detail of calming section

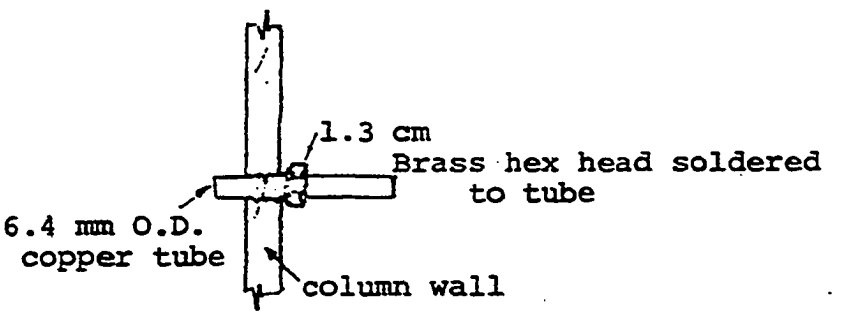

Detail of pressure tap

Figure 27. Details of calming section and pressure tap

segments of the column were connected with bolted flanges and sealed by O-rings. A 1.20 cm thick diffusing plate with 94 orifices, 3.2 mm in diameter was placed above the calming section, in order to distribute the upflow water uniformly. U.S. standard 50 mesh stainless steel screen was placed on top of the diffusion plate in order to prevent plugging of orifices and possible loss of media.

The calming section had a 1.9 cm inlet opening in the bottom flange. A 10 mesh screen was placed inside this section and was filled with 1.3 cm diameter plexiglass marbles. The fluidization column had two pressure taps inserted on it. One was about 200 cm above the base and the other was just above the diffusing plate. The pressure taps were constructed of 6.4 mm copper tubes that were soldered into 1.3 cm brass hexhead plugs. The inner opening of the pressure taps was covered by a 50 mesh stainless steel screen. Details of the pressure taps and the calming section are shown in Figure 27.

A cloth tape was attached to the column from the top of diffusing plate, and was extended about 140 cm in height above the plate. The bed height during fluidization was measured by this tape in cm. To ensure the cloth tape was not stretched, the cloth tape markings were checked against a metal tape marking in the mounted position.

Monometer

The two pressure taps on the fluidization column were connected by a tygon tubing to an inverted glass monometer. The water levels in the glass manometer tubes could be read to 0.1 in. from the scale on the monometer.

Sieves

U.S. standard sieves were used to separate uniform sizes of material from wider size ranges.

Air Permeability Apparatus

Layout of the air permeability apparatus used to find the specific surface of the media are shown in Figure 28. The air supply was from the air supply line in the Iowa State University Sanitary Engineering Laboratory.

While pressure drop measurements are taken, the stopcock valves D1 and D2 are open and D3 is closed. The needle valve N1 is used to regulate the flow of air through the column. The pressure drop across the bed was measured in the u-tube monometer. Water was used as the momometric fluid.

Flow meter

One rotameter type flow meter F_4, was used to measure the flow rate of air through the column. This flow meter was calibrated against a wet test gas meter capable of measuring up to 190 SCFM. The wet test gas meter was connected to the outlet side of the flow meter in the air permeability apparatus. The outlet of the wet test gas meter was open to the atmosphere. The time required to pass 10 ft^3 of air at high flow rates and 5 ft^3 of air at low flow rates through the wet test gas meter was recorded. The temperature of the air leaving the wet test meter and the atmospheric pressure in the laboratory were

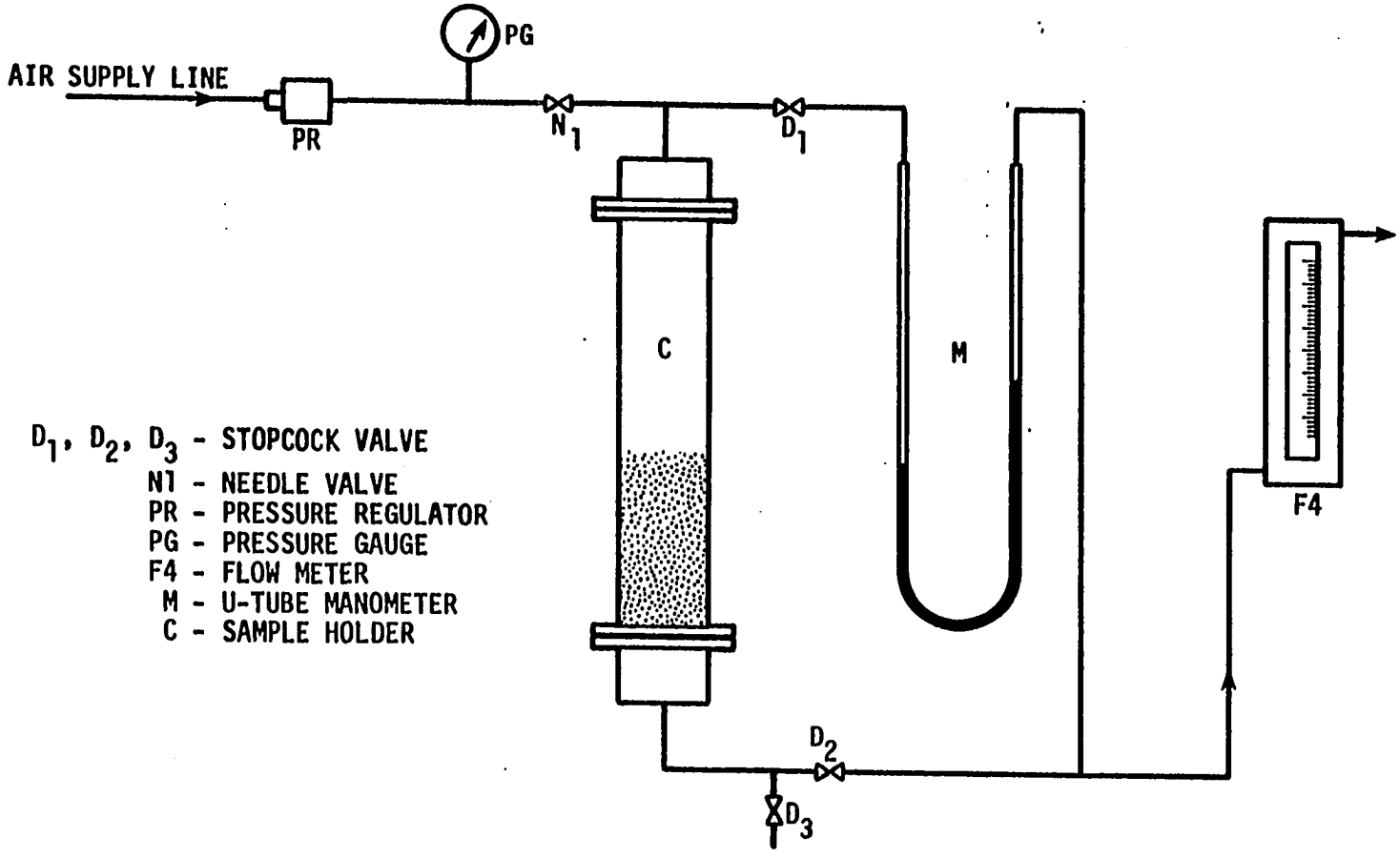

Figure 28. Layout of the air permeability apparatus

also recorded. At flow rates used in the calibration, the pressure differential across the wet test gas meter was not significant, and therefore was not considered in the subsequent calculations.

The following example is presented to illustrate the conversion of measured flow rate at prevailing conditions to standard conditions at 14.7 psiA and 70° F.

Atmospheric pressure = 736.7 mm Hg

Temperature of Air = 24° C

Flow meter reading = 90 %

Volume of air passed = 10 ft^3

Time to pass this volume of air = 3 m 26 s = 3.433 min

The wet test gas meter measures the flow rate under prevailing test conditions.

$$\text{Flow rate at 736.7 mm Hg and 24° C at 90\% of meter reading} = \frac{10\ ft^3}{4.344\ min} = 2.91\ ft^3/min$$

Manufacturer's full scale rating for this rotameter at 14.7 psiA and 70° F = 3.17 SCFM.

To obtain full scale rating at the test condition, the following equation is used:

$$\text{Full scale at test conditions} = (\text{full scale at 14.7 psiA and } 70°\ F) \times \left(\frac{P_{standard}}{P_{test}} \times \frac{T_{test}}{T_{standard}} \right)$$

where

$P_{standard}$ = Pressure at standard conditions

P_{test} = Pressure at test conditions

$T_{standard}$ = Absolute temperature at standard conditions

T_{test} = Absolute temperature at test conditions.

Full scale reading at 736.7 mm Hg and 24° C

$$= 3.17 \frac{760}{736.7} \times \frac{273.15 + 24}{273.15 + 21.1} = 1.021 \times 3.17$$

$$= 3.235 \text{ ft}^3/\text{min}$$

90% Reading = $0.9 \times 3.235 = 2.91 \text{ ft}^3/\text{min}$.

Thus, in the above example, the manufacturer's full scale reading at standard conditions is correct.

The results of this calibration at several flow rates between 20 percent and 100 percent were within 2 percent of the manufacturers calibration for this rotameter at flow meter readings above 50 percent, and reached within 5 percent at lower flow rates. Therefore, the manufacturers calibration was accepted to be correct.

The following example illustrates how the mass flow rate can be obtained by knowing the rotameter reading and the pressure and temperature at test conditions.

Rotameter reading = 60 percent

Pressure at test conditions = 741.4 mm Hg

Temperature of air = 24° C

Density of dry air at 0° C and 760 mm Hg = $1.2929 \times 10^{-3} \text{ g/cm}^3$

Diameter of sample holding column= 5.08 cm.

Full scale reading at 741.4 mm Hg and 24° C

$$= 3.17 \times \frac{760}{741.4} \times \frac{(273.15 + 24)}{(273.15 + 21.1)}$$

$$= 3.225 \text{ ft}^3/\text{min.}$$

60 percent of full scale reading = $0.6 \times 3.225 = 1.935 \text{ ft}^3/\text{min}$

Superficial velocity of air flow in $= \frac{1.935 \text{ ft}^3}{\text{min}} \times \frac{1 \text{ min}}{60 \text{ sec}} \times$

$$\frac{2.832 \times 10^4}{1 \text{ ft}^3} \text{ cm}^3 \times \frac{1}{\frac{\pi}{4} \times (5.08)^2 \text{ cm}^2}$$

$$= 45.06 \text{ cm/sec.}$$

Density of air at 741.4 mm Hg and 24° C

$$= 1.2929 \times 10^{-3} \frac{\text{g}}{\text{cm}^3} \times \frac{741.4}{760} \times \frac{273.15}{(273.15 + 24)}$$

$$= 1.1594 \times 10^{-3} \text{ g/cm}^3$$

Mass flow rate $G = \rho u = 1.1594 \times 45.06 \frac{\text{g}}{\text{cm}^3} \times \frac{\text{cm}}{\text{sec}}$

$$= 52.24 \times 10^{-3} \frac{\text{g}}{\text{cm}^2 - \text{sec}}$$

Sample holding column

The sample holder is a 5.08 cm inside diameter plexiglass column 52 cm in height. The sample rested on 50 U.S. mesh stainless steel screen.

Materials

Coarse sand, coarse and lighter coal, cube shaped polyvinyl plastic of three different densities, circular disc shaped metal punchings of brass, stainless steel and aluminum were used in the experimental investigations. The uniform sands used in the experiments were sand 5-6[a] and 6-7[a]. Four different sizes of coal were prepared by sieving MS-20 anthracite coal[b]. The uniform sizes of coal were 5-6, 6-7, 7-8, and 8-10 U.S. mesh sizes. The circular disc shaped metal punchings were obtained from a hardware supplier[c] in Chicago. The sizes of the punchings as given by the supplier is as follows:

Brass	0.406 mm dia.	0.4039 mm thick
Stainless steel	1.143 mm dia.	0.397 mm thick
Aluminum	1.143 mm dia.	0.6096 mm thick

The heavier cubic shaped polyvinyl plastic material, Kodak PET Thermoplastic Polyester 7352[d], has a specific gravity of 1.36, while the lighter Kodak Polyester PETG 6763[d] has a specific gravity of 1.26. The third polyvinyl material was obtained from Culligan Corporation and is called Culsan P[e] and has a specific gravity of 1.20.

---

[a] Obtained from Northern Gravel Co., Muscatine, Iowa.

[b] Obtained from GA Fuel Sales, a division of Blue Coal Corporation, Wilkes-Barre, Pennsylvania.

[c] Harrington and King Perforating Co., Chicago, Illinois.

[d] Eastman Chemical Products, Inc., Kingsport, Tennessee.

[e] Culligan, U.S.A., Northbrook, Illinois 60062.

The metal punchings had an oil coating on them and had to be washed with detergent and water to remove the oil film. Metal punchings were later dried at 300° C to burn off any remaining oil coating. Dry, oil free metal punchings were sieved to separate unwanted materials. From the brass metal punchings, only those passing 35 mesh and retained on 40 mesh were used in the subsequent studies.

From stainless steel and aluminum metal punchings, only those passing mesh 16 and retained on mesh 18 were used in the experiments. The polyvinyl plastics were also sieved to obtain particles of uniform sizes. From Polyester 7352 and Copolyester PETG 6763, only the material retained between meshes 7 and 8 were used in fluidization studies while with Cullsan P only the material retained between sieves 8-10 was of sufficient quantity to be used in the fluidization experiments.

Experimental Procedure

Sieve analysis

Sieve analysis is a statistical process that is, there is always an element of chance as to whether a particle will or will not pass the apertures and hence there is no definite end point to sieving analysis. The end point must therefore be defined arbitrarily either by fixed time of sieving or by sieving until particles pass the sieve at a fixed rate per minute.

The ASTM standard method (6) for sieve analysis of fine and coarse aggregates recommends that at the completion of the sieving operation, not more than one percent by weight of the residue on any

individual sieve will pass that sieve in one additional minute of hand shaking of that sieve. Otherwise, additional sieving of the nest of sieves is required.

Fan (45) developed a procedure by combining ASTM standard method and British Standard Method to prepare uniform sized granular materials.

The procedure is as follows:

1. Load about 200 g of sample into selected nest of sieves.

2. Sieve for 10 minutes with Combs Gyratory sifting machine.

3. Remove the material from each sieve and clean the sieves. Then return the material to each sieve on which it had been retained.

4. Test the adequacy of sieving by one minute hand shaking. If the weight of particles passing an individual sieve is more than 1 percent of the weight of the residue on it, then repeat steps 2, 3 and 4.

In preparing sand 5-6 and 6-7 sizes, the steps 2, 3, and 4 were repeated 3 times. Even then the standards were not exactly met. But after 30 minutes of machine shaking the material retained on meshes 6 and 7 were assumed to be of uniform size.

Fan (45) adopted 10 minutes of machine shaking and a further one minute of hand shaking to produce uniform size coal samples. Although this procedure did not meet the standards, longer shaking time could potentially degrade the size of the coal media. The same procedure was adopted in preparing the coal samples 5-6, 6-7, 7-8, and 8-10.

Polyvinyl plastic material and circular disc shaped metal punchings were also sieved. With these materials, only those materials retained between two adjacent sieves were taken and the rest discarded.

This ensured these materials are also of uniform size.

Equivalent spherical diameters

The mean equivalent diameter of a sphere (d_{eq}) is defined as the diameter of a spherical particle of the same volume as the irregular particle being considered. The d_{eq} was obtained by counting about 100 dried and cooled representative grains of each size and weighing them. The equivalent spherical diameter of the particle was calculated as follows:

$$d_{eq} = \left(\frac{6w}{N\pi\gamma_s}\right)^{1/3}$$

where

γ_s = particle specific weight

w = total weight of N particles

N = number of particles.

Density

The densities of sand, coal, metal punchings and polyvinyl materials were determined by a water displacement technique using a 50 ml pycnometer bottle. All materials were washed and dried at 100° C for 3 hours as a preliminary procedure prior to the test. When determining the density of coal, the weight W was determined at different times after shaking the bottle periodically to eliminate any air bubbles which had collected due to water filling the pores in the coal (W = weight of pycnometer + coal after soaking for a time + water required to fill the pycnometer). The weighings for W continued until two successive weighings did not differ significantly. For all materials,

two measurements of density were made and the mean was reported as the average density for the material.

Unhindered settling velocity

The unhindered settling velocity was measured by dropping individual particles in a plexiglass column which was about 150 cm in height and 14.0 cm in diameter. Two marks, 100 cm apart were made on the column, the first mark was 27 cm below the water surface. The particles were allowed to soak in water overnight to ensure they are fully wetted before the test. Representative grains from each uniform sized material were dropped into the water individually and the travelling time between those two marks was recorded. For each uniform sized material, the settling time of about 50 grains was recorded and the average unhindered settling velocity was computed from these data. The settling velocities were measured at two different temperature ranges, one at room temperature which ranged from 20° C to 24° C and another at around 36° C. The higher temperature settling velocity measurements were made in the digestor room in the Sanitary Engineering Laboratory.

Porosity

The porosity of the unexpanded bed was measured in the fluidization column by allowing the media to freely settle from a higher degree of expansion when the upflow water was shut off suddenly. The free settling is assumed to prevent packing among the particles and thus the porosity obtained would be a loose bed porosity. Before the material was introduced into the fluidization column, it was washed

and dried at 105° C for 4 hours, and then was allowed to cool to room temperature. The dry media were then weighed to the nearest 1.0 gram and introduced into the fluidization column and was allowed to soak in water for about 15 hours. The fully wetted media were then fluidized to maximum possible expansion (usually about 300 percent except for brass and stainless steel metal punchings) for about 5 minutes, and the valve was shut off suddenly. After all the particles had settled freely the height of the settled bed was recorded. From this height the total volume occupied by media and water was calculated. The initial porosity was calculated using the following equation:

$$\varepsilon_o = 1 - \frac{w/\gamma_s}{c_1}$$

where

w = the weight of media

c_1 = the volume occupied by media and water (i.e. the column volume up to the top of the media).

Fluidization experiments

These experiments were made in the fluidization column previously described. The media of known weight were placed in the column and soaked for 15 hours. The media were then backwashed for about 5 minutes to get rid of air bubbles entrapped in the media and wash out any fines in the media. Expanded bed height readings were not made until the bed had stabilized.

A summary of observations made during an upflow experiment is as follows:

a. Flow rate in gpm

b. height of bed cm

c. pressure drop across the bed (in. of water)

d. temperature of water in recirculation reservoir (° C).

Some problems were encountered during these experiments. The water temperature increased slowly during fluidization because the cooler was not adequate to offset the heat input of the pump. If the water temperature rose close to 26° C, some water was removed from the recirculation reservoir and cold water was introduced. This helped to bring down the temperature. The average temperature was maintained between 24.5 and 25.5° C. At very low upflow rates some degree of channelling was observed with all the materials. Generally, the upper surface of the fluidized media could be easily observed at lower degrees of expansion but became increasingly difficult at higher expansions. With brass and stainless steel metal punchings, the interface was oscillating violently at moderately high flow rates although the expansion was not very much (about 30 percent). With lighter materials such as plastics and coal at high expansion, 200-300 percent, the interface of the fluidized bed was not steady at a particular height, but rather oscillated about 5 cm on either side of the mean value (the visually estimated mean value was recorded).

Air permeability experiments

These experiments were conducted to determine the specific surface of materials used in the fluidization experiments. The experiments were conducted in the air permeability apparatus described previously.

Sufficient quantity of material that would produce a fixed bed height about 25 cm in the sample holding column, was weighed accurately to 0.1 g and was introduced into the column. For the brass metal punchings, since the material was fine, a fixed bed height of about 15 cm was used. Pressure drop and air flow rate data were recorded at two different fixed bed porosities. Initially, the air was sent through the column in an upflow mode and the bed was expanded to a loosest state and the air supply was shut off suddenly, allowing the particles to fall freely to a fixed state. The fixed bed in this condition was termed a loosely packed bed. Air was then sent in a downflow mode through the bed and the pressure drop across the bed was measured with air flow rate, starting with highest air flow rate at the beginning and decreasing air flow rate in steps. The same bed was then tapped on the side of the column to produce a tightly packed fixed bed. The fixed bed height was recorded and the air flow rate and corresponding pressure drop was also recorded for number of air flow rates for this fixed bed condition. The air flowed through the column and rotameter discharged into free atmosphere. The temperature of the exiting air was measured with a thermometer. The atmospheric pressure in the laboratory was recorded at the beginning and end of each run. The variation of pressure drop in the empty tube with air flow rate was also recorded. In the subsequent calculations, to determine the pressure drop across the bed, the empty tube pressure drop corresponding to the same mass flow rate was subtracted from the observed pressure drop. The empty column pressure drop versus mass flow rate is shown in Figure 29 .

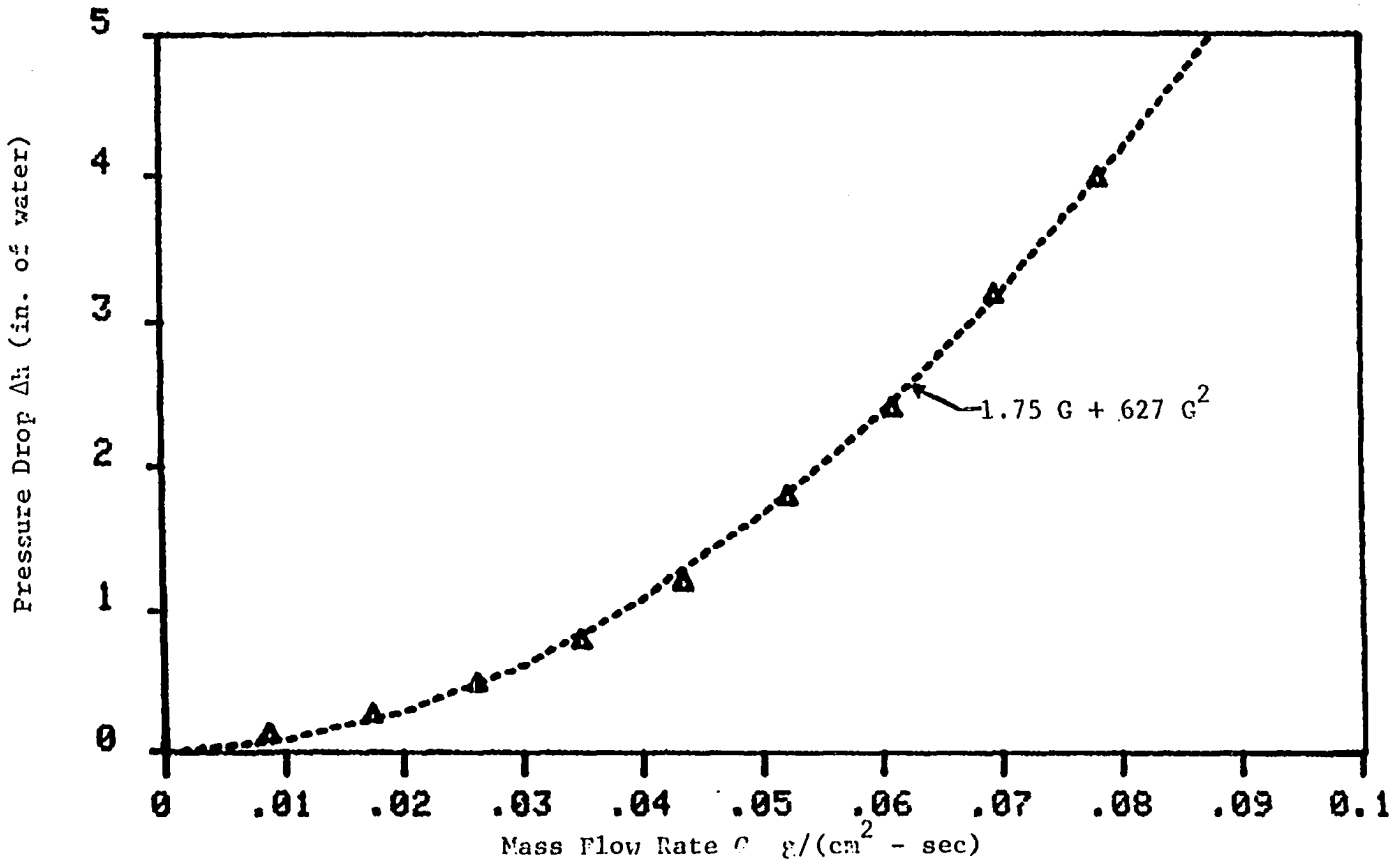

Figure 29. The relationship between empty tube pressure drop and mass flow rate for the air permeability apparatus

Illustrative Calculations

Average particle size determinations

From sieve analysis: The arithmetic mean or geometric mean of two adjacent sieve openings can be considered as the average size and are denoted by d_m and d_{gm}, respectively. For example, the average size for the coal between 7 and 8 mesh sieves is calculated as

$$d_m = \frac{0.283 + 0.238}{2} = 0.2605 \text{ cm}$$

$$d_{gm} = \sqrt{(0.283)(0.238)} = 0.2595 \text{ cm}$$

Equivalent diameter of a sphere (d_{eq})

Number of particles = 111

Total weight of particles = 1.6811 g

Density of particles = 1.485 g/cm^3

Mean equivalent diameter of a sphere $= \left(\frac{1.6811}{1.485} \times \frac{1}{111} \times \frac{6}{\pi}\right)^{1/3}$

$= 0.269$ cm.

Unhindered settling velocity of 7-8 mesh MS-20 coal

Number of particles dropped = 50

Distance of timed fall = 100 cm

Avg. temperature of water = 20.1° C

Observed settling time of single particle (sec)

15.0	12.5	10.0	11.5	12.1	15.7	11.0	13.5	10.1	8.8
12.2	9.9	12.5	8.8	12.0	9.0	12.0	11.5	10.5	15.0
14.0	10.0	10.5	12.3	11.0	13.8	11.8	9.7	13.8	12.1
8.0	13.7	11.0	14.4	12.9	14.0	10.9	10.0	13.8	13.9
10.8	9.5	9.5	8.4	10.2	11.4	9.4	10.5	11.7	10.0

Mean time of fall = 11.53 sec

Standard deviation = 1.91 sec

Mean velocity of fall u_t = 8.673 (cm/sec)

Dynamic shape factor (DSF) and hydraulically equivalent diameter shape factor (Ω).

Measured settling velocity (u_t) at 20.1° C = 8.76 cm/sec

Density of water at 20.1° C = 0.998 g/cm^3

Viscosity of water at 20.1° C = 1.022 cp

$$C_D \, Re_{t\infty}^{\,2} = \frac{4g(\rho_s - \rho) \; d_{eq}^{\,3}}{3\mu^2} = 118474$$

$Re_{N\infty}$ (from $C_D Re_{t\infty}^{\,2}$ vs. Re_t for spheres presented in Appendix I) = 467.3

$u_{N\infty} = \mu . Re_{n\infty} / \rho . d_{eq}$ = 17.406 cm/sec.

$a + b = 1$

$\frac{b}{a} = Re_N$

$a = \frac{1}{Re_N + 1} = 0.002$

$$b = 0.998$$

$$DSF = a\left(\frac{u_t}{u_N}\right) + b\left(\frac{u_t}{u_N}\right)^2$$

$$= 0.002\left(\frac{8.673}{17.406}\right) + 0.998\left(\frac{8.673}{17.406}\right)^2$$

$$= 0.249.$$

$$C_D/Re_{t\infty} = \frac{4g(\rho_s - \rho)}{3\rho^2 u_t^3} = 0.009803$$

$Re_{N\infty}$ (from $C_D/Re_{t\infty}$ vs. $Re_{t\infty}$ relationship for spheres presented in Appendix I) = 109.5

$$d_h = \frac{Re_{N\infty}\mu}{\rho u_t} = 0.1265 \text{ cm.}$$

Hydraulically equivalent diameter shape factor

$$= \frac{d_h}{d_{eq}} = \frac{0.1265}{0.269}$$

$$= 0.470$$

Sphericity

Two methods were used to calculate the sphericity. Both the methods were based on Ergun equation for calculating pressure drop for flow through fixed bed. In the water fluidization experiments, for the unexpanded bed, the sphericity was back calculated from Ergun equation at each upflow velocity. A mean value for sphericity was calculated from these values. In the air permeability method, the sphericity was calculated by two approaches.

1. Back calculation from Ergun equation at each air flow rate.
2. From the intercept of the plot of $\frac{\Delta P}{Lu}$ vs. G of the air permeability data.

Equation 45a can be rearranged as follows:

$$\frac{\Delta P}{Lu} = \frac{150}{36} \mu \frac{(1-\varepsilon)^2}{\varepsilon^3} S^2 + \frac{1.75}{6} \frac{(1-\varepsilon)}{\varepsilon^3} S (\rho u)$$

$$G = \rho u$$

If $\frac{\Delta p}{Lu}$ is plotted against G

$$\text{intercept} = 4.17 \mu S^2 \frac{(1-\varepsilon)^2}{\varepsilon^3}$$

$$\text{slope} = 0.29 S \frac{(1-\varepsilon)}{\varepsilon^3}$$

(a) From fixed bed data of fluidization experiments for 7-8 mesh:

Porosity of fixed bed = 0.5579

Density of water at 25° C = 0.997 g/cm^3

Viscosity of water at 25° C = 0.008904 poise

Bed depth = 41.5 cm

Pressure drop = 1.905 cm of water

Superficial velocity = 0.5446 cm/sec.

$$\frac{\Delta p}{L} = 150 \mu \frac{(1-\varepsilon)^2}{\varepsilon^3} \left(\frac{S}{6}\right)^2 u + 1.75 \frac{(1-\varepsilon)}{\varepsilon^3} \left(\frac{S}{6}\right) \cdot \rho u^2$$

$$\frac{1.905 \times 0.997 \times 981}{41.5} = 150 \times 0.0089 \frac{(1-0.5579)^2}{(0.5579)^3} \cdot (0.5446)\frac{S^2}{36}$$

$$+ 1.75 \frac{(1-0.5579)}{(0.5579)^3} (0.997)(0.5446)^2 \frac{S}{6}$$

$$44.94 = 0.02277\ S^2 + 0.2198\ S$$

$$S^2 + 9.653\ S - 1973.6 = 0$$

$$S = 39.6\ cm^{-1}$$

$$\text{Sphericity } \psi = \frac{6}{S.d_{eq}} = \frac{6}{39.9 \times 0.269} = 0.559$$

Mean sphericity = 0.533

Number of data points = 9

Standard deviation = 0.0276.

(b) Sphericity from air permeability method for the same material from the plot of $\frac{\Delta p}{Lu}$ vs. G for loosely packed MS-20 coal 7-8:

Fixed bed porosity = 0.535

Viscosity of air at 23° C = 0.018 cp

$$\text{Intercept} = 4.17\mu\ S^2 \frac{(1 - \varepsilon)^2}{\varepsilon^3} = 1.195$$

$$S^2 = 1.145 \frac{(0.535)^3}{(1 - 0.535)^2} \times \frac{1}{4.17 \times 0.018 \times 10^{-2}}$$

$$= 1127.5\ cm^{-2}$$

$$S = 33.58\ cm^{-1}$$

$$\text{Sphericity} = \frac{6}{S.d_{eq}} = \frac{6}{33.58 \times 0.269} = 0.664$$

$$\text{Slope} = k_2 \frac{S(1-\varepsilon)}{\varepsilon^3}$$

$$k_2 = \text{slope} \frac{\varepsilon^3}{(1-\varepsilon)} \frac{1}{S}$$

$$= 41.5 \frac{(0.535)^3}{(1-0.535)^2} \quad \frac{1}{33.58} = 0.407$$

In addition, sphericity was also calculated from back calculation from Ergun equation as explained in section (a).

Average sphericity from seven measurements = 0.585

Standard deviation = 0.0165

Porosity of fixed bed

i	Weight of 7-8 mesh coal in column	= 2374.0 g
ii	Fixed bed height after expansion and free settling	= 44.7 cm
iii	Cross-sectional area of column	= 81.07 cm^2
iv	Total volume of sand and water (ii) x (iii)	= 3623.83 cm^3
v	Specific weight of coal	= 1.485 g/cm^3
vi	Volume of coal (i)/(v)	= 1598.65 cm^3
	Fixed bed porosity $1 - \frac{(vi)}{(iv)}$	= 0.558

Minimum fluidization velocities

Minimum fluidization velocities for each material was calculated by equations 71, 74, 75, 78.

Wen and Yu - Equation 71: For mesh 7-8, MS-20 coal

Sphericity ψ = 0.533

Porosity at minimum fluidization velocity $\varepsilon_{mf} = 0.5579$

Galileo number Ga, at 25° C $= 117062$

$$\frac{1.75\ Re_{mf}^{2}}{\psi\ \varepsilon_{mf}^{3}} + \frac{150(1 - \varepsilon_{mf})}{\psi^{2}\ \varepsilon_{mf}^{3}} \quad Re_{mf} - Ga = 0$$

$$18.907\ Re_{mf}^{2} + 1344.27\ Re_{mf} - 117062 = 0$$

$$Re_{mf}^{2} + 71.1\ Re_{mf} - 6191.46 = 0$$

$$Re_{mf} = \frac{-71.1 + \sqrt{(71.1)^{2} + 4(6191.46)}}{2}$$

$$= 50.79$$

$$Re_{mf} = d_{eq}\ u_{mf}\ \rho/\mu$$

$$u_{mf} = \frac{50.79 \times 0.008904}{0.997 \times 0.269} = 1.688 \text{ cm/sec}$$

Wen and Yu, equation 74:

$$Re_{mf} = \sqrt{(33.7)^{2} + 0.0408\ Ga} - 33.7$$

$$Re_{mf} = \{(33.7)^{2} + 0.0408\ (117062)\}^{1/2} - 33.7$$

$$= 43.19$$

$$u_{mf} = \frac{Re_{mf} \cdot \mu}{\rho \cdot d_{eq}} = \frac{43.19 \times 0.008904}{0.997 \times 0.269} = 1.435 \text{ cm/sec}$$

Bena et al. method, equation 75:

$$Re_{mf} = \frac{0.00138\ Ga}{(Ga + 19)0.11} \qquad \begin{matrix} Ga \leq 1.06 \times 10^5 \\ Re_{mf} < 41.0 \end{matrix}$$

and

$$Re_{mf} = 0.03865 Ga^{0.602} \qquad 1.06 \times 10^5 < Ga < 2.13 \times 10^8$$

Since

$$Ga = 117062$$

$$Re_{mf} = 0.03865 \times (117062)^{0.602}$$

$$= 43.48$$

$$u_{mf} = \frac{Re_{mf} \cdot \mu}{\rho . d_{eq}} = \frac{43.48 \times 0.008904}{0.997 \times 0.269} = 1.443 \text{ cm/sec}$$

Beranek method, equation 78:

$$B_o = \frac{u_N^3\ \rho^2}{g\mu(\rho_s - \rho)}$$

Settling velocity of a sphere with diameter = 0.269 cm at 25° C, u_N = 17.77 cm/sec

$$B_o = \frac{(17.77)^3 \times (0.997)^2}{981 \times 0.008904\ (1.485 - 0.997)} = 1314$$

since $B_o > 10^3$

$$\frac{u_{mf}}{u_t} = 0.09 \pm 0.05$$

Settling velocity u_t, adjusted for 25° C = 8.89 cm/sec

$$u_{mf} = 0.09 \times 8.89 = 0.800 \text{ cm/sec.}$$

Adjustment of unhindered settling velocity for temperature

In order to compare the intercept velocity u_i at $\varepsilon = 1.0$ with unhindered settling velocity u_t, it is necessary to correct settling velocity which were measured at temperatures other than at 25° C. Settling velocity measurements were made at temperatures ranging from 19.8 to 24.8° C. An assumption was made that DSF will not change appreciably in the temperature range from 20° C to 25° C. This assumption was checked later by making settling velocity measurements at near 36° C.

The measured velocity was adjusted to 25° C as follows:

The DSF corresponding to the test conditions was calculated as shown in the DSF calculations. Assuming that DSF at 25° C has the same value at 25° C, the settling velocity at 25° C was calculated from the definition of DSF.

DSF of 7-8 mesh MS-20 coal at 20.1° C = 0.249.

Settling velocity of a equivalent volume sphere at 25° C

$$u_N = 17.80 \text{ cm/sec.}$$

$$Re_N = 536.46$$

at 25° C

$$DSF = a. \left(\frac{u_t}{u_N}\right) + b \left(\frac{u_t}{u_N}\right)^2$$

$$a = \frac{1}{1 + Re_N} = \frac{1}{1 + 536.4} = 0.002$$

$$b = 1 - a = 0.998$$

Since a is very small

$$DSF = \left(\frac{u_t}{u_N}\right)^2$$

$$u_t = \sqrt{DSF} \times u_N$$

$$= \sqrt{0.249} \times 17.80 = 8.89 \text{ cm/sec.}$$

This can be compared with the u_t of 8.673 cm/sec at the test temperature of 20.1° C.

RESULTS AND ANALYSIS

Results

The results are first presented in a tabular form in this section. These data will be discussed in the analysis section which follows.

Sieve analysis

Sieve analysis was carried out on the materials which were previously separated into uniform size fractions to test the adequacy of sieving operations. A representative sample of each material was resieved on the gyratory shaking machine for 5 minutes followed by 1 minute of hand shaking. Table 9 gives the results of the sieving procedure. The weight of the representative sample was 200 grams for each size. From Table 9 it is apparent that the preparation sieving was satisfactory.

Size determinations

The equivalent spherical diameter of each uniform sized material was determined by the count and weigh procedure as described previously. Table 10 shows the equivalent diameter of a sphere, d_{eq}, arithmetic average of adjacent sieves, d_m, and the geometric mean of the adjacent sieves d_{gm}.

Densities

Table 11 gives the results of the density determination for all the material used in the experiments.

Porosities

Fixed bed porosities of materials in the fluidization column as determined by the column technique are shown in Table 12.

Settling velocities

The experimentally determined terminal settling velocity for all the

Table 9. Sieve analysis of uniform sized material

Sieve No.	Sieve Opening mm	Wt. Retained g	% Retained
Brass metal punchings 35-40			
30-35	0.59-0.50	3.0	1.5
35-40	0.50-0.42	196.0	98.0
40-45	0.42-0.35	1.0	0.5
Stainless steel punchings 16-18			
14-16	1.41-1.19	4.0	2.0
16-18	1.19-1.00	193.0	96.5
18-20	1.00-0.84	3.0	1.5
Aluminum punchings 16-18			
14-16	1.41-1.19	2.0	1.0
16-18	1.19-1.00	197.0	98.5
18-20	1.00-0.84	1.0	0.5
Sand 5-6			
4-5	4.76-4.00	2.0	1.0
5-6	4.00-3.36	175.0	88.8
6-7	3.36-2.83	20.0	10.2
Sand 6-7			
5-6	4.00-3.36	17.0	10.2
6-7	3.36-2.83	150.0	89.8
7-8	2.83-2.38	-	
MS-20 Coal 5-6			
4-5	4.76-4.00	8.0	4.2
5-6	4.00-3.36	171.0	89.5
6-7	3.36-2.83	12.0	6.3
MS-20 Coal 6-7			
5-6	4.00-3.36	14.0	7.1
6-7	3.36-2.83	171.0	87.2
7-8	2.83-2.38	8.0	4.1
8-10	2.38-2.00	3.0	1.6
MS-20 Coal 7-8			
6-7	3.36-2.83	9.0	4.5
7-8	2.83-2.38	180.0	90.5
8-10	2.38-2.00	10.0	5.0

Table 9. continued

Sieve No.	Sieve Opening mm	Wt. Retained g	% Retained
MS-20 coal 8-10			
6-7	3.36-2.83	18.0	9.1
7-8	2.83-2.38	170.0	85.6
8-10	2.38-2.00	10.0	5.3
Poly PET 7352 7-8			
5-6	4.00-3.36	3.0	1.5
6-7	3.36-2.83	8.0	4.0
7-8	2.83-2.38	178.0	89.0
8-10	2.38-2.00	11.0	5.5
Poly PETG 6763 7-8			
5-6	4.00-3.36	2.0	1.0
6-7	3.36-2.83	5.0	2.5
7-8	2.83-2.38	180.0	90.0
8-10	2.38-2.00	13.0	6.5
Cullsan P 8-10			
5-6	4.00-3.36	1.0	0.5
6-7	3.36-2.83	4.0	2.0
7-8	2.83-2.38	18.0	9.0
8-10	2.38-2.00	172.0	86.0
10-12	2.00-1.68	5.0	2.5

Table 10. Equivalent volume diameter of sphere (d_{eq}), arithmetic average of adjacent sieves (d_m) and geometric mean of adjacent sieves (d_{gm}) of uniform sized materials

Material	d_{eq} cm	d_m cm	d_{gm} cm
Brass 35-40	0.0475	0.0460	0.0458
Stainless steel 16-18	0.0956	0.1095	0.1091
Aluminum 16-18	0.1090	0.1095	0.1091
Sand 5-6	0.3749	0.3680	0.3666
Sand 6-7	0.3497	0.3095	0.3083
MS-20 Coal 5-6	0.3865	0.3680	0.3666
MS-20 Coal 6-7	0.3167	0.3095	0.3083
MS-20 Coal 7-8	0.2690	0.2605	0.2595
MS-20 Coal 8-10	0.2339	0.2190	0.2182
Poly PET 7352 7-8	0.3085	0.2605	0.2595
Poly PETG 6763 7-8	0.3040	0.2605	0.2595
Cullsan P 8-10	0.2693	0.2190	0.2182

Table 11. Densities of the materials used in the experiments

Material	Density (g/cm^3)
Brass 35-40	8.550
Stainless steel 16-18	7.780
Aluminum 16-18	2.734
Sand 5-6	2.646
Sand 6-7	2.640
MS-20 coal 5-6	1.485
MS-20 coal 6-7	1.485
MS-20 coal 7-8	1.485
MS-20 coal 8-10	1.485
Poly PET 7352 7-8	1.360
Poly PETG 6763 7-8	1.270
Cullsan P 8-10	1.200

Table 12. Fixed bed porosities of the material determined by the column technique - ε_{mf} at 25° C

Material	Dry Wt. of Media, g	Fixed Bed Height cm	Porosity ε_{mf}
Brass 35-40	11383.0	28.6	0.426
Stainless steel 16-18	10091.0	28.8	0.444
Aluminum 16-18	4295.0	34.7	0.442
Sand 5-6	4914.0	42.0	0.455
Sand 6-7	3659.0	31.2	0.452
MS-20 coal 5-6	2387.0	45.0	0.559
MS-20 coal 6-7	2369.0	44.6	0.556
MS-20 coal 7-8	2374.0	44.7	0.558
MS-20 coal 8-10	2507.0	47.7	0.563
Poly PET 7352 7-8	2516.0	38.7	0.410
Poly PETG 6763 7-8	2225.0	40.3	0.440
Cullsan P 8-10	2217.0	41.6	0.429

material is given in Table 13. The temperature, mean settling time, standard deviation of settling time are also tabulated in Table 13. The adjusted settling velocities at 25° C are presented in Table 14.

Dynamic shape factor (DSF) and hydraulically equivalent diameter shape factor (Ω)

The two hydraulic shape factors were calculated for each material at the two different temperatures at which settling velocities were determined. The results are tabulated in Table 15.

Sphericity

Sphericities of the material used in the experiments were calculated by two methods. In the first method, the pressure drop versus superficial velocity data of the fixed bed of the fluidization experiments were used to calculate sphericity using Ergun equation. All the data points on the rising limb of pressure drop versus superficial velocity plot were used in the sphericity calculations, including those obtained during increasing flow rate as well as decreasing flow rate.

The actual porosity of the bed at each velocity was used in the calculation since the porosities were slightly different for expanding and contracting flow data for the same material.

The sphericities were also calculated using air permeability method. In this method, the pressure drop versus superficial velocity data were obtained for two different fixed bed porosities. One was under loosely packed conditions and the other under tightly packed conditions. For each fixed bed porosity the sphericity was calculated by two methods. One was similar to the method described for fixed bed

Table 13. Settling velocities of uniform size materials

Material	Temperature	No. of Particles Observed	Mean Time to Travel 100 cm,-sec.	Std. Deviation sec.	Mean Settling Velocity cm/sec.
Brass 35-40	23.3	50	5.50	0.02	18.18
	36.0	30	5.13	0.09	19.49
Stainless steel 16-18	23.3	40	4.49	0.12	22.27
	36.0	30	4.36	0.18	22.93
Aluminum 16-18	24.9	50	7.27	0.15	13.76
	36.3	25	6.97	0.11	14.35
Sand 5-6	23.4	50	3.65	0.30	27.40
	36.6	50	3.48	0.30	28.73
Sand 6-7	22.5	50	3.66	0.28	27.32
	36.7	50	3.62	0.29	27.62
MS-20 coal 5-6	19.8	50	9.34	0.79	10.71
	36.3	30	8.64	0.89	11.57
MS-20 coal 6-7	19.8	50	10.29	1.61	9.72
	36.5	53	9.49	1.01	10.54
MS-20 coal 7-8	20.1	50	11.53	1.91	8.67
	36.6	50	11.66	1.50	8.58
MS-20 coal 8-10	20.3	50	12.24	1.73	8.17
	36.6	50	12.15	1.59	8.23
Poly PET 7352 7-8	23.4	50	8.00	0.42	12.50
	36.6	50	7.91	0.38	12.64
Poly PETG 6763 7-8	24.7	50	9.99	0.68	10.00
	36.5	50	10.04	0.50	9.96
Cullsan P 8-10	24.7	50	13.39	0.74	7.47
	36.7	50	12.95	0.88	7.72

Table 14. Settling velocity adjusted to 25° C[a]

Material	Settling Velocity (cm/sec)
Brass 35-40	18.49
Stainless steel 16-18	22.48
Aluminum 16-18	13.80
Sand 5-6	27.41
Sand 6-7	27.31
MS-20 coal 5-6	10.81
MS-20 coal 6-7	9.96
MS-20 coal 7-8	8.89
MS-20 coal 8-10	8.37
Poly PET 7352 7-8	12.65
Poly PETG 6763 7-8	10.04
Cullsan P 8-10	7.52

[a]Settling velocities were adjusted assuming the DSF at temperature of measurement (near 25° C) is same as the DSF at 25° C, as shown in the illustrative calculations.

Table 15. Dynamic shape factor (DSF) and hydraulically equivalent diameter shape factor (Ω)

Material	Temp.	DSF	Ω
Brass 35-40	23.3	0.693	0.849
	36.0	0.676	0.855
Stainless steel 16-18	23.3	0.350	0.572
	36.0	0.336	0.538
Aluminum 16-18	24.9	0.543	0.759
	36.3	0.533	0.729
Sand 5-6	23.4	0.407	0.505
	36.6	0.446	0.503
Sand 6-7	22.5	0.436	0.543
	36.7	0.444	0.513
MS-20 coal 5-6	19.8	0.217	0.404
	36.3	0.236	0.386
MS-20 coal 6-7	19.8	0.243	0.448
	36.5	0.239	0.427
MS-20 coal 7-8	20.1	0.249	0.470
	36.6	0.211	0.410
MS-20 coal 8-10	20.3	0.273	0.492
	36.6	0.241	0.452
Poly PET 7352 7-8	23.4	0.575	0.702
	36.6	0.524	0.662
Poly PETG 6763 7-8	24.7	0.520	0.681
	36.5	0.464	0.619
Cullsan P 8-10	24.7	0.497	0.700
	36.7	0.475	0.658

data of fluidization experiments, that is, back calculation from Ergun equation using the pressure drop and velocity for each data point. In the other method with the same set of data, a plot of $\frac{\Delta p}{Lu}$ vs. G, was drawn and from the intercept of the plot the specific surface of the material was calculated. From the slope of the plot, the coefficient k_2 was calculated to compare with coefficient on the second term of the Ergun equation 45a.

Table 16 shows the average sphericities obtained from water permeability data (i.e. fixed bed pressure drop data). It also gives the number of data points used and the standard deviation of the sphericity values obtained.

Table 16. Average sphericities of the media determined from water permeability data

Material	Avg. Sphericity	No. of Observations	Std. Devia.
Brass 35-40	0.930	11	0.011
Stainless steel 16-18	0.833	11	0.009
Aluminum 16-18	0.836	16	0.024
Sand 5-6	0.753	15	0.054
Sand 6-7	0.772	17	0.043
MS-20 coal 5-6	0.483	14	0.021
MS-20 coal 6-7	0.534	14	0.023
MS-20 coal 7-8	0.533	9	0.028
MS-20 coal 8-10	0.541	10	0.038
Poly PET 7352 7-8	0.851	10	0.037
Poly PET 6763 7-8	0.869	10	0.049
Cullsan P 8-10	0.878	10	0.023

Table 17 presents the fixed bed porosity, sphericity determined from the air permeability measurements. The table also includes the sphericity data obtained from the intercept of $\frac{\Delta P}{Lu}$ vs. G plot and the coefficient K_2 calculated from the slope of plot using the specific surface obtained from the intercept. The data are presented for both the loosely packed bed and tightly packed bed. The same table also gives the average sphericity values calculated by back calculation from Ergun equation 45a using the air permeability method.

Figure 30 shows a sample plot of $\frac{\Delta P}{Lu}$ versus mass flow rate G for loosely packed 7-8 mesh MS-20 coal in the air permeability experiment.

Heywood's volume coefficient Z

Heywood's volume coefficient Z was calculated for all the material used in present research and the materials used in Fan's (45) study. The average projected area of the particles when lying in most stable position was determined by a image analyzer[a]. The measurements were made by the personnel of the Materials Research Lab of the Engineering Research Institute.

By the image analyzer, the projected areas of at least fifty particles were determined. From these measurements, an average area was computed for each material. Transparent materials such as Polyester PETG 6763 and Cullsan P did not produce a sharp image, therefore had to be coated with black paint to produce a sharper image. The volume

---

[a]Lemont Scientific System B-10, 2011, Pine Hall Drive, Science Park State College, PA. 16801. Lemont Scientific & Image Analysis - Program P - ϕ1641 V 4.1 - IH81A.

Table 17. Sphericities of different materials obtained by air permeability method

Material	Loosely Packed[a] Bed ψ and k_2 from eq. 45b			Tightly Packed[a] Bed ψ and k_2 from eq. 45b			Sphericity from Equation 45a		
	Bed Porosity ε_o	Sphericity ψ	Coeff. k_2	Bed Porosity ε_o	Sphericity ψ	Coeff. k_2	Loosely Packed Bed[a]	Tightly Packed Bed[a]	Fluidization Fixed Bed Data[b]
Brass 35-40	0.420	0.877	0.307	0.379	0.895	0.109	0.881	0.876	0.930
Stainless Steel 16-18	0.446	0.797	0.334	0.418	0.795	0.335	0.778	0.779	0.833
Aluminum 16-18	0.429	0.857	0.310	0.384	0.875	0.289	0.846	0.876	0.836
Sand 5-6	0.437	0.808	0.326	0.408	0.800	0.329	0.765	0.755	0.753
Sand 6-7	0.438	0.734	0.248	0.404	0.774	0.290	0.780	0.773	0.772
Coal 5-6	0.537	0.607	0.379	0.497	0.579	0.383	0.541	0.517	0.483
Coal 6-7	0.534	0.575	0.338	0.481	0.625	0.443	0.544	0.531	0.534
Coal 7-8	0.535	0.664	0.407	0.505	0.688	0.482	0.585	0.559	0.533
Coal 8-10	0.532	0.724	0.577	0.476	0.584	0.459	0.545	0.506	0.541
Poly PET 7352 7-8	0.401	0.905	0.297	0.348	0.765	0.345	0.896	0.718	0.869
Poly PETG 6763 7-8	0.445	0.799	0.380	0.398	0.751	0.343	0.721	0.709	0.857
Cullsan P 8-10	0.436	0.747	0.270	0.375	0.764	0.335	0.766	0.727	0.878

[a]Using air permeability data.

[b]Using water permeability data.

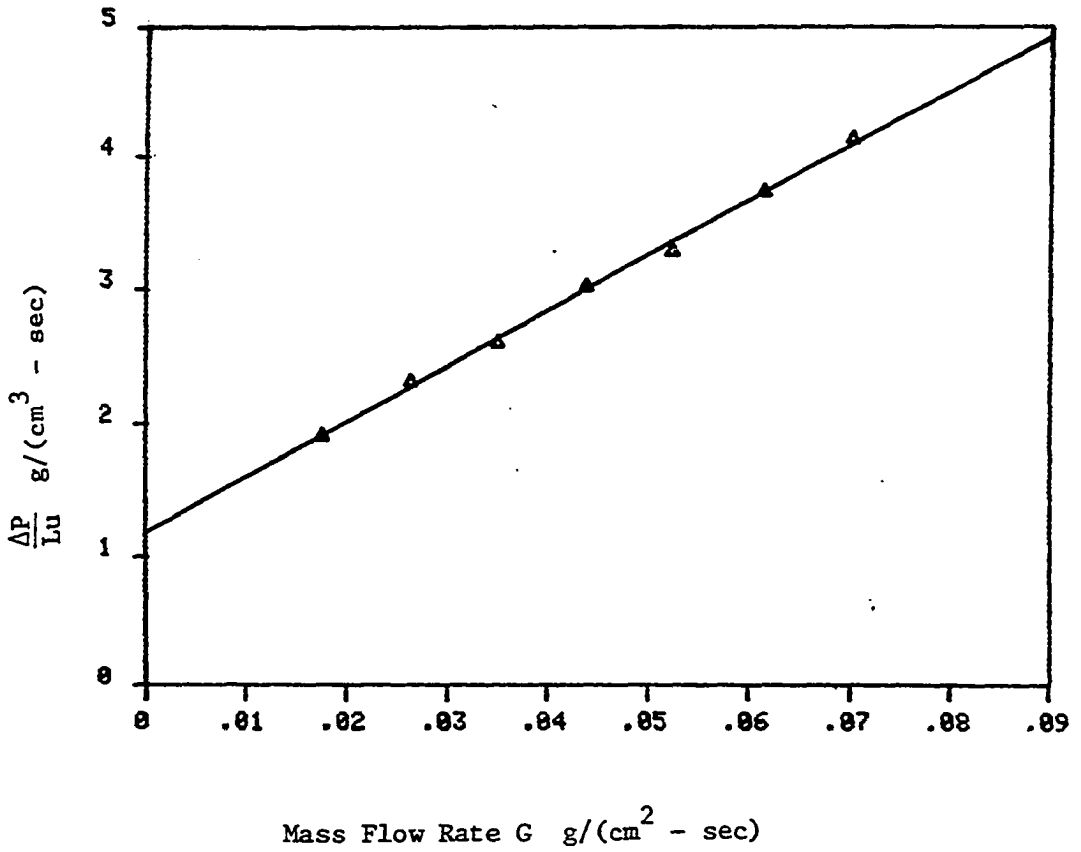

Figure 30. The relationship between $\frac{\Delta p}{Lu}$ and mass flow rate, G, for 7-8 mesh MS-20 coal in the loosely packed state

coefficient Z values are tabulated in Table 18.

Minimum fluidization velocities

Figures 31 through 36 show the head loss versus velocity for different materials. Table 19 summarizes the minimum fluidization velocity u_{mf} obtained experimentally and calculated by equations 74, 71, 75 and 78. In Table 19, in addition to the material used in the present experiment, the materials studied by Fan (45), are also included.

In each fluidization experiment, the bed was expanded gradually until an expansion about 300 percent was achieved or for heavier material maximum flow rate was reached. Then the fluidized bed was contracted slowly by closing the valve until fixed bed state was reached again. Two minimum fluidization velocities u_{mf}, can be determined in each experiment, one going from fixed bed state to fluidized state and the other going from fluidized state to fixed bed state. There is no real advantage in choosing one or the other since the reproducibility of these values will depend to some extent on the fixed bed porosities for each case. Nevertheless, the two values of u_{mf} do not differ very much. In this thesis, the minimum fluidization velocity was determined on the expanding curve and u_{mf} was selected as the point where the nearly horizontal portion of the pressure drop curve intersected the line through increasing pressure drop data points.

Table 18. Heywood's volume coefficient Z

Material	Avg. Projected Area Diameter d_a cm	Equivalent Spherical Dia. d_{eq} cm	Volume Coefficient Z^d
Brass 35-40	0.04569[a]	0.047	1.124
Stainless Steel 16-18	0.1143[a]	0.956	0.306
Aluminum 16-18	0.1143[a]	0.109	0.454
Sand 5-6	0.4541[b]	0.374	0.295
Sand 6-7	0.4111[b]	0.349	0.322
MS-20 coal 5-6	0.4853[b]	0.386	0.264
MS-20 coal 6-7	0.4146[b]	0.316	0.233
MS-20 coal 7-8	0.3467[b]	0.269	0.244
MS-20 coal 8-10	0.304[b]	0.233	0.238
Poly PET 7352 7-8	0.3461[b]	0.308	0.371
Poly PET 6763 7-8	0.3514[b]	0.304	0.339
Cullsan P 8-10	0.3378[b]	0.269	0.264
Sand 10-12	0.2558[b]	0.196	0.236
Sand 14-16	0.1711[b]	0.146	0.327
Sand 18-20	0.1125[b]	0.100	0.374
Sand 30-35	0.0746[b]	0.059	0.270
US Anthracite 5-6	0.5280[b]	0.368	0.177
US Anthracite 12-14	0.2237[b]	0.154	0.171
Ballotini 18-22	0.0813[c]	0.078	0.468
Flintag 18-22	0.1129[c]	0.078	0.174
Flintag 25-30	0.0828[c]	0.052	0.134
U.K. Anthracite 18-22	0.1115[c]	0.081	0.204
U.K. Anthracite 25-30	0.0801[c]	0.050	0.131

[a]Diameter of the disc as given by the supplier.

[b]Average projected area of the grain's were determined using Lemont Scientific Image Analyzer with Program P-ϕ 1641 V4.1-IH81A.

[c]As reported by Fisher (47).

$$Z^d = \frac{\frac{\pi}{6} d_{eq}^3}{d_a^3}$$

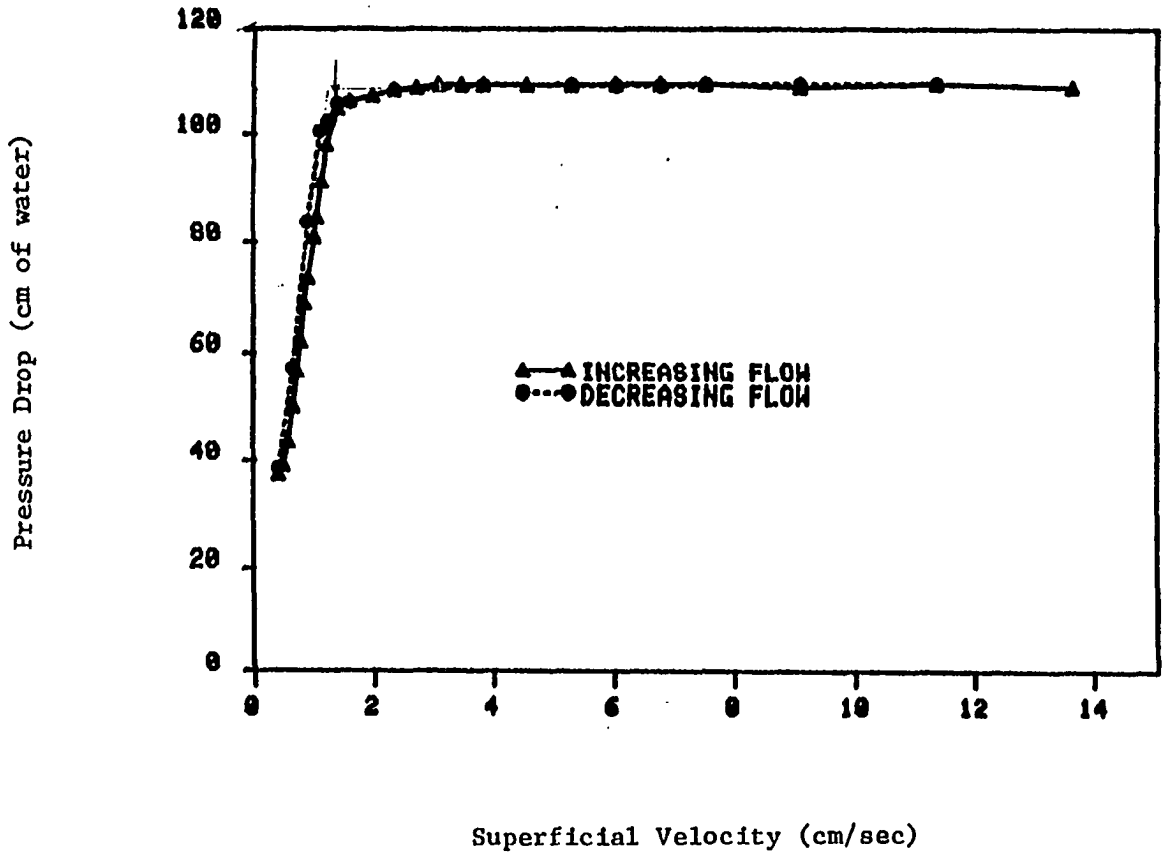

Figure 31. Pressure drop versus superficial velocity for 35-40 mesh brass metal punchings

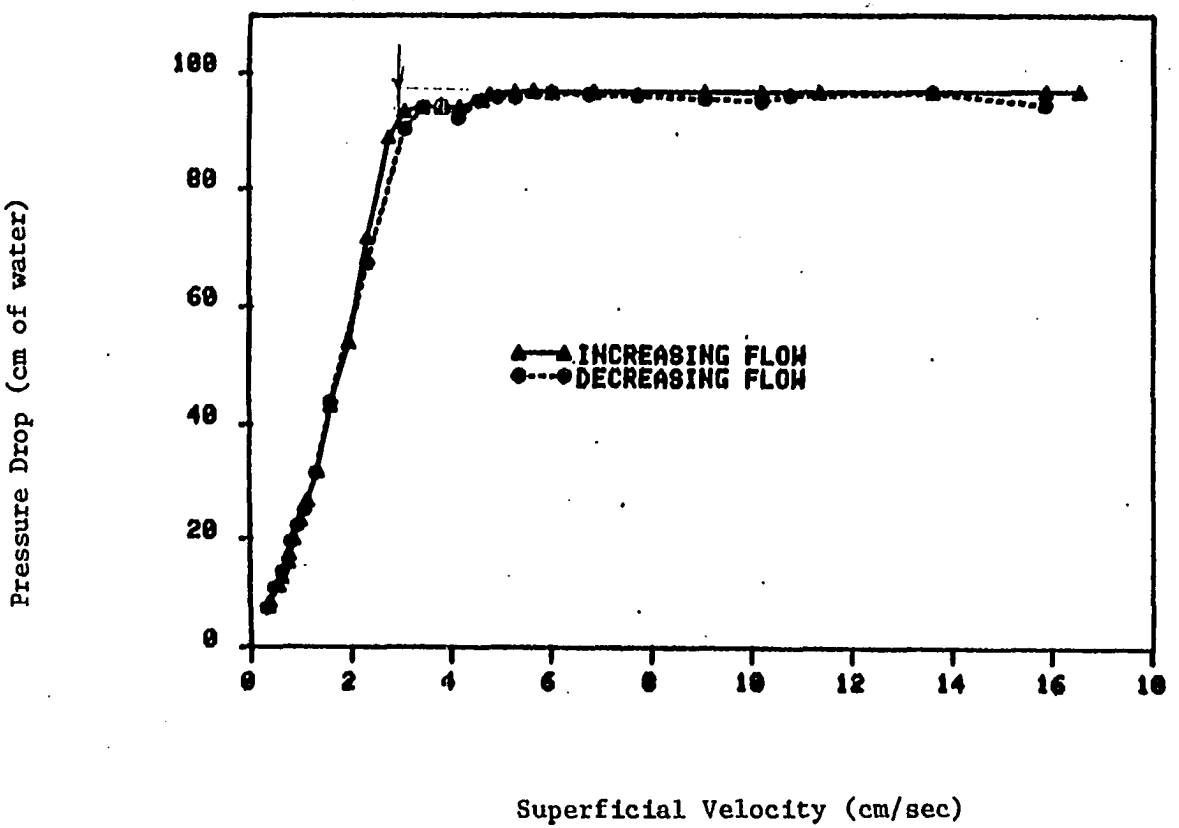

Figure 32. Pressure drop versus superficial velocity for 16-18 mesh stainless steel metal punchings

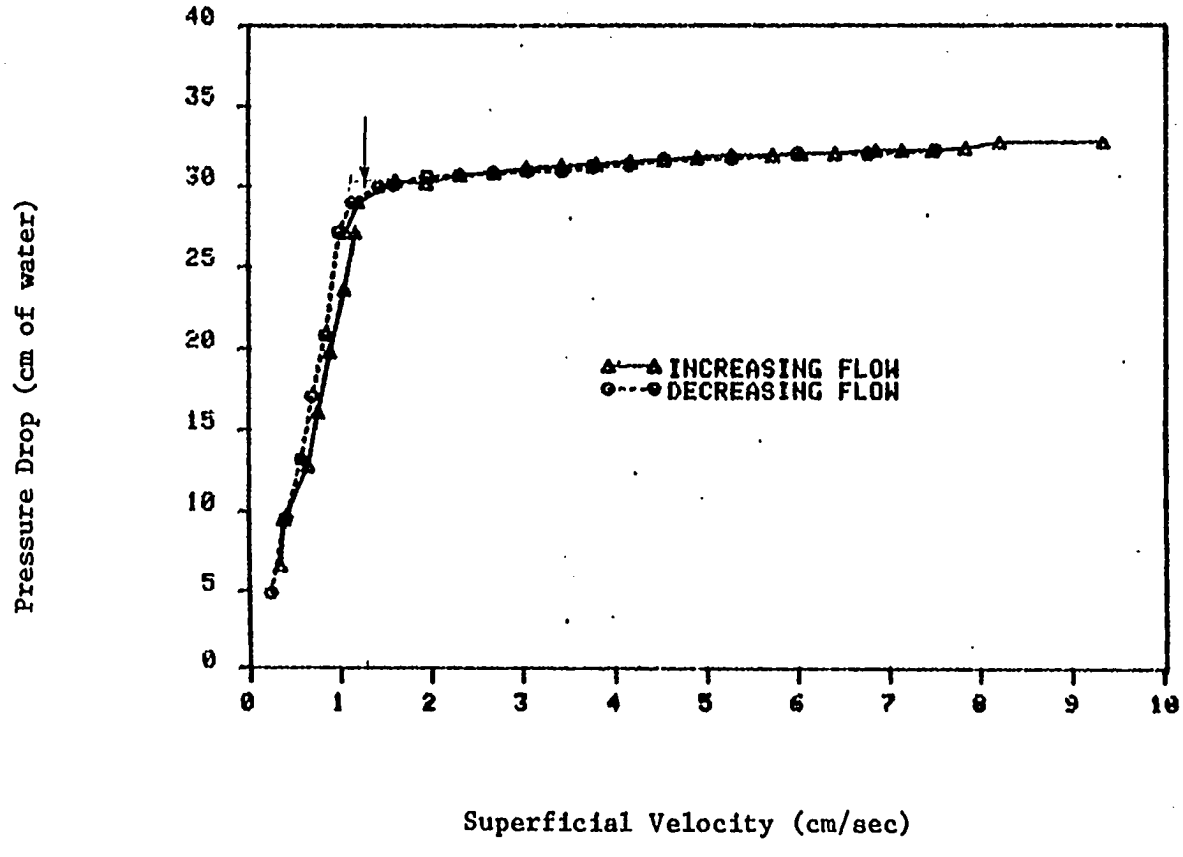

Figure 33. Pressure drop versus superficial velocity for 16-18 mesh aluminum metal punchings

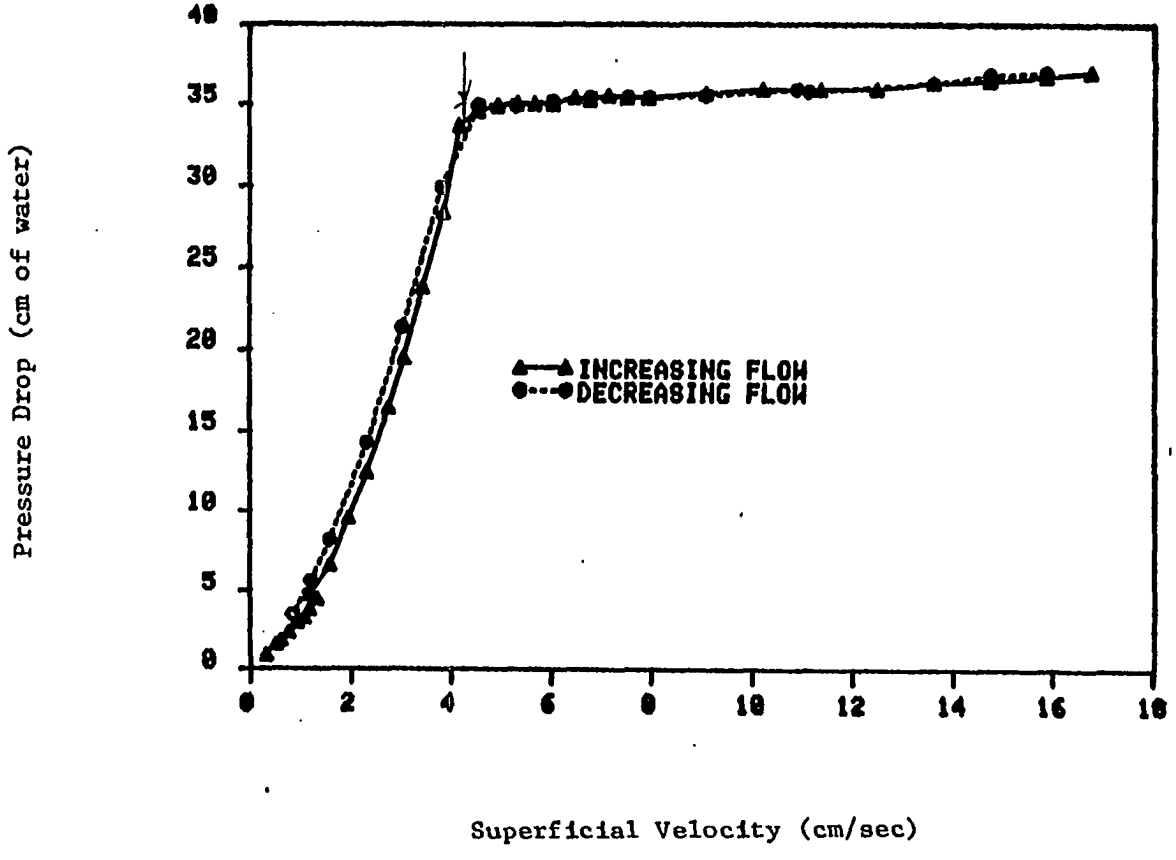

Figure 34. Pressure drop versus superficial velocity for 5-6 mesh silica sand

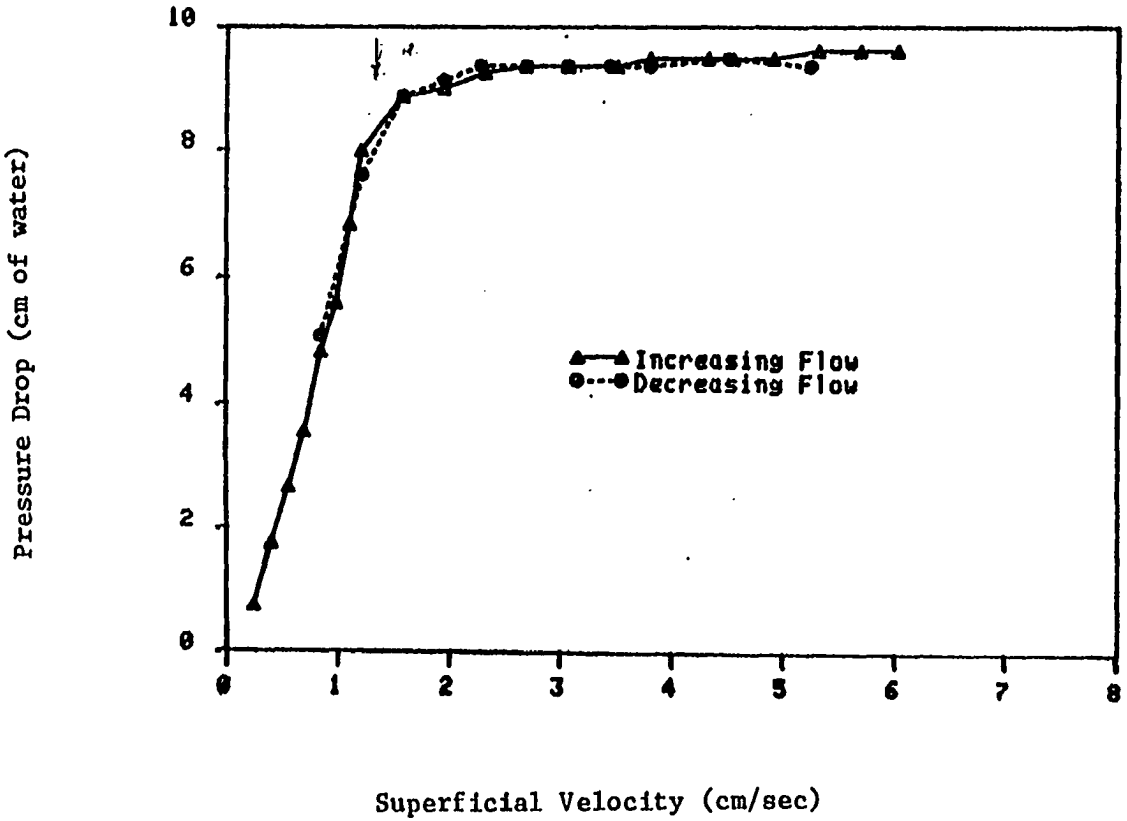

Figure 35. Pressure drop versus superficial velocity for 8-10 mesh MS-20 coal

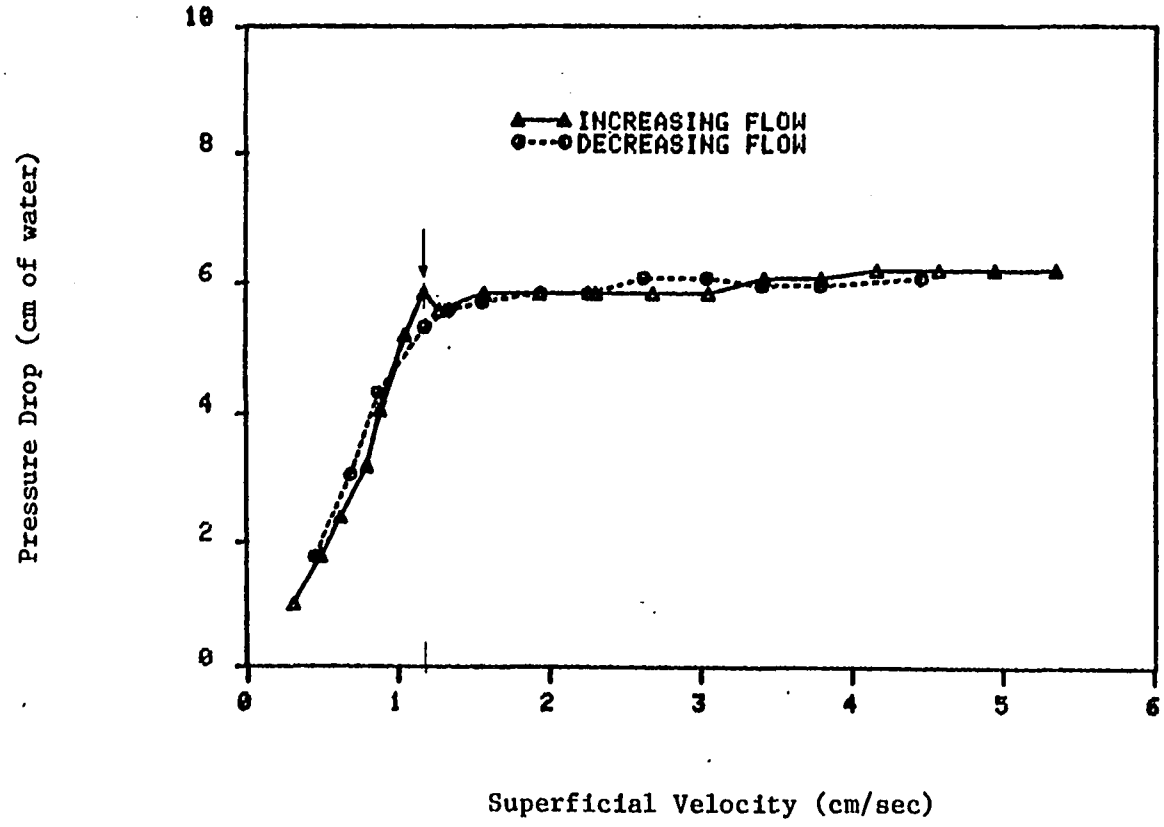

Figure 36. Pressure drop versus superficial velocity for 7-8 mesh Polyester PETG 6763

Table 19. Minimum fluidization velocities observed and calculated (cm/sec at 25° C)

Material	u_{mf} Observed cm/sec	u_{mf} Calculated cm/sec			
		Wen & Yu Eq. 74	Wen & Yu Eq. 71	Bena Eq. 75	Beranek Eq. 78
Brass 35-40	1.35	1.05	1.29	0.95	1.13
Stainless Steel 16-18	3.00	2.85	3.14	2.75	1.93
Aluminum 16-18	1.11	1.13	1.28	1.01	1.01
Sand 5-6	4.30	4.24	4.28	7.65	2.47
Sand 6-7	4.25	4.01	4.08	6.78	2.45
MS-20 Coal 5-6	2.14	2.08	2.22	2.72	0.97
MS-20 coal 6-7	1.91	1.72	1.99	1.95	0.90
MS-20 coal 7-8	1.69	1.42	1.69	1.49	0.80
MS-20 coal 8-10	1.36	1.21	1.50	1.18	0.73
Poly PET 7352 7-8	1.66	1.35	1.27	1.42	1.13
Poly PETG 6763 7-8	1.17	1.09	1.19	1.10	0.90
Cullsan P 8-10	0.81	0.74	0.80	0.68	0.61
Sand 10-12	2.20	2.39	2.18	2.60	1.72
Sand 14-16	1.60	1.68	1.71	1.59	1.38
Sand 18-20	0.90	0.96	1.06	0.85	0.88
Sand 30-35	0.50	0.38	0.47	0.36	0.42
Anthracite 5-6	2.70	2.56	1.99	3.58	1.10
Anthracite 6-7	2.40	2.21	1.83	2.73	1.00
Anthracite 7-8	2.00	2.00	1.67	2.32	0.94
Anthracite 12-14	1.00	0.88	0.84	0.79	0.52
Flintag 18-22	0.95	0.61	1.04	0.55	0.50
Flintag 25-30	0.50	0.29	0.59	0.28	0.29
U.K.anthracite 18-22	0.24	0.20	0.37	0.19	0.19
U.K.anthracite 25-30	0.15	0.08	0.20	0.09	0.09
U.K.sand 18-22	0.70	0.72	0.61	0.64	0.68
Ballotini 18-22	0.80	0.74	0.95	0.65	0.93

Slope and intercept of log u vs log ε graphs

Figure 37 through 42 show representative curves of log u versus log ε at 25° C. Table 20 summarizes the 'n' values and intercept velocity u_i at ε = 1 for the different materials determined by regression analysis of the experimental data. Also, u_t values from Table 14 are repeated here for convenience for comparison with the u_i values. All the data points above a bed expansion of ten percent including the data for increasing and also decreasing flow rates were used in the least square regression calculation to obtain 'n' and u_i. Table 20 also gives the 'n' value calculated by Richardson and Zaki's equation 81.

Table 20. 'n' slope, u_i from log u versus log ε plots at 25° C

Material	n	u_i (cm/sec)	u_t (cm/sec)[a]	n^b	r^2%
Brass 35-40	5.244	89.53	18.49	2.797	98.4
Stainless Steel 16-18	4.116	74.13	22.48	2.555	98.5
Aluminum 16-18	2.891	14.06	13.80	2.636	99.0
Sand 5-6	2.306	26.18	27.41	2.400	99.9
Sand 6-7	2.277	24.83	27.31	2.400	99.9
MS-20 coal 5-6	2.791	13.30	10.81	2.409	99.9
MS-20 coal 6-7	2.883	11.97	9.96	2.482	99.9
MS-20 coal 7-8	2.955	10.79	8.89	2.551	99.9
MS-20 coal 8-10	3.061	10.00	8.37	2.601	100.0
Poly PET 7352 7-8	2.325	10.64	12.65	2.408	100.0
Poly PETG 6763 7-8	2.460	8.53	10.04	2.458	100.0
Cullsan P 7-8	2.547	6.62	7.52	2.562	100.0

[a]Repeated here from Table 14.

[b]Calculated from appropriate equation in equation 81.

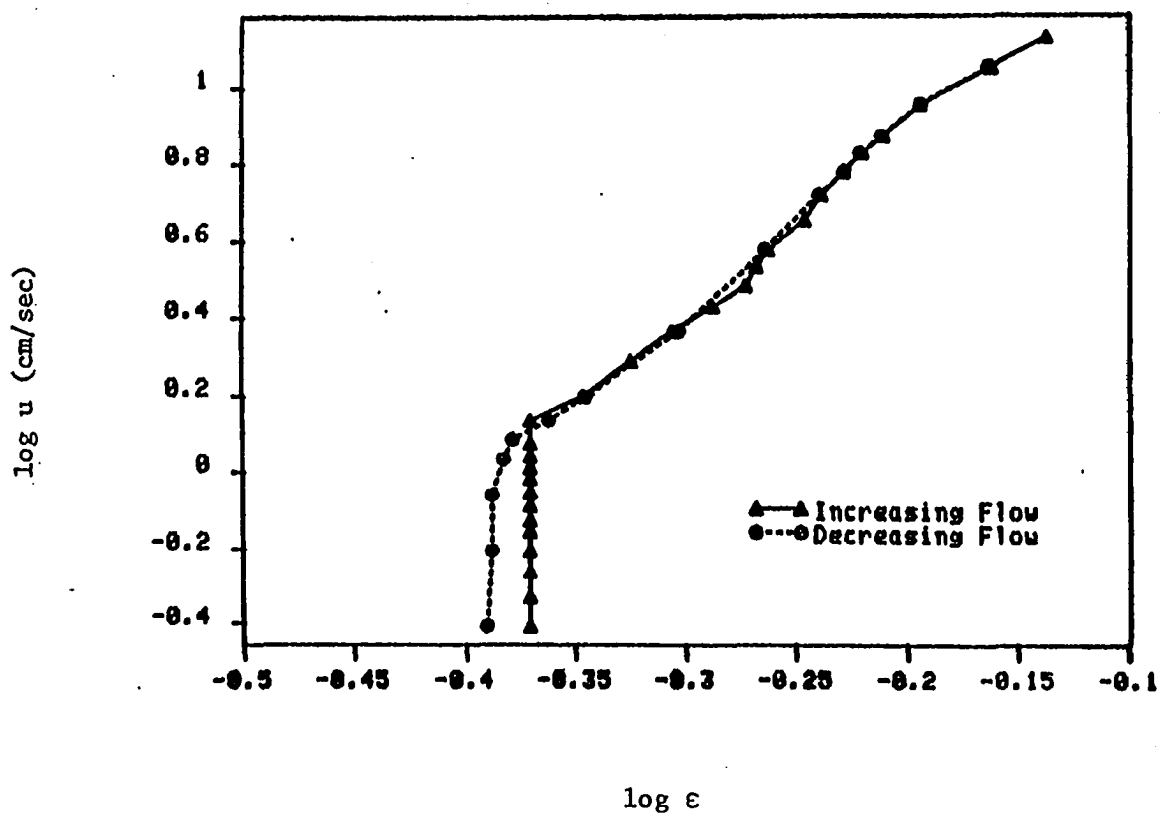

Figure 37. Log superficial velocity versus log porosity for 35-40 mesh brass metal punchings

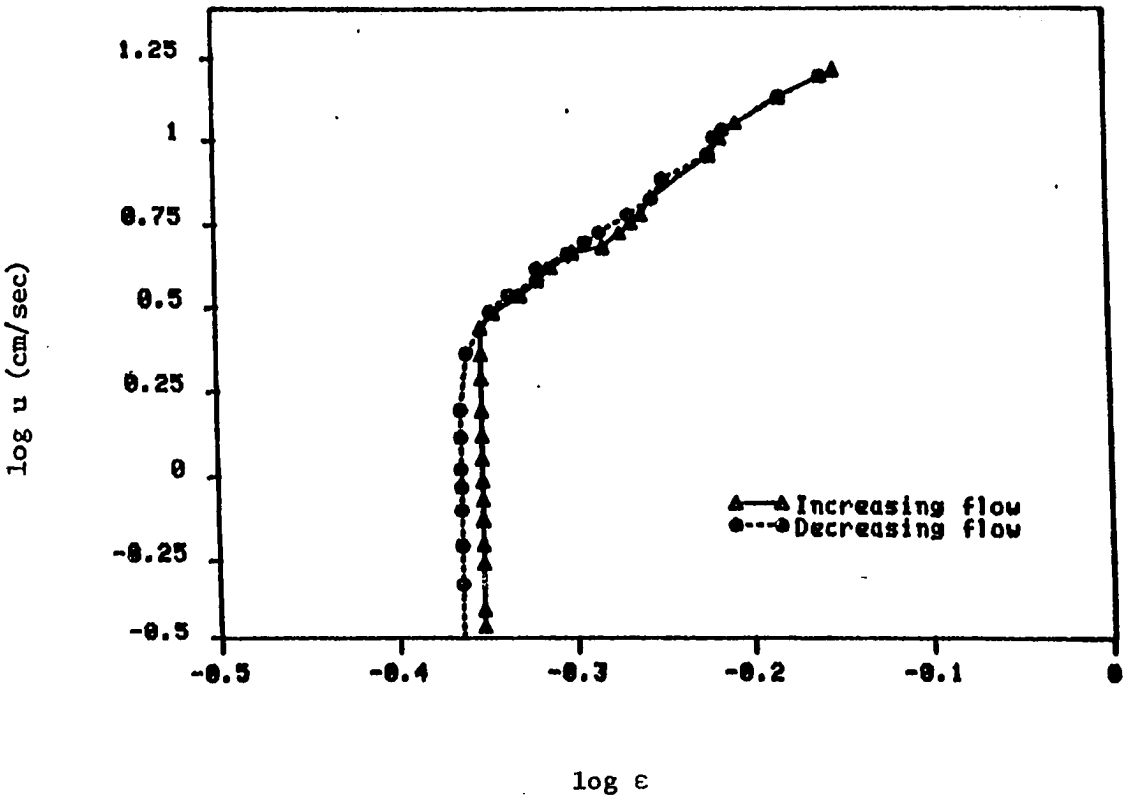

Figure 38. Log superficial velocity versus log porosity for 16-18 mesh stainless steel metal punchings

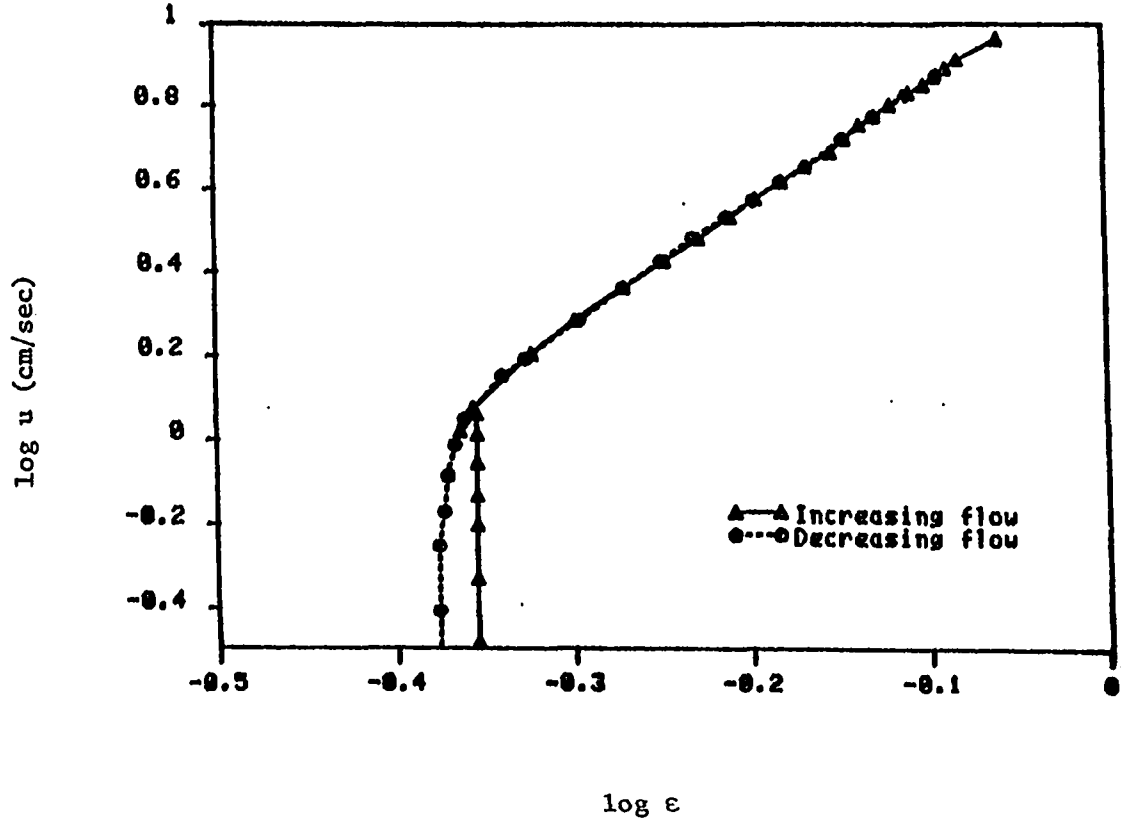

Figure 39. Log superficial velocity versus log porosity for 16-18 mesh aluminum metal punchings

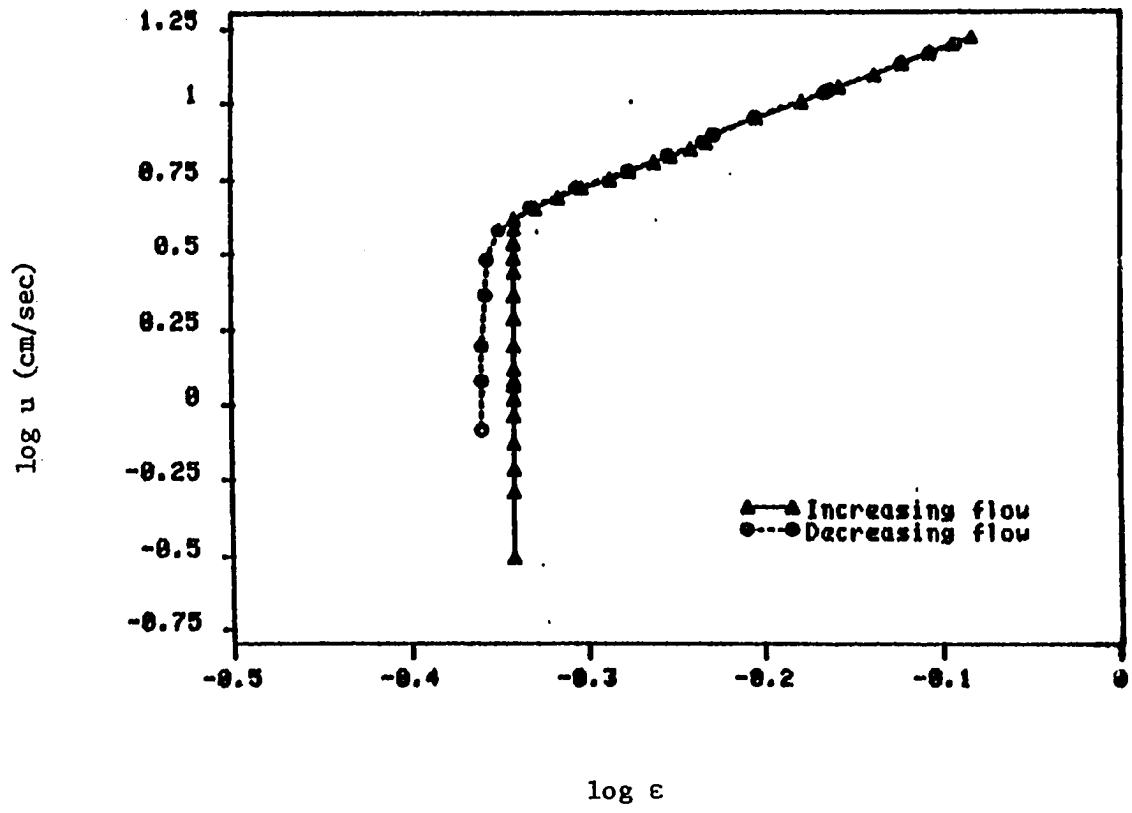

Figure 40. Log superficial velocity versus log porosity for 5-6 mesh silica sand

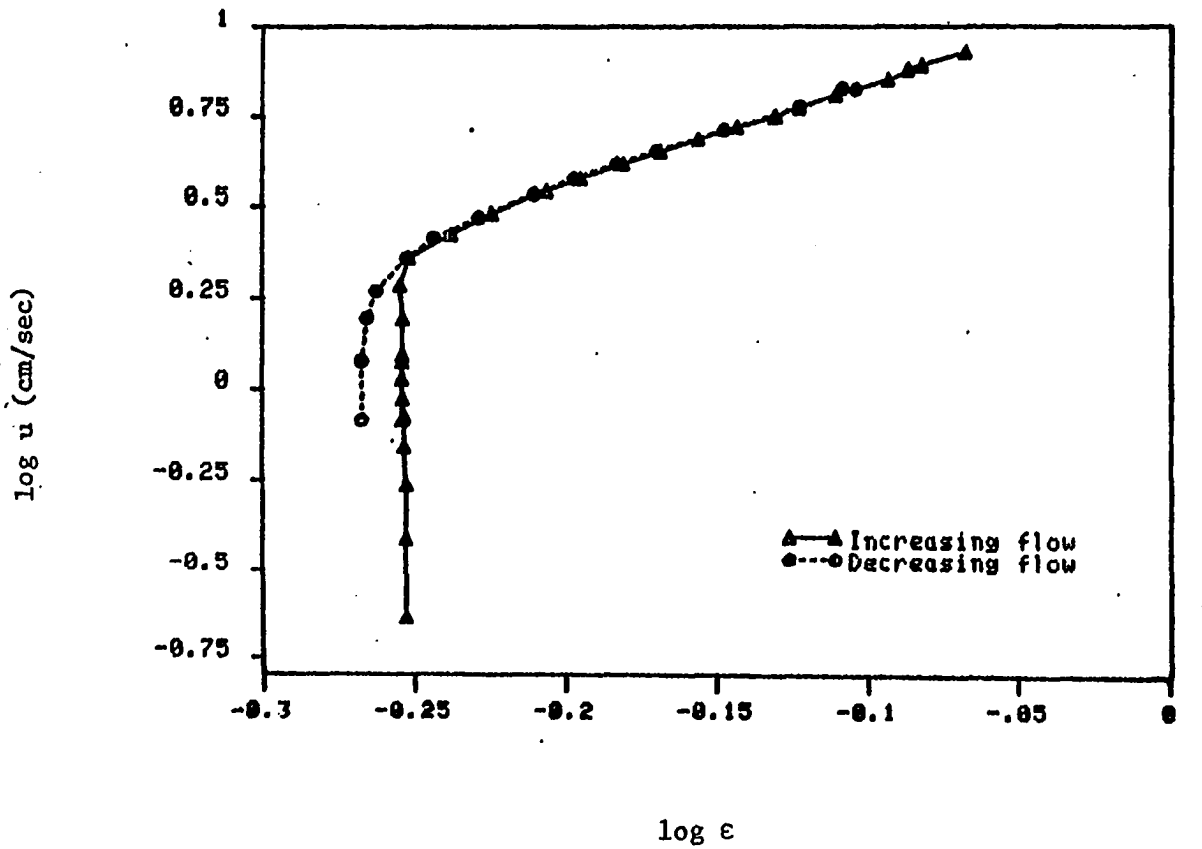

Figure 41. Log superficial velocity versus log porosity for 5-6 mesh MS-20 coal

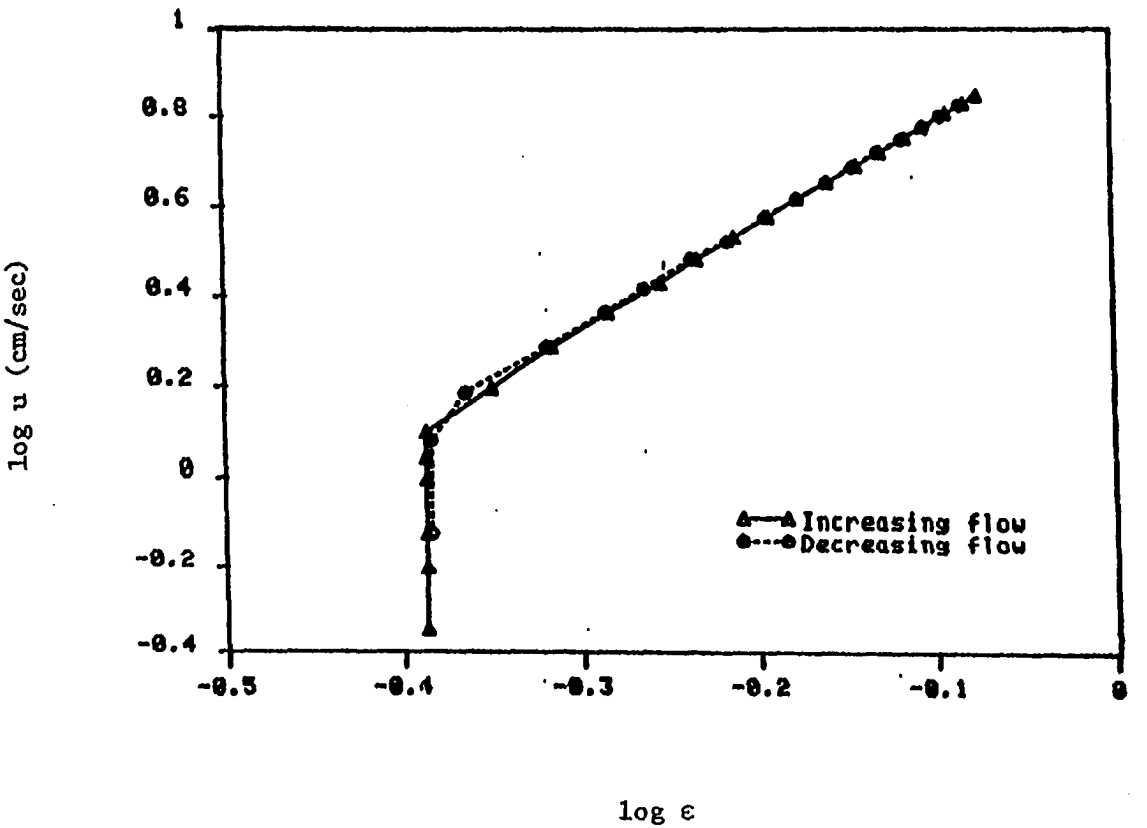

Figure 42. Log superficial velocity versus log porosity for 7-8 mesh Polyester PET 7352

Analysis

Equivalent spherical diameter and mean sieve diameter

The equivalent spherical diameter is always higher than the mean sieve diameter (d_m or d_{gm}) except for stainless steel and aluminum punchings. Most of the material presented in Table 10 show very close agreement between equivalent spherical diameter and mean sieve diameter. The exceptions are Poly PET 7352, Poly PETG 6763 and Cullsan P. These three materials show a difference of about 15 percent between deg and d_m or d_{gm}.

Settling velocities

The settling velocities for each material were determined at two different temperatures. Table 13 presents the mean settling velocities at two different temperatures. By examining this table, one sees that the standard deviation of settling time for coal is higher than that for any other material. Among the manufactured particles studied, Cullsan P showed the highest standard deviation for settling time. The deviation of settling time is proportional to the amount of particles which are out of specified size range as well as to the various shapes of the particle in the sample. Although Polyester PETG 6763 and Cullsan P are manufactured particles, the length of the particles were not uniform even after sieving. This may explain why even these particles had a moderate standard deviation for settling time.

Theoretically, the settling velocity should be higher at a higher temperature, and the difference in settling velocity should decrease

with increasing particle Reynolds number. Polyester 6763 and coal 7-8 showed slightly lower settling velocities at higher temperatures, this error is probably due to errors involved in determining the settling time or because of the range of settling time recorded. At higher temperatures, all particles except brass 35-40, coal 7-8, and coal 8-10, followed a helical path of descent. In this case, the actual velocity of the particle along the particle trajectory is greater than the value computed by assuming a straight line descent. This also could account for any discrepancy in settling velocity determined at higher temperatures.

Table 14 shows the settling velocity adjusted to 25° C. These settling velocity adjustments were made by assuming DSF at the temperature of measurement is equal to DSF at 25° C. The settling velocity determined near 25° C was used in these calculations. This assumption basically boils down to assuming $\left(\frac{u_t}{u_N}\right)_{t°C} = \left(\frac{u_t}{u_N}\right)_{25° C}$. This assumption may not be valid over a wide range of temperatures, but for small temperature difference, the error involved is small.

Table 15 shows the DSF and Ω shape factor for different materials at the two temperatures at which settling velocities were determined. The variation of DSF and Ω shape factors at the two temperatures are within 5 to 8 percent. Sand 5-6, sand 6-7, and coal 5-6 showed an increase in DSF with temperature while the rest showed a decrease in DSF with temperature. In case of Ω shape factor, only brass 35-40 metal punchings showed an increase with temperature, all the others showed a decrease with increasing temperature. Theoretically, as it

was shown in the literature review section, as the particle Reynolds number increases both DSF and Ω should decrease or remain the same depending on Reynolds number regime. The increase in DSF or Ω with temperature observed results from the uncertainties involved in determining the settling velocity accurately. Nevertheless, the variation is less than 10 percent for an increase of 10 to 15° C and as it will be shown later in this section, such a high precision is not warranted for DSF or Ω in the prediction model. Akkoyunlu (2) assumed a linear decrease in DSF with increase in particle size for sand and coal. This approximation is reasonable only if the particle Reynolds number falls within a certain range, since both DSF and Ω reach a asymptotic constant value at high and low particle Reynolds numbers. Figure 43 reproduced from Schulz et al. (95) shows the variation of $1/\Omega$ with Reynolds number. Note that the curved lines in this figure represent lines of equal shape factor (SF). This figure shows the lower S.F., the wider the Reynolds number range over which Ω changes.

Sphericity

For each material, 5 different sphericity values were calculated. Four from air permeability measurements and one from fixed bed data of the water fluidization experiments. In the air permeability method, as shown in Table 17, the sphericity values obtained from the intercept of $\frac{\Delta P}{Lu}$ vs. G plot for each material in the loosely packed bed and tightly packed, did not differ significantly except for Polyester 7352 and coal 8-10. Further, the coefficient k_2 (based on the slope of this plot) is much different from 0.292 proposed in equation 45 for different sizes of coal and Polyester 6763. Ergun (42) himself

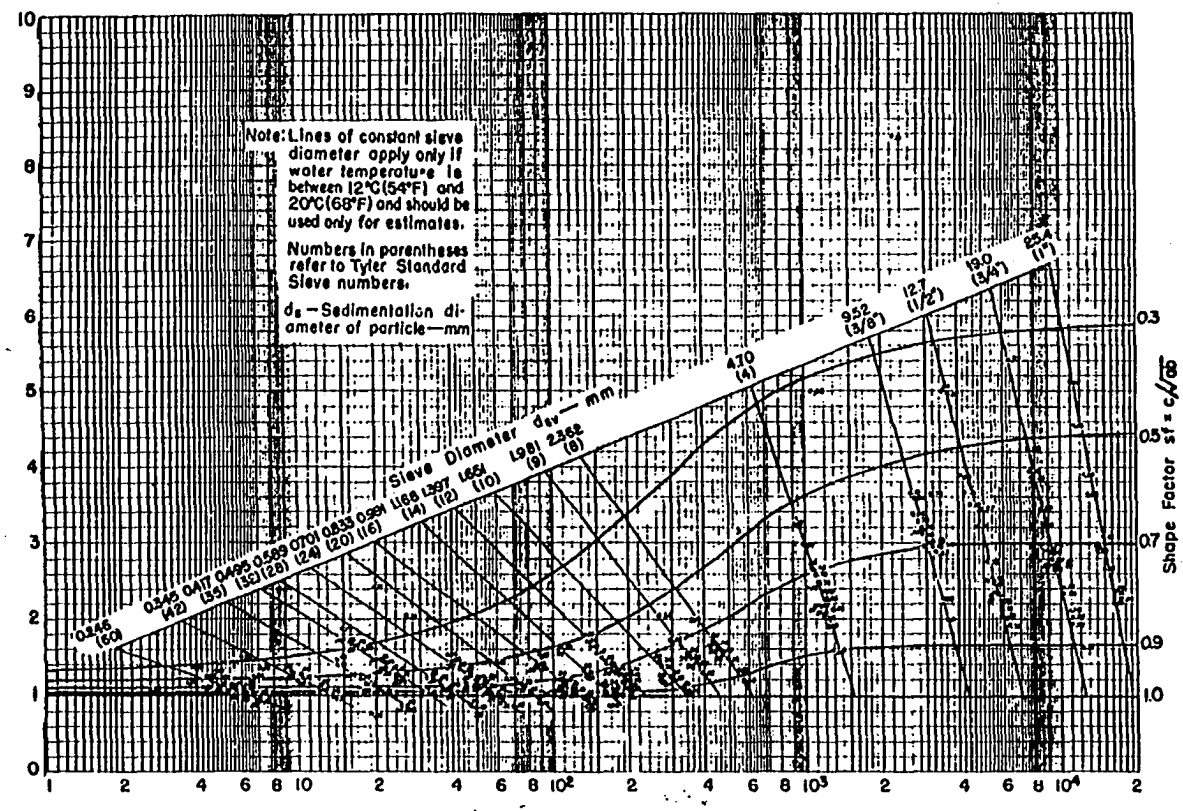

Figure 43. The relationship between $1/\Omega$ and particle Reynolds number, Re_t, at constant shape factor S.F. (95)

suggested this value should be adjusted to 0.48 to yield consistent values for sphericities calculated either from the intercept or the slope of $\frac{\Delta P}{Lu}$ vs. G plot for crushed porous solids.

With the limited air permeability data of Table 17, no definite conclusion can be reached as to how coefficient k_2 should be changed for different shaped materials. Nevertheless, it appears advisable to calculate the sphericity from the intercept of $\frac{\Delta P}{Lu}$ vs. G plot rather than the slope since k_2 was rather variable. The sphericities obtained from the intercept for the loosely packed bed and the tightly packed bed show very close agreement for all materials except for Polyester PET 7352 and mesh 8-10 MS-20 coal.

The sphericity obtained by back calculating from the air permeability data using Ergun equation 45a, for the loosely packed bed data and the tightly packed bed data show close agreement for all material except for Polyester PET 7352. The average sphericity thus obtained for each material is not significantly different from the sphericity obtained from the intercept of $\frac{\Delta P}{Lu}$ vs. G for that material. Thus, both methods using air permeability data are about equivalent. The first method (intercept of $\frac{\Delta P}{Lu}$ vs. G) is more amenable to manual calculation.

The sphericities obtained from the fixed bed data of the water fluidization experiments are also in close agreement with the values obtained from air permeability measurements. The exceptions are Polyester PETG 6763 and Cullsan P. For these materials, the water permeability data yield a higher value for sphericity than the air permeability

data.

The sphericities for metal punchings and Polyester PET 7352, calculated from the geometric dimension given by the supplier are as follows:

Material	Sphericity
Brass 35-40	0.916
Stainless steel 16-18	0.826
Aluminum 16-18	0.888
Polyester 7352 (cube)	0.806

These values indicate that the sphericity values obtained from air permeability method or water permeability method are generally within 5 to 10 percent of the actual value obtained from the geometric dimensions. Although no general conclusion can be reached with this limited verification it can be said the sphericity values obtained by permeability data are not accurate to 3 decimal places.

Minimum fluidization velocities

The minimum fluidization velocity of each material determined experimentally is shown in Table 19. Also shown in Table 19 are the minimum fluidization velocities predicted by the Wen and Yu equations, 71 and 74, Bena et al. (17), equation 75 and Beranek (18) equation 78. By far, the most simplistic and easiest to use is equation 74. Except for Flintag 18-22, Flintag 25-30 and U.K. anthracite 25-30 (data obtained from Cleasby and Fan (32)) u_{mf} predicted by equation 74 are not significantly different from that predicted by equation 71. The advantage in using 74 compared to equation 71 is that no values of ε_{mf}

and sphericity (ψ) are required. For the material presented in Table 19, Bena et al. (17) equation 75 and Beranek (18) equation 78 are not as accurate as the Wen and Yu equations for predicting u_{mf}.

For sand 5-6 and sand 6-7, the u_{mf} predicted by equation 75 and 78 are way off. From Table 19, it is seen that Wen and Yu equation 71 generally predicts better than equation 74. Equation 74 resulted in a few values of u_{mf} at low flow rates which differed substantially from the measured values. The better prediction obtained with equation 71 may be partly due to the fact that the experimental data was used to compute the ψ value from the Ergun equation, and the Ergun equation is used in development of equation 71. In general, if good values of ψ and loose bed ε_{mf} are available, equation 71 would be preferred to equation 74.

Prediction Model Based on Blakes Modified Reynolds Number

In this section, a prediction model to predict the velocity-voidage relationship during liquid fluidization will be developed using the modified Reynolds number and a voidage function dependent on the Galileo number and porosity of the bed.

A fluidized bed system is considered to be fully defined by the following eight quantities:

	Notation	Dimension
Superficial velocity	u	LT^{-1}
Fluid density	ρ	ML^{-3}
Fluid viscosity	μ	$ML^{-1}T^{-1}$

Particle density	ρ_s	ML^{-3}
Particle specific surface (characteristic dimension)	S	L^{-1}
Voidage of the bed	ε	None
Acceleration due to gravity	g	LT^{-2}
For non-spherical particle, a shape factor	ψ, DSF or Ω	None

Since there are eight quantities and three dimensions, five dimensionless groups may be written. The relationship between these groups cannot be inferred and therefore must be found by experiment. Five possible dimensionless groups are:

$$\frac{g}{Su^2} , \frac{\rho u}{S\mu} , \frac{\rho_s - \rho}{\rho} , \varepsilon, \psi$$

If a fluidized bed system can be fully described by these eight quantities, then a unique relationship can be established by plotting the five dimensionless groups. Such a procedure would be very unwieldly and attempts must be made to simplify it by choosing fewer non-dimensional groups.

As shown in equation 39, the linear dimension is taken as

$$\underset{\sim}{d} = \frac{\varepsilon}{S(1 - \varepsilon)}$$

and the characteristic velocity is taken as the average interstitial velocity

$$\underset{\sim}{u} = u/\varepsilon .$$

The modified Reynolds number $Re_1 = \frac{u}{\varepsilon} \cdot \frac{\varepsilon}{(1 - \varepsilon)S} \cdot \frac{\rho}{\mu}$

$$= \frac{\rho u}{S\mu(1 - \varepsilon)}$$

To correlate the pressure drop through fixed beds, Blake (20) and Carman (27) used the modified Reynolds number Re_1 and the following voidage function ϕ_1. A function based on this ϕ_1 will be used to correlate the fluidization data in this method.

$$\phi_1 = \frac{\Delta P}{L} \cdot \frac{g}{S\rho u^2} \frac{\varepsilon^3}{1 - \varepsilon} \tag{148}$$

In fluidized beds

$$\frac{\Delta P}{L} = (\rho_s - \rho)(1 - \varepsilon)g \tag{149}$$

Substituting equation 149 in 148.

$$\phi_1 = (\rho_s - \rho)(1 - \varepsilon) \frac{g}{S\rho u^2} \cdot \frac{\varepsilon^3}{1 - \varepsilon}$$

$$\phi_1 = \frac{g(\rho_s - \rho)}{S\rho u^2} \varepsilon^3 \tag{150}$$

Since ϕ_1 and Re_1 contain u, it is desirable to define a new function Al which is not a function of u. Al is defined as follows

$$Al = \phi_1 \times Re_1^2$$

$$= \frac{g(\rho_s - \rho)\varepsilon^3}{S\rho u^2} \quad \frac{u^2\rho^2}{S^2\mu^2(1 - \varepsilon)^2}$$

$$Al = \frac{\varepsilon^3}{(1-\varepsilon)^2} \frac{\rho(\rho_s - \rho)g}{S^3 \mu^2} \tag{151}$$

How the functions Al and Re_1 could be used to correlate the fluidization data will be considered next.

Log Al was plotted against log Re_1 for data obtained by different investigators including the data obtained during the experimental investigations reported herein. Since S appears in both Al and Re_1, a suitable definition of S must be selected. For spherical particle,

$$S = \frac{6}{d}$$

where d = diameter of the spheres.

For non-spherical particles, 3 different shape factors were tried:

(a) Sphericity

$$S = \frac{6}{\psi . d_{eq}}$$

(b) Dynamic shape factor (DSF).

$$S = \frac{6}{DSF . d_{eq}}$$

(c) Hydraulically equivalent diameter shape factor (Ω).

$$S = \frac{6}{\Omega . d_{eq}}$$

Figure 44 shows the plot of log Al vs. log Re_1 for the data obtained in the present experiments if the shape factor used is ψ. If the model is adequate and if the shape is adequately described by the shape factor used, the data for various shaped materials should plot on a single line (i.e. the scatter will be minimized).

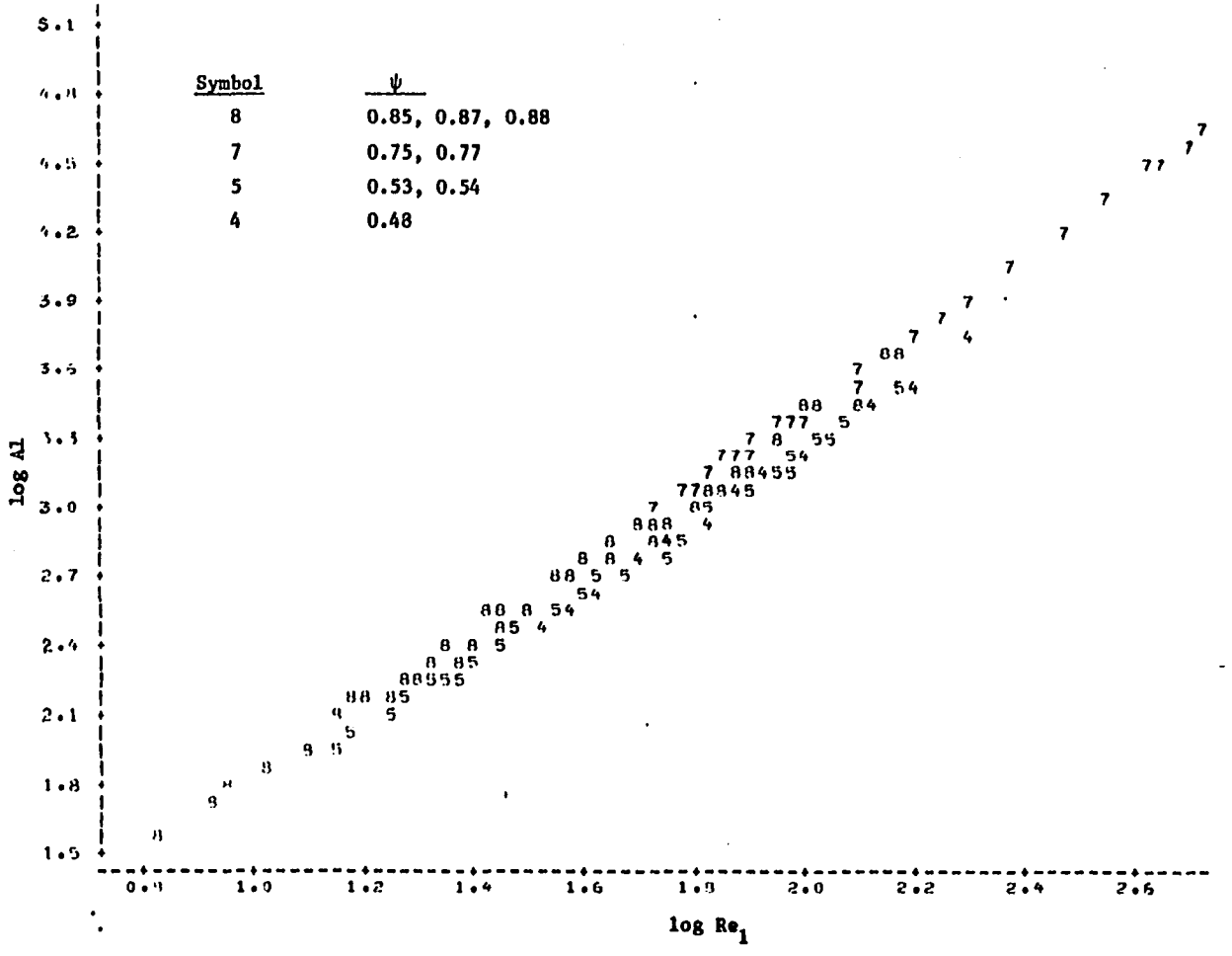

Figure 44. The relationship between log Al and log Re_1 for the data of present experiments. The shape factor is ψ

However, even for spherical particles, the data show some scatter as illustrated by Figure 45. The relative degree of scatter in 44 and in subsequent figures can be compared with Figure 45 for a visual impression of the adequacy of the shape factor used in each figure.

The fluidization data obtained for metal punchings, brass 35-40, and stainless steel 16-18 were omitted in Figure 44 since these data plotted far away from the rest of the data. This is probably because the fluidization of these two materials was not particulate. The criterion used by Davidson and Harrison (36) as given in equation 66 can be used to check whether the fluidization of these materials would be expected to be particulate or not.

Brass 35-40:

$$\frac{D_M}{d_{eq}} = \frac{u_t^2}{0.5\, g\, d_{eq}} \left[\frac{\left(\frac{\rho_s}{\rho_s - \rho}\right) - \varepsilon_{mf}}{1 - \varepsilon_{mf}} \right]$$

$$= \frac{(18.18)^2}{0.5 \times 981 \times 0.0475} \left\{ \frac{\frac{8.55}{8.55 - 0.997} - 0.426}{(1 - 0.426)} \right\}$$

$$= 17.45.$$

If $\frac{D_M}{d_{eq}} > 10$ aggregative fluidization is expected.

Stainless steel 16-18:

$$\frac{D_M}{d_{eq}} = \frac{(22.27)^2}{0.5 \times 981 \times 0.0956} \left\{ \frac{\frac{7.78}{7.78 - 0.998} - 0.444}{(1 - 0.0444)} \right\}$$

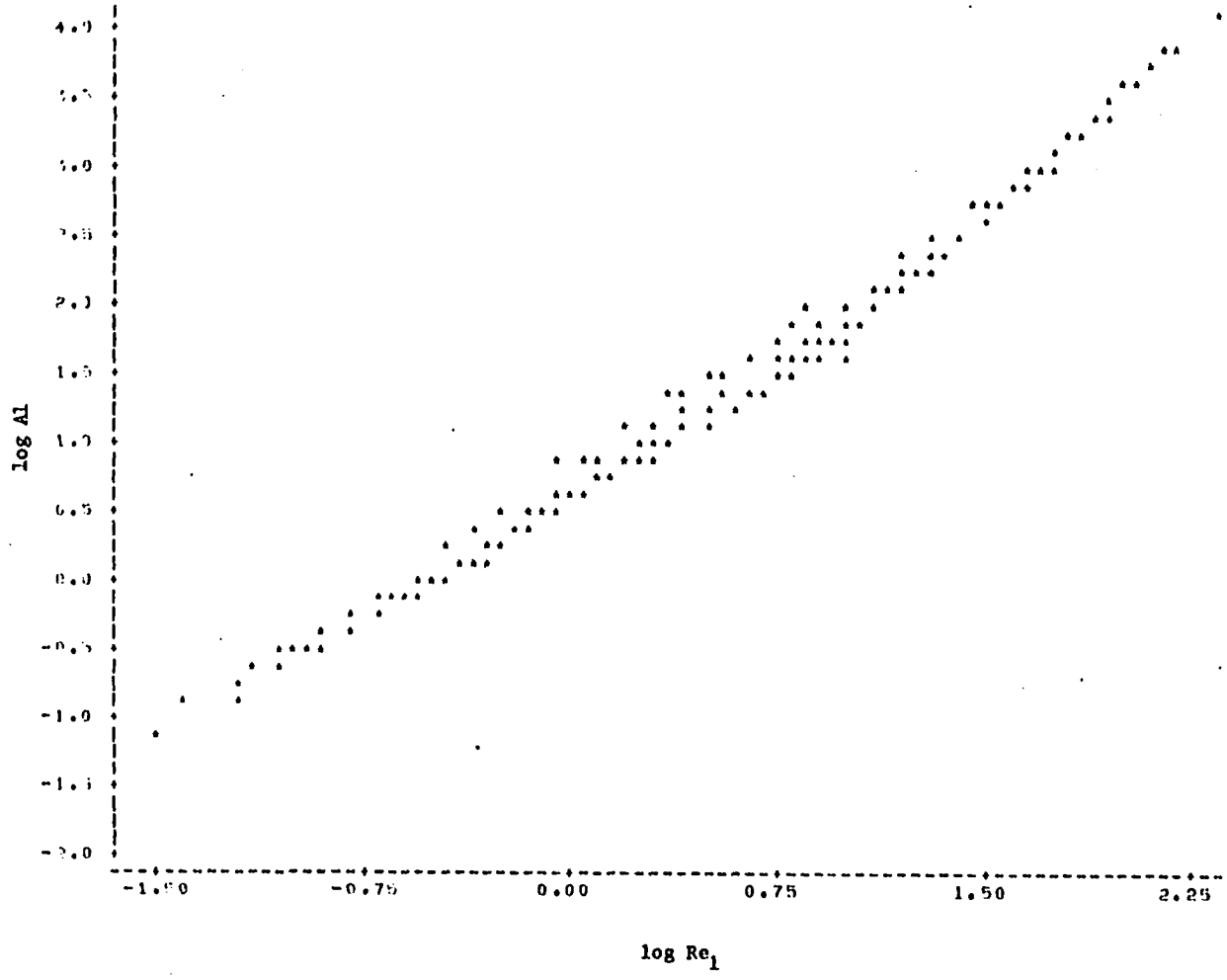

Figure 45. The relationship between log A1 and log Re_1 for the spherical particle data of Loeffler (76)

$$= 13.37.$$

Since $\frac{D_M}{d_{eq}} > 10$ the fluidization is expected to be aggregative.

The same criterion will be used to check the fluidization of aluminum 16-18, and sand 5-6.

Aluminum 16-18:

$$\frac{D_M}{d_{eq}} = \frac{(13.76)^2}{0.5 \times 981 \times 0.109} \quad \frac{\{\frac{2.7345}{(2.7345-0.997)} - 0.442\}}{(1 - 0.442)}$$

$$= 7.18.$$

Sand 5-6:

$$\frac{D_M}{d_{eq}} = \frac{(27.4)^2}{0.5 \times 981 \times 0.3749} \quad \frac{\{\frac{2.646}{(2.646 - 0.997)} - 0.455\}}{(1 - 0.455)}$$

$$= 8.61.$$

Since $\frac{D_M}{d_{eq}}$ is between 1 and 10 fluidization is in the transitional region i.e., not strictly particulate nor aggregative.

Figure 45 shows the Loeffler data (76) for spherical particles, when plotted log Al against log Re_1. One can see some scatter in the data points. This scatter is probably due to high d/D_T ratios, because the fluidization was carried out in a column of only 2.6 cm in diameter.

Figures 46 and 47 show the plot log Al vs. log Re_1 for the present experimental data with shape factors DSF and Ω, respectively.

Figures 48 through 50 show log Al vs. log Re_1 relationship for Fan's data (45) with appropriate shape factors.

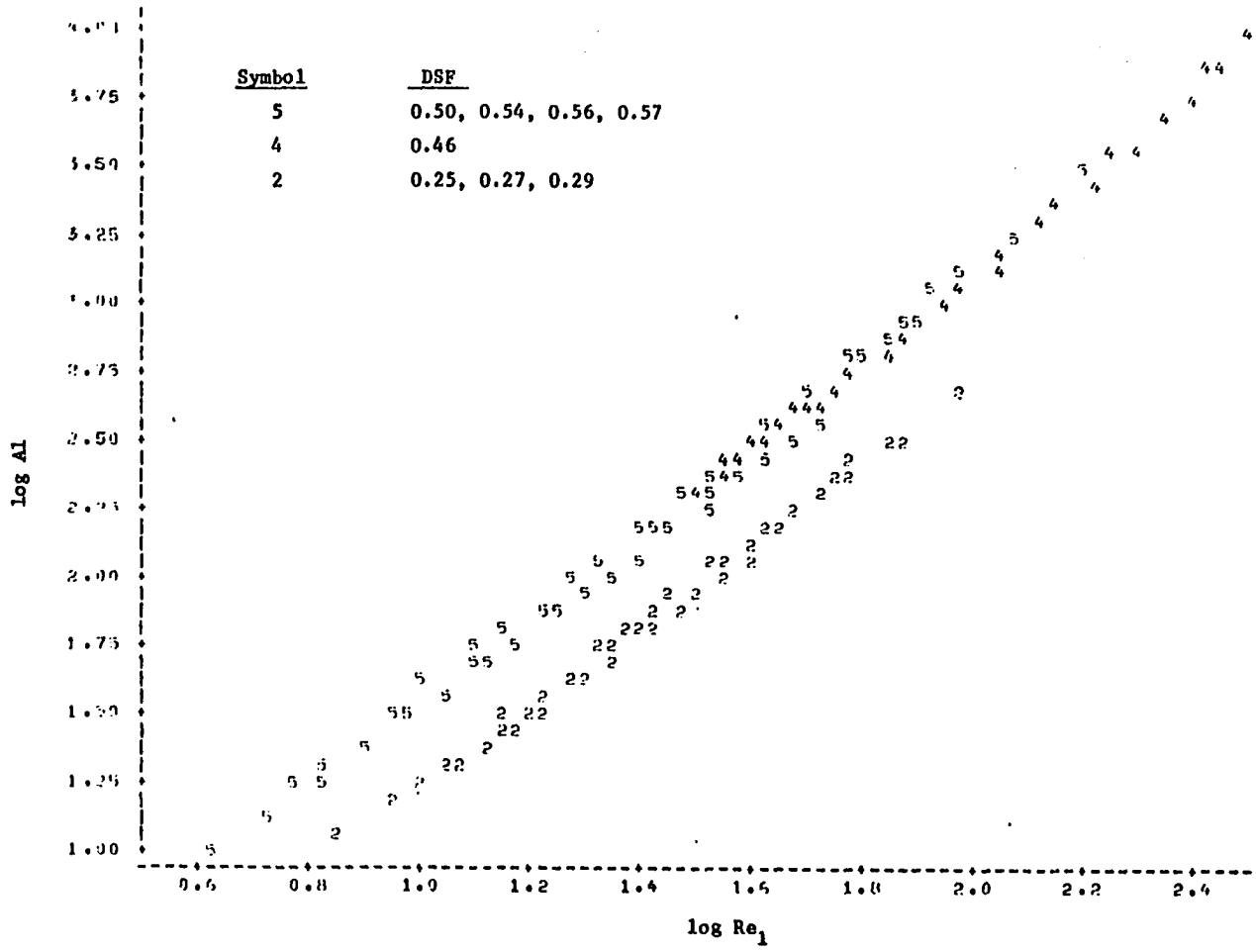

Figure 46. The relationship between log A1 and log Re_1 for the data of present experiments. The shape factor is DSF

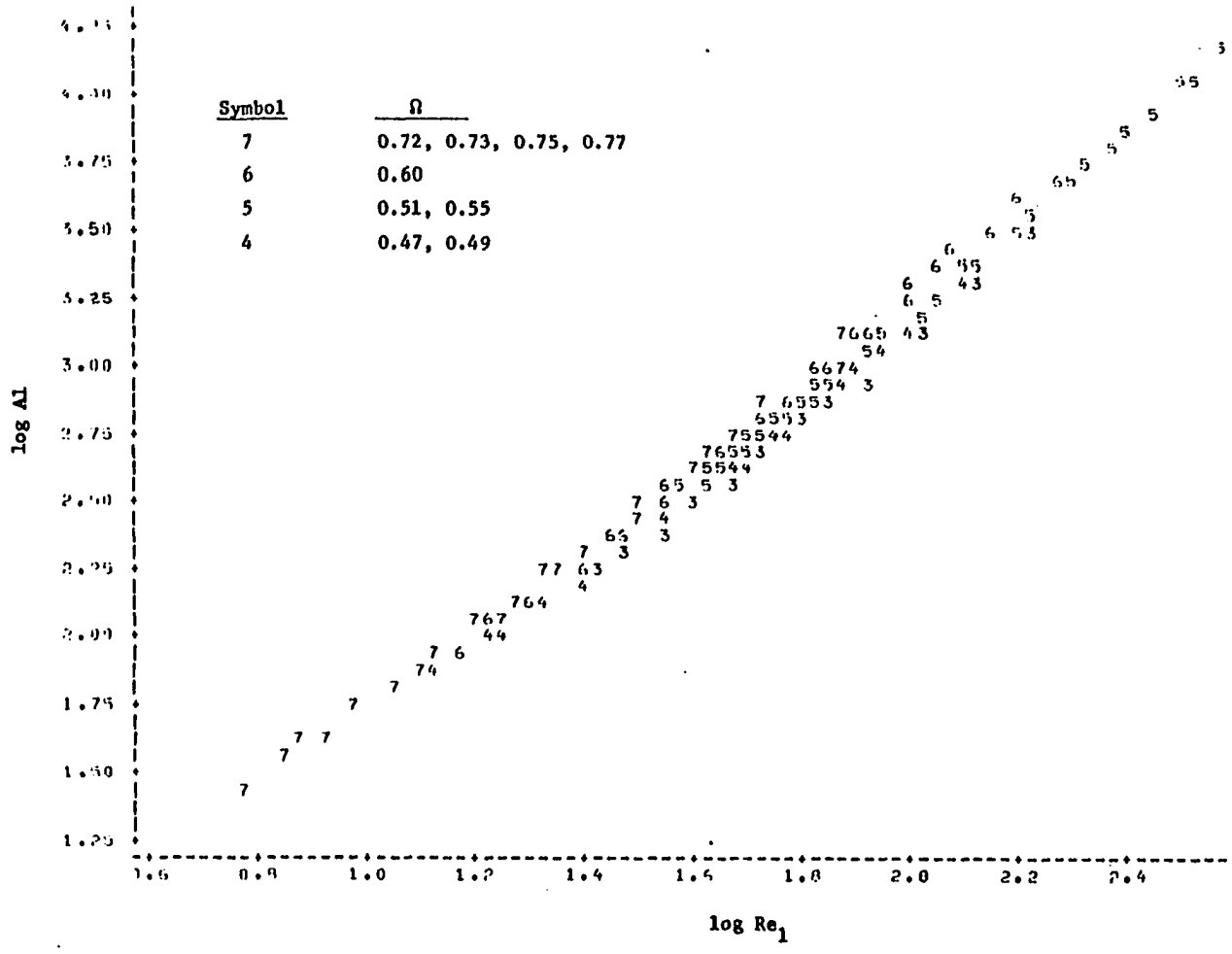

Figure 47. The relationship between log A1 and log Re_1 for the data of present experiments. The shape factor is Ω

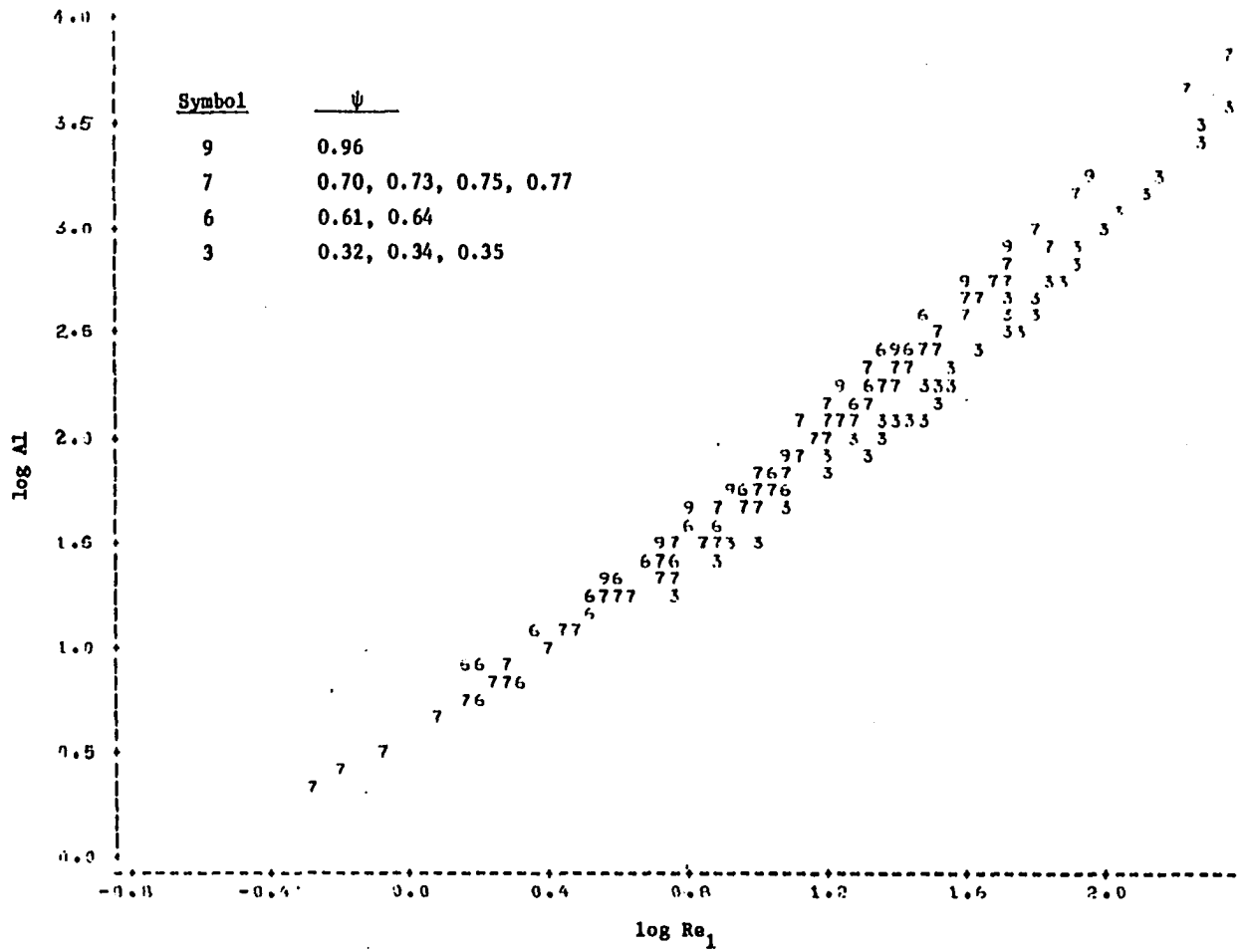

Figure 48. The relationship between log Al and log Re_1 for the data of Fan (45). The shape factor is ψ

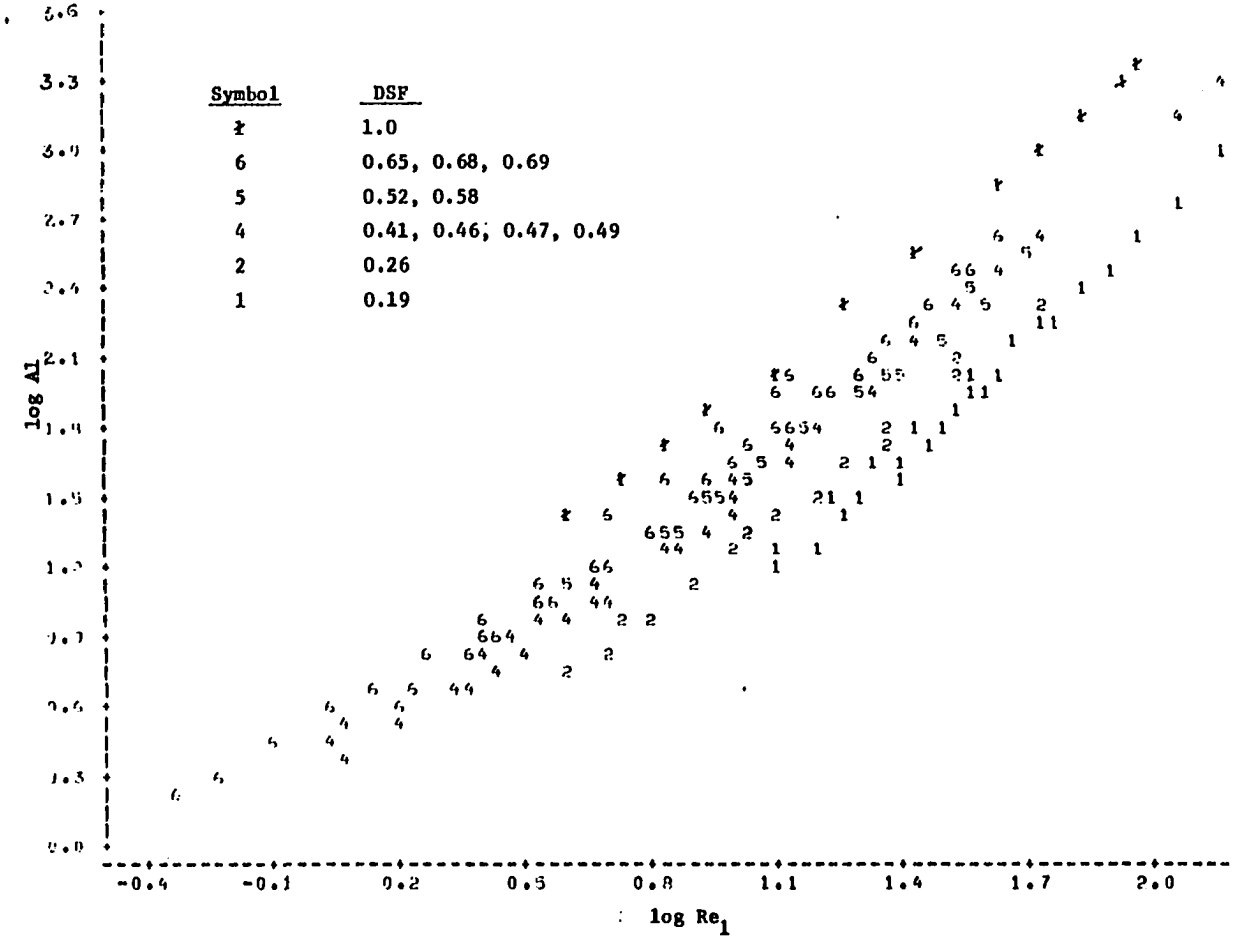

Figure 49. The relationship between log A1 and log Re_1 for the data of Fan (45). The shape factor is DSF

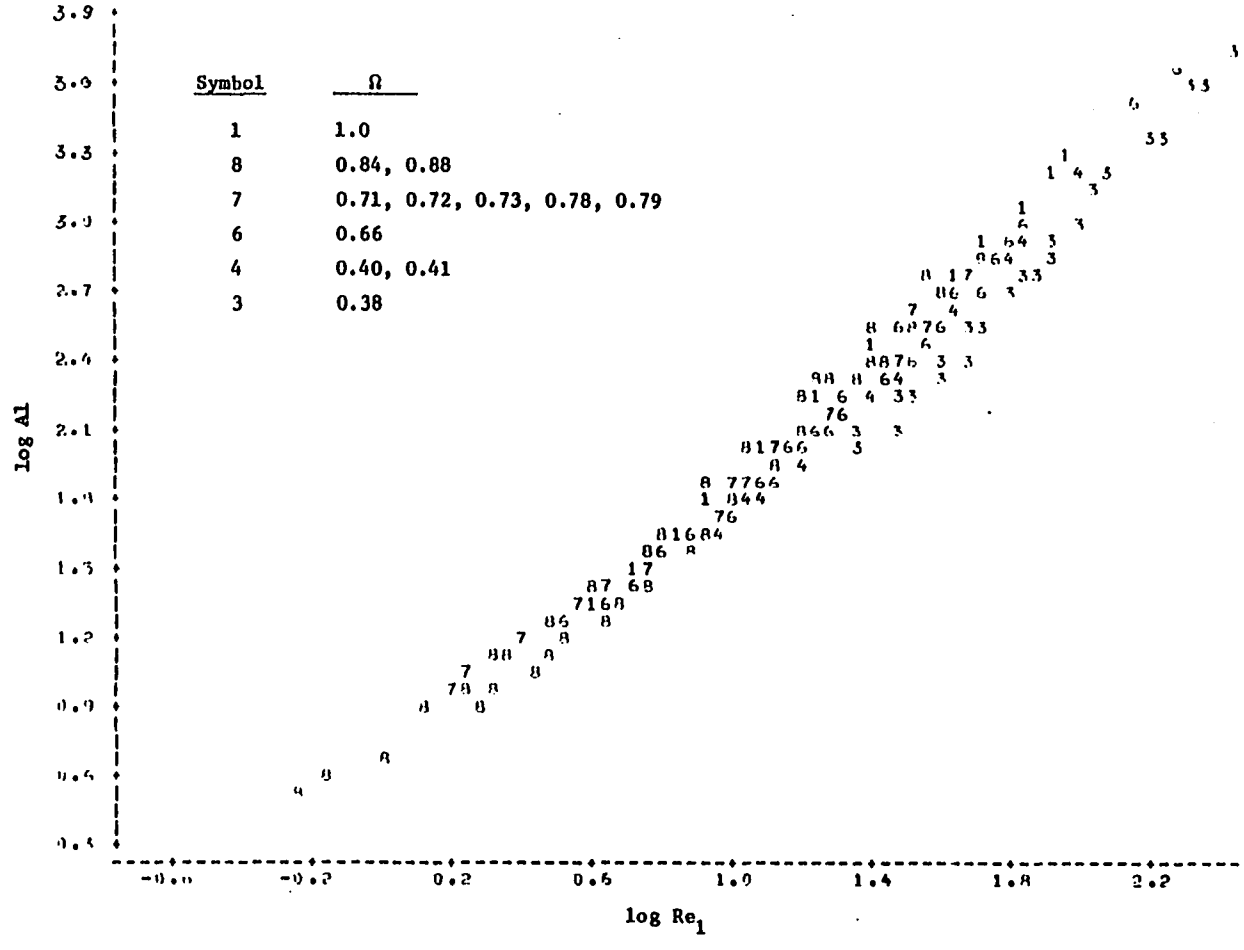

Figure 50. The relationship between log A1 and log Re_1 for the data of Fan (45). The shape factor is Ω

Figure 51 shows the data of Presler (85) when plotted log Al, against log Re_1 with ψ as shape factor.

Gunasingham et al. (57) did not measure sphericity of the material they used in their study. From the original data of Gunasingham, obtained from Graham, DSF and ψ were calculated for all the materials. Figure 52 and 53 show the data of Gunasingham et al. on the log Al vs. log Re_1 plot with DSF and ψ as shape factors, respectively.

Wilhelm and Kwauk (109) claimed all the materials they investigated were nearly spherical. From the pressure drop data they reported, the sphericity was calculated for each material from the Ergun equation 45a. Figure 54 shows the data of Wilhelm and Kwauk in log Al vs. log Re_1 plot.

By studying these figures, one notices that generally the particles with higher value for shape factor plot above the data for lower shape factors. The spread of the points is wider when the shape DSF is used in calculation of Al and Re_1.

Several types of curves were tried to describe the data on a log Al vs. log Re_1 plot. An equation of the form:

$$\log Al = a + b \log Re_1 + c(\log Re_1)^2 + d \log (\text{shape factor}) \qquad (152)$$

where shape factor = ψ, DSF or Ω was found to yield all coefficients a, b, c and d statistically significant with coefficient of determination r^2, around 0.99.

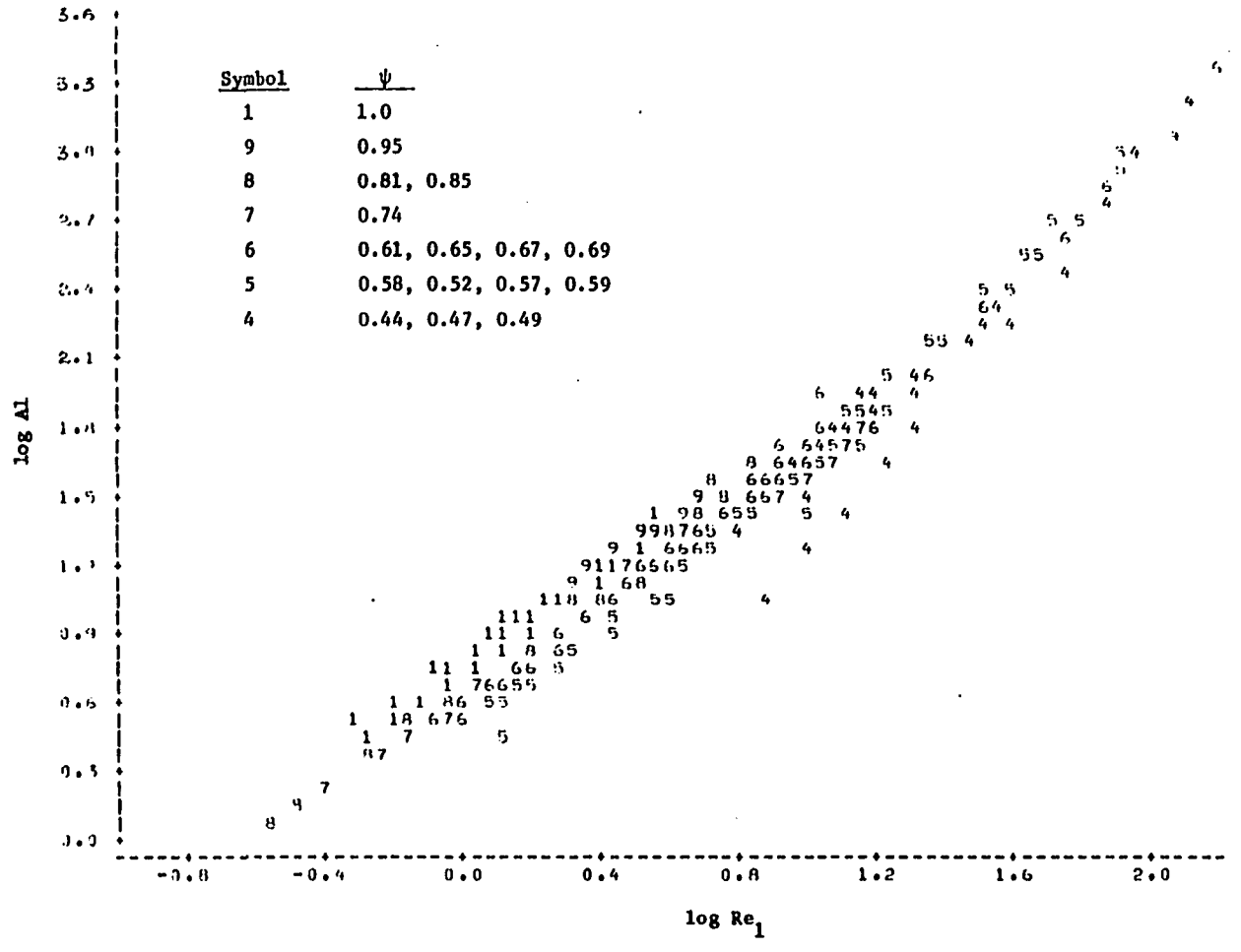

Figure 51. The relationship between log A1 and log Re_1 for the data of Presler (85). The shape factor is ψ

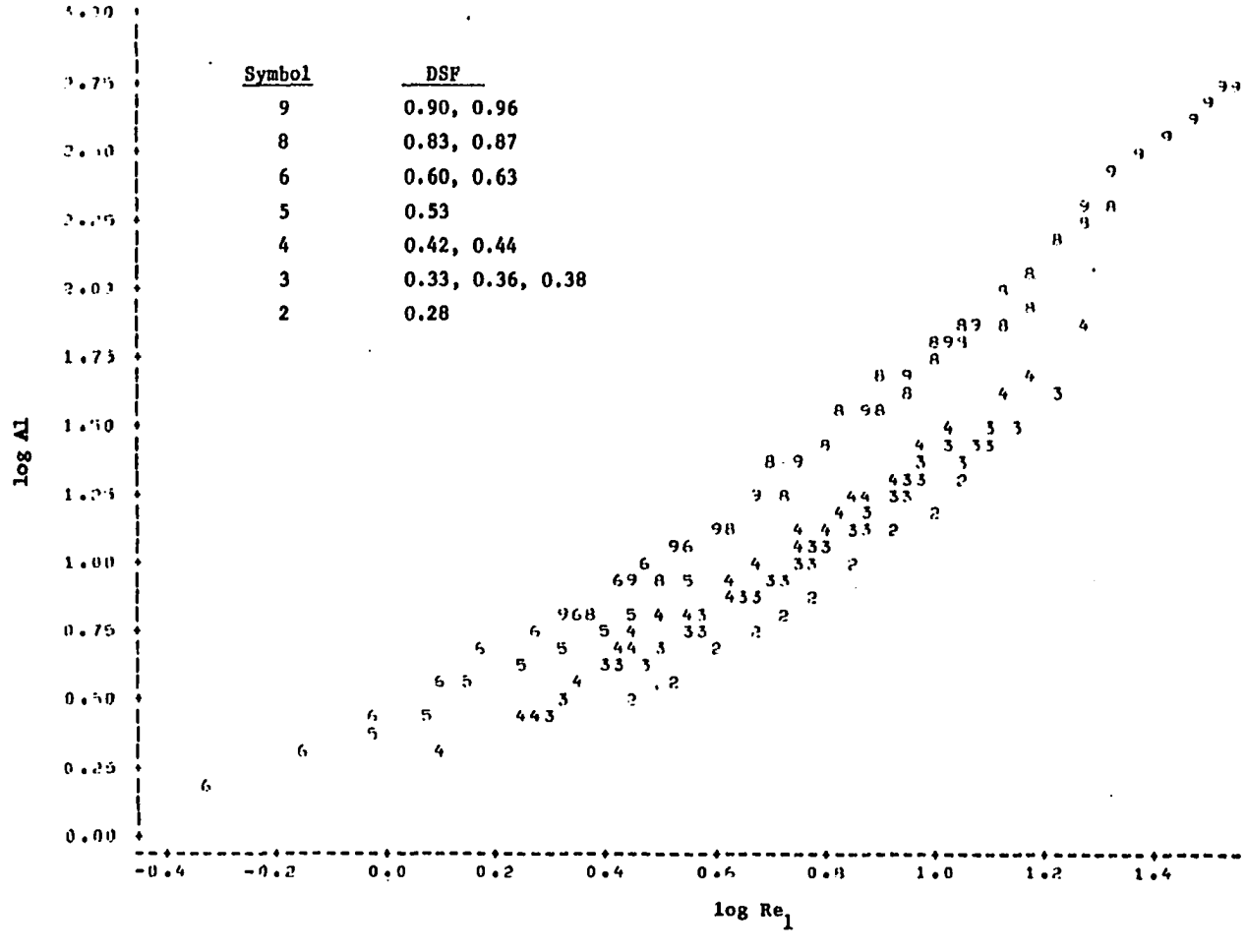

Figure 52. The relationship between log A1 and log Re_1 for the data of Gunasingham et al. (57). The shape factor is DSF

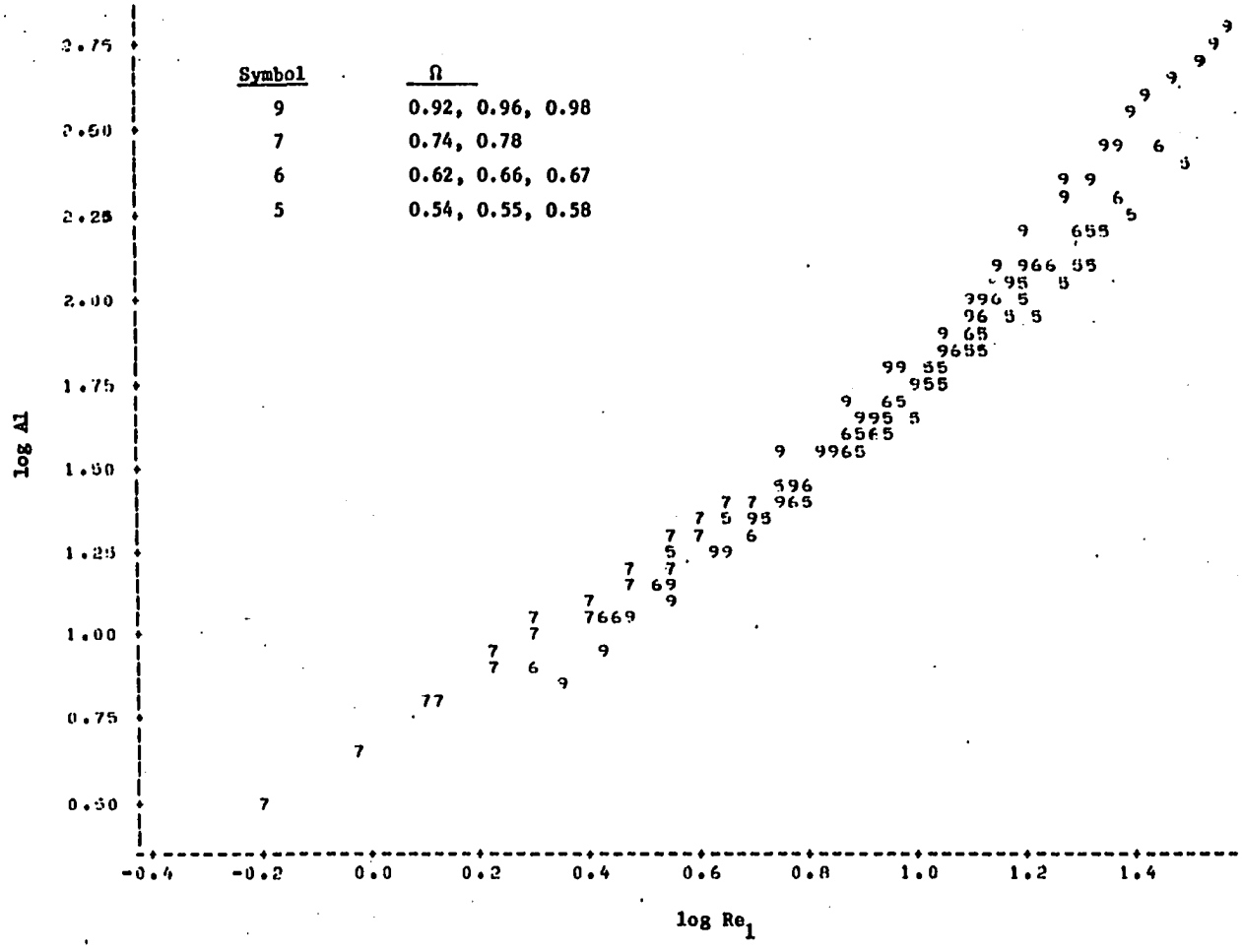

Figure 53. The relationship between log A1 and log Re_1 for the data of Gunasingham et al. (57). The shape factor is Ω

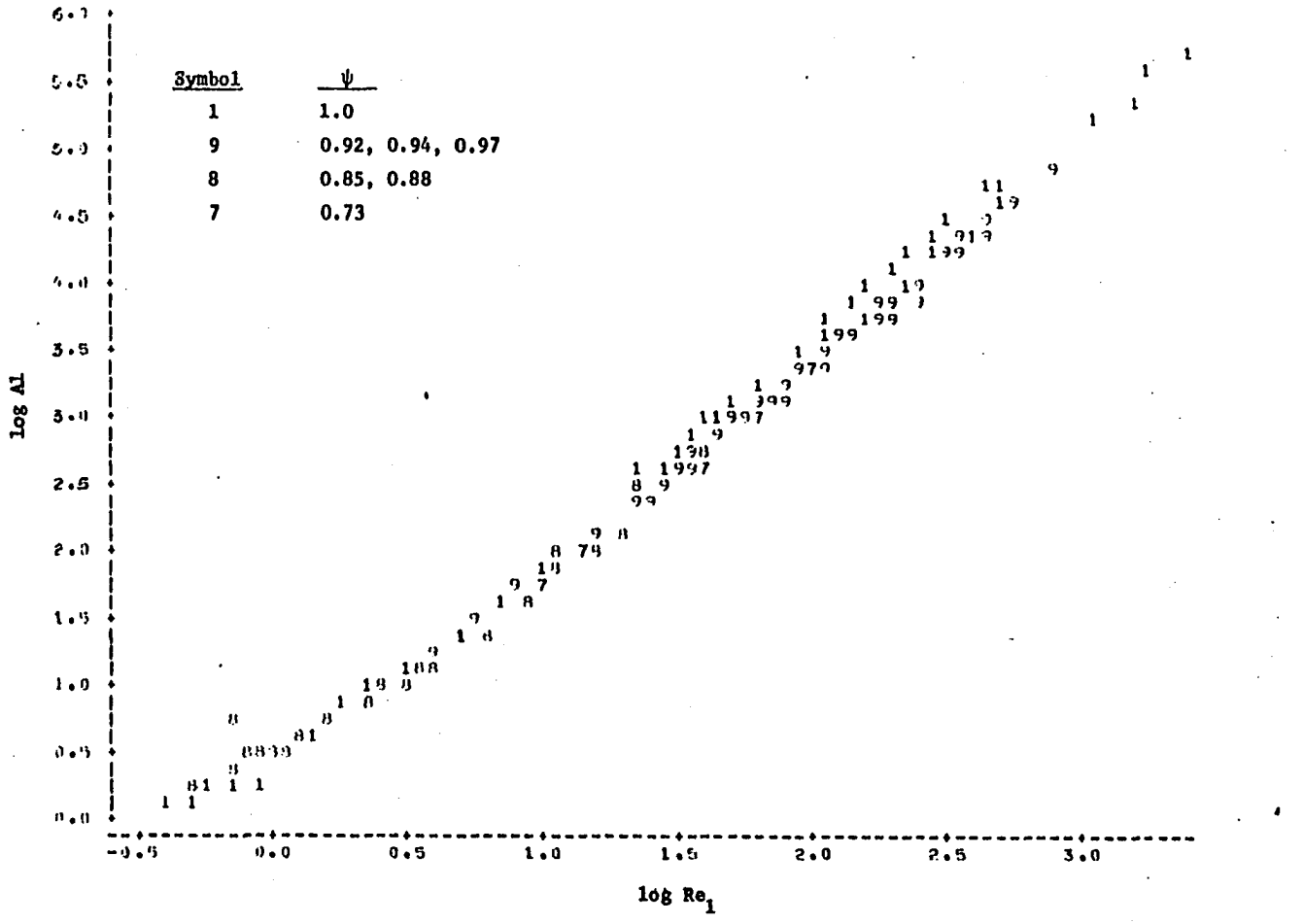

Figure 54. The relationship between log A1 and log Re_1 for the data of Wilhelm and Kwauk (109). The shape factor is ψ

In equation 152, in addition to the last term incorporating the shape factor explicitly, the term Re_1 is also a function of shape factor. Therefore, the lines describing different shape factors are not parallel in the log Al vs. log Re_1 plot.

Table 21 shows the coefficient a, b, c and d obtained for data of different investigators. When Table 21 is examined one finds that although each experimentors data yielded an equation with a high coefficient of determination (r^2), the coefficient a, b, c and d are different for each set of data. When ψ is used as the shape factor, Wilhelm and Kwauk data produced the lowest value for the intercept (a). In analyzing Presler's (85) data, since he did not measure his equivalent diameter by count and weigh method, the average of passing and retaining sieves was used as the diameter for the different size fractions of the ores he fluidized.

Equations obtained for Loeffler's (76) data, Richardson and Zaki's (92) data are for spherical particles and any equation for non-spherical particle should be checked against these equations for effectiveness of shape correction factor. However, these equations should not be used as absolute standard since for Loeffler's (76) data, the d/D_T ratio was high. It is probable that high d/D_T ratios may have some influence on the coefficients.

The equation obtained with the Richardson and Zaki data and the equation obtained with the data obtained in the present experiments compare reasonably well when the shape factor is ψ.

Table 21. The values of the coefficients a, b, c and d of equation 152 for data of different investigators

Investigator	a	b	c	d	Coefficient of Determination r^2
Shape factor = ψ[a]					
Present Experiments	0.655	1.157	0.124	0.7678	0.998
Fan (45)	0.714	1.016	0.153	0.800	0.994
Combined data of Fan (45) and present experiments	0.71162	1.03956	0.16572	0.900	0.995
Wilhelm and Kwauk (109)	0.552	1.303	0.0767	1.25	0.995
Presler (85)	0.754	1.010	0.131	1.00	0.990
Loeffler (76)	0.608	1.223	0.1099	-	0.995
Richardson and Zaki (92)	0.606	1.128	0.124	-	0.992
Shape factor = DSF					
Present Experiment	0.3783	1.118	0.182	0.821	0.976
Gunasingham et al.(57)	0.654	0.770	0.395	1.011	0.995
Fan (45)	0.687	0.984	0.182	1.034	0.994
Shape factor = Ω					
Present Experiments	0.572	1.1486	0.1225	0.614	0.999
Gunasingham et al.(57)	0.756	0.708	0.370	0.5185	0.988
Fan (45)	0.780	0.973	0.156	0.742	0.992

[a]Sphericity values obtained from water permeability data were used.

The equations obtained when DSF or Ω is used as the shape factor do not agree well with the equations obtained with spherical particles. The coefficients obtained for data obtained in the present experiment differ significantly from the coefficients for Fan's (45) data or

Gunasingham et al. (57) data. As it was pointed out before, DSF and Ω are not geometric shape factors, and their values, are dependent on the particle Reynolds number. This indicates DSF or Ω should not be substituted for ψ as shape factor in the above approach for analyzing fluidization data.

It will be demonstrated later with Gunasingham et al. data where information on ψ is not available, by assuming reported ψ values for sand, coal and polyester, it is possible to predict velocity-voidage relationship reasonably well with equation developed with ψ as shape factor.

Since Fan's data and the data obtained in the present experiments covered a wide range of sphericity values, a combined equation was developed from these data. The combined equation is

$$\log Al = 0.71162 + 1.03956 \log Re_1 + 0.16572 (\log Re_1)^2 + 0.900 \log (\psi) \qquad r^2 = 0.995 \qquad (153)$$

The equation will be used as the prediction equation.

Since both Al and Re_1 are functions of porosity, the prediction of porosity at a given superficial velocity, will be a trial and error procedure. To eliminate the need for a trial and error solution, design curves such as shown in Figures 55 to 59 have been prepared. Each figure is for a particular ψ value and includes a family of constant porosity lines at ε = 0.45, 0.50, 0.55, 0.60, 0.65, 0.70, 0.72, 0.80, 0.85, and 0.90. Separate figures for ψ values of 0.3, 0.5, 0.7 and 1.0 are presented. The basis of these graphs is as follows.

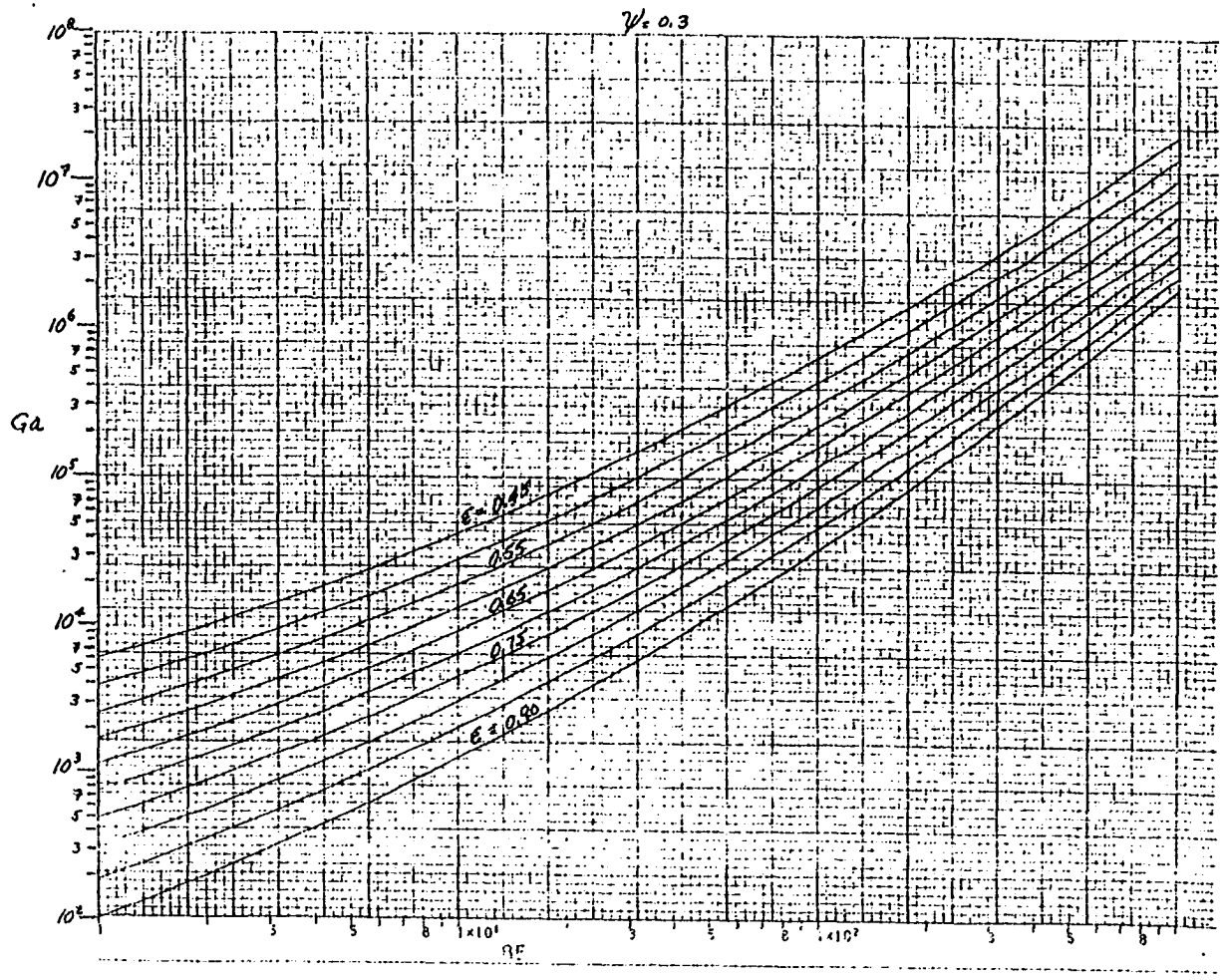

Figure 55. The relationship between Ga and Re at different expanded bed porosity for material with $\psi = 0.3$

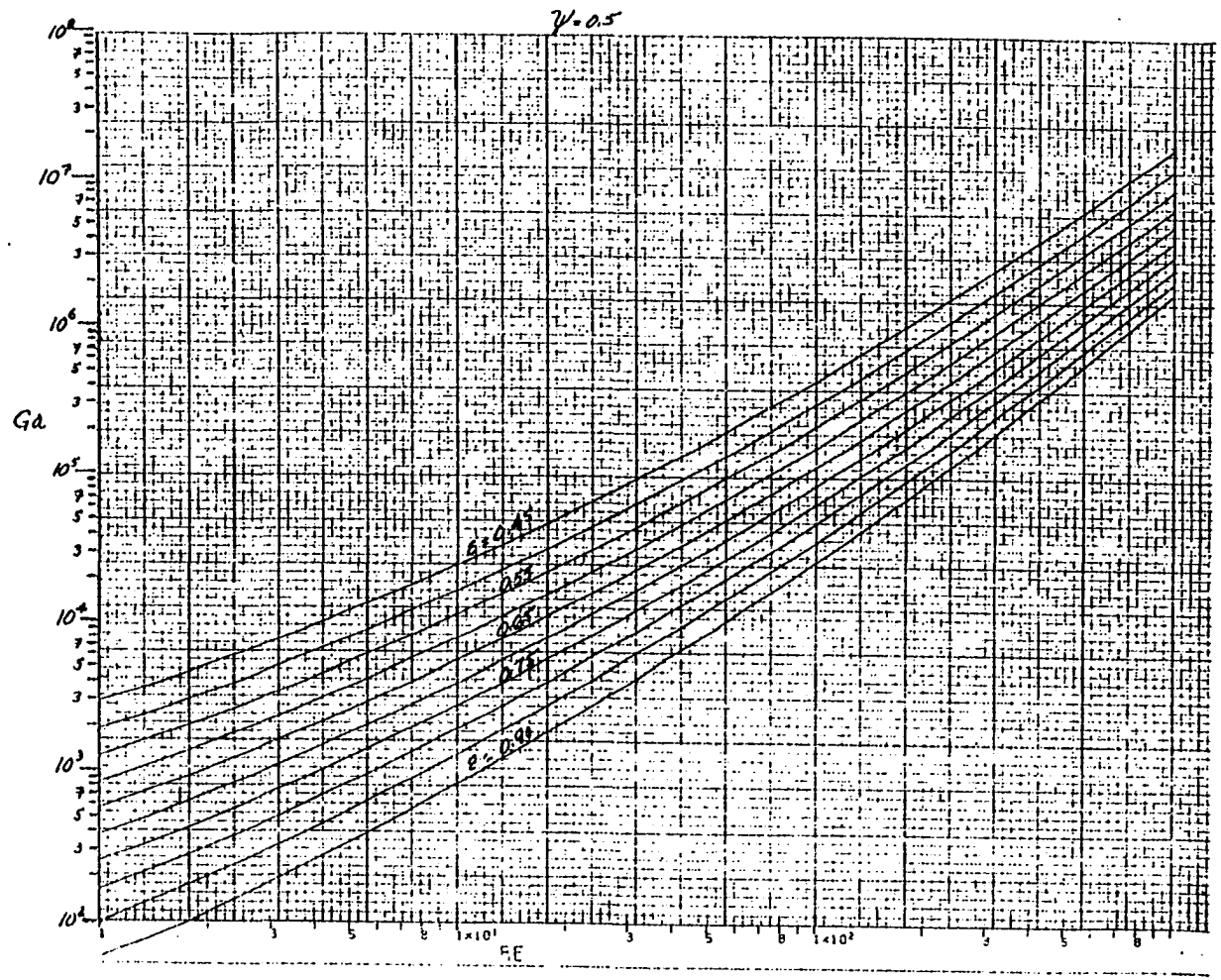

Figure 56. The relationship between log Ga and log Re at different expanded bed porosity for material with $\psi = 0.5$

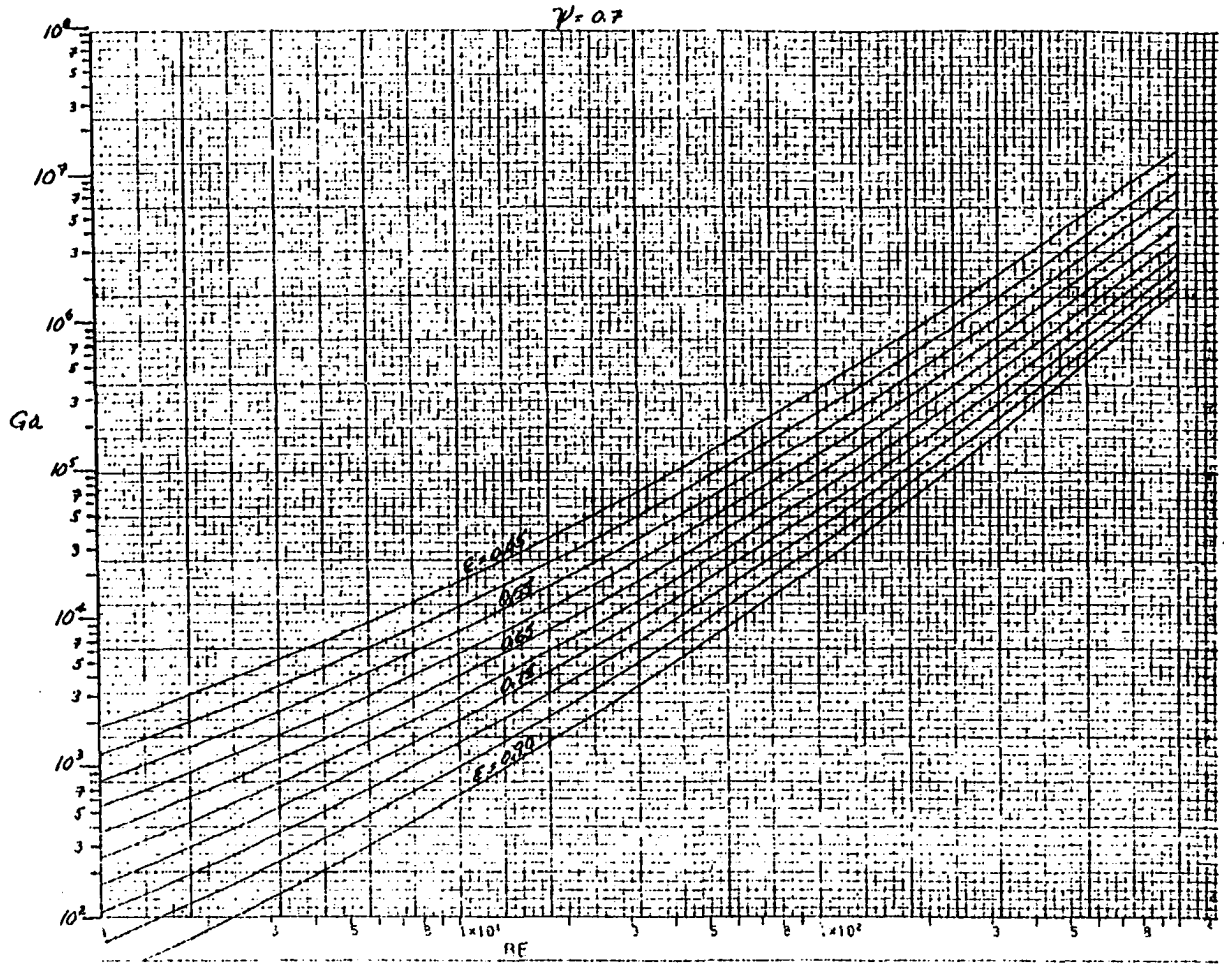

Figure 57. The relationship between Ga and Re at different expanded bed porosity for material with ψ = 0.7

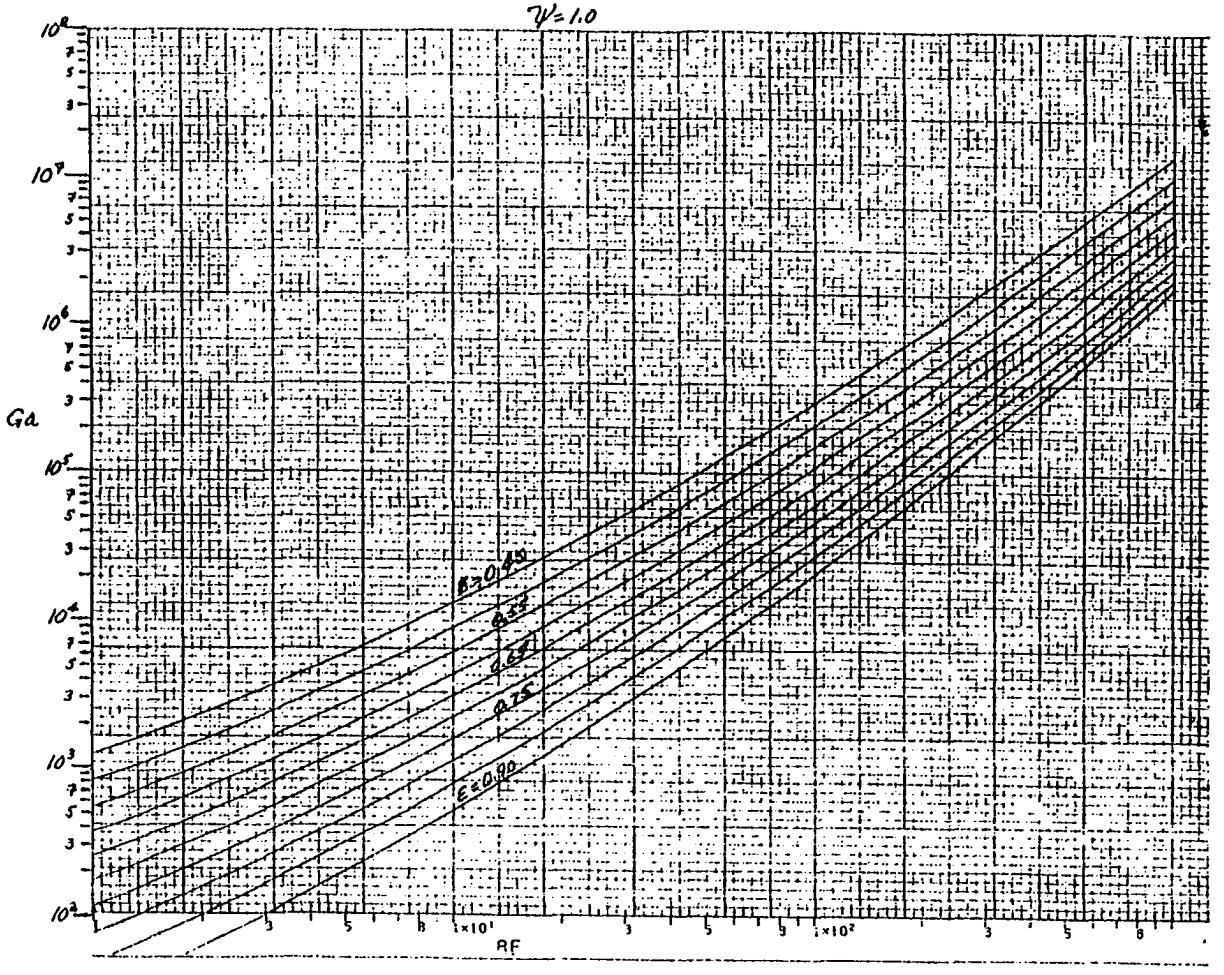

Figure 58. The relationship between Ga and Re at different expanded bed porosity for material with ψ = 1.0

$$\log Al = \log \frac{\rho(\rho_s - \rho)g(\psi)^3}{\mu^2} \frac{d_{eq}^3}{(6)^3} \frac{\varepsilon^3}{(1-\varepsilon)^2}$$

$$= \log \frac{\rho(\rho_s - \rho)g\, d_{eq}^3}{\mu^2} + \log \frac{\psi^3 \varepsilon^3}{(6)^3(1-\varepsilon)^2}$$

$$= \log y + \log \frac{\psi^3 \varepsilon^3}{(6)^3 (1-\varepsilon)^2} \qquad (153a)$$

where

$$\log y = \log \frac{\rho(\rho_s - \rho)g\, d_{eq}^3}{\mu^2} .$$

$$Re_1 = \frac{\rho u \ \psi d_{eq}}{6\mu (1-\varepsilon)}$$

$$\log Re_1 = \log \frac{\rho u \ d_{eq}}{\mu} + \log \frac{\psi}{6(1-\varepsilon)}$$

$$= \log x + \log \frac{\psi}{6(1-\varepsilon)} \qquad (153b)$$

where

$$\log x = \log \frac{\rho u \ d_{eq}}{\mu} .$$

In equation 153, for log Al and log Re_1, equations 153a and 153b are substituted. This enables one to draw on the plot of log y versus log x constant porosity lines at a selected value of ψ as shown in Figures 55 to 59.

To use these figures one calculates the ordinate from

$$\log y = \log \frac{(\rho_s - \rho)\rho \ g \ d_{eq}^3}{\mu^2}$$

and abscissa from

$$\log x = \log \left(\frac{\rho u_t d_{eq}}{\mu}\right)$$

and then from the graph of appropriate ψ, the expanded bed porosity is obtained.

In addition, the computer program ROOTS, given in Appendix II, is written in FORTRAN language to obtain the porosity at a given superficial velocity. The additional information required are density ρ_s, equivalent spherical diameter d_{eq}, sphericity ψ and the viscosity of liquid μ.

The prediction equation is not valid beyond porosity 0.9 because in the data used to develop the equation, the expanded bed porosity was less than 0.9. Moreover, for porosities beyond 0.9, the fixed bed approach used in developing the functions Al and Re_1 is not valid. This is because the system approaches the unhindered settling behavior of the particles which is not taken into account in defining the modified Reynolds number and function ϕ_1.

The computer program was used to check the accuracy of the prediction equation 153 by calculating the predicted porosity at the superficial velocities at which experimental measurements were made. These calculations were made for data of Fan (45), Gunasingham et al. (85), Presler (85), Wilhelm and Kwauk (109) and the data obtained in the present experiments.

Figures 59 to 61 show the predicted porosity against actual porosity for some of the material studied in the present investigation.

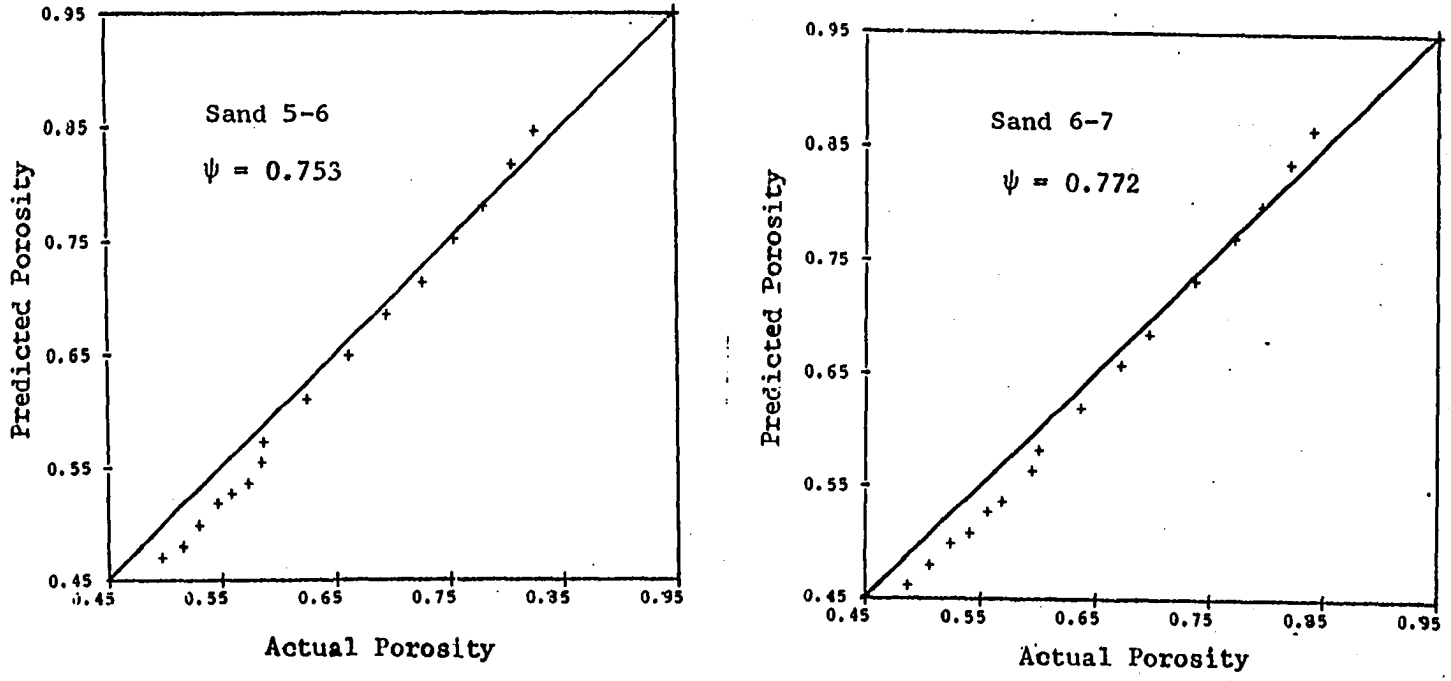

Figure 59. The relationship between predicted porosity and actual porosity for 5-6 mesh and 6-7 mesh silica sand

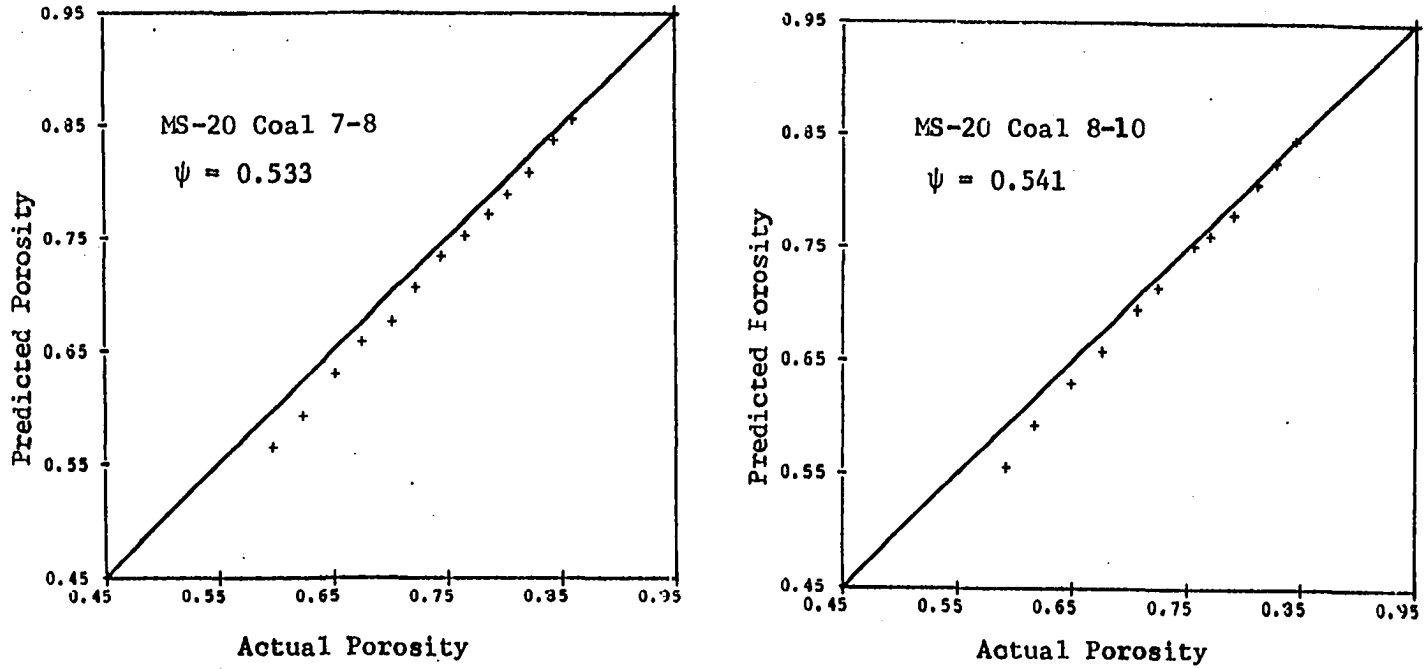

Figure 60. The relationship between predicted porosity and actual porosity for 7-8 mesh and 8-10 mesh MS-20 coal

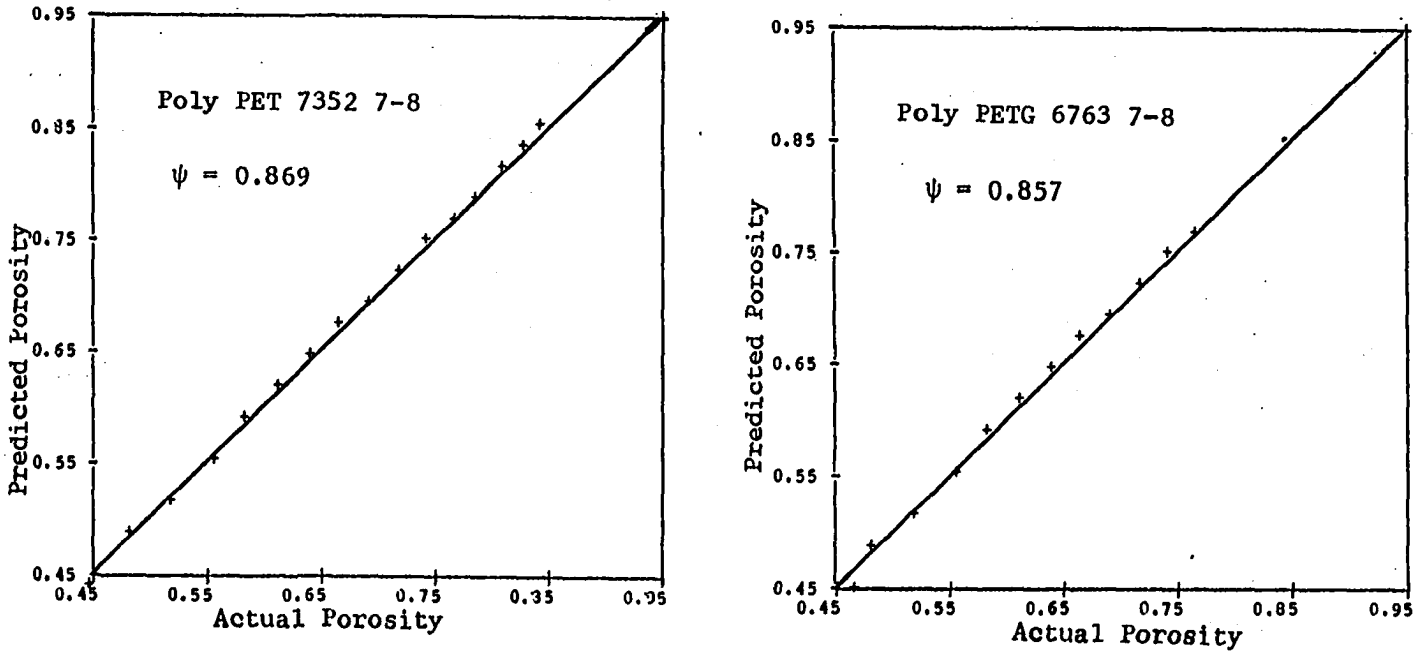

Figure 61. The relationship between predicted porosity and actual porosity for 7-8 mesh Polyester PET 7352 and 7-8 mesh Polyester PETG 6763

Figures 62 and 63 show the actual porosity against predicted porosity for two sand sizes and two U.S. anthracite studied by Fan (45). Figures 64 and 65 show the relationship between predicted porosity and actual porosity for two polystyrene sizes and two uniform sizes of U.K. Anthracite data reported by Gunasingham et al. (57). The plots of predicted porosity against porosity of rest of the material studied in the experiments conducted herein and by some other investigators are given in Appendix III. For Presler's (85) data the predicted height is plotted against the measured height in Appendix III.

From Table 21 it is seen that the coefficients a, b, c and d show some degree of variability even on the equations obtained for sphericial particles for Richardson and Zaki's data and Loeffler's data are not identical. Therefore, two more equations were developed, one for sand and the other for coal using the data obtained in the present experiments and the data from Fan (45). The equation obtained with sand data is

$$\log Al = 0.6056 + 1.1585 \log Re_1 + 0.1452 (\log Re_1)^2 + 1.3 \log (\psi) \qquad r^2 = 0.9967 \tag{154}$$

The equation obtained with coal data is as follows:

$$\log Al = 0.9815 + 0.9767 \log Re_1 + 0.1730 (\log Re_1)^2 + 1.389 \log (\psi) \qquad r^2 = 0.9968 \tag{155}$$

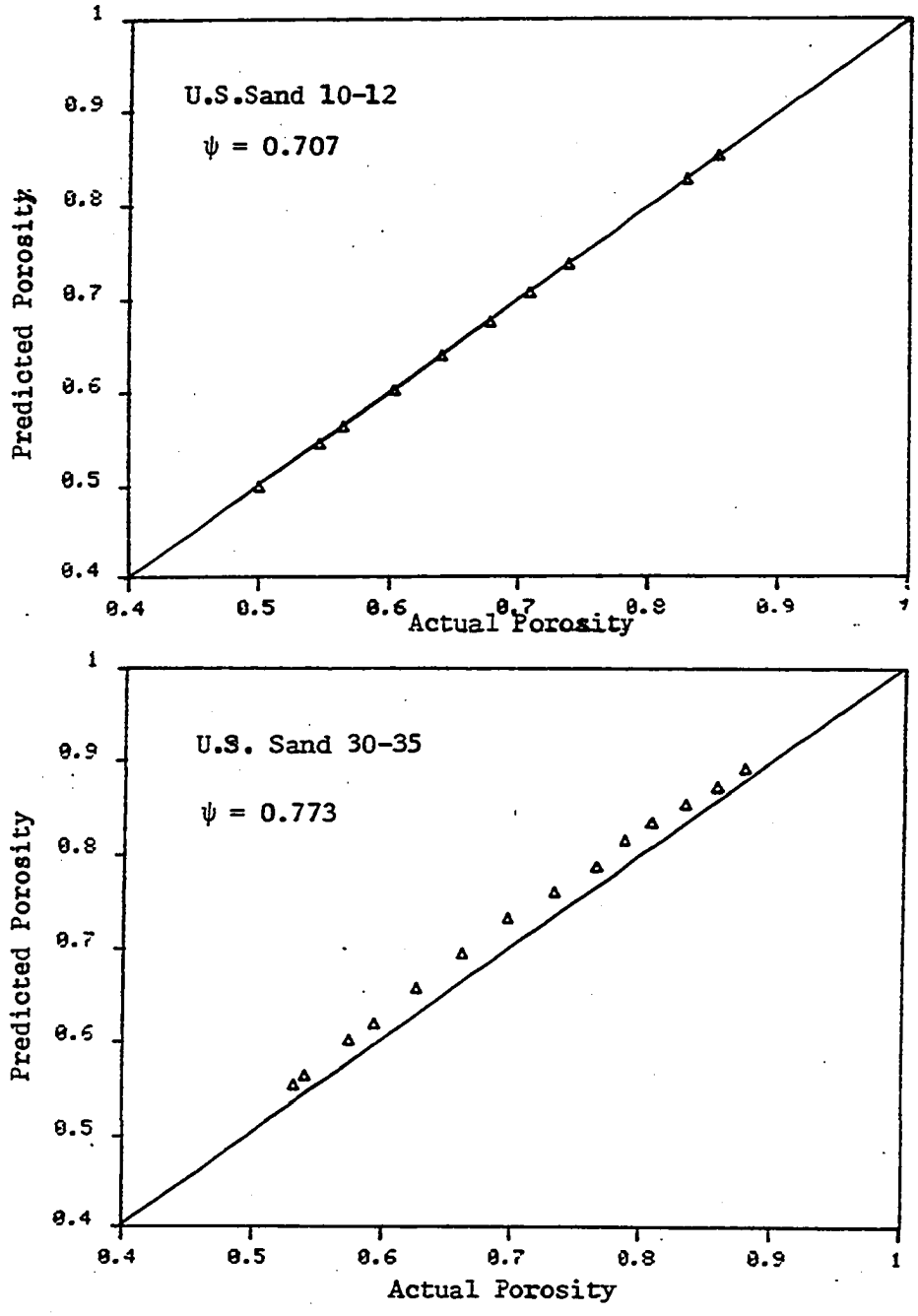

Figure 62. The relationship between predicted porosity and actual porosity 10-12 mesh and 30-35 mesh U.S. sand (Fan's data (45))

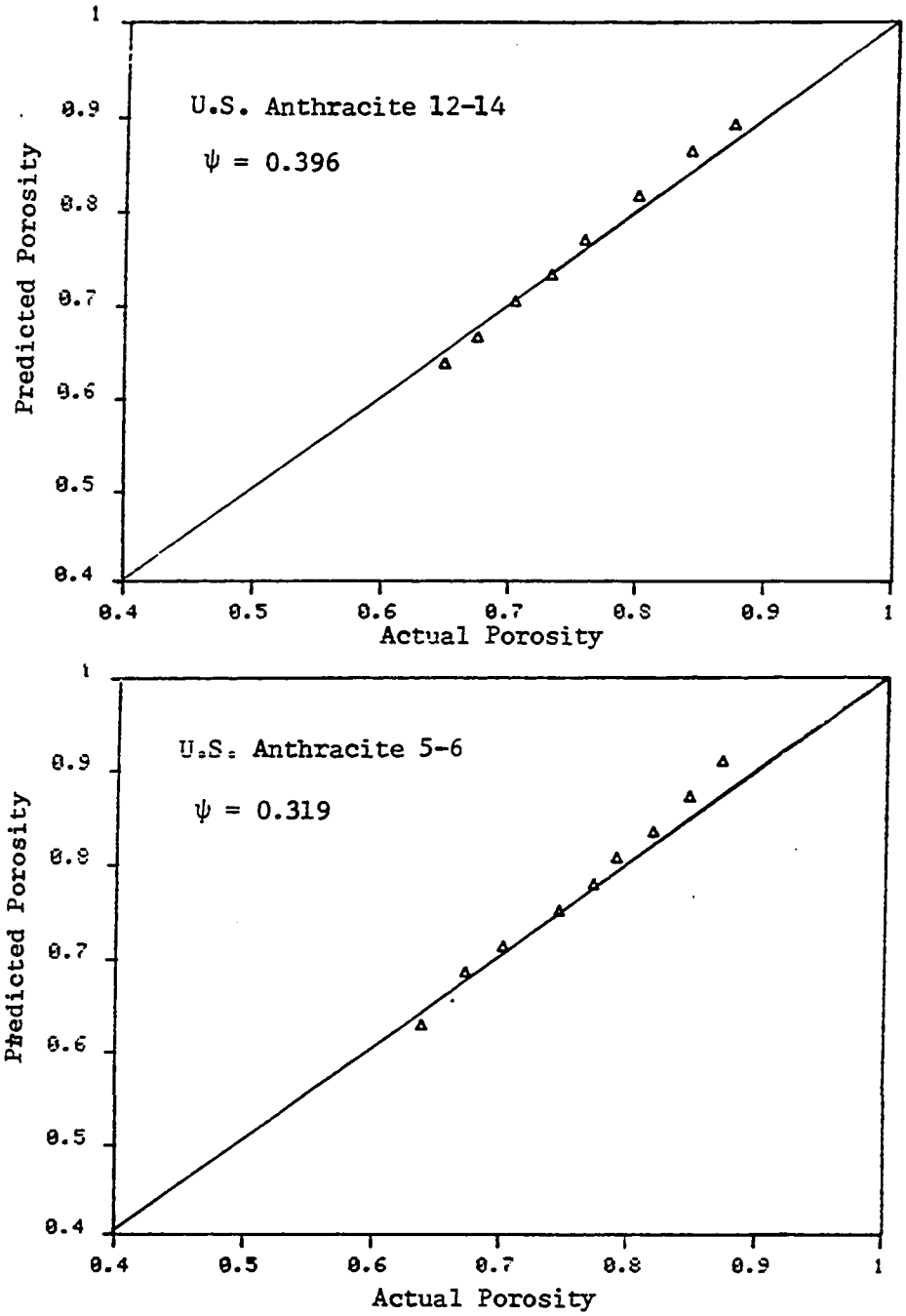

Figure 63. The relationship between predicted and actual porosity for 5-6 mesh and 12-14 mesh U.S. Anthracite coal (Fan's data (45))

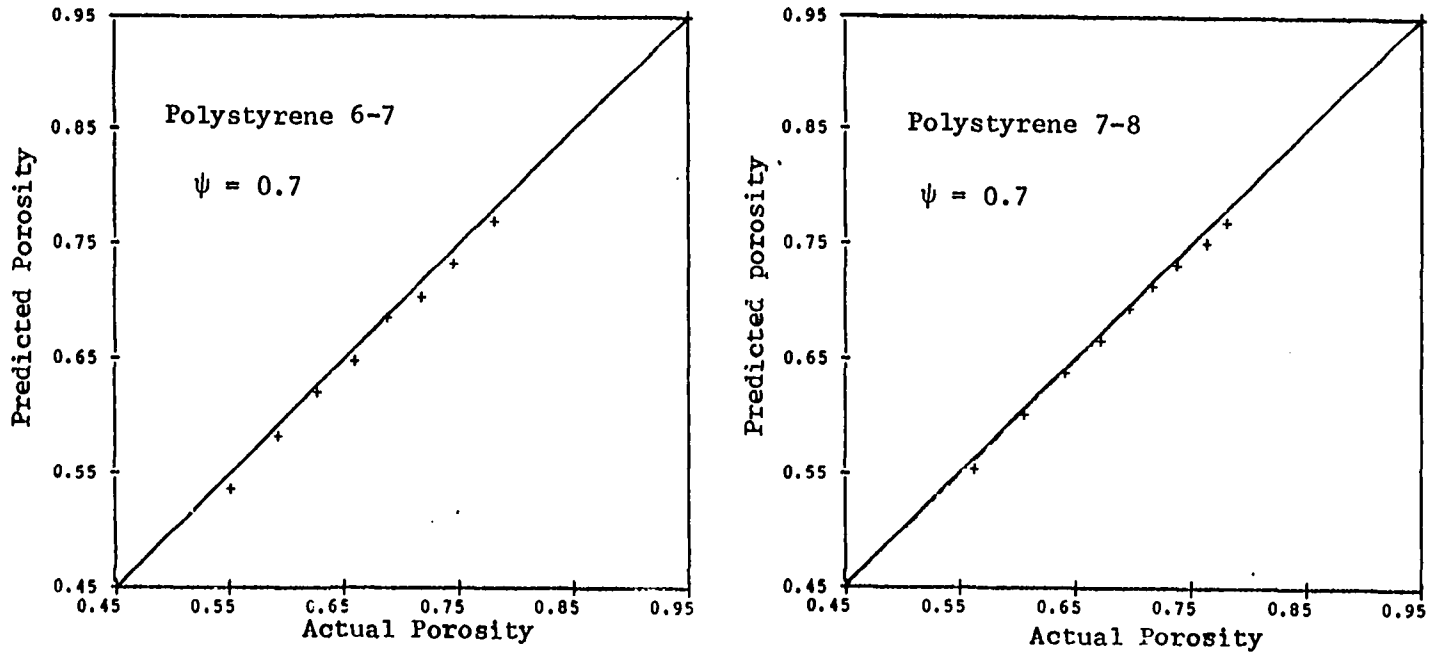

Figure 64. The relationship between predicted porosity and actual porosity for 6-7 mesh and 7-8 mesh polystyrene (Gunasingham et al. data (57))

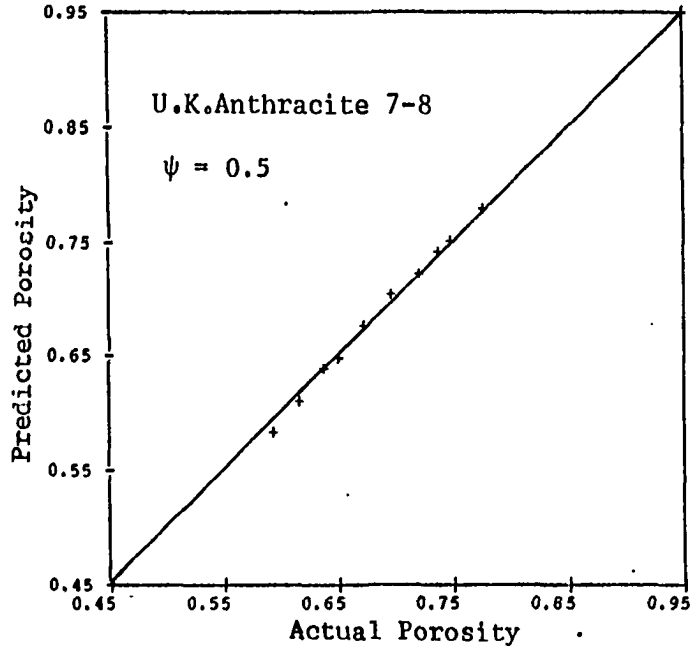

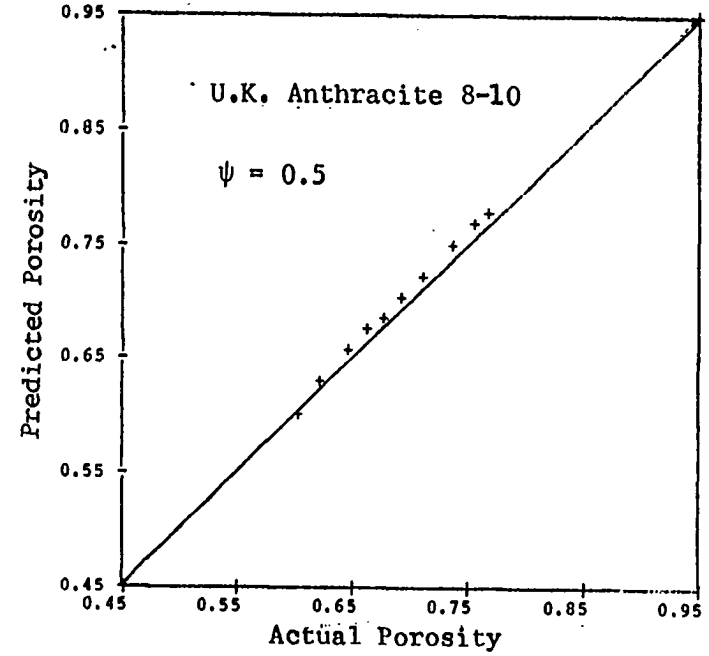

Figure 65. The relationship between predicted and actual porosity for 7-8 mesh and 8-10 mesh U.K. Anthracite (Gunasingham, et al. (57))

The different values obtained for the coefficients indicate the difficulties involved obtaining a satisfactory shape factor to describe the behavior of two different shaped materials. These two specific equations should be more accurate for prediction for the specific materials.

Reexamination of Cleasby and Fan (32) Prediction Method

In the following section, an attempt was made to improve the prediction model proposed by Cleasby and Fan (32). Cleasby and Fan used limited data obtained in their experiments to develop their prediction model. Table 22 presents the 'n' slope, particle Reynolds number, shape factors Ω, DSF and ψ and d/D_T ratio for different investigators. These data will be used to expand the data base for the model developed by Cleasby and Fan (32).

Certain observations have to be made from Table 20 regarding 'n' and u_i values for some of the materials studied in the present investigations. Although Polyester 7352, Polyester PETG 6763, and Cullsan P had a sphericity of about 0.85, their 'n' values are close to those predicted by Richardson and Zaki equations for sphericial particles. Sand 5-6 and sand 6-7 had 'n' values of about 2.3 which is slightly below the value for spherical particle at Re_t greater than 500. Brass 35-40 and stainless steel 16-18 had 'n' values which are very much higher than those expected for particles with their Re_t and sphericity ψ. This may be because the fluidization of these two materials was not particulate. Further, for sand 5-6, sand 6-7,

Polyester PETG 6763 and Cullsan P, the intercept velocity at $\varepsilon = 1$ was less than the terminal settling velocity at the same temperature.

Figures 66 and 67 show the 'n' vs. Re_t relationship with DSF and ψ as shape parameters, respectively. On these plots, relationships predicted by equations 135 and 136 are also plotted for constant DSF or ψ values, neglicting d/D_T ratios. Figure 68 shows the'n' vs. Re_t relationship with Ω as the shape parameter. The data points for brass 35-40 and stainless steel 16-18 have been omitted in Figures 66 through 68 because their fluidization was not particulate.

When one examines these figures,one cannot fail to realize that as the particle Reynolds number increases,the effect of shape factor on 'n' values becomes less significant. It can only be said that equations 135 and 136 predict the correct trend as shown in these figures. However, the data points with nearly same DSF or ψ values fall on either side of the constant shape factor line predicted by equations 135 and 136. Wood's (110) data on garnet 14-16 and 25-30 fell well outside the predicted curve. Further, when the exponents on DSF, ψ or Ω were calculated as

$$\begin{aligned} n &= n_{spherical} \times (DSF)^{\alpha} \\ n &= n_{spherical} \times (\psi)^{\beta} \\ n &= n_{spherical} \times (\Omega)^{\gamma} \end{aligned} \qquad (156)$$

for data points with $Re_t < 500$, not all the points produced a negative value for α, β and γ as would be expected from equations 135 and 136 (the values are not presented here). $n_{spherical}$ was approximated as

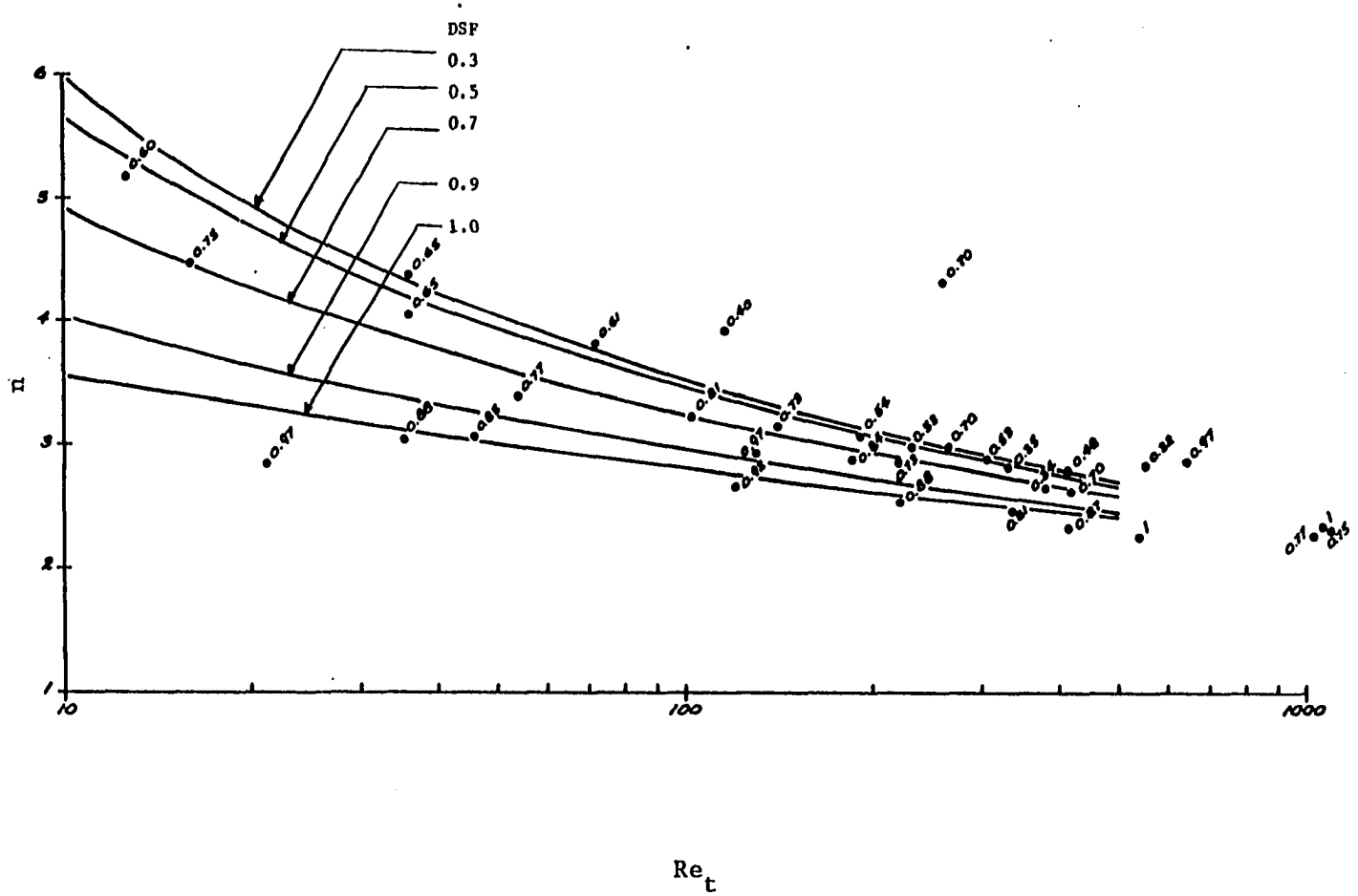

Figure 66. Relationship between 'n' slope and Re_t with DSF as shape parameter. Solid lines represent prediction by equation 135. Actual DSF values are shown adjacent to the data points

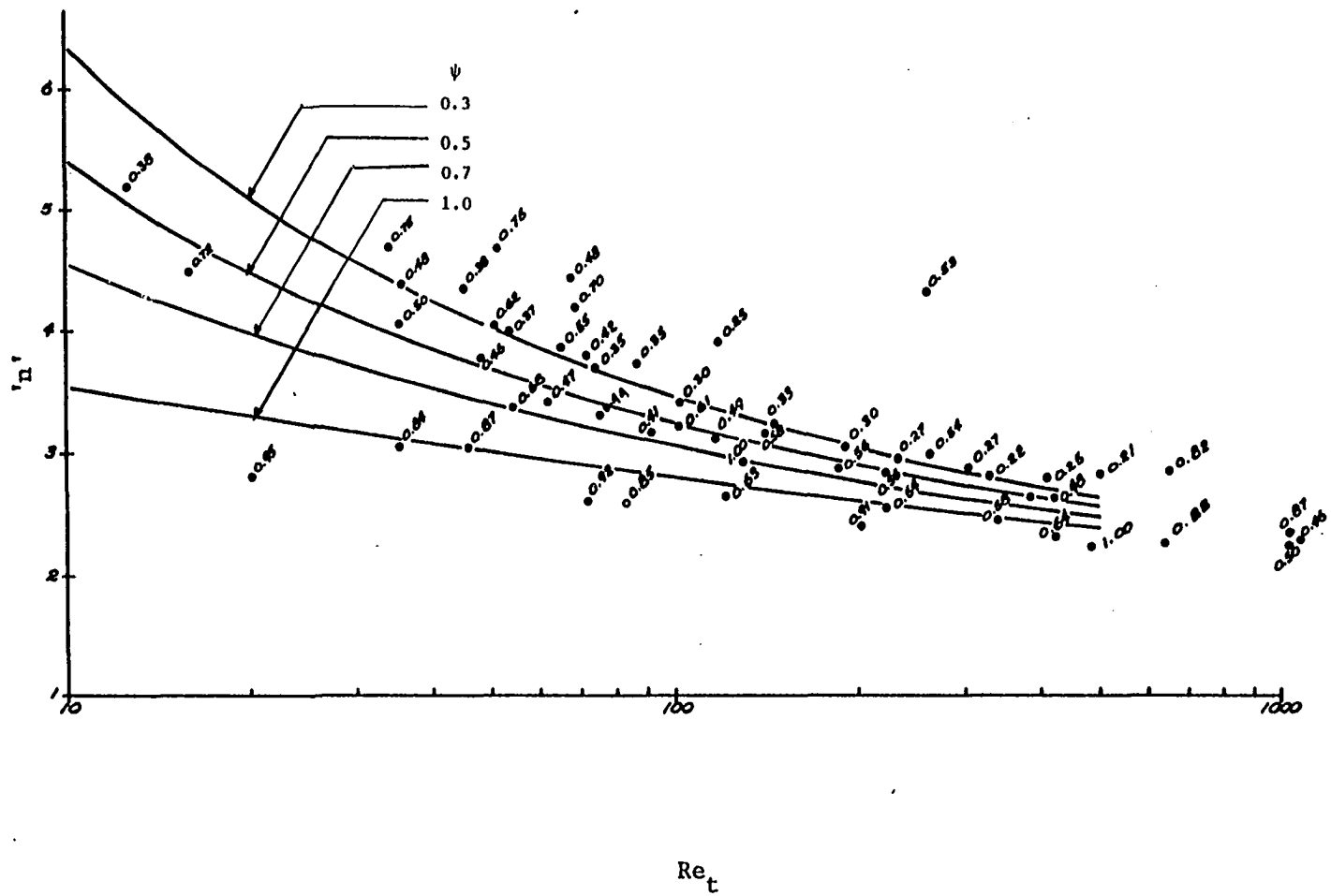

Figure 67. Relationship between 'n' slope and Re_t with ψ as shape parameter. Solid lines represent prediction by equation 136. Actual values of ψ are shown adjacent to the data points

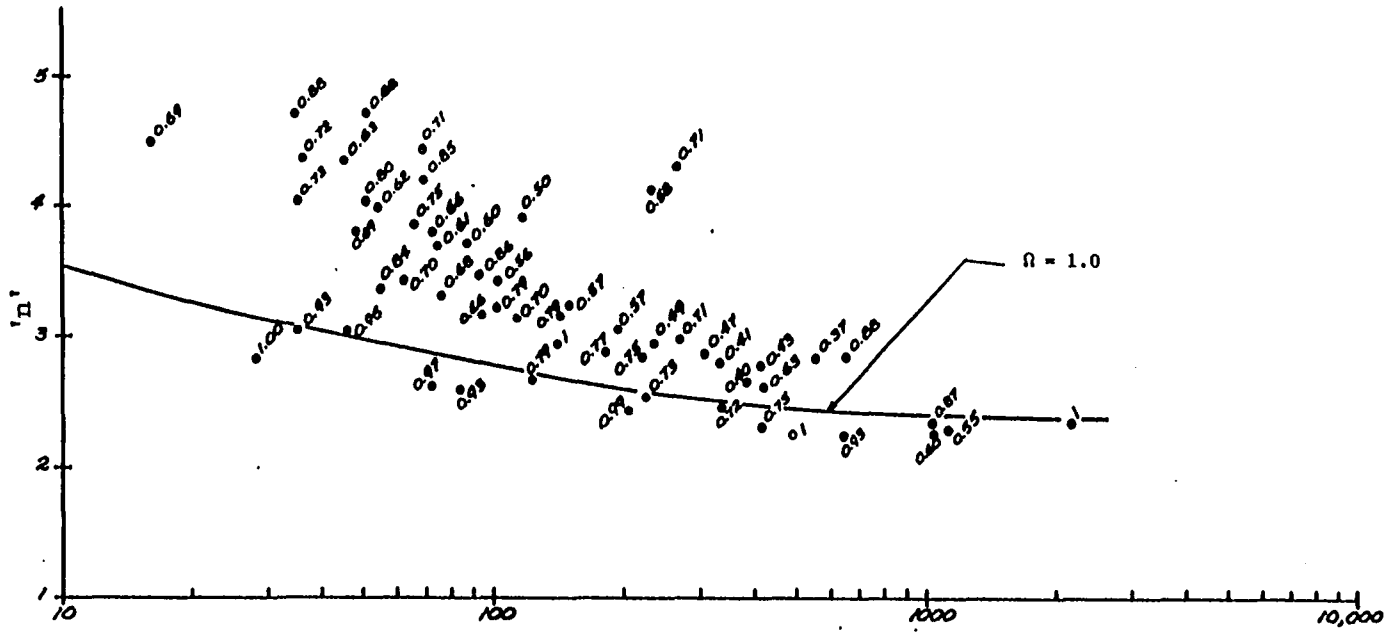

Figure 68. Relationship between 'n' slope and Re_t with Ω as shape parameter. Solid line represents prediction by equation 157. Actual values of Ω are shown adjacent to the data points

Table 22. 'n' slope values for various materials with their corresponding Re_t, Ω, DSF and ψ values

Material	n	Re_t	Ω	DSF	ψ	d/D_T	Ref.
Brass 35-40	5.244	92.98	0.856	0.704	0.930	0.0047	present expts.
Stainless steel 16-18	4.116	229.22	0.581	0.362	0.833	0.0094	"
Aluminum 16-18	2.891	187.86	0.773	0.563	0.836	0.0107	"
Sand 5-6	2.306	1105.75	0.548	0.461	0.753	0.0369	"
Sand 6-7	2.277	1024.37	0.598	0.504	0.772	0.0344	"
Polyester 6763 7-8	2.460	338.27	0.717	0.575	0.851	0.0299	"
Polyester 7352 7-8	2.325	415.15	0.749	0.636	0.869	0.0300	"
Cullsan P 8-10	2.547	223.53	0.732	0.543	0.878	0.0264	"
MS-20 coal 5-6	2.791	413.00	0.431	0.246	0.483	0.0380	"
MS-20 coal 6-7	2.883	307.15	0.472	0.270	0.534	0.0321	"
MS-20 coal 7-8	2.955	232.84	0.492	0.272	0.533	0.0265	"
MS-20 coal 8-10	3.061	191.69	0.511	0.295	0.541	0.0230	"
U.S. sand 10-12	2.629	420.27	0.627	0.475	0.707	0.0193	(45)
U.S. sand 14-16	2.998	267.84	0.711	0.535	0.707	0.0144	"
U.S. sand 18-20	3.169	141.71	0.789	0.582	0.734	0.0099	"
U.S. sand 30-35	3.384	54.71	0.837	0.676	0.773	0.0059	"
U.S. anthracite 5-6	2.834	503.00	0.380	0.212	0.319	0.0361	"
U.S. anthracite 6-7	2.670	387.86	0.402	0.214	0.341	0.0307	"
U.S. anthracite 7-8	2.808	330.99	0.414	0.218	0.348	0.0278	"
U.S. anthracite 12-14	3.916	117.97	0.503	0.253	0.396	0.0149	"
Flintag 18-22	3.801	71.89	0.664	0.421	0.613	0.0150	"

Flintag 25-30	4.049	35.57	0.733	0.497	0.646	0.0101	(45)
U.K. anthracite 18-22	4.380	35.96	0.721	0.482	0.645	0.0156	"
U.K. anthracite 25-30	4.498	16.0	0.881	0.724	0.752	0.0096	"
U.K. sand 18-22	3.212	102.31	0.788	0.605	0.809	0.0163	"
Ballotini	2.931	129.76	1.000	1.000	0.965	0.0150	"
Garnet 14-16	4.326	260.77	0.711	0.532	0.703	0.0088	(110)
Garnet 25-30	4.437	68.01	0.708	0.474	0.595	0.0043	"
Garnet 50-60	5.197	12.62	0.690	0.382	0.600	0.0018	"
Sea sand 1	2.826	20.77	0.996	0.948	0.965	0.0049	(109)
Sea sand 2	3.056	45.90	0.951	0.869	0.850	0.0073	"
Scony bead small	2.263	639.67	0.932	0.884	1.05	0.0430	"
Scony bead large	2.345	1013.60	0.866	0.872	0.937	0.0580	"
Glass beads 5mm	2.359	2174.57	1.000	1.000	0.983	0.0683	"
Lead shot #12	2.868	648.24	0.883	0.820	0.966	0.0168	"
Sea sand 3	2.680	122.64	0.794	0.628	0.921	0.0131	"
Crushed Rock	2.846	219.86	0.746	0.562	0.732	0.0185	"
Glass beads #7	3.068	35.17	0.930	0.841	0.884	0.0067	"
U.K. sand 22-25	3.873	65.80	0.749	0.545	-	0.0060	(57)
U.K. sand 25-30	4.041	50.88	0.801	0.617	-	0.0051	"
Ballotini 8-10	2.230	487.88	1.000	1.000	-	0.0149	"
Ballotini 14-16	2.429	202.30	0.985	0.907	-	0.0092	"
Ballotini 18-22	2.596	83.20	0.930	0.853	-	0.0061	"
Ballotini 22-25	2.611	71.94	0.974	0.927	-	0.0054	"
U.K. Anthracite 7-8	3.242	146.80	0.567	0.332	-	0.0165	"
U.K. Anthracite 8-10	3.417	102.75	0.555	0.304	-	0.0142	"

Table 22. continued

Material	n	Re_t	Ω	DSF	ψ	d/D_T	Ref.
U.K. Anthracite 10-12	3.719	86.88	0.600	0.349	-	0.0125	(57)
U.K. Anthracite 14-16	3.795	48.31	0.691	0.459	-	0.0092	"
Polystyrene 5-6	3.117	116.47	0.703	0.489	-	0.0274	"
Polystyrene 6-7	3.180	92.71	0.657	0.414	-	0.0249	"
Polystyrene 7-8	3.301	75.83	0.675	0.436	-	0.0225	"
Polystyrene 8-10	3.420	62.33	0.697	0.474	-	0.0199	"
Anthrfilt 14-16	4.20	69.09	0.847	0.701	-	0.0085	(28)
Anthrafilt 16-18	4.70	51.62	0.884	0.751	-	0.0072	"
Anthrafilt 18-20	4.70	34.37	0.882	0.750	-	0.0059	"
Philterkol 14-16	3.70	74.36	0.606	0.352	-	0.0085	"
Philterkol 16-18	4.00	54.00	0.615	0.367	-	0.0072	"
Philterkol 18-20	4.35	45.31	0.628	0.376	-	0.0066	"

$$n_{spherical} = 4.4\ Re_t^{-0.1} \qquad \text{if } Re_t < 500 \tag{157}$$

The d/D_T correction of equation 81 was deemed unnecessary because:

1. The Re_t values are experimentally determined values in small columns comparable in diameter to the fluidization column.

2. The scatter of data points with equal shape factors in Figures 66, 67, and 68 suggest that d/D_T correction unnecessarily complicates the prediction equation.

The following equation was obtained when a two variable correlation was performed with DSF as shape parameter with 32 data points which produced negative values for α.

$$\alpha = -3.6475\ Re_t^{-0.464}\ (DSF)^{0.639} \qquad r^2 = 79.4\ \% \tag{158}$$

The standard deviations of the coefficients are as follows:

Coefficient	Std. Deviation
3.6475	1.336
-0.464	0.0765
0.639	0.186

The equation to predict 'n' will be

$$n = 4.4\ Re_t^{-0.1}\ (DSF)^{-3.6475\ Re_t^{-0.464}\ (DSF)^{0.639}} \tag{159}$$

Similarly, a two variable correlation was performed with the same 32 data points that gave negative values for γ.

$$\gamma = -9.078\ \ Re_t^{-0.509}\ (\Omega)^{1.25} \qquad r^2 = 83.6\ \% \tag{160}$$

The standard deviations of the coefficients are as follows:

Coefficient	Std. Deviation
9.078	1.385
-0.509	0.089
1.25	0.340

The equation to predict 'n' using Ω as the shape factor is

$$n = 4.4\ Re_t^{-0.1}\ (\Omega)^{-9.078\ Re_t^{-0.509}(\Omega)^{1.25}} \qquad (161)$$

Figure 69 shows the variation of 'n' with Re_t as predicted by equations 135 and 159. From this figure, it is seen that the difference in predicted 'n' is not significant except at low Reynolds numbers.

Figure 70 shows the relationship of 'n' vs. Re_t at Ω = 0.3, 0.5, 0.7 and 1.0 as obtained from equation 161. In this plot curve corresponding to Ω = 0.5, plots above the curve corresponding to Ω = 0.3. This apparent contradiction is due to the fact the data used to obtain equation 160 did not contain any Ω values below 0.38. Therefore, extrapolation of equation 161 below Ω = 0.38 is likely to cause a error of greater magnitude.

The weakest link in predicting the expansion during fluidization by Cleasby and Fan (32) method is the estimation of intercept velocity u_i. Table 23 presents $\frac{u_i}{u_t}$, Re_t, DSF, Ω and ψ as reported by different investigators or calculated from their data. Figure 71 shows the plot of $\frac{u_i}{u_t}$ versus DSF and the relationship predicted by equation 137. Figure 72 shows the data of $\frac{u_i}{u_t}$ against sphericity ψ and relationship predicted by equation 138.

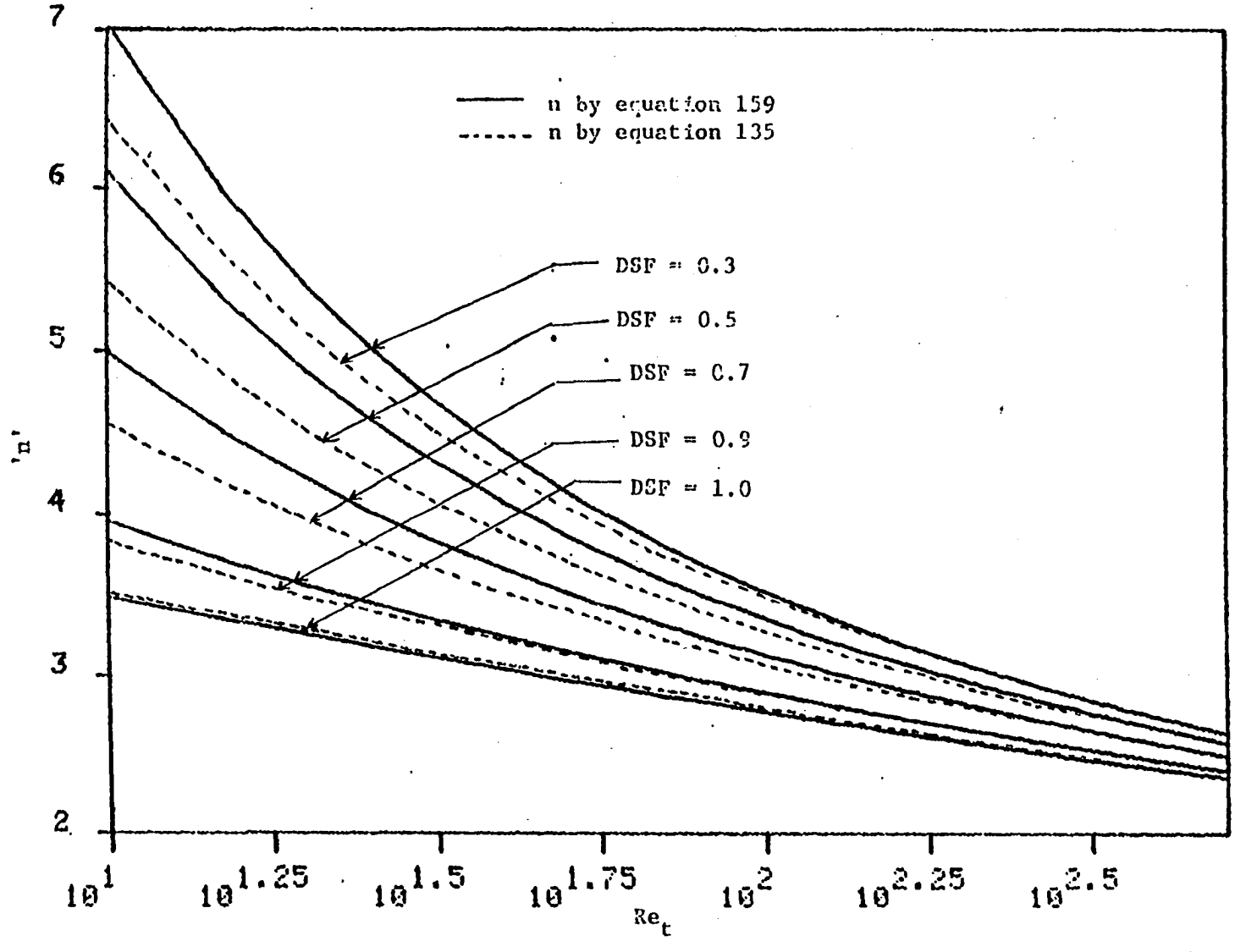

Figure 69. The relationship between 'n' slope and Re_t at different values of DSF as predicted by equation 135 and 159

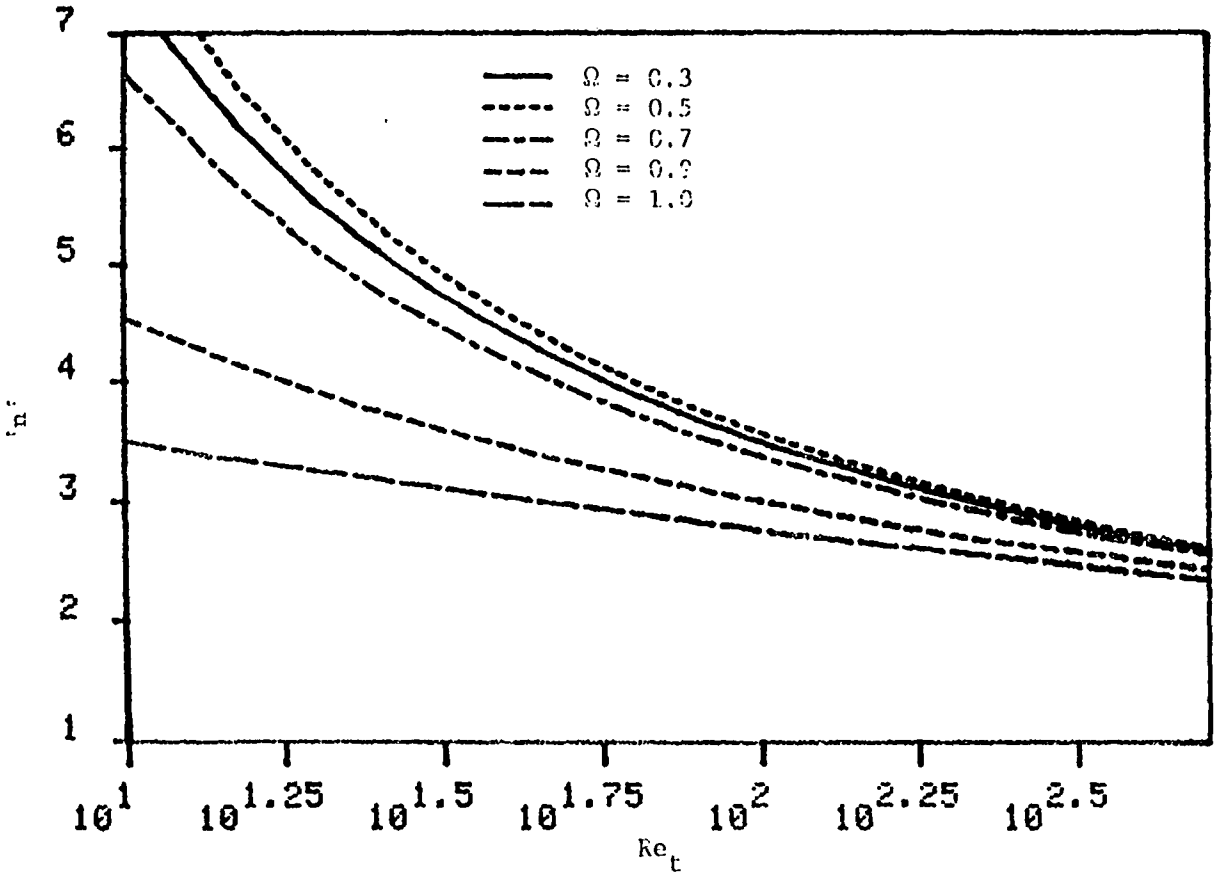

Figure 70. The relationship between 'n' slope and Re_t at different values of Ω as predicted by equation 161

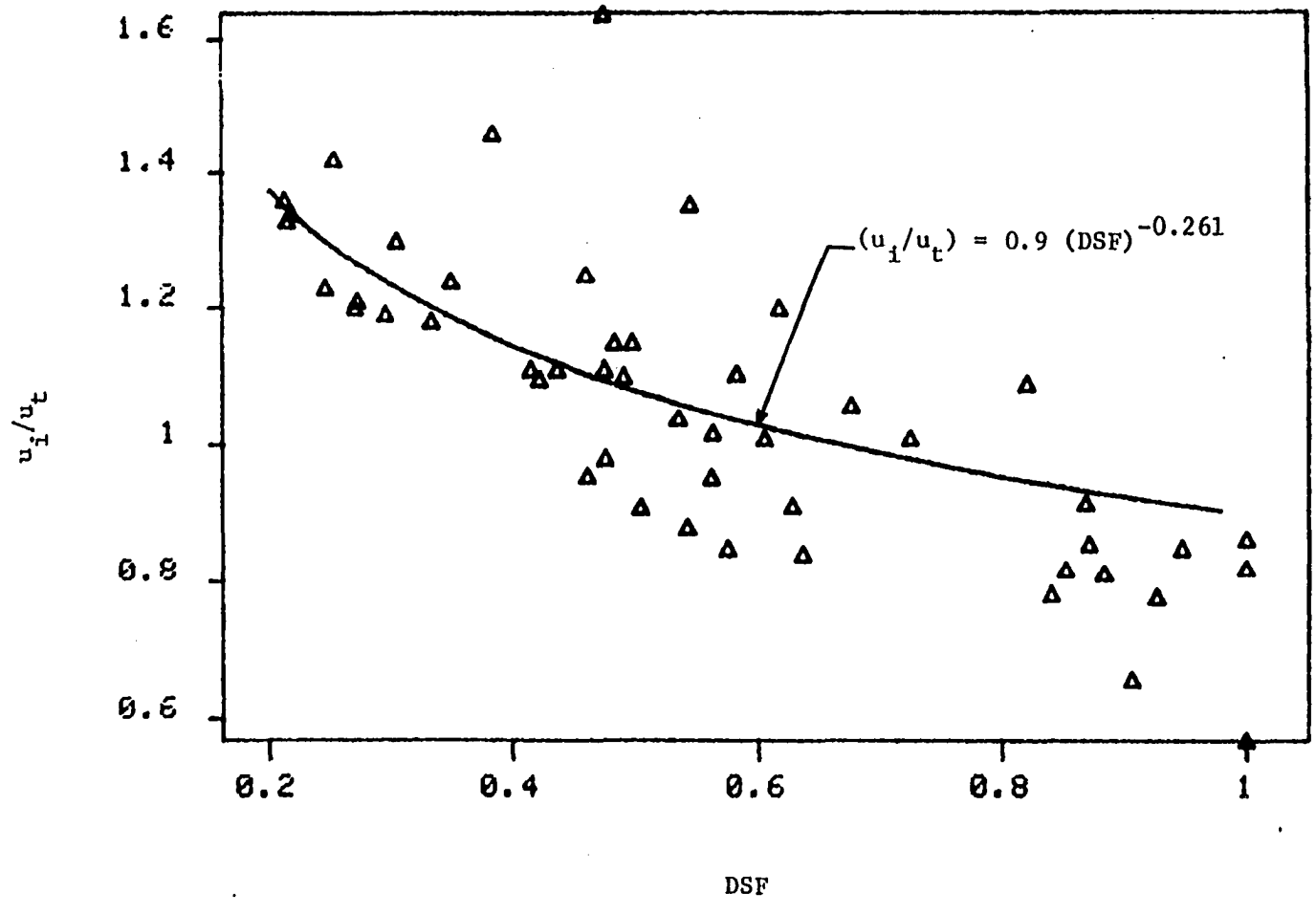

Figure 71. The relationship between u_i/u_t ratio and DSF and the solid line as predicted by equation 137

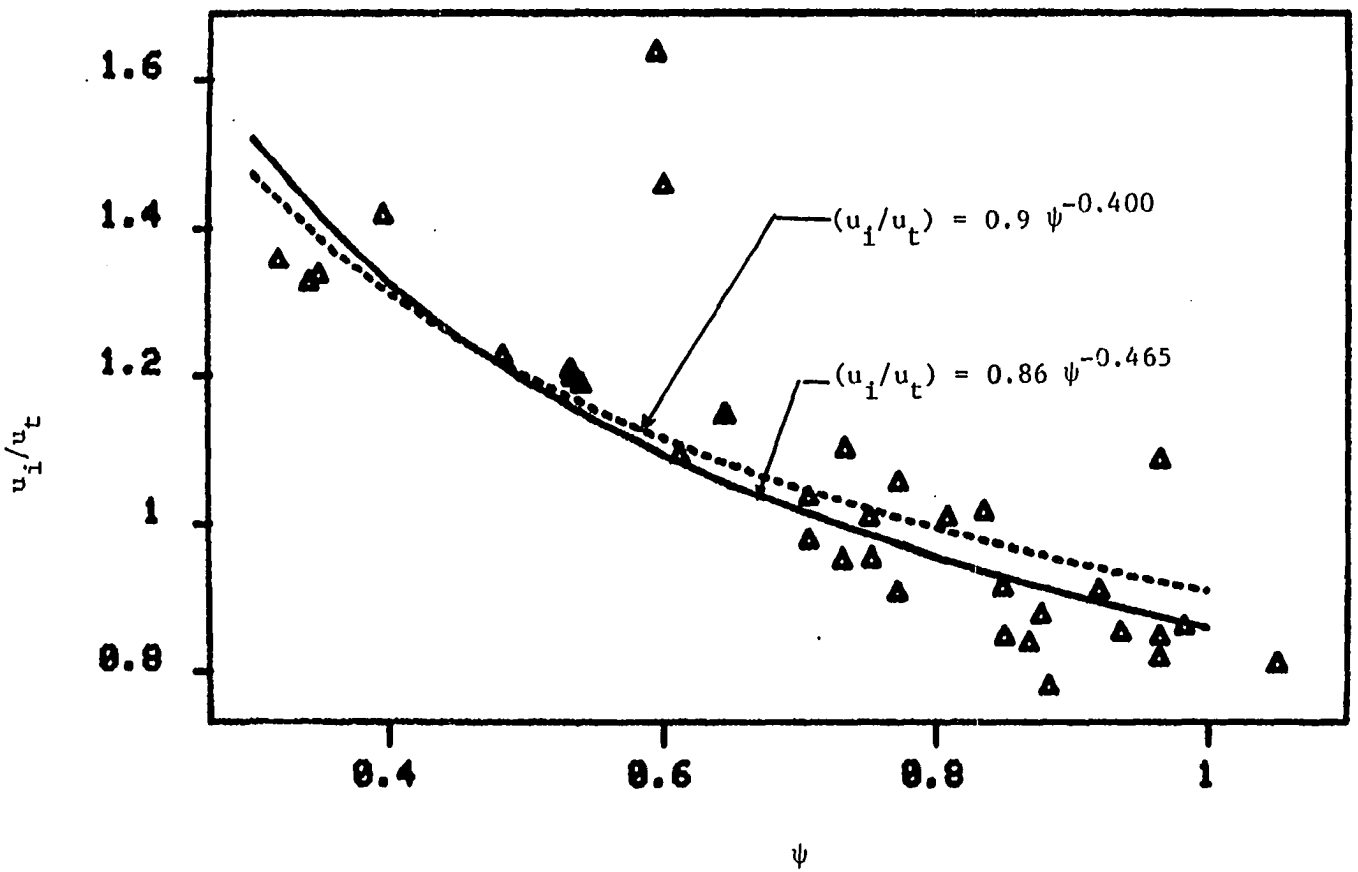

Figure 72. The relationship between u_i/u_t ratio and ψ with dotted line showing equation 138 and the solid line showing the best fit regression for the data presented herein

Table 23. $\frac{u_i}{u_t}$ values for various material with their corresponding Re_t, Ω, DSF and ψ

Material	u_i/u_t	Re_t	Ω	DSF	ψ	Ref.
Aluminum 16-18	1.018	186.9	0.773	0.563	0.836	Present
Sand 5-6	0.955	1105.8	0.548	0.461	0.753	Expt.
Sand 6-7	0.960	1024.4	0.598	0.504	0.772	"
Polyester 7352 7-8	0.841	338.3	0.717	0.575	0.851	"
Polyester 6763 7-8	0.850	415.2	0.749	0.636	0.869	"
Cullsan P 8-10	0.880	223.5	0.732	0.543	0.878	"
MS-20 coal 5-6	1.230	413.0	0.431	0.246	0.483	"
MS-20 coal 6-7	1.200	307.2	0.472	0.270	0.534	"
MS-20 coal 7-8	1.210	232.8	0.492	0.272	0.533	"
MS-20 coal 8-10	1.190	191.7	0.511	0.295	0.541	"
U.S. sand 10-12	0.980	420.3	0.627	0.475	0.707	(45)
U.S. sand 14-16	1.040	267.8	0.711	0.535	0.707	"
U.S. sand 18-20	1.105	141.7	0.789	0.582	0.734	"
U.S. sand 30-35	1.060	54.7	0.837	0.676	0.773	"
U.S. Anthracite 5-6	1.360	503.0	0.380	0.212	0.319	"
U.S. Anthracite 6-7	1.330	387.9	0.401	0.214	0.341	"
U.S. Anthracite 7-8	1.340	331.0	0.414	0.218	0.348	"
U.S. Anthracite 12-14	1.420	118.0	0.503	0.253	0.396	"
Flintag 18-22	1.096	71.9	0.664	0.421	0.613	"
Flintag 25-20	1.150	35.5	0.733	0.497	0.646	"
U.K. Anthracite 18-22	1.150	36.0	0.721	0.482	0.645	"
U.K. Anthracite 25-30	1.010	16.0	0.881	0.724	0.752	"
U.K. sand 18-22	1.010	102.3	0.788	0.605	0.809	"
Ballotini 18-22	0.820	129.8	1.000	1.000	0.965	"
Garnet 14-16	2.538	260.8	0.711	0.515	0.703	110
Garnet 25-30	1.640	68.0	0.708	0.520	0.595	110
Garnet 50-60	1.460	12.6	0.690	0.530	0.600	"

Table 23. continued

Material	u_i/u_t	Re_t	Ω	DSF	ψ	Ref.
Sea Sand 1	0.849	20.8	0.996	0.948	0.965	(109)
Sea Sand 2	0.916	45.9	0.951	0.869	0.850	"
Scony bead small	0.812	639.7	0.932	0.884	1.050	"
Scony bead large	0.855	1013.6	0.866	0.872	0.937	"
Glass beads 5 mm	0.864	2174.5	1.000	1.000	0.983	"
Lead shot #12	1.090	648.2	0.883	0.820	0.966	"
Sea sand 3	0.913	122.6	0.794	0.628	0.921	"
Crushed rock	0.953	219.9	0.746	0.562	0.732	"
Glass bead 7 mm	0.782	35.2	0.930	0.841	0.884	"
Sand 22-25	1.354	65.8	0.749	0.545	-	(57)
Sand 25-30	1.201	50.9	0.801	0.617	-	"
Ballotini 8-10	0.568	487.8	1.000	1.00	-	"
Ballotini 14-16	0.666	202.3	0.985	0.907	-	"
Ballotini 18-22	0.818	83.2	0.930	0.853	-	"
Ballotini 22-25	0.779	71.9	0.974	0.927	-	"
U.K. Anthracite 7-8	1.180	146.8	0.567	0.332	-	"
U.K. Anthracite 8-10	1.300	102.7	0.555	0.304	-	"
U.K. Anthracite 10-12	1.240	86.9	0.600	0.349	-	"
U.K. Anthracite 14-16	1.250	48.3	0.691	0.459	-	"
Polystyrene 5-6	1.100	116.5	0.703	0.489	-	"
Polystyrene 6-7	1.110	92.7	0.651	0.414	-	"
Polystyrene 7-8	1.110	75.8	0.675	0.436	-	"
Polystyrene 8-10	1.110	62.3	0.697	0.474	-	"

Figure 73 shows the data of $\frac{u_i}{u_t}$ when plotted against Ω. Data for brass 35-40 and stainless steel 16-18 are omitted from Table 23 and Figure 71 through 73. Figures 71 and 73 show considerable scatter of data points when u_i/u_t is plotted against DSF or Ω. In Figure 72,where the u_i/u_t is plotted against ψ the scatter is less but the number of data points used are also less.

An attempt was made to check whether Re_t influenced the value of u_i/u_t ratio in addition to DSF, ψ or Ω. Three plots showing the relationship between u_i/u_t and Re_t with DSF, ψ or Ω a shape parameter were prepared. But it was not possible to draw any inferences from these plots so they are not presented herein. As discussed previously in the literature review section, the intercept velocity u_i is a mathematical artifact and as shown in Figure 19 it is not possible to obtain a satisfactory relationship even for spherical particles. Equations 137 and 138 can be used only as an approximate guide to estimate the u_i values.

An attempt was also made to develop an equation to predict'n' with Heywood's volume coefficient Z as a shape parameter. The exponent on Z was calculated as it was done with the other shape parameter such as DSF, ψ or Ω.

$$n = n_{spherical}\ Z^{\sigma}$$

where

$n_{spherical} = 4.4\ Re_t^{-0.1}$ if $Re_t < 500$

Z = Heywood's volume coefficient

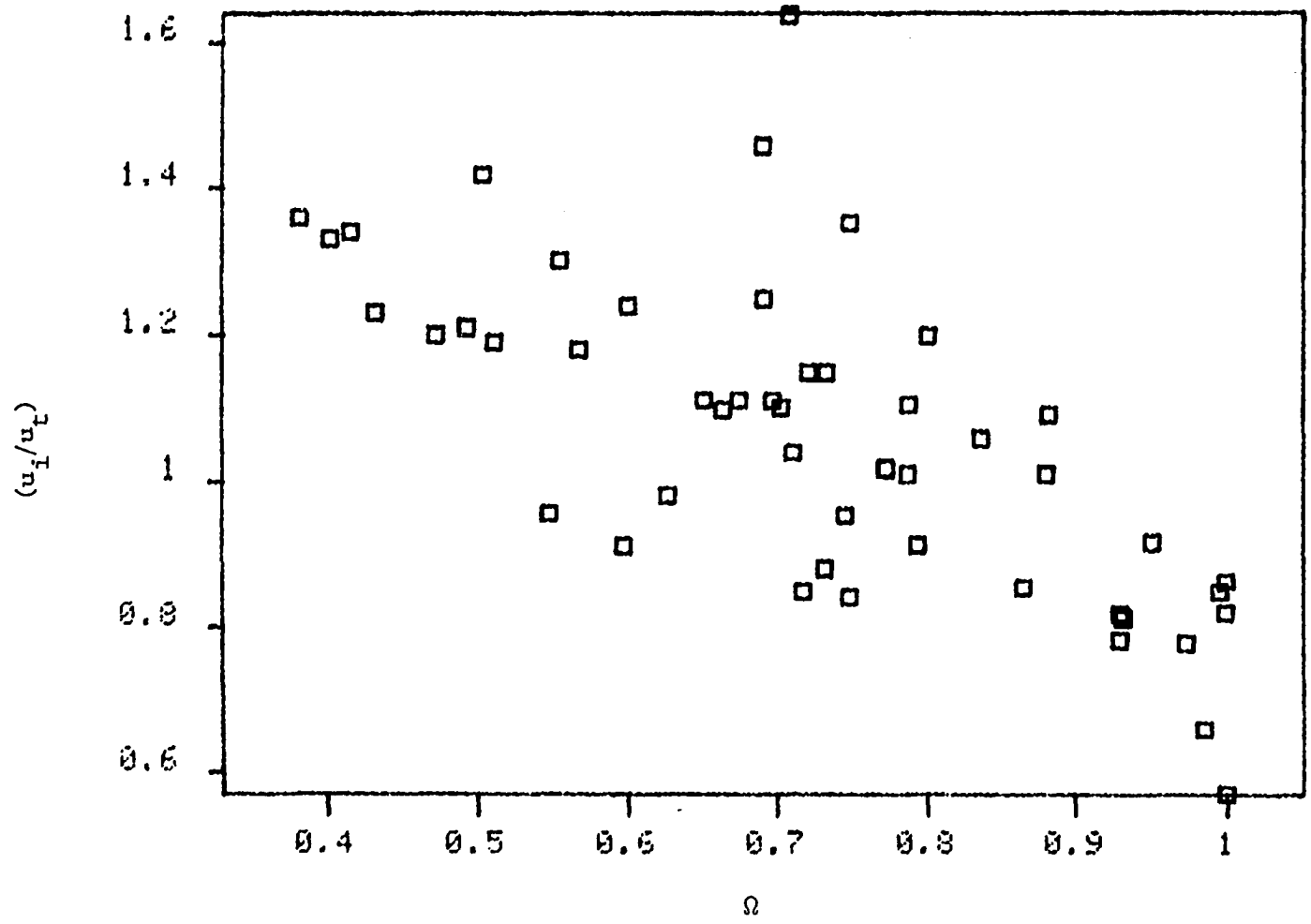

Figure 73. The relationship between u_i/u_t ratio and Ω

$\sigma = f(Z, Re_t)$

But when a two variable correlation was tried for σ against Z and Re_t, the coefficient determination r^2, was only 26.3 percent and the coefficients of the prediction equation were not statistically significant from zero. This shows that the Heywood's volume coefficient Z is not a satisfactory tool for predicting 'n' slope by the type of model employed by Cleasby and Fan (32).

Garside and Al-Dibouni's Prediction Method

Table 24 shows the ratio of $\frac{u}{u_t}$ ratio to attain a specified expanded bed porosity for different materials. This table was prepared to check whether Garside and Al-Dibouni's (54) approach could be extended to non-spherical material too. The value predicted for u_R by equation 112 and 113 were plotted against the actual measured values for porosities 0.5, 0.6, 0.7 and 0.8 in Figure 74. The data points fall on either side of 45 degree line, and at higher porosities such as 0.7 and 0.8, most of the points are on the right side of this 45 degree line. This shows that Garside and Al-Dibouni approach in its present form cannot be used for non-spherical particles. A modification to account for non-sphericity of the particles was not attempted because the data available did not span from very low Reynolds number to very high Reynolds number at a particular shape factor.

Beranek and Klumpar's Prediction Method

Beranek and Klumpar (19) suggested that the fluidization data of spherical and non-spherical data can be correlated by plotting $\frac{1 - \varepsilon}{1 - \varepsilon_{mf}}$ against $\frac{u - u_{mf}}{u_t}$ in logarithmic coordinates. This method was

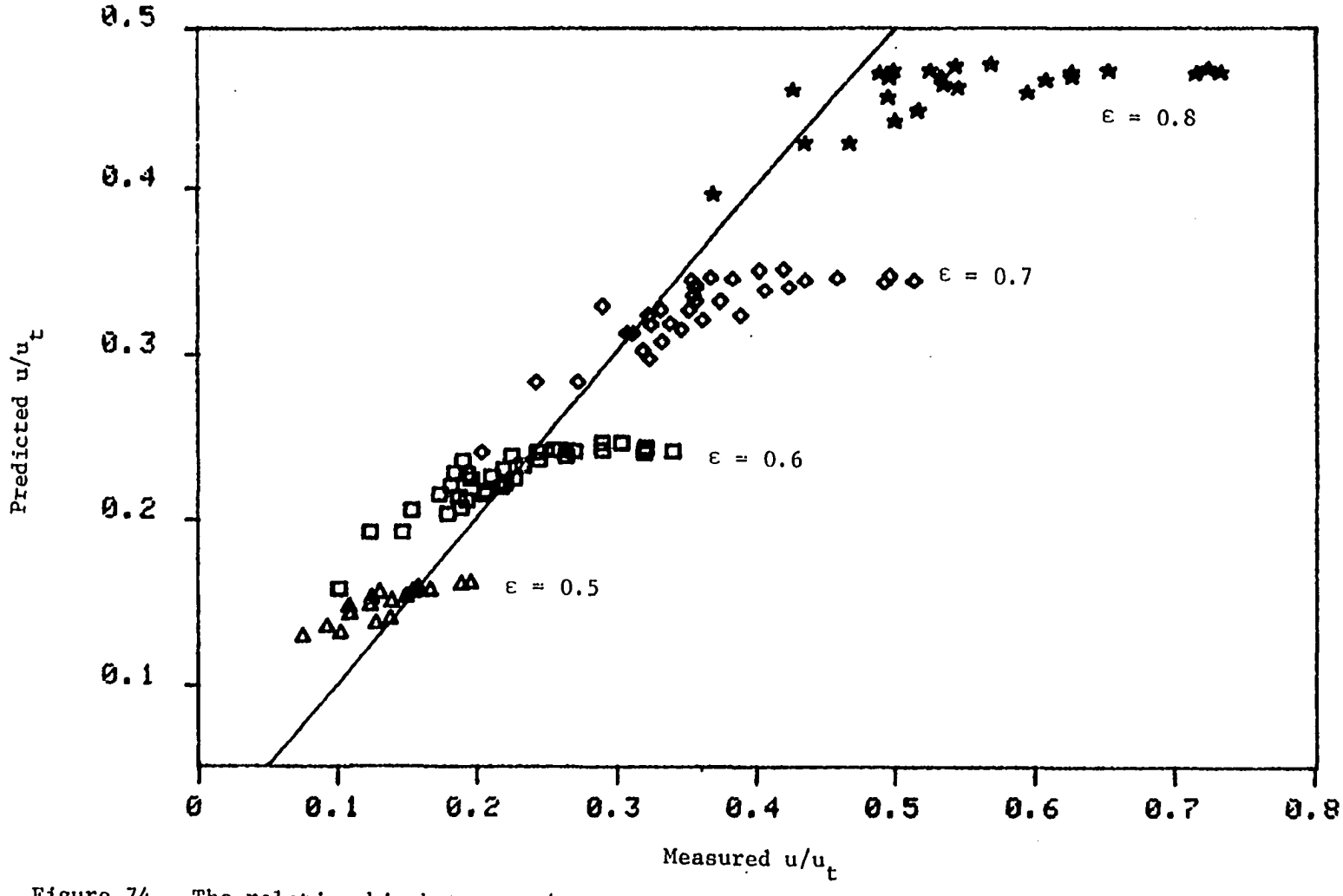

Figure 74. The relationship between u/u_t values predicted by equation 112 and 113 and actual u/u_t for non-spherical materials at porosities 0.5, 0.6, 0.7 and 0.8

Table 24. u/u_t ratio to attain a specified expanded bed porosity for different materials

Material	Re_t	u/u_t				Ref.
		$\varepsilon = 0.5$	$\varepsilon = 0.6$	$\varepsilon = 0.7$	$\varepsilon = 0.8$	
Silica sand 5-6	1150.8	0.1961	0.3032	0.4200	0.5691	Present
Silica sand 6-7	1069.6	0.1893	0.2887	0.4020	0.5430	Expt.
Polyester 7352 7-8	432.6	0.1672	0.2585	0.3684	0.4986	"
Polyester 6763 7-8	346.1	0.1543	0.2431	0.3543	0.4886	"
Cullsan P 8-10	226.7	0.1495	0.2435	0.3568	0.4964	"
MS-20 coal 5-6	468.2	-	0.2887	0.4581	0.6533	"
MS-20 coal 6-7	353.5	-	0.2690	0.4352	0.6269	"
MS-20 coal 7-8	260.1	-	0.2630	0.4241	0.6274	"
MS-20 coal 8-10	219.4	-	0.2435	0.4058	0.6078	"
Aluminum 16-18	166.8	0.1386	0.2319	0.3548	0.5354	"
U.S. sand 10-12	420.0	0.1580	0.2552	0.3827	0.5248	(45)
U.S. sand 14-16	266.0	0.1301	0.2248	0.3569	0.5326	"
U.S. sand 18-20	143.0	0.1228	0.2189	0.3565	0.5447	"
U.S. sand 30-35	54.7	0.1019	0.1890	0.3184	0.5000	"
U.S. Anthracite 5-6	503.0	-	0.3200	0.4961	0.7243	"
U.S. Anthracite 6-7	388.0	-	0.3403	0.5136	0.7335	"
U.S. Anthracite 7-8	331.0	-	0.3188	0.4916	0.7153	"
U.S. Anthracite 12-14	118.0	-	0.1927	0.3524	0.5945	"
Flintag 18-22	71.5	-	0.1730	0.3108	0.5163	"
Flintag 25-30	35.3	-	0.1456	0.2720	0.4670	"
U.K. Anthracite 18-22	35.7	-	0.1235	0.2427	0.4345	"
U.K. Anthracite 25-30	15.9	-	0.1014	0.2032	0.3703	"
U.K. sand 18-22	101.7	0.1093	0.1964	0.3221	0.4947	"
Ballotini 18-22	129.0	0.1077	0.1838	0.2888	0.4272	"
Ballotini 14-16	202.1	0.1242	0.1895	-	-	(57)
Ballotini 18-22	83.1	0.1377	0.2175	0.3238	-	"
Ballotini 22-25	71.9	0.1272	0.2053	0.3074	-	"
U.K. Anthracite 7-8	144.7	-	0.2193	0.3740	-	"

Table 24. continued

Material	Re_t	u/u_t				Ref.
		$\varepsilon = 0.5$	$\varepsilon = 0.6$	$\varepsilon = 0.7$	$\varepsilon = 0.8$	
U.K. Anthracite 8-10	102.6	-	0.2266	0.3886	-	(57)
U.K. Anthracite 10-12	86.8	-	0.1813	0.3385	-	"
U.K. Anthracite 14-16	48.3	-	0.1786	0.3231	-	"
Polystyrene 5-6	116.3	-	0.2100	0.3310	-	"
Polystyrene 6-7	92.6	-	0.2200	0.3620	-	"
Polystyrene 7-8	75.7	-	0.2059	0.3457	-	"
Polystyrene 8-10	62.2	-	0.1925	0.3324	-	"
U.K. sand 22-25	65.8	0.0924	0.1874	-	-	"
U.K. sand 25-30	50.9	0.0750	0.1533	-	-	"

tried for data obtained in the present experiments and Fan's data (45). Figure 75 shows the plot of $\frac{1 - \varepsilon}{1 - \varepsilon_{mf}}$ vs. $\frac{u - u_{mf}}{u_t}$. u_t is replaced by the intercept velocity u_i in Figure 76 and $\frac{1 - \varepsilon}{1 - \varepsilon_{mf}}$ was plotted against $\frac{u - u_{mf}}{u_i}$. The scatter of data points in Figure 76 is considerably less compared to that in Figure 75. In both the plots, generally, data with higher values of sphericity, ψ plotted above the points with lower sphericity. However, because of the difficulties involved in predicting u_{mf} and u_i accurately, this method may not find much acceptance among design engineers.

Comments on Various Prediction Models

The author of this dissertation believes that the prediction equation 153 will serve as an alternative method to predict the velocity-voidage relationship of particulately fluidized systems. The author's method offers an advantage in that it does not require the terminal settling velocity of the material to predict the velocity-voidage relationship. The calculation of terminal settling velocity of non-spherical particle is rather tedious and cumbersome.

The method proposed by Cleasby and Fan requires the terminal settling velocity of the particle to predict the velocity-voidage relationship. They propose that the terminal settling velocity u_t can be obtained by knowing the DSF of the material. However, as demonstrated herein, the DSF for a material changes with the particle Reynolds number. The practice of calculating the DSF from the sphericity is not recommended because DSF does not bear any fixed

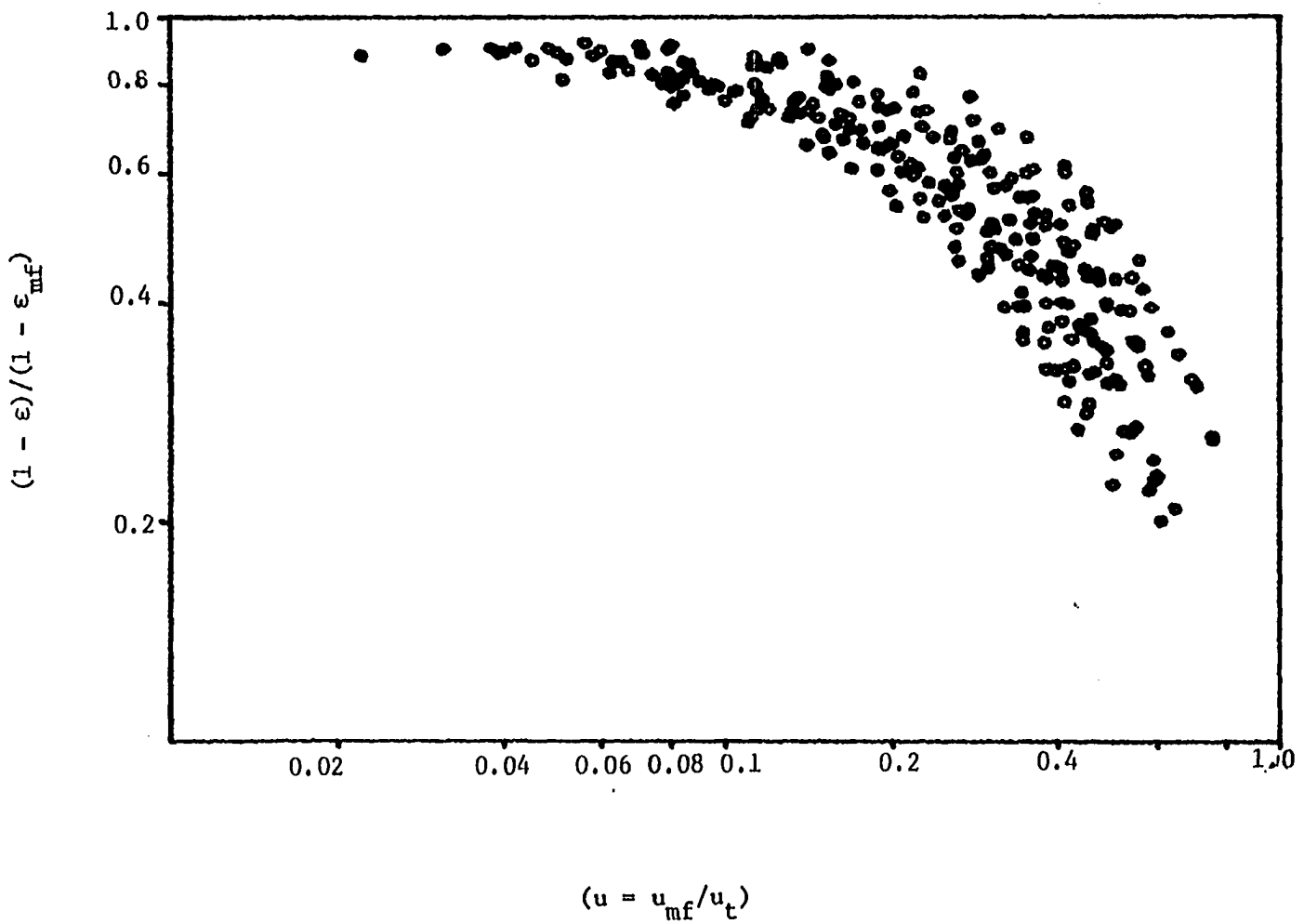

Figure 75. The relationship between log $((1-\varepsilon)/(1-\varepsilon_{mf}))$ and log $((u-u_{mf})/u_t)$ for fluidization data of present experiments and Fan (45)

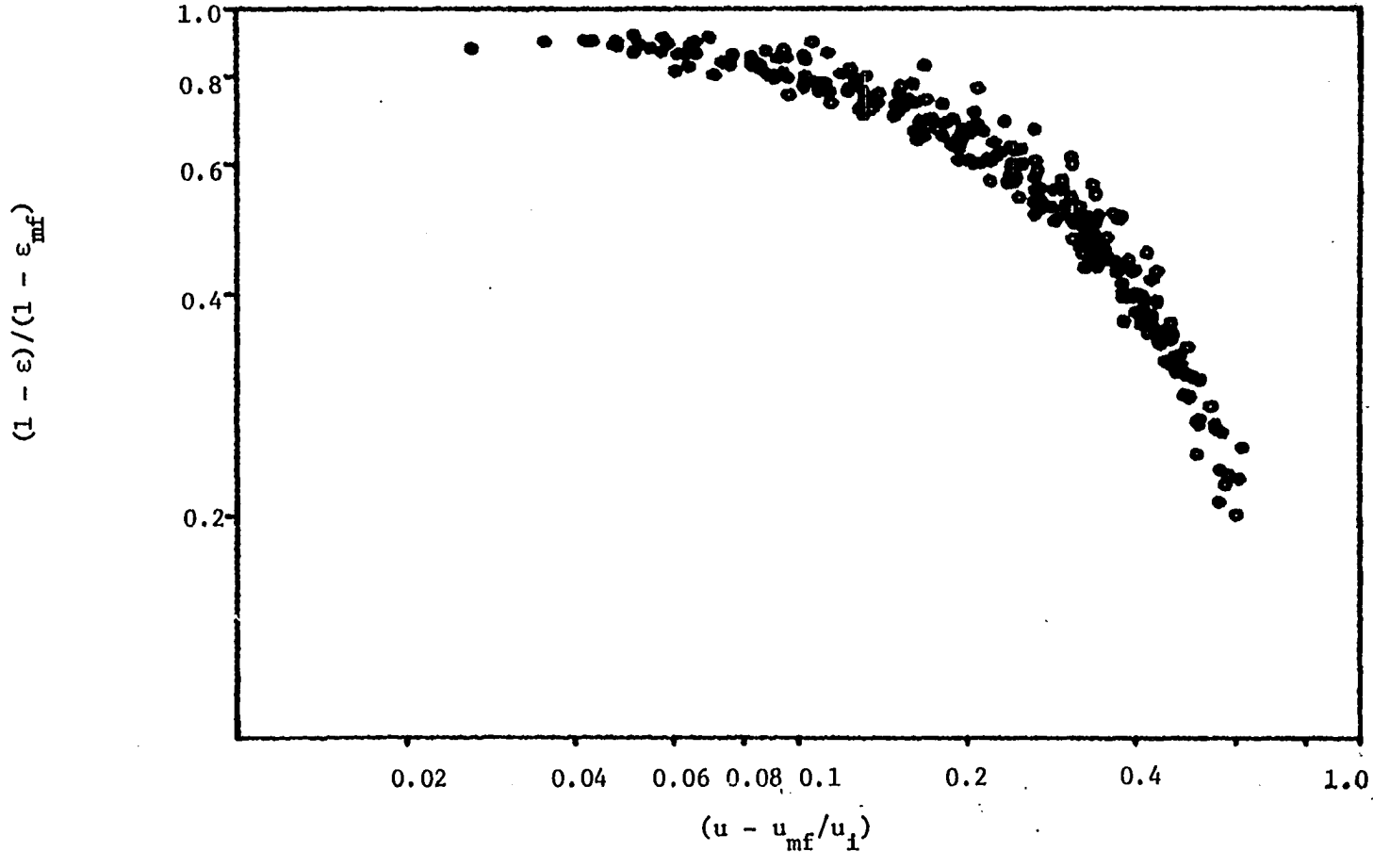

Figure 76. The relationship between log $((1-\varepsilon)/(1-\varepsilon_{mf}))$ and log $((u-u_{mf})/u_i)$ for fluidization data of present experiments and Fan (45)

relationship to the geometric shape factor. Therefore, calculating DSF from measured sphericity and obtaining the terminal settling velocity from DSF is rather unsound practice. Further, it was shown that the intercept velocity u_i cannot be predicted accurately for spherical or non-spherical particles. The prediction accuracy of velocity-voidage relationship by Cleasby and Fan method is also dependent upon an accurate estimation u_i. They present an empirical relationship between u_i, DSF and u_t to predict u_i which is a weak relationship as shown in Figure 71. Both of these foregoing difficulties will be reflected in the prediction accuracy of the velocity-voidage relationship.

Both the author's method and Cleasby and Fan's method were found to be unsatisfactory for heavier material such as garnet sand, brass metal punchings or stainless steel metal punchings. This is probably because the fluidization of these materials was not particulate. At present, no satisfactory model is available to predict the expansion data for materials which exhibit aggregative fluidization behavior. Until a satisfactory model is developed to predict the expansion data of garnet sand, the method proposed by Wood (110) could be used.

CONCLUSIONS AND RECOMMENDATIONS

A model to predict the expansion data of particulately fluidized non-spherical materials was developed in this study. In addition, certain fundamental questions regarding settling velocity, shape factors based on settling velocity and different permeability methods of determining sphericity were also studied. The conclusions of this study are as follows:

1. Theoretically it was shown that hydraulic shape factors such as DSF and Ω shape factors do not bear any relationship to geometric shape factors since both of these hydraulic shape factors are functions of Reynolds number. Any agreement between ψ and Ω is merely coincidental. However, this does not suggest that use of DSF or Ω as a shape factor in prediction models is inappropriate or unsatisfactory. Rather, it alludes to the fact that these two shape factors may change with particle size or temperature depending on the Reynolds number region, even though the material has a consistent geometric shape.

2. The sphericity values obtained for a loosely packed bed and tightly packed bed using an air permeability method were not very much different. But the sphericities obtained from the intercept of $\frac{\Delta P}{Lu}$ versus mass flow rate (equation 45b) and from back calculations from Ergun equation 45a did show some variability. This variation is due to variation of coefficient k_2 from 0.292, the value used in the Ergun equation.

The sphericities obtained from water permeability experiments were not significantly different from sphericities obtained from air

permeability data for most of the materials. Therefore, the air permeability can be used to obtain the sphericity needed in the prediction equation. The air permeability method is favored because the equipment is small and only a small sample volume is needed.

3. The Wen and Yu equations, number 71 and 74, for predicting minimum fluidization velocity were found to be very satisfactory to predict the minimum fluidization velocities of the materials studied herein. Equation 71 is somewhat superior but equation 74 is advantageous because it does not require a value of porosity or sphericity ψ for calculation.

The following conclusions relate to several models available for prediction of the velocity-voidage relationship for non-spherical materials.

4. The equation developed herein, which involves plotting $\log \frac{\varepsilon^3}{(1-\varepsilon)2} \cdot \frac{\rho(\rho_s - \rho)g}{S^3 \mu^2}$ versus $\log \frac{\rho u}{S(1-\varepsilon)\mu}$ for different non-spherical materials provides an alternative approach to predict the velocity-voidage relationship of particulately fluidized systems. The prediction equation is

$$\log Al = 0.71162 + 1.03956 \log Re_1 + 0.16572 (\log Re_1)^2 + 0.9 \log (\psi) \qquad (153)$$

This relationship is to be used only when the expanded bed porosity is below 0.9. Sphericity was found to be the most satisfactory shape factor for this method of prediction. This method does not require the unhindered settling velocity of the material to predict the expansion.

5. The 'n' slope of non-spherical materials can be predicted reasonably well by the equations proposed by Cleasby and Fan (equations 135 and 136). However, the intercept velocity u_i, shows considerable scatter from the relationship proposed by them (equation 137).

6. Garside and Al-Dibouni's logistic equations cannot be used in their present form to predict the expansion data of non-spherical particles.

7. A plot of $\frac{1 - \varepsilon}{1 - \varepsilon_{mf}}$ versus $\frac{u - u_{mf}}{u_i}$ to correlate the fluidization data as suggested by Beranek and Klumper, shows some degree of promise as a predictive tool. However, the scatter of data points from a mean line is too high for an accurate prediction to be obtained. Furthermore, the need for values of u_i and u_{mf} detract from this model. Recommendation for future work include the following:

The present expansion models for non-spherical particles are not satisfactory for predicting expansions at very high porosities ($\varepsilon < 0.9$). Garside and Al-Dibounis logistic approach is more accurate for predicting expansion at very high porosities. Therefore, it would be advantageous if a model similar to the logistic model proposed by them is developed for non-spherical materials. In order to do this, fluidization data are required from very low particle Reynolds number to very high particle Reynolds number for a material of particular shape. It would be advantageous to use manufactured particles of known shape, since it would eliminate the variability in particle shape with size

fraction typically observed for natural materials such as coal. This method of prediction needs no knowledge of intercept velocity u_i; therefore, any inaccuracies that result from poor estimation of u_i will also be eliminated.

BIBLIOGRAPHY

1. Adler, I. L. and Happel, J. The fluidization of uniform smooth spheres in liquid media. Chem. Eng. Proc. Sym. Ser. 58, No. 38 (1962), 98-105.

2. Akkoyunlu, A. Prediction of expansion of graded filter media. Unpublished technical report. Library, Iowa State University of Science and Technology, Ames, Iowa, 1981.

3. Albertson, M. L. Effect of shape on fall velocity of gravel particles. University of Iowa, College of Engineering Studies in Engineering Bulletin No. 34 (1953), 241-261.

4. Al-Dibouni, M. R. and Garside, J. Particle mixing and classification in liquid fluidized beds. Transactions of Institute of Chemical Engineers, 57 (1979), 94-103.

5. Allen, T. Particle size measurement. 2nd edition. Hall, London: Chapman and Hall, 1975.

6. American Society for Testing and Materials. 1968 Book of ASTM Standards. Part 2. Philadelphia, Pa: 1968.

7. Austin, L. G., Gardner, R. P. and Walker, P. L., Jr. The shape factors of coal ground in standard hardgrove mill. Fuel, Journal of Fuel Science, 42 (1963), 319-323.

8. Bailey, A. B. Sphere drag coefficients for subsonic speeds in continuum and free molecule flows. Journal of Fluid Mechanics, 65 (1973), 401-410.

9. Bakhmeteff, B. A. and Feodoroff, N. V. Flow through granular media. Journal of Applied Mechanics. Transactions of ASME, 59 (1937), A97-A104.

10. Barnea, E. and Mendick, R. L. Correlation for minimum fluidization velocity. Transactions of the Institute of Chemical Engineers, 53 (1975), 278-281.

11. Barnea, E. and Mizrahi, J. A generalized approach to the fluid dynamics of particulate systems. Part 1: General correlation for fluidization and sedimentation in solid multiparticle systems. The Chemical Engineering Journal, 5 (1973), 171-189.

12. Becker, H. A. The effects of shape and Reynolds number on drag in the motion of a freely oriented body in an infinite fluid. The Canadian Journal of Chemical Engineering, 37 (1959), 85-91.

13. Bena, J., Havalda, I. and Matas, J. Incipient fluidization velocities of polydisperse materials. Collection of Czech. Chem. Communications, 36 (1971), 3563-3587.

14. Bena, J., Havalda, I., Bafrnec, M. and Ilavsky, J. The velocities at incipient fluidization of polydisperse materials I. Theoretical. Collection of Czech. Chem. Communications, 33 (1968), 2620-2635.

15. Bena, J., Havalda, I., Bafrnec, M. and Ilavsky, J. The velocities at incipient fluidization of polydisperse materials II. Experimental results and design equation. Collection of Czech. Chem. Communications, 33 (1968), 2833-2853.

16. Bena, J., Ilavsky, J., Kossaczsky, E., and Nenzil, L. Changes of the flow character in a fluidized bed. Collection of Czech. Chem. Communications, 28 (1963), 293-308.

17. Bena, J., Ilavsky, J., Kossaczsky, E. and Valtyni, J. Fluidizing-point velocities of non-spherical particles. Collection of Czech. Chem. Communications, 28 (1963), 555-569.

18. Beranek, J. Dynamic properties of fluidized beds III. Influence of particle shape on the dynamic properties of the bed. Collection of Czech. Chem. Communications, 25 (1960), 2319-2233.

19. Beranek, J., and Klumpar, I. Dynamic properties of fluidized beds II. A new theory of fluidization. Collection of Czech. Chem. Communications, 23 (1958), 18-29.

20. Blake, C. F. The resistance of packing to fluid flow. Transactions of American Institute of Chemical Engineers, 14 (1922), 415-421.

21. Bourgeoise, P. and Grenier, P. The ratio of terminal velocity to minimum fluidizing velocity for spherical particles. The Canadian Journal of Chemical Engineering, 46 (1968), 325-328.

22. Briggs, L. T., McCulloch, D. S. and Moser, F. The hydraulic shape of sand particles. Journal of Sedimentary Petrology, 32 (1962), 645-657.

23. Brownell, L. G. and Katz, D. L. Flow of fluids through porous media. I. Single homogeneous fluids. Chemical Engineering Progress 43 (1947), 537-545.

24. Burke, S. P. and Plummer, W. B. Gas flow through packed columns. Industrial and Engineering Chemistry, 20 (1928), 1196-1200.

25. Cairns, E. J. and Prausnitz, J. M. Longitudinal mixing in fluidization. American Institute of Chemical Engineers Journal, 6 (1960), 400-405.

26. Camp, T. R. Theory of water filtration. Journal of the Sanitary Engineering Division, American Society of Civil Engineers, 90 (1964), 1-30.

27. Carman, P. C. Flow through granular beds. Transactions of Institute of Chemical Engineers, London, 15 (1937), 150-166.

28. Carvalho, W. J. Fluidization of crushed anthracite coal. Unpublished M.S. thesis, Library, Iowa State University of Science and Technology, Ames, Iowa, 1970.

29. Chilton, T. H. and Colburn, A. P. Pressure drop in packed tubes. Industrial and Engineering Chemistry, 23 (1931), 913-919.

30. Chong, Y. S. Ratkowsky, A. and Epstein, N. Effect of particle shape on hindered settling in creeping flow. Powder Technology, 23 (1979), 55-66.

31. Clark, J. W., Viessman, W. and Hammer, M. J. Water supply and pollution control. Scranton, Pennsylvania: International Textbook Company, 1971.

32. Cleasby, J. L. and Fan, K. S. Predicting fluidization and expansion of filter media. Journal of the Sanitary Engineering Division, American Society of Civil Engineers, 107 (1981), 455-471.

33. Corey, A. T. Influence of shape on fall velocity of sand grains. Unpublished M.S. Thesis, Library, Colorado A. M. College, Fort Collins, Colorado, 1949.

34. Coulson, J. M. The flow of fluids through granular beds: Effect of particle shape and voids in streamline flow. Transactions of Institute of Chemical Engineers, 27 (1949), 237-259.

35. Coulson, J. M. and Richardson, J. F. Chemical Engineering. Volume 2. 2nd Edition. New York, N.Y.: Pergamon Press, Inc., 1968.

36. Davidson, J. F. and Harrison, D. Fluidized particles. New York, N.Y.: The syndics of the Cambridge University Press, 1963.

37. Davidson, J. F. and Harrison, D. Fluidization. New York, N.Y.: Academic Press, 1971.

38. Davies, R. A simple feature-space representation of particle shape. Powder Technology, 12 (1975), 111-124.

39. Davis, C. N. Definitive equations for the fluid resistance of spheres. Proceedings of the Physical Society (London) 57 (1945), 259-270.

40. Epstein, N., Leclair, B. P., and Pruden, B. B. Liquid fluidization of binary particle mixtures I. Overall bed expansion. Chemical Engineering Science 36 (1981), 1803-1809.

41. Ergun, S. Fluid flow through packed columns. Chemical Engineering Progress 48 (1952), 89-94.

42. Ergun, S. Determination of geometric surface area of crushed porous solids. Analytical Chemistry 24 (1952), 388-393.

43. Fair, G. M. and Hatch, L. P. Fundamental factors governing stream-like flow of water through sand. Journal of American Water Works Association 25 (1963), 1551-1565.

44. Fair, G. M., Geyer, J. C., and Okun, D. A. Water and Wastewater Engineering. Volume 2. New York, N.Y.: John Wiley and Sons, 1968.

45. Fan, K. S. Sphericity and fluidization of granular filter media. Unpublished M.S. Thesis. Library, Iowa State University of Science and Technology, Ames, Iowa, 1978.

46. Fidleris V. and Whitmore, R. L. Experimental determination of the wall effect for spheres falling axially in cylindrical vessels. British Journal of Applied Physics, 12 (1961), 490-494.

47. Fisher, J. W. Methods of particle shape measurement for use in correlation of expansion and flow rate in granular filter beds. Unpublished paper. London: London, England Library, University College, 1976.

48. Fleming, N. C. Form and function of sedimentary particles. Journal of Sedimentary Petrology 35 (1965), 381-390.

49. Fouda, A. F., and Capes, C. E. Calculation of large numbers of terminal velocities or equivalent particle diameters using polynomial equations fitted to the Heywoods tables. Powder Technology 13 (1976), 291-293.

50. Fouda, A. F., and Capes, C. E. Hydrodynamic particle volume and fluidized bed expansion. The Canadian Journal of Chemical Engineering 55 (1977), 386-391.

51. Francis, A. W. Wall effect in falling ball method for viscosity. Physics 4 (1933), 403-406.

52. Frantz, J. F. Minimum fluidization velocities and pressure drop in fluidized beds. Chemical Engineering Progress Symposium 62 (1966), 21-31.

53. Furukawa, J. and Ohmae T. Liquid like properties of fluidized systems. Industrial and Engineering Chemistry 50. (1958), 821-828.

54. Garside, J. and Al-Dibouni, M. R. Velocity-voidage relationship for fluidization and sedimentation in solid-liquid systems. Ind. Eng. Chem. Process Design and Development 16 (1977), 206-214.

55. Goddard, K., and Richardson, J. F. Correlation of data for minimum fluidizing velocity and bed expansion in particulately fluidized systems. Chemical Engineering Science 24 (1969), 363-367.

56. Graton, L. C., and Fraser, H. J. Systematic packing of spheres with particular relation to porosity and permeability. Journal of Geology 43 (1935), 785-909.

57. Gunasingham, K., Lekkas, T. D., Fox, G. T. J., and Graham, N. J. D. Predicting the expansion of granular filter beds. Filtration and Separation 16:619-623, 1979. (Original data were obtained from N.J.D. Graham, Imperial College of Science and Technology, London, private communication, 1981).

58. Harrison, D., Davidson, J. F. and Kock, J. W. On the nature of aggregative and particulate fluidization. Transactions of Institute of Chemical Engineers 39 (1961), 202-211.

59. Heiss, J. F. and Coull, J. The effect of orientation and shape on the settling of non-isometric particles in a viscous medium. Chemical Engineering Progress 48 (1952), 133-140.

60. Hessett, N. J. Mechanism of fluidization. British Chemical Engineer 6 (1961), 777-780.

61. Heywood, H. The scope of particle size analysis and standardization. Symposium on Particle Size Analysis Supplement Transaction of Institute of Chemical Engineers 25 (1947), 14-24.

62. Heywood, H. Calculation of particle terminal velocities. Journal of Imperial College Chemical Engineering Society, 4 (1948), 17-29.

63. Heywood, H. Uniform and non-uniform motion of particles in fluids. Symposium on the interaction between fluids and particles. Proceeding of Institution of Chemical Engineers 1962 (1962), 1-8.

64. Hoffman, R. F., Lapidus, L. and Elgin, J. C. The mechanics of vertically moving fluidized systems: IV. Application to batch-fluidized systems with mixed particle sizes. A. I. Ch. E. Journal 6 (1960), 321-324.

65. Johnstone, H. F., Pigford, R. L. and Chapin, J. H. Heat transfer to cloud of particles. Transactions of the American Institute of Chemical Engineers 37 (1941), 95-135.

66. Jottrand, R. An experimental study of mechanism of fluidization. Journal of Applied Chemistry, Vol. 2, Supplementary Issue, No. 1 (1952), 517-526.

67. Kozeny, J. Über Kapillare Leitung des Wassers in Boden. Sitzungsber. Abstract IIIa. Akad Sirs. (Vienna, Austria) 136 (1927), 276-283.

68. Krumbein, W. C. Measurement of geological significance of shape and roundness of sedimentary particles. Journal of Sedimentary Petrology 2 (1941), 64-72.

69. Kumar, A. Effect of surface texture on fall behavior of cylinders and disks in a quiescent fluid. Unpublished Ph.D. Dissertation. Library, Colorado State University, Fort Collins, Colorado, 1967.

70. Kunii, D. and Levenspiel, D. Fluidization Engineering. John Wiley, New York, N.Y., 1969.

71. Lamb, H. Hydrodynamics. New York: Dover Publications, 1945.

72. Letan, R. On vertical dispersed two phase flow. Shorter Communications. Chemical Engineering Science 29 (1974), 621-624.

73. Leva, Max. Fluidization. McGraw-Hill Book Co., Inc., New York, N.Y., 1959.

74. Lewis, E. W. and Bowerman, E. W. Fluidization of solid particles in liquids. Chemical Engineering Progress 48 (1952), 603-610.

75. Lewis, W. K., Gilleland, E. R., and Bauer, W. C. Characteristics of fluidized particles. Industry Engineering Chemistry 41 (1949), 1117-1949.

76. Loeffler, A. L., Jr. Mechanism of hindered settling and fluidization. Unpublished Ph.D. dissertation, Library, Iowa State University of Science and Technology, Ames, Iowa, 1953.

77. Malaika, J. Effect of shape of particles on their settling velocity. Unpublished Ph.D. dissertation. Library, University of Iowa, Iowa City, Iowa, 1949.

78. McNown, J. S., Lee, H. M., McPherson, M. B., Engez, S. M. Influence of boundary proximity on the drag of spheres, VII. International Congress of Applied Mechanics, London, England, September, 1948.

79. McNown, J. S. and Malaika, J. Effect of particle shape on settling at low Reynolds numbers. Transactions of the American Geophysical Union 31 (1950), 74-82.

80. Mertes, T. S., Rhodes, H. B. Liquid-Particle behavior Part I. Chemical Engineering Progress 51 (1959), 429-432.

81. Neuzil, L. and Hrdina, M. Effect of wall on the expansion of a fluidized bed. Collection of Czech. Chem. Communications 30 (1965), 752-767.

82. Pettyjohn, E. S. and Christiansen, G. B. Effect of particle shape on free-settling rates of isometric particles. Chemical Engineering Progress 44 (1948), 157-172.

83. Pinchbeck, P. H. and Popper F. Critical and terminal velocities in fluidization. Chemical Engineering Science 6 (1956), 57-64.

84. Pirie, J. M. in the discussion of Coulson, J. M. Flow of fluids through granular beds: Effect of particle shape and voids in stream line flow. Transactions of Institute of Chemical Engineers 27 (1949), 237-257.

85. Presler, A. F. Effect of particle shape on fluidization and hindered settling. Unpublished Ph.D. thesis. Library, Iowa State University of Science and Technology, Ames, Iowa, 1956.

86. Pruden, B. B. Particle size segregation in particulately fluidized beds. Unpublished M.A. Sc. Thesis. Library, University of British Columbia, British Columbia, Canada, 1964.

87. Reuter, H. On the nature of bubbles in gas and liquid fluidized beds. Chemical Engineering Progress Symposium Series 62, No. 62 (1966), 92-99.

88. Richardson, J. F. Fluidization. Chapter 2. Incipient fluidization and particulate systems. In J. F. Davidson and D. Herrison, eds. New York, N.Y.: Academic Press, 1971.

89. Richardson, J. F. and Jeromino, M. A. de S. Velocity-voidage relationship for sedimentation and fluidization. Chemical Engineering Science 34 (1979), 1419-1422.

90. Richardson, J. F. and Meikle, R. A. Sedimentation and fluidization Part III. The sedimentation of uniform fine particles and of two component mixture of solids. Transactions of Institute of Chemical Engineers 39 (1961), 348-356.

91. Richardson, J. F. and Smith, J. W. Heat transfer to liquid fluidized systems and to suspensions of coarse particles in vertical transport. Transactions of Institute of Chemical Engineers 40 (1962), 13-22.

92. Richardson, J. F. and Zaki, W. N. Sedimentation and fluidization Part I. Transactions of Institute of Chemical Engineers 32 (1954), 35-53.

93. Romero, J. B. and Johnson, L. N. Factors affecting fluidized beds quality. Chemical Engineering Progress, Symposium Series 58, No. 38 (1962), 28-37.

94. Roscoe, R. Viscosity of suspensions of rigid spheres. British Journal of Applied Physics 3 (1952), 267-269.

95. Schulz, E. F., Wilde, R. H., and Albertson, M. L. Influence of shape on fall velocity of sediment particles. Missouri River Division Sedimentation Series Report No. 5. Corps of Engineers, U.S. Army, Omaha, Nebraska.

96. Sen-Gupta, P. and Rao, M. N. The prediction of minimum fluidization velocity. Indian Chemical Engineer 13 (1971), 11-16.

97. Simpson, H. C. and Rodger B. W. The fluidization of light solids by gases under pressure and heavy solids by water. Chemical Engineering Science 16 (1961), 153-180.

98. Sneed, E. D. and Folk, R. L. Pebbles in the lower Colorado River, Texas: A study in particle morpho genesis. Journal of Geology 66 (1958), 114-150.

99. Squires, L. and Squires, W. Sedimentation of thin discs. Transactions of American Institute of Chemical Engineers 33 (1937), 1-11.

100. Tiller, F. M. Compressible cake filtration. In Scientific Basis of Filtration. NATO Advanced Study Institute Series. Ed. K. J. Ives. Leyden: Noordhoff, 1975.

101. U.S. Inter Agency Committee on Water Resources. A study of methods used in measurement and analysis of sediment load in streams. Subcommittee on Sedimentation Report No. 12: Some fundamentals of particle size analysis. Washington, D.C.: Govt. Printing Office, Dec. 1957.

102. Wadell, H. Volume shape and roundness of rock particles. Journal of Geology 40 (1932), 443-457.

103. Wadell, H. Sphericity and roundness of rock particles. Journal of Geology 41 (1933), 310-331.

104. Wadell, H. The coefficient of resistance as a function of Reynolds number for solids of various shapes. Journal of Franklin Institute 217 (1934), 459-490.

105. Wadell, H. Volume, shape and roundness of quartz particles. Journal of Geology 43 (1935), 250-280.

106. Wen, C. Y. and Yu, Y. H. Mechanics of fluidization. Chemical Engineering Progress Symposium Series 62, No. 62 (1966), 100-111.

107. Whitmore, R. L. The relationship of the viscosity to the settling rate of slurries. Journal of the Institute of Fuel 30 (1957), 328-342.

108. Wicke, E., Hedden, K. Stromungsformen und Warmeubetragung in von tuft aufgewirbelten Schuttgutschichten. Chem. Eng. Tech. 24 (1952), 82-91.

109. Wilhelm, R. H. and Kwauk, M. Fluidization of solid particles. Chemical Engineering Progress 44 (1948), 201-218.

110. Wood, C. F. Expansion and intermixing of garnet and silica sand during backwashing of granular filters. Unpublished M.S. Thesis. Library, Iowa State University of Science and Technology, Ames, Iowa, 1973.

111. Zabrodsky, S. S. Hydrodynamics and heat transfer in fluidized beds. Cambridge, Mass.: M.I.T. Press, 1966.

112. Zenz, F. A. and Othmer, D. F. Fluidization and fluid particle systems. New York, N.Y.: Reinhold Publishing Corporation, 1960.

113. Zuber, N. On the dispersed two-phase flow in laminar flow. Chem. Eng. Science 19 (1964), 897-917.

ACKNOWLEDGMENTS

The author wishes to express his sincere appreciation to his major professor Dr. J. L. Cleasby for his guidance and helpful suggestions, encouragement and unstinted cooperation during the entire course of this study.

Acknowledgment is also expressed to Professor E. R. Baumann who by providing necessary funds whole heartedly supported the author and his studies.

The author wishes to thank Dr. R. G. Bautista who served as the committee member for the minor and Dr. C. S. Oulman and Dr. B. R. Munson for serving as the members of the graduate committee.

The author also would like to thank his friends and colleagues for their help during his academic program at Iowa State University.

Last but not the least, the author expresses his gratitude to his parents for all the help they have extended to him.

APPENDIX I

The algorithims used to describe $C_D\ Re_t^2$ vs. Re_t and C_D/Re_t vs. Re_t plot for spherical particles.

$$y_1 = C_D\ Re_t^2 = \frac{4}{3}\ g\ d_{eq}^3\ \rho(\rho_s - \rho)/\mu^2$$

$$y_2 = C_D/Re_t = \frac{4g(\rho_s - \rho)\mu}{3\rho^2\ u_t^3}$$

$$REN1 = \rho\ u_N.d_{eq}/\mu\ .$$

$$REN2 = \rho.u_t.d_h/\mu\ .$$

(a) To obtain u_N

```
IF(Y1.LE.12.4) REN1 = Y1/24
IF((Y1.LE.26.5).AND.(Y1.GT.12.4)) RENI = 0.05023*Y1**0.9127
IF((Y1.LE.94).AND.(Y1.GT.26.5)) REN1 = 0.0578*Y1**0.86987
IF((Y1.LE.410).AND.(Y1.GT.94)) REN1 = 0.07393*Y1**0.8157
IF((Y1.LE.1000).AND.(Y1.GT.410)) REN1 = 0.093*Y1**0.7743
IF((Y1.LE.3700).AND.(Y1.GT.1000)) REN1 = 0.1585*Y1**0.70035
IF((Y1.LE.10000).AND.(Y1.GT.3700)) REN1 = 0.228*Y1**0.5561
IF((Y1.LE.40000).AND.(Y1.GT.10000)) REN1 = 0.25*Y1**0.648
IF((Y1.LE.400000).AND.(Y1.GT.40000)) REN1 = 0.464*Y1**0.5897
IF(Y1.GT.400000) REN1 = SQRT (Y1/0.44)
```

(b) To obtain d_h

```
IF(Y2.GT.99) REN2 = SQRT(24/Y2)
IF((Y2.LE.99).AND.(Y2.GT.26.5)) REN2 = 5.6042*Y2**-0.52592
IF((Y2.LE.26.5).AND.(Y2.GT.3.4667)) REN2 = 5.8715*Y2**-0.54014
IF((Y2.LE.3.4667).AND.(Y2.GT.1.38)) REN2 = 5.97783*Y2**-0.55458
IF((Y2.LE.1.38).AND.(Y2.GT.0.41)) REN2 = 6.00975*Y2**-0.57111
IF((Y2.LE.0.41).AND.(Y2.GT.0.0667)) REN2 = 5.83186*Y2**-0.6048
IF((Y2.LE.0.0667).AND.(Y2.GT.0.03)) REN2 = 5.30574*Y2**-0.63976
IF((Y2.LE.0.03).AND.(Y2.GT.0.0107)) REN2 = 4.732427*Y2**-0.67233
IF((Y2.LE.0.0107).AND.(Y2.GT.0.002167)) REN2 = 4.40975*Y2**-0.6879
IF((Y2.LE.0.002167).AND.(Y2.GT.0.0011))) REN2 = 2.94761*Y2**-0.75356
IF((Y2.LE.0.0011).AND.(Y2.GT.0.00046)) REN2 = 2.22207*Y288-0.79504
```

APPENDIX II

```
C THIS PROGRAM CALCULATES THE POROSITY AT A GIVEN SUPERFICIAL
C VELOCITY USING THE COMBINED EQUATION OF
      CHARACTER*30 TITLE
      COMMON RHO, RHOS,S,XMU, PSI,G
      REAL LEFT, RIGHT, EPS,M
      LEFT = 0.40
      RIGHT = 1.0
      EPS = 0.005
      G = 32.17
10    READ(5,11) TITLE
11    FORMAT (A30)
      WRITE(6.12) TITLE
12    FORMAT('0',20X,A30)
      WRITE(6,14)
14    FORMAT('0','U(CM/S)', T12,'ACTUAL',T24,'PREDICTED'/
     + T12,'POROSITY",T24,'POROSITY')
      READ(5,*) RHOS,RHO,DEQ,PSI,EO,XMU,DOD,DSF,PSI1
      S=6/(PSI*DEQ)
15    READ(5,*)U,EA,REO,K,1
      CALL SOLVE(LEFT,RIGHT,E,EPS,U)
20    WRITE(6,40) U,EA,E
40    FORMAT('0',F8.3,5X,2(F6.3,3X))
      IF(K-1)15,50,15
50    IF(L-1)10,60,10
60    CONTINUE
      CALL EXIT
      END
      SUBROUTINE SOLVE (LEFT,RIGHT,ROOT,EPS,B)
      COMMON RHO,RHOS,S,XMU,PSI,G
      REAL LEFT, RIGHT, ROOT, EPS
      REAL X1,X2,F1
      FUNC(X,B)=A10G10(X**3*(RHOS-RHO)*RHO*G/(1-X)**2/S**3/XMU**2)
     1-0,71162-1.03956*A10810(R*RHO/(S*XMU*(1-X)))
     2-0,165/7*(ALOG10(R*RHO/(S*XMU*(1-X))))**2
     3-0.89895*AL0610(PSI)
      X1=LEFT
      X2=RIGHT
      F1=FUNC(X1,B)
      ROOT=(X1+X2)/2.0
5     IF((ROOT-XL).LE.EPS) GO TO 10
      IF(F1*FUNC(ROOT,B).GT.0.0) THEN
      XL=ROOT
      ELSE
      X2=ROOT
      END IF
      ROOT=(X1+X2)/2.0
```

```
4300          GO TO 5
4400   10     CONTINUE
4500          RETURN
4600          END
```

APPENDIX III

Plots of Predicted Porosity Versus Actual Porosity for the Data of Various Investigators

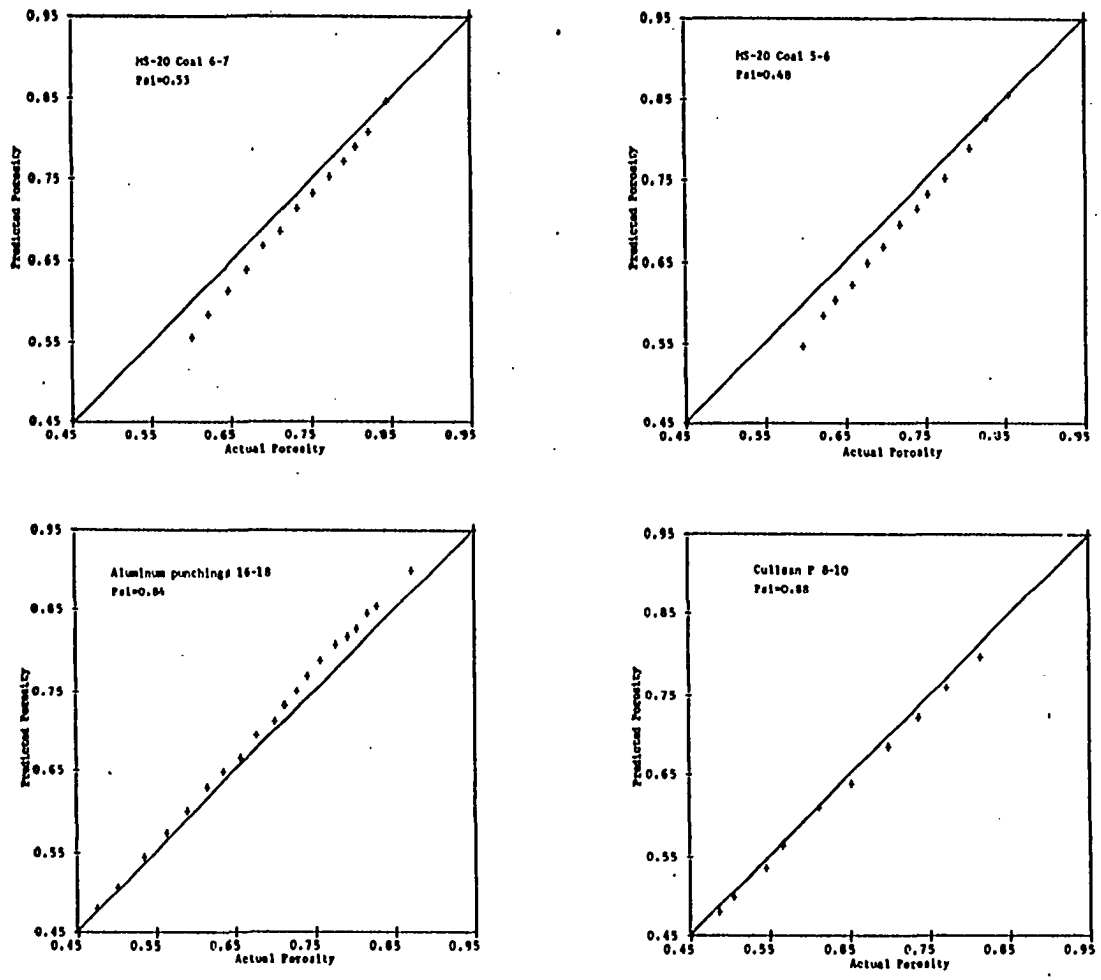

Figure 77. The relationship between predicted porosity and actual porosity for some materials used in present experiments

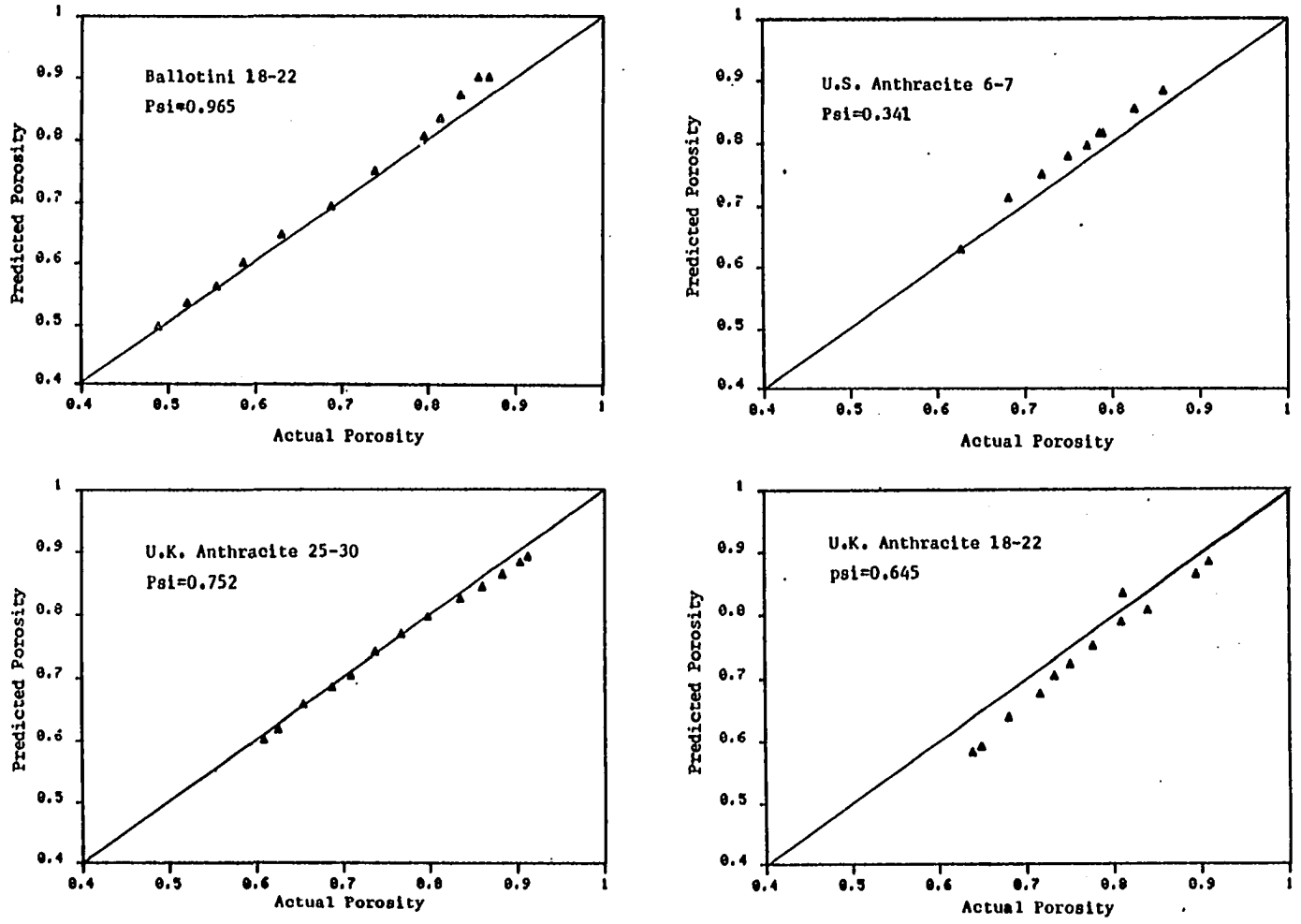

Figure 78. The relationship between predicted porosity and actual porosity for the data of Fan (45)

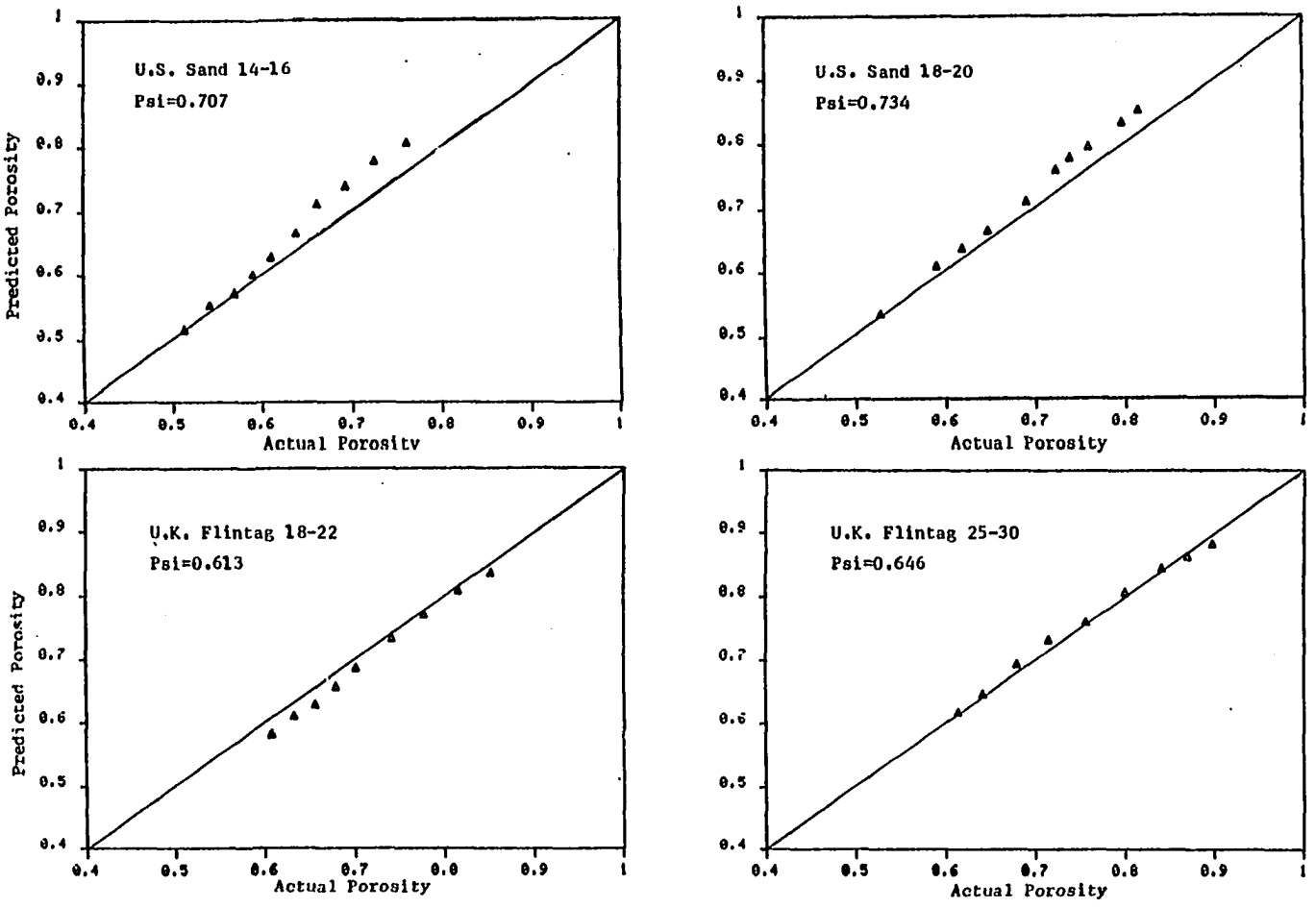

Figure 78. continued

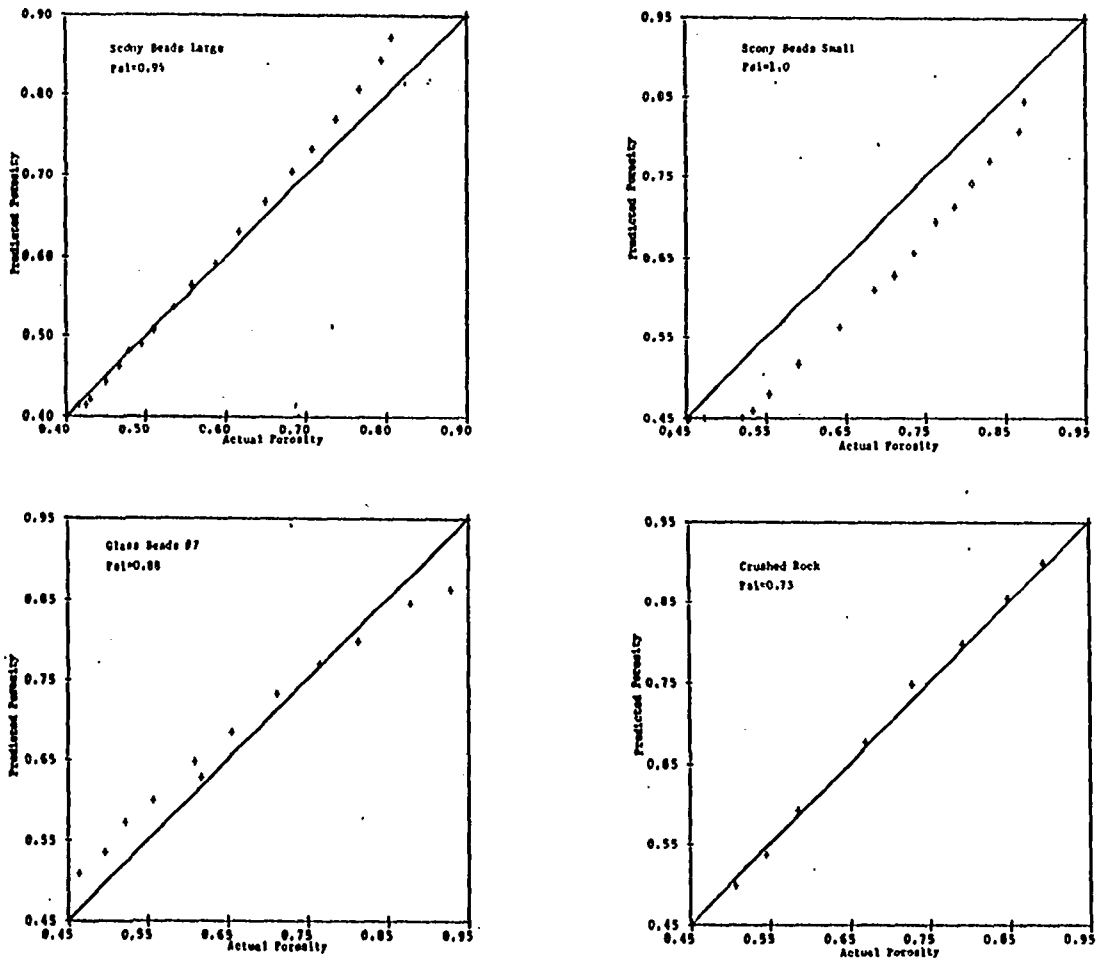

Figure 79. The relationship between predicted porosity and actual porosity for the data of Wilhelm and Kwauk (109)

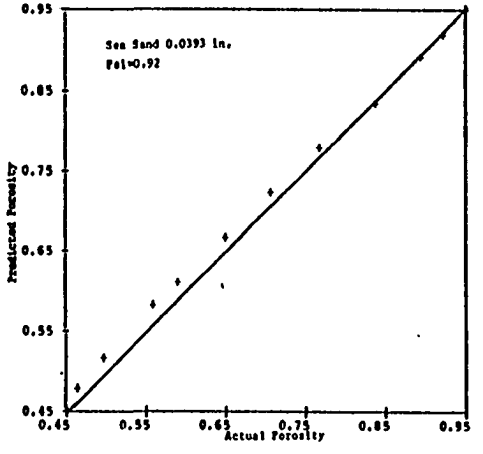

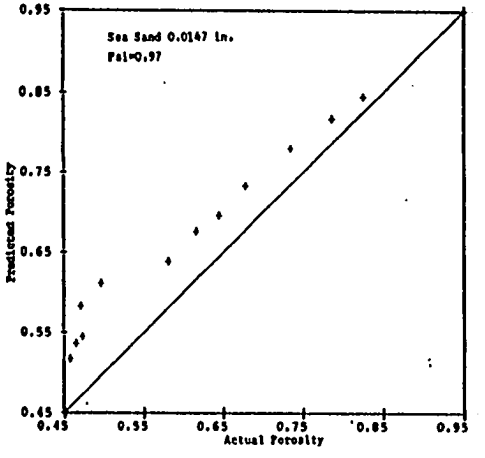

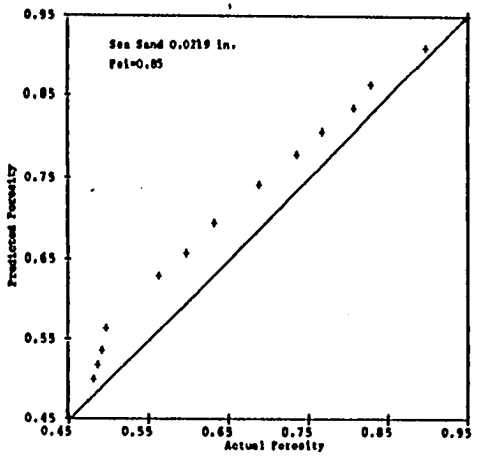

Figure 79. continued

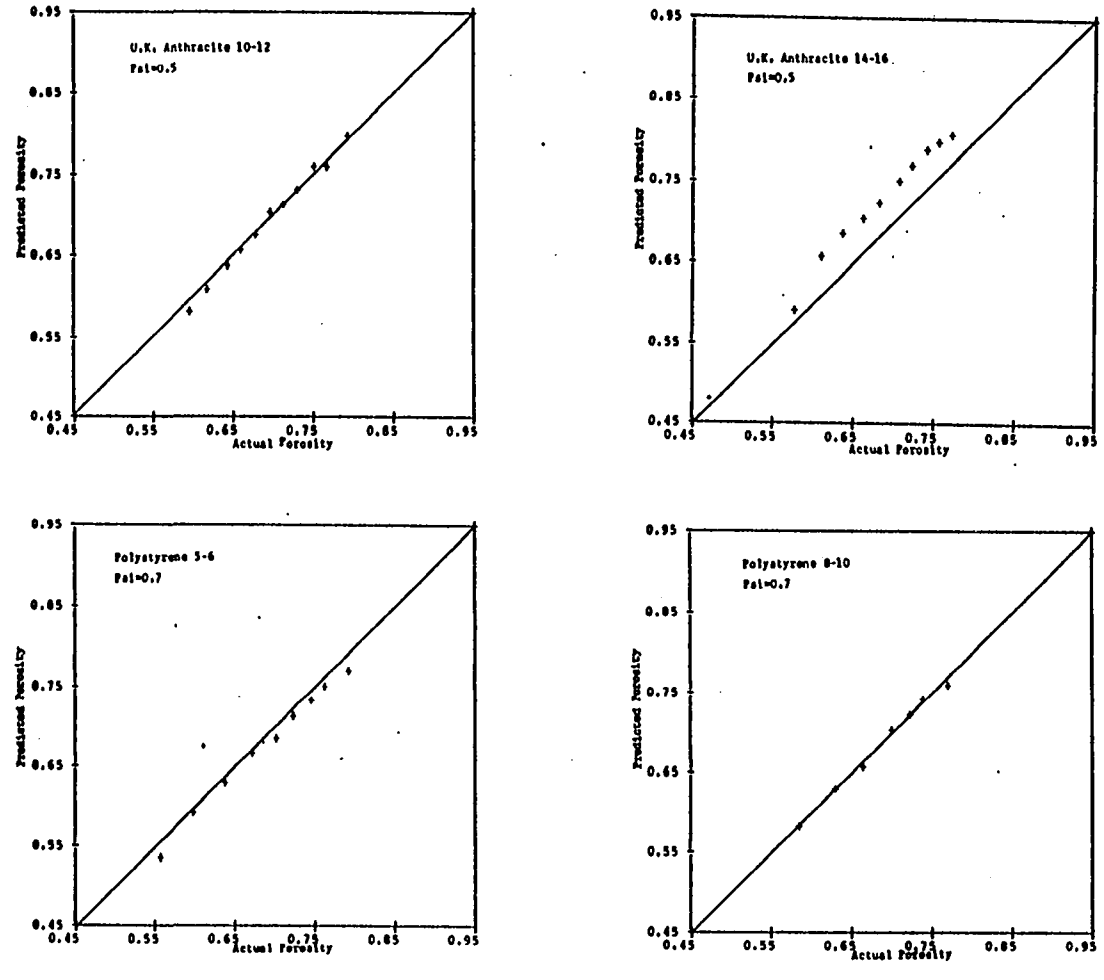

Figure 80. The relationship between predicted porosity and actual porosity for data of Gunasingham et al. (57)

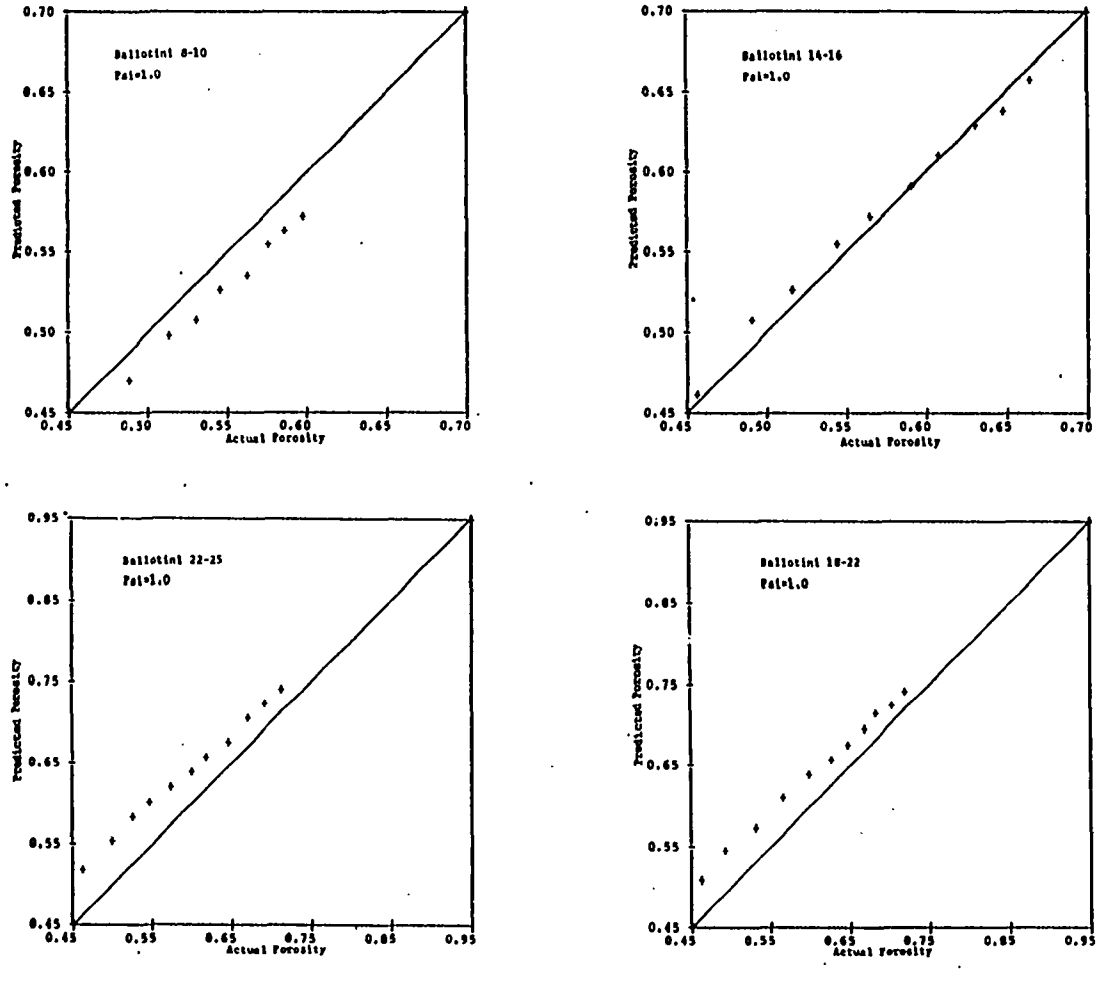

Figure 80. continued

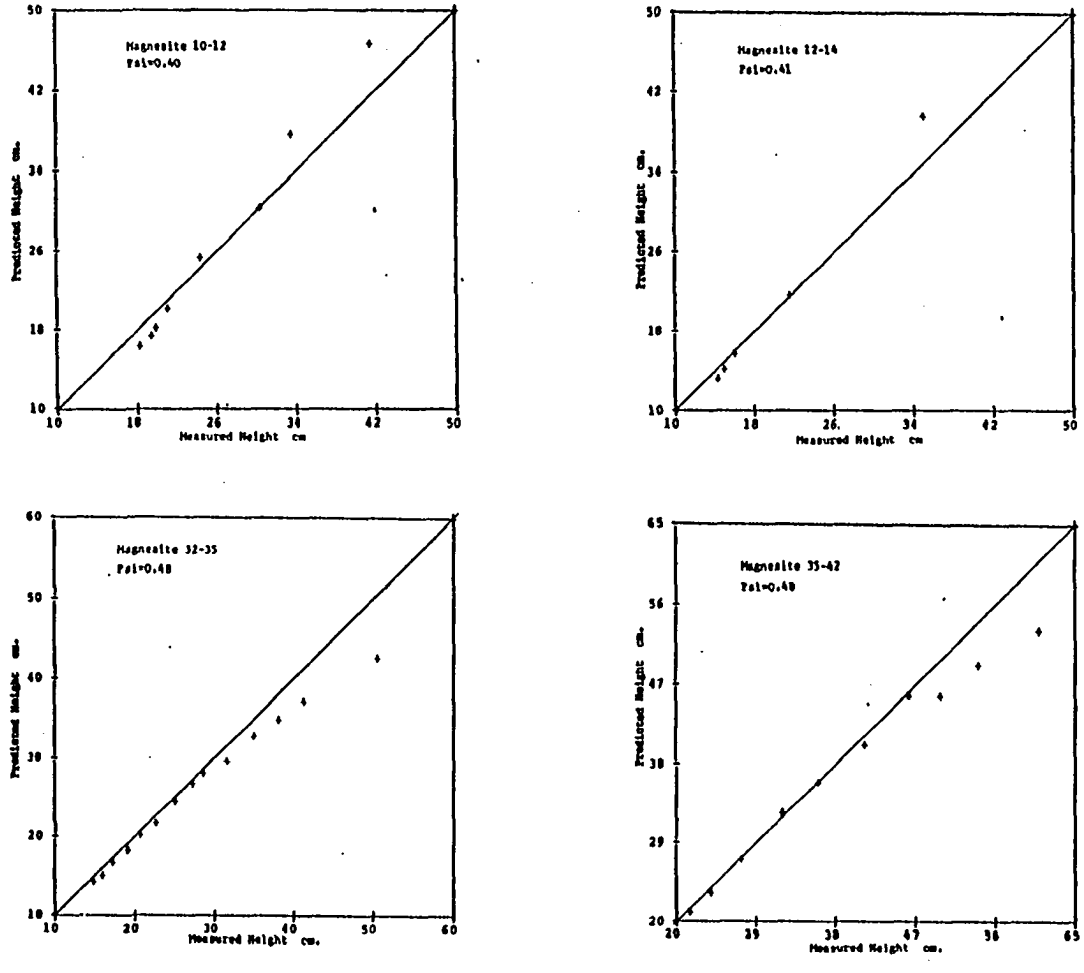

Figure 81. The relationship between predicted height and measured height for the data of Presler (85)

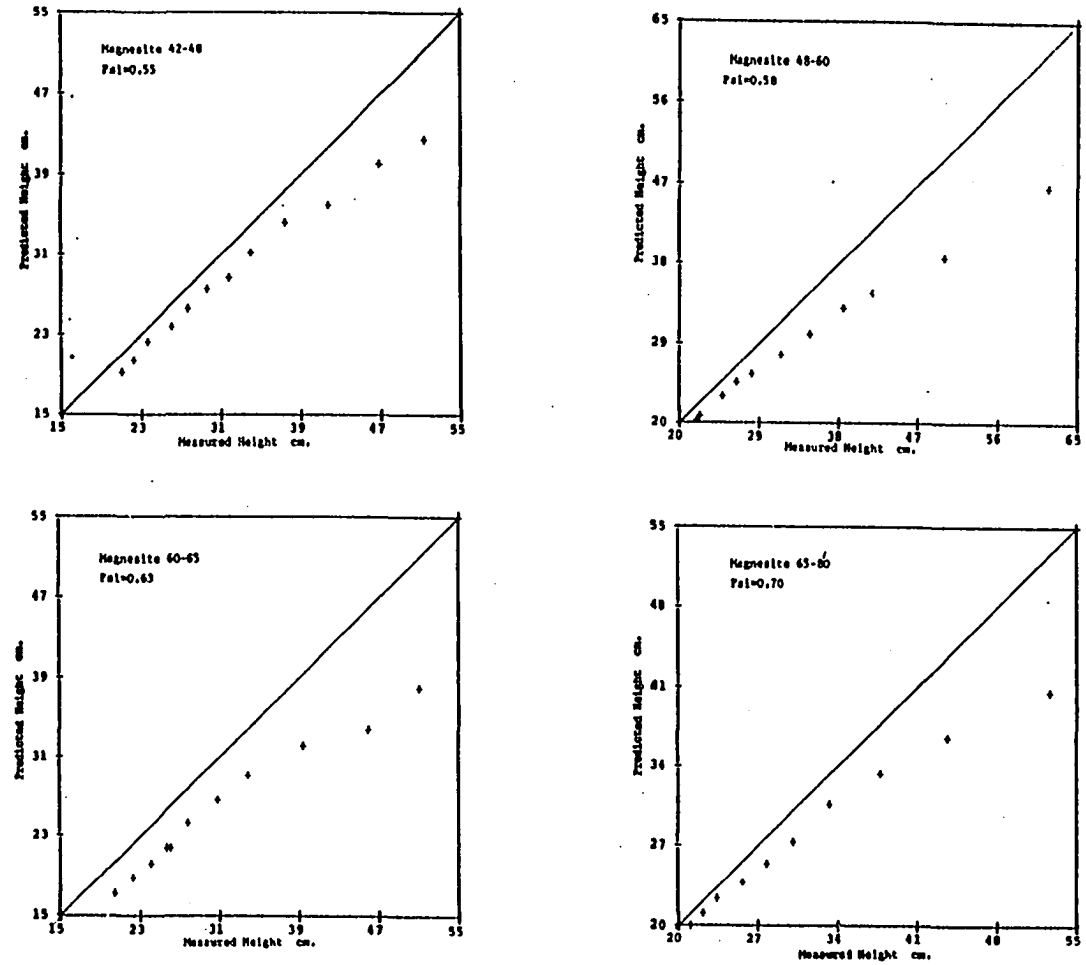

Figure 81. continued